Technical Physics, Vol. 49, No. 4, 2004, pp. 379–387. Translated from Zhurnal Tekhnicheskoĭ Fiziki, Vol. 74, No. 4, 2004, pp. 1–9.

THEORETICAL AND MATHEMATICAL PHYSICS

Calculation of the Vortex Pinning Energy in a Long Periodically Modulated Josephson Contact

M. A. Zelikman

St. Petersburg State Technical University, ul. Politekhnicheskaya 29, St. Petersburg, 195251 Russia

e-mail: outex@city.com.ru

Received June 25, 2003

Abstract—An analytical method for evaluating the Josephson and magnetic energies of a vortex, as well as the vortex pinning energy and its components, in a long periodically modulated Josephson contact is suggested. The method allows one to take into account the variation of the vortex shape with the position of the vortex. The results obtained with this method are much closer to those of exact computer analysis compared with results of the conventional techniques. The discrepancy between the exact shape of the vortex and a function obtained by solving a differential equation approximating the exact difference equation is studied. © *2004 MAIK "Nauka/Interperiodica"*.

INTRODUCTION

Recent investigations of high-temperature superconductors have shown that vortex structures have a considerable effect on processes occurring in the material. Specifically, those taking place when the sample is placed in a magnetic field are governed by vortex pinning and interaction.

Field penetration into the material is usually analyzed in terms of the Bean critical-state model, according to which vortices in the range occupied by the magnetic field are in equilibrium. In other words, the force exerted on a vortex by other vortices equals the maximal pinning force of the vortex. To calculate the field profile in the framework of the Bean model, it is necessary to know the field dependence of the pinning force. To verify the Bean model and to find its applicability domain, one should have an idea of the vortex structure and the behavior of vortices in the material.

Moreover, vortex motion gives rise to a specific energy loss mechanism that is different from usual Joule heating. Accordingly, energy losses exist (i.e., the superconducting state is broken) even in the absence of an electric resistance. Vortex pinning suppresses this mechanism. Therefore, increasing the critical currents and fields, a topical problem of superconductor science and technology, needs detailed knowledge of vortex behavior, structure, interaction, as well as the amount and mechanisms of pinning.

In recent years, the attention of the theorists and experimentalists has been focused on the problem of magnetic field penetration into a long periodically modulated Josephson contact. On the one hand, this is associated with recent interest in artificial structures of this type [1], with which theoretical predictions can be confirmed. On the other hand, it is a model problem that combines the processes taking place in superconductors: magnetic field expulsion, vortex generation, vortex pinning, and related phenomena (such as magnetic field penetration into the contact). Mathematically, this problem is much easier than the same problem for a 3D superconductor. Its solution is straightforward, which makes it possible to evaluate the vortex structure, find the pinning force and energy, verify the Bean model, shed light into occurring processes.

A periodically modulated Josephson contact (Fig. 1a) represents a thin insulating layer (the *xz* plane) sandwiched in superconductors and crossed by parallel infinitely long (in the *z* direction) insulating strips of thickness $2l$ (in the *y* direction) and width d (in the *x* direction). The strip spacing is L. An external magnetic field and the axes of vortices are aligned with the *z* axis. Figure 1b shows the structure of an artificially created periodically modulated Josephson contact [1]. Between the strips, the phase slowly varies with coordinate, while in crossing a strip, it changes in discrete steps. Let φ_k be the mean phase within a kth segment between the strips (Fig. 1a). The distribution of φ_k defines the steady state of the current.

The energy of a stationary vortex per meter of its length is given by [2, 3]

$$E = E_0 \sum_{k=-\infty}^{\infty} \left[\frac{1}{2}(\varphi_{k+1} - \varphi_k)^2 + I(1 - \cos\varphi_k)\right], \quad (1)$$

where $E_0 = hj_c\lambda^2/4el$, $I = 2Ll/\lambda^2$ is the pinning parameter, $\lambda = \sqrt{hc^2/8\pi j_c ed}$ is the Josephson length, j_c is the critical current density, e is the charge of an electron, and h is the Planck constant.

Later on, all energies will be expressed in units of E_0. The first term in (1) describes the magnetic energy

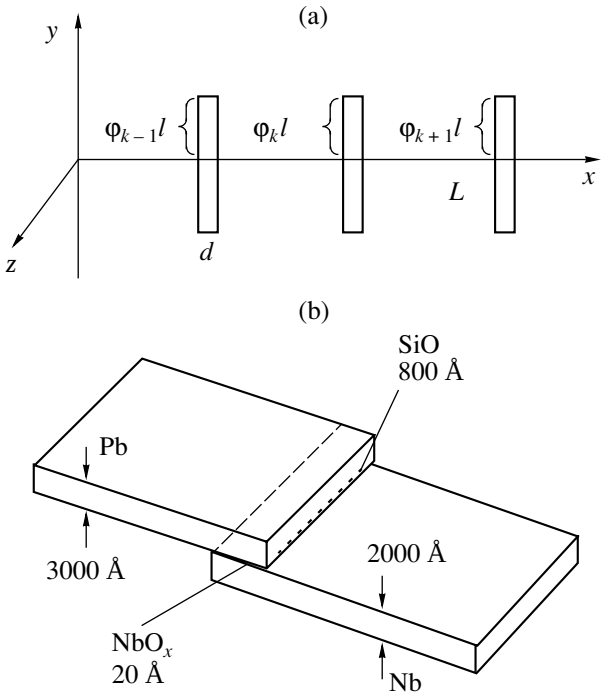

Fig. 1. (a) Model of a periodically modulated Josephson contact (the line is the projection of the contact plane onto the plane *xy*) and (b) structure of an artificially produced periodically modulated Josephson contact.

of a vortex; the second, the energy of Josephson contacts.

The equilibrium states of a vortex that correspond to extrema of its energy are described by a set of difference equations that follow from the condition $\partial E/\partial\varphi_m = 0$:

$$\varphi_{m+1} - 2\varphi_m + \varphi_{m-1} = I\sin\varphi_m. \quad (2)$$

A set of equations that is similar to (2) describes the behavior of planar vortices in a 3D Josephson medium [4].

Set (2) was first derived by Frenkel and Kontorova [5] for describing the behavior of edge dislocations in a crystal. Because of its discreteness, this set of equations allows one to study the behavior of solitons with allowance of pinning. The amount of pinning depends on a finite energy that is necessary to displace a vortex from one cell to another.

An exact analytical solution to nonlinear system (2) of finite difference equations is impossible to obtain. If the parameter I is small, the vortex distribution becomes quasi-continuous and set (2) turns into the differential equation

$$\frac{d^2\varphi}{dx^2} = I\sin\varphi, \quad (3)$$

where x is measured in units of L.

The Josephson, E_J, and magnetic, E_H, energies obtained from the quasi-continuous scheme when I tends to zero, do approach their exact values. However, the question remaining to be tackled is whether the total pinning energy may be extracted by using such a scheme. The fact is that the Josephson and magnetic components of the pinning energy, which are equal to the difference between the related energies at different positions of a vortex are of a much higher order in I and so may be disregarded in measurements. Below, it will be shown that the pinning energy components are proportional to $\exp(-\pi^2/\sqrt{I})$ and so cannot be expanded into a power series in I, which substantiates the above doubts.

In [6], the author analyzed the potential of different approximate approaches based on Eq. (3) to calculating the energies and compared different approximations with each other and with the exact solution to the starting problem. From this analysis, the following conclusions were drawn.

Exact computation of the vortex energy showed that (i) the Josephson and magnetic energies of a vortex diverge and (ii) the Josephson and magnetic components of the pinning energy are close in value but differ in sign, so that the total pinning energy is one order of magnitude lower than its components.

Theoretical analysis shows that the total pinning energy of a vortex having the shape described by a solution to set (2) of finite difference equations is independent of its position relative to cells of the medium under the assumption that its shape remains the same. In other words, the pinning energy equals zero. This means that the Josephson and magnetic components of the pinning energy are exactly the same in magnitude but differ in sign. A nonzero total pinning energy implies that the shape of a vortex depends on its position, the pinning energy being much lower than its components. It is such a relationship that results from exact computation.

Thus, the difference between the Josephson and magnetic components of the vortex energy, as well as different signs and almost equal magnitudes of the Josephson and magnetic components of the pinning energy, may be considered as typical features of the given problem. It is desirable that approximate approaches based on a solution to the differential equation include these features.

In our case, the discrete statement of the problem differs from the continuous one in that (i) summation in Eq. (1) for the energy is discrete; (ii) Eq. (1) has difference terms, such as $(\varphi_{k+1} - \varphi_k)^2$; and (iii) the shape of a vortex is found from finite difference set (2).

Elimination of all three items (i.e., the transition from summation to integration in (1), from finite differences to differentials in (1), and from finite difference set (2) to differential equation (3)) would mean complete rejection of discreteness. In this case, the Josephson and magnetic energies E_J and E_H turn our to be equal to each other and both components of the pinning energy vanish.

If the pinning energy is calculated using discrete equation (1) for energy (item "i"), the Josephson and magnetic energies E_J and E_H turn our to be equal to each other and are expressed by the same relationships as in the continuous approach; in this case, the pinning energy components are exactly the same but other than zero [3].

If difference terms in the expression for the magnetic energy (items "i" and "ii") are retained, the Josephson and magnetic energies of a vortex differ in magnitude and the Josephson and magnetic components of the pinning energy differ in sign [6]. Thus, with such an approach, we preserve both features mentioned above, i.e., make a step on the road to an exact solution.

Yet, comparing the energies obtained by this approach with those derived by exactly solving difference set (2) (items "i"–"iii" are valid) highlights the following considerable discrepancies.

(1) The Josephson and magnetic energies obtained with the two approaches differ, there being the difference in the relationship between the energies: in the approximate model, the magnetic energy E_H is lower than the Josephson energy for any I, while in the case of the exact solution, the situation is reverse.

(2) The exact values of the Josephson, ΔE_J, and magnetic, ΔE_H, components of the pinning energy are much higher than those obtained by the approximate approach.

(3) The exact values of ΔE_J and ΔE_H are close to each other. The approximate approach gives ΔE_J much higher than ΔE_H.

In this work, we modify the approximate approach suggested in [6] so that the above discrepancies are eliminated. Also, the approach modified accounts for the fact (discovered in [6]) that the exact and approximate values of the total pinning energy coincide, whereas its Josephson and magnetic components differ considerably.

BASIC EQUATIONS

The pinning energy of a vortex can be found if discrete sum (1) as a function of the vortex position is known. Using the expansion of a sum of δ functions into the Fourier series,

$$\sum_{k=-\infty}^{\infty}\delta(x-k) = \sum_{n=-\infty}^{\infty}\exp(i2\pi nx) = \mathrm{Re}\sum_{n=-\infty}^{\infty}\exp(i2\pi nx), \quad (4)$$

we represent expression (1) in the form

$$E = \sum_{k=-\infty}^{\infty} f(\varphi_k) = \int_{-\infty}^{\infty} f(\varphi(x+\alpha))\sum_{k=-\infty}^{\infty}\delta(x-k)dx = \mathrm{Re}\int_{-\infty}^{\infty} f(\varphi(x))\sum_{n=-\infty}^{\infty}\exp(i2\pi n(x-\alpha))dx, \quad (5)$$

where α is the coordinate of the vortex center relative to the edge of a cell. If, for example, the vortex is centered at the boundary between two cells, $\alpha = 0$; if it is at the center of a cell, $\alpha = 0.5$.

If he function $f(x)$ is even, expression (5) takes the form

$$E = 2\sum_{n=-\infty}^{\infty}\cos(2\pi n\alpha)\mathrm{Re}\int_{0}^{\infty} f(\varphi(x))\exp(i2\pi nx)dx. \quad (6)$$

As $\varphi(x)$, one may take a solution to differential equation (3), which replaces discrete set (2). For an isolated vortex, $\varphi(x)$ has the form

$$\varphi(x) = 4\arctan(\exp(-x\sqrt{I})). \quad (7)$$

The function (7) is plotted in Fig. 2. This solution corresponds to a vortex in a continuous medium. The use of the approximate solution, which ignores the discreteness of the medium, to calculate the pinning energy is an assumption that distorts the actual pattern. Figure 3 plots the function that is the difference between the solution to finite difference set (2) and function (7) divided by I. The run of this function is independent of I. As a next approximation, one could use a solution to a differential equation that is a more accurate approximation of discrete set (2) and substitute it into (6) (for details, see the Appendix). It turns out, however, that an exact solution to this differential equation is impossible to find throughout the range of the argument. Approximation of this solution by simple smooth functions refines the vortex energy value but cannot refine the pinning energy and its components, since both are very sensitive to the vortex shape. In other words, the refinement of the vortex shape cannot

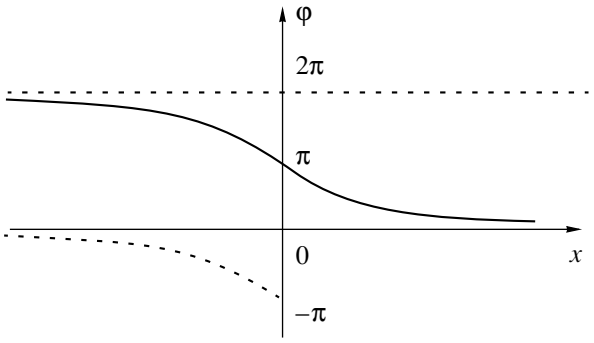

Fig. 2. Solution (7) to differential equation (3) for an isolated vortex.

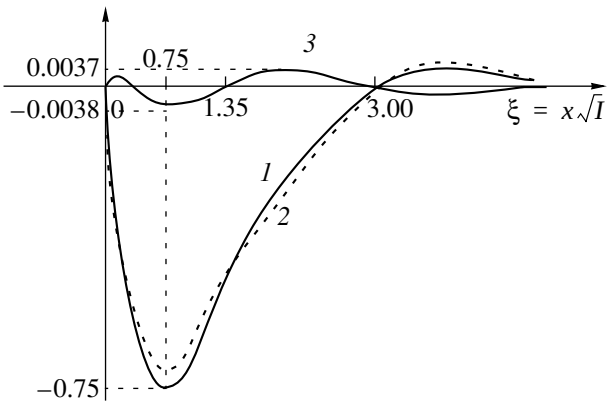

Fig. 3. (*1*) Function $\varphi_{IC}(\xi)$ calculated numerically, (*2*) its approximation $\rho(\xi)$, and (*3*) the difference $\rho(\xi) - \varphi_{IC}(\xi)$ between them.

improve the accuracy of calculating the pinning energy and its components.

We suggest a simpler yet more efficient way of refining the energy values. The basic idea is as follows. A desired exact solution must minimize the total energy given by (1). Function (7) involves the characteristic dimensionless length $1/\sqrt{I}$. This parameter arises upon solving differential equation (3), which is an approximation of exact equation (2). We take function (7) as a next approximation, substituting a reciprocal length ξ for $\sqrt{I}$. Our goal is to find the value of ξ minimizing expression (1).

While being mathematically simple, such an approach gives results that are closer to the exact solution, as will be shown below. The fact that the characteristic lengths for Eqs. (2) and (3) diverge (the difference is the most noticeable at small φ) also counts in favor of this approach. When φ is small, solution (7) to differential equation (3) takes the form $\varphi(x) = 4\exp(-x/\sqrt{I})$ and difference equation (2) is linearized and has the exact solution

$$\varphi_k = C\left(1 + \frac{I}{2} - \sqrt{I + \frac{I^2}{4}}\right)^k \approx C\exp\left(-k\sqrt{I}\left(1 - \frac{I}{24}\right)\right). \quad (8)$$

As follows from (8), the solutions to the difference and differential equations have different characteristic lengths even at small φ.

Based on formulas (6) and (7), the author derived the following expressions for the vortex energy components at $n = 0, \pm 1$ [6]:

$$E_{J0} = 4\sqrt{I}; \quad E_{J1} = 16\pi^2\exp\left(-\frac{\pi^2}{\sqrt{I}}\right)\cos(2\pi\alpha); \quad (9a)$$

$$E_{H0} = 4\sqrt{I} - \frac{1}{9}I^{3/2} + \frac{7}{1350}I^{5/2} + \ldots;$$
$$E_{H1} = -16\exp(-\pi^2/\sqrt{I})(2.43766 - I/12)\cos(2\pi\alpha). \quad (9b)$$

When ξ is substituted for $\sqrt{I}$ in formulas (9), the pinning parameter I may appear in them (i) as a result of substituting solution (7) or (ii) as the coefficient in the expression for the Josephson energy in (1). With the values of I appearing in the second way retained, we obtain for the total vortex energy

$$E_t = \frac{4I}{\zeta} + 4\zeta - \frac{\zeta^3}{9} + 16\exp(-\pi^2/\zeta)\left(\frac{\pi^2 I}{\zeta^2} - 2.4 + \zeta^2/12\right)\cos 2\pi\alpha. \quad (10)$$

When deriving formula (10), we left the first two terms in expression (9b) for the magnetic energy E_{H0}. At the same time, the last term on the right of (10), which is responsible for pinning, is retained, although it is several orders of magnitude smaller than those rejected. This term may be neglected in calculating corrections to the Josephson and magnetic energies of the vortex. Then, the total energy E_t reaches a minimum if

$$\zeta = \sqrt{I}(1 + I/24) = \sqrt{I} + \Delta, \quad (11)$$

where $\Delta = I^{1.5}/24$.

Eventually, the new values of the Josephson and magnetic energies are given by

$$\tilde{E}_{J0} = E_{J0} - 4\Delta = 4\sqrt{I} - \frac{I^{3/2}}{6}, \quad (12)$$

$$\tilde{E}_{H0} = E_{H0} + 4\Delta = 4\sqrt{I} + \frac{I^{3/2}}{18}. \quad (13)$$

When calculating the pinning energy and its components, one should leave the last term in (10), since it defines the variation of the vortex energy with vortex position. Theoretical analysis [6] showed that the total energy of a vortex whose shape is described by a solution to the set of difference equations under the assumption of shape invariability under displacement does not depend on the position of the vortex relative to cells of the medium. In other words, the pinning energy equals zero in this case. Accordingly, a nonzero total pinning energy reflects the fact that the shape of a vortex depends on its position. Formulas (9) for E_{J1} and E_{H1}, by which the pinning energy was evaluated in [6], were derived just under the assumption that the shape of a vortex is independent of its position; therefore, a nonzero pinning energy in [6] stems from the deviation of function (7) from the exact solution to Eq. (2). Hence, we may expect that the results will be greatly improved when the vortex shape variation with a coordinate is taken into account.

Importantly, the method suggested makes it possible to include the variation of the shape of a vortex when its energy is calculated in its different positions. When expression (10) is minimized with the last term on the right taken into account, the minima in different positions of the vortex center relative to the cell center are observed at various ξ, i.e., for various shapes of the vortex:

$$\zeta(\alpha) = \sqrt{I} + \Delta - \delta\cos 2\pi\alpha, \tag{14}$$

where

$$\delta = \frac{2\pi^2}{\sqrt{I}}\exp\left(-\frac{\pi^2}{\sqrt{I}}\right)\left(1 + \frac{\pi^2}{24}\sqrt{I}\right)(\pi^2 - 2.43766 - 2\sqrt{I}) \approx \frac{147}{\sqrt{I}}\exp\left(-\frac{\pi^2}{\sqrt{I}}\right)\left(1 + \frac{\sqrt{I}}{7}\right). \tag{15}$$

It should be noted that, when deriving expression (5), we took into account the next order of $\sqrt{I}$. The factor $(1 + \pi^2\sqrt{I}/24)$ arises when the second term in the expansion of $\exp(-\pi^2/(\sqrt{I} + \Delta))$ in Δ is retained.

For equilibrium positions of a vortex, i.e., when the vortex is centered at the boundary between two cells or at the center of a cell, $\cos 2\pi\alpha$ equals +1 or –1. Then, the Josephson and magnetic components of the pinning energy are given by

$$\Delta\tilde{E}_J = \Delta E_J\left(1 + \frac{\pi^2}{24}\sqrt{I}\right) + 8\delta = \frac{16\pi^2}{\sqrt{I}}\exp\left(-\frac{\pi^2}{\sqrt{I}}\right)\left(1 + \frac{\pi^2}{24}\sqrt{I}\right)(\pi^2 - 2.43766) \approx 8\delta(1 + 0.27\sqrt{I}), \tag{16}$$

$$\Delta\tilde{E}_H = \Delta E_H\left(1 + \frac{\pi^2}{24}\sqrt{I}\right) - 8\delta \approx -8\delta(1 + 0.07\sqrt{I}), \tag{17}$$

where ΔE_J and ΔE_H are the pinning energy components [6]:

$$\Delta E_J = 32\pi^2\exp\left(-\frac{\pi^2}{\sqrt{I}}\right), \quad \Delta E_H = -32\exp(-\pi^2/\sqrt{I})(2.43766 - I/12). \tag{18}$$

The total pinning energy is

$$\tilde{E}_p = \Delta\tilde{E}_J + \Delta\tilde{E}_H = E_p\left(1 + \frac{\pi^2}{24}\sqrt{I}\right) \approx 1.6\delta\sqrt{I}, \tag{19}$$

where

$$E_p = 32\exp(-\pi^2/\sqrt{I})(\pi^2 - 2.43766 + I/12) \tag{20}$$

is the pinning energy according to [6].

Thus, both the total pinning energy (19) and its components (16) and (17) are expressed through the parameter δ.

The values of $\Delta\tilde{E}_J$ and $\Delta\tilde{E}_H$ are roughly equal in magnitude but differ in sign, so that the total pinning energy $\tilde{E}_p$ modulo is much smaller than either of its components. Exact computation of the pinning energy yields exactly the same result.

It follows from (16) and (17) that, in accordance with theoretical predictions [6], the terms 8δ make a major contribution to the Josephson and magnetic components of the pinning energy. These terms describe the variation of the shape of the vortex when it is displaced relative to the cell.

Table 1. Josephson and magnetic energies found by various techniques

I	Theory [6], formula (9)		Corrected theory; formulas (12), (13), and (21)		Exact solution from [6]		Numerical calculation by (1) with φ_k from (A.9)	
	E_{J0}	E_{H0}	$\tilde{E}_{J0}$	$\tilde{E}_{H0}$	E_J	E_H	$\tilde{\tilde{E}}_J$	$\tilde{\tilde{E}}_H$
0.08	1.1314	1.1289	1.1276	1.1326				
			1.1275	1.1326	1.1275	1.1326	1.1277	1.1325
0.15	1.5492	1.5428	1.5395	1.5524				
			1.5394	1.5525	1.5393	1.5525	1.5398	1.5520
0.40	2.5298	2.5022	2.4877	2.5439				
			2.4865	2.5450	2.4860	2.5452	2.4890	2.5417
0.70	3.347	3.2836	3.2490	3.3792				
			3.2444	3.3838	3.2393	3.3853	3.252	3.373
1.00	4.000	3.894	3.833	4.055				
			3.822	4.067	3.806	4.073	3.840	4.041

Table 2. Pinning energy found by various techniques

I	Theory [6], formulas (18) and (20)			Corrected theory; formulas (16), (17), and (19)			Exact solution		
	ΔE_H	ΔE_J	E_P	$\Delta\tilde{E}_H$	$\Delta\tilde{E}_J$	$\Delta\tilde{E}_P$	ΔE_H	ΔE_J	E_P
0.08	–5.46E–14	2.22E–13	1.67E–13	–3.06E–12	3.25E–12	1.86E–13	–7.33E–12	7.77E–12	4.45E–13
0.15	–6.647E–10	2.705E–9	2.04E–9	–2.77E–8	3.009E–8	2.36E–9	–6.095E–8	6.617E–8	5.22E–9
0.40	–1.285E–5	5.27E–5	3.99E–5	–3.402E–4	3.905E–4	5.03E–5	–6.21E–4	7.14E–4	9.29E–5
0.70	–5.734E–4	2.38E–3	1.81E–3	–1.18E–2	1.42E–2	2.43E–3	–1.86E–2	2.24E–2	3.90E–3
1.00	–3.897E–3	1.63E–2	1.24E–2	–6.81E–2	8.57E–2	1.75E–2	–9.5E–2	1.21E–1	2.60E–2

Table 3. Pinning energy components with correcting factor included

I	Theory corrected by multiplying by $1.4\sqrt[4]{I}$			Exact solution from [6]		
	$\Delta\tilde{E}_H\frac{1.4}{\sqrt[4]{I}}$	$\Delta\tilde{E}_J\frac{1.4}{\sqrt[4]{I}}$	$\Delta\tilde{E}_P\frac{1.4}{\sqrt[4]{I}}$	ΔE_H	ΔE_J	E_P
0.08	–8.22E–12	8.7E–12	5.00E–13	–7.33E–12	7.77E–12	4.45E–13
0.15	–6.4E–8	6.9E–8	5.43E–9	–6.095E–8	6.617E–8	5.22E–9
0.40	–6.1E–4	7.0E–4	9.03E–5	–6.21E–4	7.14E–4	9.29E–5
0.70	–1.84E–2	2.22E–2	3.79E–3	–1.86E–2	2.24E–2	3.90E–3
1.00	–0.097	0.122	2.51E–2	–0.095	0.121	2.60E–2

RESULTS AND DISCUSSION

Table 1 lists the Josephson and magnetic energies of the vortex that are calculated by various formulas, as well as their exact values (more specifically, the half-sums of their values for a vortex in stable and unstable equilibrium) found by computer analysis [6]. It is seen that formulas (12) and (13) refined yield results, which are totally coincident with the exact values. Note that, when terms of the next order of smallness in I are taken into account in ζ and Δ,

$$\zeta = \sqrt{I}\left(1 + \frac{I}{24} + \frac{49I^2}{17\,280}\right) \qquad (21)$$

the approximate and exact values approach each other still closer (the bottom rows in Table 1). Taking into account the terms $\pm 4\Delta$ in (12) and (13) leads to the correct relationship between the Josephson and magnetic components of the vortex (the latter is smaller for any I).

Table 2 summarizes the pinning energy components found by various techniques. It is seen that the technique suggested in this work (formulas (16) and (17)) improves greatly agreement with the exact computer solution. The Josephson and magnetic components of the pinning energy are close to each other by magnitude but differ in sign. This agrees both with theoretical predictions and with the results of exact computation.

The values of the components also approach the exact values. The following fact is noteworthy. The ratio of the Josephson and magnetic components calculated by formulas (16), (17), and (19), as well as of the total pinning energy, to the related exact values is the same. To put it differently, the formulas derived yield a correct ratio of the total pinning energy to one of its component. It may be inferred that our technique for taking into account the variation of the vortex shape is adequate to the problem stated and that insignificant discrepancies of the calculated pinning energy and its components from the exact values are associated with inexact formula (15) for δ. When deriving (15), we used expressions (9), which follow from solution (7) to differential equation (3). As was mentioned above, Eq. (3) is an approximation of exact equation (2). Therefore, expression (15) is somewhat inaccurate, which comes as no surprise. Rather, the fact that the calculated and analytical (exact) results are very close to each other is surprising.

To improve agreement between the results of calculation and computer analysis, one may introduce a correcting factor of $1.4\sqrt[4]{I}$ into the expression for δ. Table 3 lists the pinning energy and its Josephson and magnetic components refined with this factor. Throughout the range of I, the calculation is in agreement with the exact values. Note that the exact computation was carried out to the 16th significant decimal place. More detailed analysis shows that, with such an accuracy, the pinning energy components cannot be calculated for $I < 0.08$. To check the validity of intro-

ducing this correcting factor in the case of low I, the accuracy of calculation should be improved.

To refine expressions (9), one would have to seek for a solution to a differential equation that approximates discrete equation (2) with a higher accuracy (see the Appendix). It turns out that such a differential equation is impossible to solve exactly throughout the range of I. Approximation of this solution by simple smooth functions refines the vortex energy value but cannot refine the pinning energy and its components, since both are very sensitive to the vortex shape. In other words, the approximate refinement of the vortex shape cannot improve the accuracy of calculating the pinning energy and its components. This fact attaches special value to the proximity of the exact values and those provided by the method suggested (recall that it is based on solving differential equation (3), which approximates exact difference equation (2)).

The given investigation allows us to answer the question [6] as to why the exact value of the pinning energy differs insignificantly from the results obtained in terms of the invariable vortex shape model, while individually the associated Josephson and magnetic components are in sharp disagreement. It follows from the aforesaid that the variation of the shape of a vortex under its displacement makes a major contribution to the pinning energy components. At the same time, the total pinning energy is found as the difference between the minimal energies of a vortex in two positions corresponding to two values of ζ (see (14)). Then, the transition to the case considered in [6] consists in substituting $\sqrt{I}$ for ζ in (14), i.e., in changing ζ by a value roughly equal to $\Delta = I^{1.5}/24$. Since a minimum of the energy corresponds to the zero first derivative of the energy with respect to ζ, a change in the energy is a quantity of the second order of smallness with respect to a change in the argument. Therefore, the energies of a vortex in its two equilibrium positions, as well as the difference in these energies, which is the total pinning energy, deviate from the related exact values insignificantly when the variation of the vortex shape is neglected (the case considered in [6]).

CONCLUSIONS

A method for calculating the Josephson and magnetic energies of a vortex, as well as the vortex pinning energy and its components, in a long periodically modulated Josephson contact is suggested. The method allows one to take into account the variation of the vortex shape with the position of the vortex.

The results obtained with this method are much closer to those of exact computer analysis than results of the conventional techniques. Specifically, (i) a correct relationship between the Josephson and magnetic energies of a vortex (the latter is smaller than the former for any value of the pinning parameter) is established, (ii) the Josephson and magnetic components of the pinning energy are close to each other but differ in sign in accordance with both theoretical predictions and results of exact computation, and (iii) the total pinning energy of a vortex and its Josephson and magnetic components approach their exact values.

The deviation of the exact vortex shape from a function obtained by solving a differential equation that approximates the exact difference equation is analyzed at length.

ACKNOWLEDGMENTS

This work was supported by the Ministry of Industry and Science of the Russian Federation (grant no. 40.012.1.1.1146) in the framework of the program "Controlled Superconductivity."

APPENDIX: FINDING OF THE REFINED VORTEX SHAPE

Let us derive a differential equation that approximates discrete equation (2) with a higher accuracy than Eq. (3). We expand φ_{m+1} and φ_{m-1} into a power series

$$\varphi_{m\pm1} = \varphi_m \pm \varphi_m^{\mathrm{I}} + \frac{1}{2}\varphi_m^{\mathrm{II}} \pm \frac{1}{6}\varphi_m^{\mathrm{III}} + \frac{1}{24}\varphi_m^{\mathrm{IV}} + \ldots. \quad \text{(A.1)}$$

Substituting (A.1) into (2) yields the differential equation

$$\varphi_m^{\mathrm{II}} + \frac{1}{12}\varphi_m^{\mathrm{IV}} + \frac{1}{360}\varphi_m^{\mathrm{VI}} + \ldots = I\sin\varphi_m. \quad \text{(A.2)}$$

Passing to the variable $\xi = x\sqrt{I}$ and omitting the subscript, we arrive at

$$\varphi^{\mathrm{II}} + \frac{I}{12}\varphi^{\mathrm{IV}} + \frac{I}{360}\varphi^{\mathrm{VI}} + \ldots = \sin\varphi. \quad \text{(A.3)}$$

Neglecting all terms but the first one on the left of (A.3), we obtain the approximation

$$\varphi^{\mathrm{II}} + \frac{I}{12}\varphi^{\mathrm{IV}} = \sin\varphi. \quad \text{(A.4)}$$

Thus, Eq. (3) approximates difference equation (2) up to the first order in I.

Having represented a solution to (A.4) as $\varphi = \varphi_0(\xi) + I\varphi_1(\xi)$, where $\varphi_0(\xi)$ is solution (7) to Eq. (3), we come to a differential equation for φ_1:

$$\varphi_1^{\mathrm{II}} - \cos\varphi_0\varphi_1 = -\frac{1}{12}\varphi_0^{\mathrm{IV}}. \quad \text{(A.5)}$$

From (A.5), it follows that φ_1 is a universal function for all sufficiently small values of I. A solution to (A.5) cannot be found analytically. Figure 3 (curve *1*) shows the plot of $\varphi_{1C}(\xi)$, which is the numerically calculated difference between the exact solution to difference equation (2) and function (7).

Table 4. Pinning energy components with corrected for vortex shape

I	Numerical calculation by (1) with function (A.9)			Exact solution from [6]		
	$\Delta\tilde{\tilde{E}}_H$	$\Delta\tilde{\tilde{E}}_J$	$\tilde{\tilde{E}}_P$	ΔE_H	ΔE_J	E_P
0.08	2.09E–6	1.98E–6	–2.3E–7	–7.33E–12	7.77E–12	4.45E–13
0.15	1.94E–5	1.86E–5	–7.6E–7	–6.095E–8	6.617E–8	5.22E–9
0.40	6.43E–4	7.45E–4	1.02E–4	–6.21E–4	7.14E–4	9.29E–5
0.70	5.12E–3	8.59E–3	3.46E–3	–1.86E–2	2.24E–2	3.90E–3
1.00	1.96E–3	4.14E–2	2.17E–2	–9.5E–2	1.21E–1	2.60E–2

Although Eq. (A.5) cannot be solved throughout the range of ξ, it can be solved at large ξ such that $\varphi_0(\xi) \ll 1$. Then, (A.5) takes the form

$$\varphi_1^{II} - \varphi_1 = -\frac{1}{3}\exp(-\xi). \qquad \text{(A.6)}$$

A solution to Eq. (A.6) that tends to zero at $\xi \longrightarrow \infty$ has the form

$$\varphi_1 = \left(C + \frac{1}{6}\xi\right)\exp(-\xi). \qquad \text{(A.7)}$$

Figure 4 shows the plot of the function $\psi(\xi) = \varphi_{1C}(\xi)\exp(\xi)$, where $\varphi_{1C}(\xi)$ is the function shown in Fig. 3. From Fig. 4, it is seen that ψ is a linear function of ξ for $\xi > 2$, which validates (A.7).

The value of the constant C is determined by the behavior of the function at small ξ. For $\xi \ll 1$ ($\varphi_0(\xi) \approx \pi$), Eq. (A.5) can also be solved and has the solution $\varphi_1 = C_1\sin\xi$. However, since the form of the function in the transition range is unknown, neither a relationship between C and C_1 nor the values of these constants can be found analytically. Using the point $\xi = 3$ where the plots in Figs. 3 and 4 intersect (this point is determined by numerical calculation), one can find that $C = -1/2$. Thus, a solution to Eq. (A.4) at $\xi \gg 1$ has the from

$$\varphi = \left(4 - \frac{I}{2} + \frac{I}{6}\xi\right)\exp(-\xi). \qquad \text{(A.8)}$$

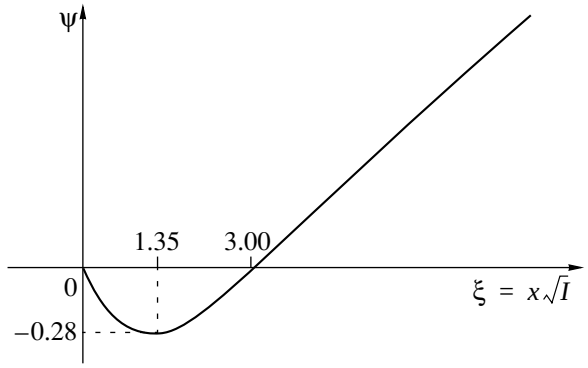

Fig. 4. Plot of the function $\psi(\xi) = \varphi_{IC}(\xi)\exp\xi$.

Note that, at $\varphi_m \ll 1$, difference equation (2) can be linearized and, hence, solved. Its solution has the form $\varphi_m = C\lambda^m$, where $\lambda = 1 + I/2 - \sqrt{I + I^2/4}$ (see formula (8)). With this solution, one can also arrive at expression (A.7).

At $\xi < 2$, difference equation (2) or differential equation (A.5) is impossible to solve. One may approximate curve *1* in Fig. 1 by a simple smooth function. For example, Fig. 3 plots the function $\rho(\xi) = -0.2\sin(\pi\xi/3)\exp(-\xi)$ (curve *2*) and the difference between this function and $\varphi_{1C}(\xi)$ calculated numerically (curve *3*).

The results of numerical calculation of the energy by formula (1) with

$$\varphi_k = \varphi_0(k) + I\rho(k) = 4\arctan\exp(-k\sqrt{I}) - 0.2I\sin(\pi k\sqrt{I}/3)\exp(-k\sqrt{I}) \qquad \text{(A.9)}$$

are listed in Tables 1 and 4. It is seen that the correction considerably narrows the gap between the Josephson and magnetic energies of the vortex and their exact values (columns 6–9 in Table 1).

However, the Josephson and magnetic components of the pinning energy differ significantly from their exact values (Table 4). This could be expected, since, as follows from formulas (5) and (6), the pinning energy components depend heavily on the form of a function used to describe the vortex shape [7]. A change in this function changes its plot insignificantly and has a minor effect on the vortex total energy but may appreciably affect the pinning energy. In particular, calculation by formula (6) causes terms varying as $I^{3.5}$ to appear in the expressions for the pinning energy components (in addition to terms of form $\exp(-\pi^2/\sqrt{I})$, see (9)). If I is small, these additional terms specify the values of the pinning energy components calculated by (6). That is why the component values differ from the exact values by several orders of magnitude (Table 4). As I grows, terms containing $\exp(-\pi^2/\sqrt{I})$ start playing a decisive role and the difference decreases yet remains significant.

As to the total pinning energy (Table 4), the correction approaches it to the exact value when I is relatively large and moves off from the exact value when $I \ll 1$.

REFERENCES

1. A. A. Golubov, I. L. Serpuchenko, and A. V. Ustinov, Zh. Éksp. Teor. Fiz. **94**, 297 (1988) [Sov. Phys. JETP **67**, 1256 (1988)].
2. S. N. Dorogovtsev and A. N. Samukhin, Europhys. Lett. **25**, 693 (1994).
3. V. V. Bryksin, A. V. Gol'tsev, S. N. Dorogovtsev, *et al.*, Zh. Éksp. Teor. Fiz. **100**, 1281 (1991) [Sov. Phys. JETP **73**, 708 (1991)].
4. M. A. Zelikman, Supercond. Sci. Technol. **9**, 795 (1997).
5. Ya. I. Frenkel and T. M. Kontorova, Fiz. Zh. **1**, 137 (1939).
6. M. A. Zelikman, Supercond. Sci. Technol. **14**, 371 (2001).
7. M. A. Zelikman, Zh. Tekh. Fiz. **72** (7), 28 (2002) [Tech. Phys. **47**, 821 (2002)].

Translated by V. Isaakyan

Technical Physics, Vol. 49, No. 4, 2004, pp. 388–395. Translated from Zhurnal Tekhnicheskoĭ Fiziki, Vol. 74, No. 4, 2004, pp. 10–17.

GASES AND LIQUIDS

On the Generation of Large Clusters in Forming Gas-Jet Targets for Lasers

A. S. Boldarev, V. A. Gasilov, and A. Ya. Faenov

Institute for Mathematical Modeling, Russian Academy of Sciences, Moscow, 125047 Russia

e-mail: boldar@imamod.ru

Received August 6, 2003

Abstract—The problem of increasing the mean size of clusters in gas-jet targets is tackled. Based on a mathematical model of clustering, the dependence of the cluster mean size on the nozzle length and rate of expansion is derived. The nozzle shape providing micrometer-size clusters is found. The parameters of gas-jet targets produced with this nozzle are studied in detail. © *2004 MAIK "Nauka/Interperiodica".*

INTRODUCTION

To date, investigation of the interaction between intense femtosecond laser pulses and cluster targets (cluster gas jets expanding into a vacuum) has become a routine experiment [1–24]. Clusters present in the gas jet (target) radically improve the efficiency of laser radiation absorption by the target, since their density is close to the density of a solid.

It has been shown [15, 18–20, 24] that, as the size of clusters increases, so do the yield of X-ray radiation and the ionization of a resulting plasma. This is because prepulses disintegrate coarse clusters to a lesser extent than fine clusters. Therefore, the plasma interacting with a major laser pulse has clear-cut dense bunches. Accordingly, the fraction of hot electrons grows.

In [10, 13, 23], a relationship between the prepulse duration τ_{pre} and the time of expansion of a cluster τ_{exp} is considered as a basic parameter governing laser pulse–target interaction. It is noted that, for $\tau_{pre} \gg \tau_{exp}$, the clusters have a chance to completely disappear before the main pulse is applied. In this case, the interaction is akin to that with an ordinary (cluster-free) gas jet, that is, has a low laser radiation absorption efficiency. Thus, of practical interest is the case $\tau_{pre} \sim \tau_{exp}$, where clusters disintegrate only partially. Since the prepulse duration is difficult to control, the ratio τ_{exp}/τ_{pre} can be increased largely by increasing the time of expansion of a cluster. This time grows with cluster size. In [23], τ_{exp} was estimated by the formula

$$\tau_{exp} \sim L_{cl}(m_i/Z_n kT_e)^{1/2}(10^{23}/N_{cr})^{1/3},$$

where Z_n and m_i is the charge and mass of an ion, N_{cr} is the cluster concentration critical for a given laser, and T_e is the electron temperature.

Hence, the time of expansion depends on the cluster linear size L_{cl}.

Thus, an increase in the cluster size is vital for improving the laser radiation absorption and X-ray radiation yield. Moreover, experiments with clusters of sizes exceeding those used today (up to 0.1 μm) may be useful for discovering resonance effects in laser absorption. The wavelength of a titanium–sapphire laser usually used in experiments [6–24] is 0.8 μm. One could expect that, as the cluster mean size reaches or exceeds this value, the type of interaction between laser radiation and a cluster will change qualitatively.

However, experimental conditions or specific applications impose certain requirements on the spatial structure of a cluster target. For example, the target parameter distribution should be as uniform as possible. Then, in experiments with an X-ray laser, such a spatially uniform cluster structure should be sufficiently wide. In other cases, conversely, the target should be as small as the beam spot to prevent the absorption of arising X-ray radiation by the cold (unheated by the laser) edges of the target.

Designing a cluster target (i.e., the selection of an appropriate nozzle shape, working material, and initial pressures and temperatures to provide desired target parameters, such as the cluster size and extent of a homogeneous cluster structure or desired spatial distribution of the parameters) runs into obstacles associated with the complex physics of clustering in gas jets (homogeneous condensation of a supercooled gas). It seems that this problem can be solved with the mathematical model of nozzle flows with homogeneous condensation that was applied earlier to the formation of cluster targets [16, 17, 23, 25]. The simulated distributions of the parameters of the two-phase medium behind the nozzle [16, 17, 20, 23–25] qualitatively agree with the situation observed experimentally. In addition [26], for a certain range of input parameters (the argon pressure between 20 and 60 bar and cluster diameters of up to 0.07 μm), quantitative agreement between calculated and experimental data, such as the

1063-7842/04/4904-0388$26.00

cluster mean size and cluster concentration, was achieved. This suggests that, in general, the model adequately describes the clustering kinetics and may so be used to calculate the cluster target parameters.

In this work, we apply numerical simulation of a cluster target [16, 17, 23, 25] with the aim to select the nozzle shape that provides the formation of clusters with a diameter of ≈1 μm. Another goal is to provide a homogeneous cluster medium with a cluster concentration as high as possible.

In the early simulation of a cluster target with this numerical technique [16, 17, 20, 23–25], we simulated two types of nozzles (Figs. 1a, 1b). The results of simulation in the form of the cluster mean radius spatial distribution at a distance of 1.5 mm away from the nozzle are shown in Fig. 2. From Fig. 2, it follows that, first, a conic nozzle (Fig. 1b) provides a much more uniform distribution of clusters than a Laval nozzle (a curved channel with the parabolic generatrix that has a cylindrical part before the outlet) (Fig. 1a). Next, the cluster mean size in the former case is noticeably higher. These observations were discussed at length in [16, 23, 25]. Finally, the cluster mean size grows with initial pressure and krypton clusters are coarser than argon ones, all other things being the same. This is because the state of a gas approaches the saturation line as the initial pressure rises and, under expansion from nozzle, condensation starts earlier. The same takes place in going from argon to krypton: the latter has a higher temperature of saturation (at the same pressure) or a lower pressure (at the same temperature) than argon.

However, even under the most favorable conditions, the cluster mean size is much smaller than 1 μm. Basically, the cluster size might be increased by raising the initial pressure. However, the pressure can hardly be raised significantly (e.g., by one order of magnitude) because of technical troubles and its slight rise (say to 100 bar) causes a minor growth of clusters. Therefore, it is necessary to find the nozzle shape generating large clusters at a moderate initial pressure. A conic nozzle providing a more uniform spatial distribution of the cluster target parameters is taken as the basis.

MATHEMATICAL MODEL OF NOZZLE FLOW WITH CLUSTERING

The flow of a finely dispersed two-phase fluid, such as a cluster gas, will be described in terms of parameters averaged over the medium (the density ρ, velocity **v**, and specific internal energy ε) and the moments of the cluster radius distribution function

$$\rho\Omega_n = \int_0^\infty f(r, \mathbf{x}, t) r^n dr; \quad n = 0, \ldots, 3.$$

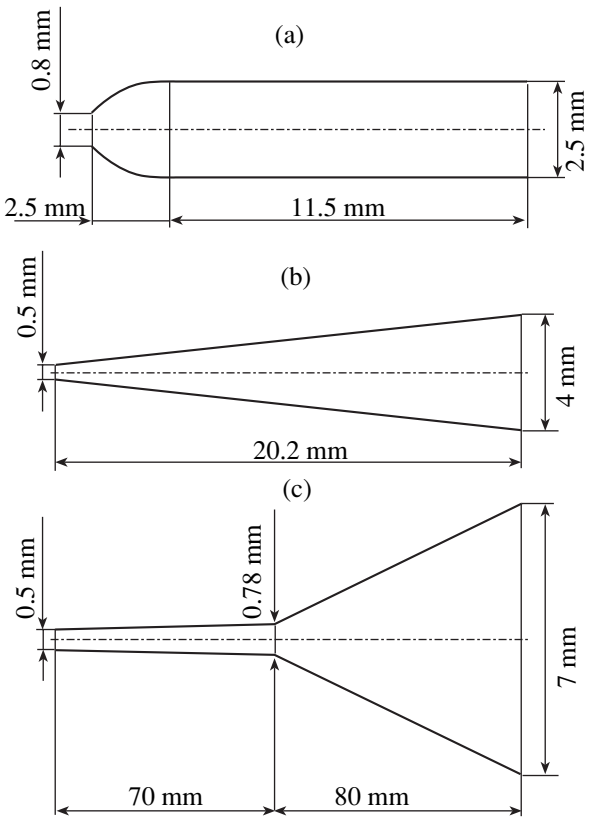

Fig. 1. (a) Laval and (b) conic nozzles used in earlier experiments and (c) nozzle optimized for the production of micrometer-size clusters.

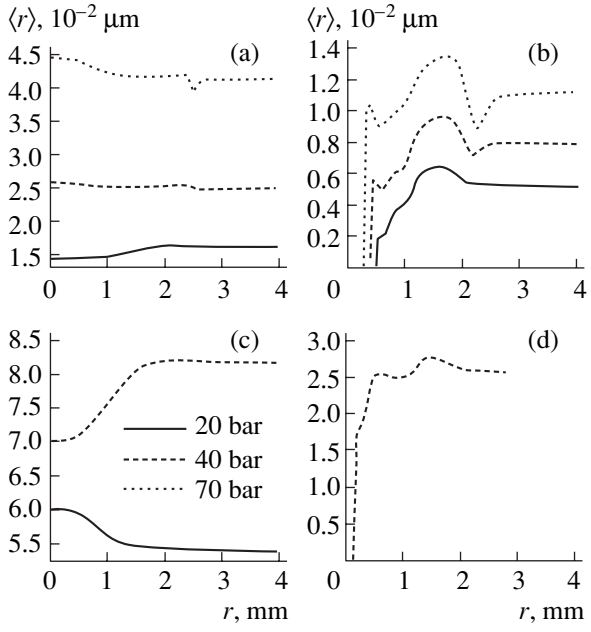

Fig. 2. Mean radius of argon and krypton clusters at different inlet pressures for variously shaped nozzles: (a) argon, conic nozzle; (b) argon, Laval nozzle; (c) krypton, conic nozzle; and (d) krypton, Laval nozzle.

Since the third moment Ω_3 is physically related to the weight ratio of the phases

$$\beta = 1 - \frac{4}{3}\pi\rho_l\Omega_3$$

(β is the dryness, i.e., the weight fraction of the gaseous phase, and ρ_l is the density of the liquid), such an approach allows us (under a number of additional assumptions) to write a closed set of differential equations:

$$\frac{\partial\rho}{\partial t} + \mathrm{div}(\rho\mathbf{v}) = 0, \quad (1)$$

$$\frac{\partial\rho\mathbf{v}}{\partial t} + \mathrm{div}\rho(\mathbf{v}\otimes\mathbf{v}) = -\mathrm{grad}P, \quad (2)$$

$$\frac{\partial}{\partial t}\left(\rho\varepsilon + \varepsilon\frac{\mathbf{v}^2}{2}\right) + \mathrm{div}\left(\rho\mathbf{v}\left(\varepsilon + \frac{\mathbf{v}^2}{2}\right)\right) = -\mathrm{div}P\mathbf{v}, \quad (3)$$

$$\frac{\partial\rho\Omega_n}{\partial t} + \mathrm{div}(\rho\mathbf{v}\Omega_0) = I, \quad (4)$$

$$\frac{\partial\rho\Omega_0}{\partial t} + \mathrm{div}(\rho\mathbf{v}\Omega_n) = Ir_*^n + n\dot{r}\rho\Omega_{n-1}\ (n = 1, 2), \quad (5)$$

$$\frac{\partial\rho\beta}{\partial t} + \mathrm{div}(\rho\mathbf{v}\beta) = -\frac{4}{3}\pi\rho_l r_*^3 I - 4\pi\rho\rho_l\dot{r}\Omega_2, \quad (6)$$

where the pressure P is estimated from the equation of state

$$P = P(\rho, \varepsilon, \beta) = \rho\frac{\varepsilon + (1-\beta)L_h}{\frac{\gamma}{\beta(\gamma-1)} - 1} \quad (7)$$

(L_h is the heat of phase transition and γ is the adiabatic index).

The kinetics of cluster formation and growth is defined by expressions for the critical nucleus radius r_*, cluster growth rate $\dot{r}$, and nucleation rate I:

$$r_* = \frac{2\sigma}{\rho_l RT\ln(P/P_s)}, \quad (8)$$

$$\dot{r} = \frac{P}{\rho_l\sqrt{2\pi RT}}\left(1 - \sqrt{\frac{T}{T_s(P)}}\right), \quad (9)$$

$$I = \frac{1}{\rho_l}\sqrt{\frac{2\sigma\mu}{\pi N_A}}\left(\frac{P}{kT}\right)^2\exp\left(-\frac{4\pi\sigma r_*^2}{3kT}\right). \quad (10)$$

Here, σ is the surface tension coefficient, R is the gas constant, $P_s(T)$ is the saturation pressure at a given temperature, $T_s(P)$ is the saturation temperature at a given pressure, μ is the molecular weight of the gas, N_A is the Avogadro number, and k is the Boltzmann constant.

The temperature T appearing in these expressions is given by

$$T = \frac{P}{\beta Z\rho R},$$

where Z is the compressibility of the gas.

Set (1)–(6) is solved in the two-dimensional or quasi-one-dimensional statement in the domain of computation that covers the cavity of a nozzle and (for the two-dimensional statement) a part of the free space adjacent to its exit section. At the entrance boundary, the boundary conditions are the equality of stagnation parameters to given P_0 and T_0:

$$\varepsilon + \frac{P}{\rho} + \frac{\mathbf{v}^2}{2} = \varepsilon_0 + \frac{P_0}{\rho_0},$$

$$S(P, \rho) = S(P_0, \rho_0),$$

where S is the entropy.

The nature of a specific gas (argon, krypton, etc.) is thus taken into consideration via the following parameters: $\rho_l(T)$, the density of the liquid; $\sigma(T)$, the surface tension coefficient; μ, the molar mass; $P_s(T)$ and $T_s(P)$, functions defining the shape of the saturation line; L_h, the heat of vaporization; γ, the adiabatic index; and Z, the compressibility.

For a more detailed description of the model, see [23, 25]. Use of the model, numerical methods, etc., are considered in [25].

NOZZLE SHAPE DESIGN

Our goal is to design a nozzle whose shape provides the formation of as many micrometer-size clusters as possible in argon and krypton jets. The initial parameters of the gas are $P_0 = 60$ bar and $T_0 = 293$ K. The nozzle critical diameter is taken to be 0.5 mm, and the outlet diameter is 7 mm (these values are typical of nozzles used in practice). Also, we will consider nozzles whose generatrix is a jogged line.

Numerous calculations and observations of the nozzle flow of a homogeneously condensing vapor have discovered a so-called condensation shock typically arising in such flows. This shock represents a thin layer where liquid phase nuclei originate intensely and, as a consequence, the vapor passes from the metastable supercooled state into the near-equilibrium state. Downstream of the condensation shock, the parameters of the medium are usually equilibrium; that is, in this area, the nuclei that have originated grow, while new nuclei do not form.

Thus, the cluster size is bound to depend largely on the number of nuclei in the condensation shock: the smaller the number of nuclei, the larger their size at the outlet. Several conic nozzles were tentatively analyzed in terms of the quasi-one-dimensional model (see table). Three initial parameters were given: the nozzle

Results of quasi-one-dimensional analysis of conic nozzles

α	L, mm	P_0, bar	β	n_{clust}, 10^{11} cm^{-3}	$\langle r\rangle$, μm	$\sigma(r)$, μm	$\langle N\rangle$, 10^5	n_{at}, 10^{18} cm^{-3}	n_{clust}/n_{at}, 10^{-8}
3.065	10.1	20	0.88	45	0.017	0.0028	5.2	20	22
3.065	10.1	40	0.86	28	0.028	0.0041	21	40	7.0
3.065	10.1	60	0.84	25	0.035	0.0047	39	60	4.1
3.065	20.2	20	0.88	11	0.028	0.0044	22	20	5.5
3.065	20.2	40	0.86	6.8	0.045	0.0061	84	40	1.7
3.065	20.2	60	0.84	5.6	0.057	0.0071	170	60	0.94
3.065	40.4	20	0.88	2.5	0.046	0.0069	99	20	1.2
3.065	40.4	40	0.85	1.4	0.076	0.010	410	40	0.36
3.065	40.4	60	0.84	1.1	0.098	0.012	860	60	0.19
6.13	10.1	20	0.80	60	0.012	0.0017	1.6	4.7	130
6.13	10.1	40	0.77	42	0.018	0.0021	5.2	9.4	45
6.13	10.1	60	0.75	35	0.022	0.0026	10	14	25
6.13	20.2	20	0.79	16	0.018	0.0025	6.1	4.7	34
6.13	20.2	40	0.76	11	0.027	0.0033	20	9.4	12
6.13	20.2	60	0.75	9.2	0.035	0.0039	39	14	6.5
6.13	40.4	20	0.79	4.3	0.029	0.0035	23	4.7	9.1
6.13	40.4	40	0.76	2.4	0.046	0.0055	94	9.4	2.5
6.13	40.4	60	0.74	1.9	0.059	0.0069	190	14	1.4
12.258	10.1	20	0.73	55	0.008	0.0011	0.54	1.1	490
12.258	10.1	40	0.70	42	0.012	0.0015	1.6	2.2	190
12.258	10.1	60	0.68	37	0.014	0.0017	2.9	3.3	110
12.258	20.2	20	0.73	19	0.012	0.0015	1.6	1.1	170
12.258	20.2	40	0.70	12	0.018	0.0021	5.5	2.2	55
12.258	20.2	60	0.68	9.6	0.023	0.0027	11	3.3	29
12.258	40.4	20	0.72	4.8	0.019	0.0024	6.5	1.1	43
12.258	40.4	40	0.69	2.7	0.030	0.0038	25	2.2	12
12.258	40.4	60	0.68	1.9	0.039	0.0048	56	3.3	5.8

area expansion α, which is the ratio of the outlet-to-critical diameter, the nozzle length L, and the gas initial pressure P_0. In all three cases, the initial temperature was taken to be 293 K, the gas was argon, and the nozzle was a truncated cone. On the right of the table, the parameters calculated at the exit section of each of the nozzles are listed. The notation is as follows: n_{clust}, the cluster concentration; $\langle r\rangle$, the cluster mean radius; $\sigma(r)$, the standard deviation of the radius from its mean; $\langle N\rangle$, the mean number of atoms in a cluster; and n_{at}, the mean atomic concentration in the two-phase target.

It follows from the table that the mean atomic concentration n_{at} is independent of the nozzle length but is uniquely defined by the nozzle area expansion α and inlet (initial) pressure, the pressure dependence being almost linear. This is because the atomic concentration depends on gasdynamic factors and remains virtually the same upon clustering.

The dryness β is also almost independent of the nozzle length and is defined by the expansion and inlet pressure. The explanation is that, at the outlet, we have essentially an equilibrium two-phase medium, as was noted above. Therefore, the fraction of one or the other phase at this point depends on thermodynamic equilibrium rather than on kinetic factors; so, it does not vary with rate of expansion.

At the same time, the parameters related to the cluster size (the mean radius $\langle r\rangle$ and the mean number of atoms $\langle N\rangle$) depend considerably on the nozzle length. With the expansion and inlet pressure fixed, the lower the rate of expansion, the larger the clusters. This fact is supported by the observation that the cluster concentration declines with increasing inlet pressure. The reason for such an effect is that, as the inlet pressure rises, the condensation shock shifts upstream, where the rate of expansion of the square of the nozzle is lower, because the nozzle is axisymmetric and its cross-sectional area

is proportional to the square of the nozzle radius in a given section. The cluster concentration is naturally related to the cluster size, since the total amount of the cluster material is uniquely determined by the mean atomic concentration and dryness.

From the aforesaid, the basic qualitative conclusion can be drawn: to produce coarse clusters, a nozzle must expand as smoothly as possible (at least, near the condensation shock), while the cluster concentration is high if large-α (fast expanding) nozzles are employed.

Thus, the dispersity of the medium at the nozzle outlet depend mostly on the relative concentration of clusters n_{clust}/n_{at}. Since nucleation is absent downstream of the condensation shock, the relative cluster concentration rises in the vicinity of the condensation shock from zero to a value characteristic of a given nozzle and then remains unchanged.

The relative number of clusters, mean number of atoms in a cluster, and dryness are related through the obvious relationship

$$\frac{n_{clust}}{n_{at}}\langle N\rangle = 1-\beta.$$

Using this relationship, one can estimate the value of n_{clust}/n_{at} that is necessary for the formation of micrometer-size clusters. From the best variant given in the table ($\alpha = 3.065$, $L = 40.4$ mm, and $P_0 = 60$ bar), it follows that we must increase the mean radius fivefold, i.e., increase $\langle N\rangle$ by a factor of 125. However, $1-\beta = 0.16$ in this variant, while the nozzle being designed has $\alpha = 14$. Hence, $1-\beta$ at the outlet will be no less than 0.32; that is, we may rely on a twofold increase in $1-\beta$. Thus, the relative concentration of clusters is bound to decrease by a factor of 62.5 to $n_{clust}/n_{at} = 3\times10^{-11}$.

The next stage is selecting a conic nozzle with an expansion angle such that it provides the desired value of n_{clust}/n_{at}. From a series of tentative quasi-one-dimensional calculations with decreasing expansion angles of conic nozzles, we chose a 70-mm-long cone with larger and smaller diameters of 0.78 and 0.5 mm, respectively. For these values, the condensation shock was observed in the immediate vicinity of the outlet section.

It will be recalled, however, that our nozzle must have an outlet diameter of 7 mm. To merely extend the cone with the expansion angle found seems unacceptable, since the nozzle would be too long (longer than 150 mm), difficult to make, and experimentally inappropriate. It was therefore decided to attach a cone with a wider expansion angle. Since clustering is absent in this new part of the nozzle, the faster expansion of the gas downstream of the condensation shock was expected not to adversely affect the parameters of the medium (namely, n_{clust}/n_{at}) that were achieved at the shock.

However, tentative quasi-one-dimensional calculations showed that the second condensation shock

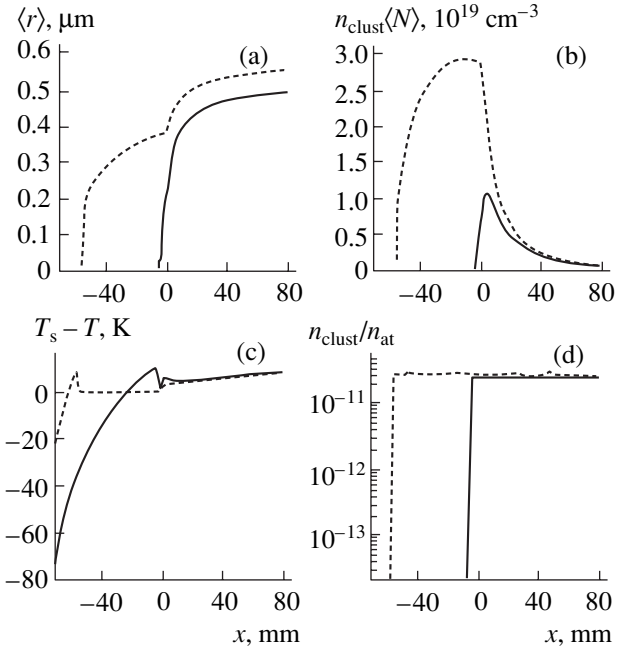

Fig. 3. Parameter distributions along the nozzle (quasi-one-dimensional calculation): (a) cluster mean radius $\langle r\rangle$ (b) concentration $n_{clust}\langle N\rangle$ of clustered atoms, (c) supercooling $T_s - T$, and (d) relative concentration of clusters n_{clust}/n_{at}. Data for argon and krypton are shown by the solid and dashed curves, respectively.

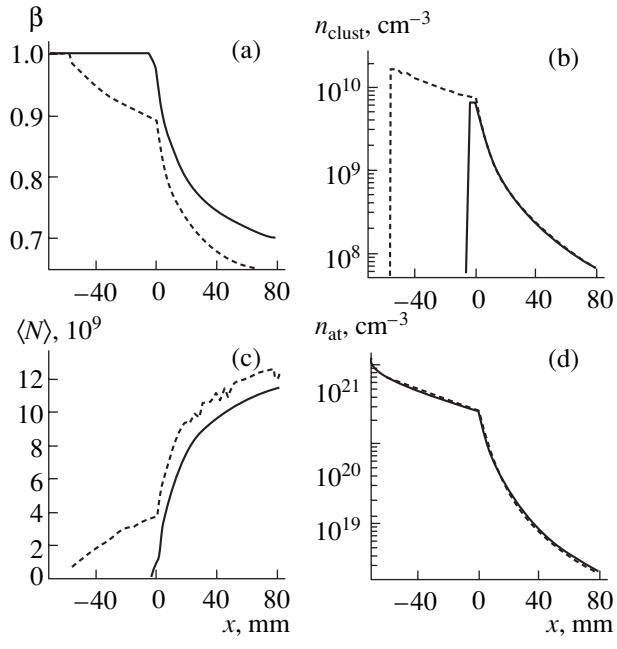

Fig. 4. Parameter distributions along the nozzle (quasi-one-dimensional calculation): (a) dryness β (b) cluster concentration n_{clust}, (c) mean number $\langle N\rangle$ of atoms in a cluster, and (d) mean concentration n_{at} of atoms. Data for argon and krypton are shown by the solid and dashed curves, respectively.

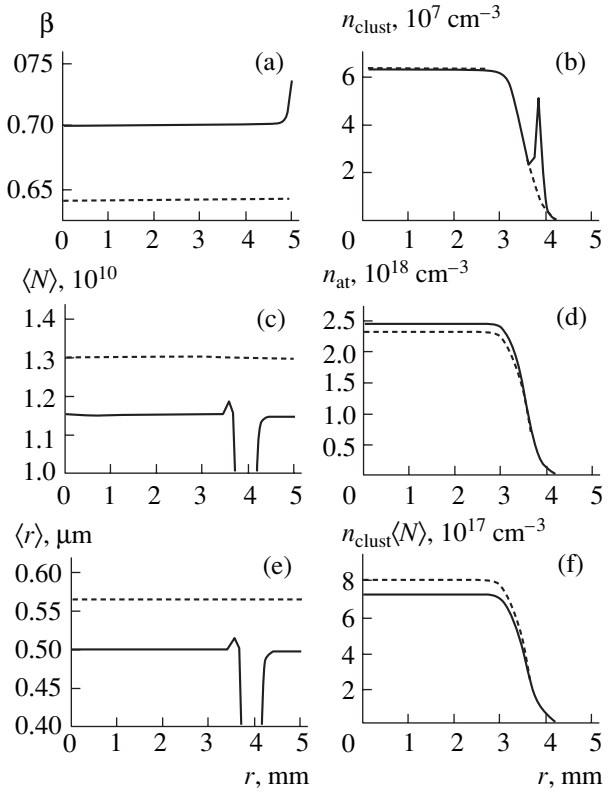

Fig. 5. Parameter distributions across the jet at a distance of 1.5 mm away from the nozzle exit section (two-dimensional calculation): (a) dryness β (b) cluster concentration n_{clust}, (c) mean number $\langle N \rangle$ of atoms in a cluster, (d) mean concentration n_{at} of atoms, (e) cluster mean radius $\langle r \rangle$, and (f) concentration $n_{clust}\langle N \rangle$ of clustered atoms. Data for argon and krypton are shown by the solid and dashed curves, respectively.

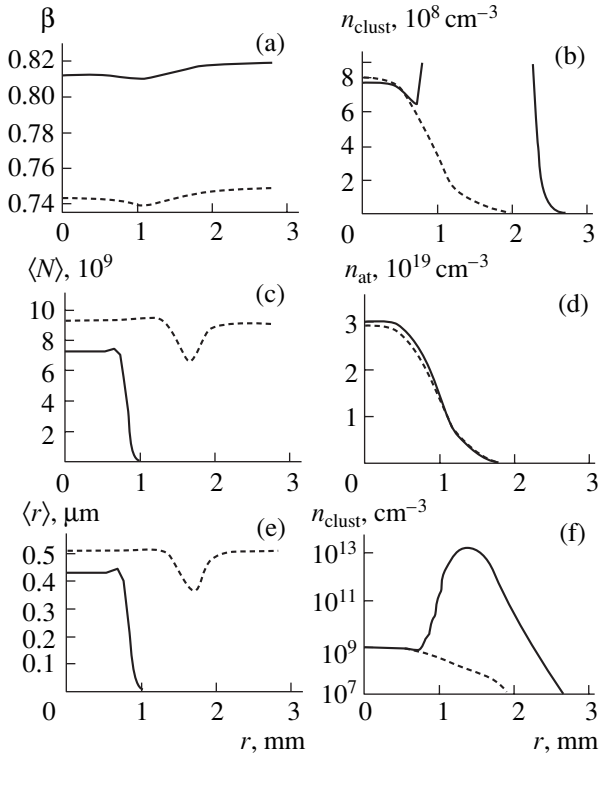

Fig. 6. Parameter distributions across the jet at a distance of 1.5 mm away from the exit section of the shortened nozzle (two-dimensional calculation): (a) dryness β, (b) cluster concentration n_{clust}, (c) mean number $\langle N \rangle$ of atoms in a cluster, (d) mean concentration n_{at} of atoms, (e) cluster mean radius $\langle r \rangle$, and (f) cluster concentration on the semilog scale. Data for argon and krypton are shown by the solid and dashed curves, respectively.

appears now in the fast-expanding part of the nozzle if a gas containing a very small number of clusters expands too rapidly. The parameter n_{clust}/n_{at} grows by several orders of magnitude in this case and micrometer-size clusters do not form at the outlet of such a nozzle.

Therefore, we had to make the second, fast-expanding, cone fairly long. As follows from our quasi-one-dimensional estimations, reasonable results are obtained when its length is 80 mm.

NOZZLE ANALYSIS

Thus, we have designed a 150-mm-long nozzle (Fig. 1c), which is composed of two base-connected truncated cones. The former (smaller) cone expands from a base diameter of 0.5 mm (the critical diameter of the nozzle) to a base diameter of 0.78 mm over a length of 70 mm. The latter (larger) cone expands from a diameter of 0.78 mm to a diameter of 7 mm over a length of 80 mm.

Figures 3 and 4 demonstrate the parameter distributions along the nozzle according to our quasi-one-dimensional calculations for an inlet pressure P_0 = 60 bar. The results for argon and krypton are shown by solid and dashed curves, respectively.

In the case of krypton, which has a higher boiling temperature than argon (at the same pressure), the condensation shock is usually observed upstream of the shock for argon. As a rule, krypton clusters are larger. It is seen that, in our case, krypton clusters are actually larger, though insignificantly, than argon ones.

Figure 3c shows that the flow in the larger cone (at $x > 0$) is no longer equilibrium: the supercooling in it grows both for argon and krypton. However, nucleation in the larger cone is absent under the given conditions (the relative cluster concentration n_{clust}/n_{at} remains constant at a level of $\approx 3 \times 10^{-11}$). As a result, clusters formed in the smaller cone reach micrometer sizes at the nozzle outlet.

The parameter distributions across the jet at a distance of 1.5 mm away from the outlet section of the nozzle are shown in Fig. 5 (two-dimensional calculations). The distributions are seen to be fairly uniform and agree well with the quasi-one-dimensional calcula-

tions. This is of no surprise, since the nozzle of necessity was made long and narrow with a very smooth variation of the cross-sectional size, and the quasi-one-dimensional model is quite adequate for such a nozzle.

Along with the basic design (Fig. 1c), a shortened version of the nozzle was also considered. Here, the former larger cone expands to 2 mm (rather than to 7 mm) with the same expansion angle. Accordingly, its length diminishes to 15.7 mm. Such a version is of interest, because the cluster mean radius increases insignificantly over most of the larger cone (Fig. 3a). At the same time, the concentration of clusters (Fig. 4b) drops considerably. It might therefore be expected that, using the shortened nozzle, we can produce a cluster target of lesser extent in which the mean size of clusters is somewhat smaller but their concentration is appreciably higher. Figure 6 shows the parameter distributions at a distance of 1.5 mm away from the shortened nozzle outlet. The cluster concentration did increase by one order of magnitude, whereas the cluster size diminished insignificantly (for both argon and krypton). For the shortened nozzle, the quasi-one-dimensional model falls short of ideal and the parameters across the jet vary much more considerably than for the long design. However, in this case, too, there is an area of diameter 1.0–1.5 mm where the parameters remain invariable.

A supersonic gas jet leaving the nozzle expands into a vacuum, and rarefaction waves therewith form at its edges. Within these waves, the gas expands further, which may lead to the formation of one more condensation shock. In this case, a high concentration of tiny clusters is observed; that is, the situation is the same as for large-α nozzles. This is certainly a pure two-dimensional effect, since the quasi-one-dimensional model applies to the nozzle flow alone.

This effect is illustrated in Fig. 6: visually argon clusters at the edges of the jet become negligibly small, but their concentration grows sharply. The growth is so sharp that we failed to scale Fig. 6b in such a way that both plots (for argon and krypton) are seen simultaneously on the normal scale. Therefore, Fig. 6f is constructed on the semilog scale. It follows from Fig. 6 that the concentration of argon clusters rises by four orders of magnitude.

For krypton, this effect is less pronounced: only a small dip is observed in the related curves (Figs. 6c, 6e) and the concentration profile remains monotonic (Fig. 6b).

In the case of the long nozzle, the effect of secondary clustering at jet expansion is much weaker (Fig. 5). The concentration of argon clusters somewhat rises at $r \approx 3.8$ mm (Fig. 5), and accordingly the cluster size decreases (Figs. 5c, 5e). For krypton clusters, such an effect is not observed.

CONCLUSIONS

Thus, our mathematical model of nozzle flow with homogeneous condensation basically may be applied to designing nozzles that provide a cluster target with the desired parameters. A nozzle generating coarse (about 1 μm in size) clusters in argon and krypton jets is suggested. The parameter distributions simulated for a two-phase medium at the outlet are highly uniform.

It should be noted that earlier this model was not applied to such coarse clusters and such fast expansion. It is therefore not improbable that any side effects, e.g., disintegration of drops, are not included in the model. There may be other reasons why the model fails in a specific case. For example, an error in the nucleation rate shifts the condensation shock down- or upstream. In this case, the parameters of the medium at the nozzle outlet depend heavily on whether the condensation shock will fall into the smaller or larger cone. Experimental verification of the results obtained in this work would shed more light on the adequacy of the model and its applicability domain.

The nozzle designed in this work makes it possible to experiment with very large clusters (≈1 μm), for which the ratio τ_{exp}/τ_{pre} is very high. One therefore may expect an appreciable increase in X-ray radiation yield, i.e., in the efficiency of laser-to-X-ray-radiation conversion.

ACKNOWLEDGMENTS

This work was supported by the CRDF (project no. RP1-2328-ME-02) and the Russian Foundation for Basic Research (project no. 02-01-00708).

REFERENCES

1. A. McPherson, B. D. Tompson, A. B. Borisov, *et al.*, Nature **370**, 631 (1994).
2. T. Ditmire, T. Donnelly, A. M. Rubenchik, *et al.*, Phys. Rev. A **53**, 3379 (1996).
3. T. Ditmire, J. Zweiback, V. P. Yanovsky, *et al.*, Nature **398**, 490 (1999).
4. T. Ditmire, R. A. Smith, J. W. G. Smith, *et al.*, Phys. Rev. Lett. **78**, 3121 (1997).
5. T. Ditmire, J. W. G. Tisch, E. Springate, *et al.*, Phys. Rev. Lett. **78**, 2732 (1997).
6. J. Zweiback, R. A. Smith, T. E. Cowan, *et al.*, Phys. Rev. Lett. **84**, 2634 (2000).
7. E. Parra, T. Alexeev, J. Fan, *et al.*, Phys. Rev. E **62**, R5931 (2000).
8. E. Lamour, S. Dreuil, J.-C. Gauthier, *et al.*, Proc. SPIE **4504**, 97 (2001).
9. J.-P. Rozet, M. Cornille, S. Dobosz, *et al.*, Phys. Scr. **T92**, 113 (2001).
10. T. Auguste, P. d'Oliveira, S. Hulin, *et al.*, Pis'ma Zh. Éksp. Teor. Fiz. **72**, 54 (2000) [JETP Lett. **72**, 38 (2000)].

11. S. Dobosz, M. Schmidt, M. Perdrix, *et al.*, Pis'ma Zh. Éksp. Teor. Fiz. **68**, 454 (1998) [JETP Lett. **68**, 485 (1998)].
12. C. Stents, V. Bagnoud, F. Blasco, *et al.*, Kvantovaya Élektron. (Moscow) **30**, 721 (2000).
13. J. Abdallah, Jr., A. Ya. Faenov, I. Yu. Skobelev, *et al.*, Phys. Rev. A **63**, 032706 (2001).
14. S. Dobosz, M. Schmidt, M. Perdrix, *et al.*, Zh. Éksp. Teor. Fiz. **115**, 2051 (1999) [JETP **88**, 1122 (1999)].
15. A. I. Magunov, T. A. Pikuz, I. Yu. Skobelev, *et al.*, Pis'ma Zh. Éksp. Teor. Fiz. **74**, 412 (2001) [JETP Lett. **74**, 375 (2001)].
16. A. S. Boldarev, V. A. Gasilov, F. Blasco, *et al.*, Pis'ma Zh. Éksp. Teor. Fiz. **73**, 583 (2001) [JETP Lett. **73**, 514 (2001)].
17. G. C. Junkel-Vives, J. Abdallah, Jr., T. Auguste, *et al.*, Phys. Rev. E **65**, 036410 (2002).
18. G. C. Junkel-Vives, J. Abdallah, Jr., F. Blasco, *et al.*, J. Quant. Spectrosc. Radiat. Transf. **71**, 417 (2001).
19. G. C. Junkel-Vives, J. Abdallah, Jr., F. Blasco, *et al.*, Phys. Rev. A **64**, 021201 (2001).
20. A. Y. Faenov, I. Y. Skobelev, A. I. Magunov, *et al.*, Proc. SPIE **4504**, 121 (2001).
21. G. C. Junkel-Vives, J. Abdallah, Jr., F. Blasco, *et al.*, Phys. Rev. A **66**, 033204 (2002).
22. S. B. Hansen, A. S. Shlyaptseva, A. Y. Faenov, *et al.*, Phys. Rev. E **66**, 046412 (2002).
23. I. Yu. Skobelev, A. Ya. Faenov, A. I. Magunov, *et al.*, Zh. Éksp. Teor. Fiz. **121**, 88 (2002) [JETP **94**, 73 (2002)].
24. I. Yu. Skobelev, A. Ya. Faenov, A. I. Magunov, *et al.*, Zh. Éksp. Teor. Fiz. **121**, 1124 (2002) [JETP **94**, 966 (2002)].
25. A. S. Boldarev and V. A. Gasilov, Mat. Model. **15** (3), 55 (2003).
26. A. S. Boldarev, V. A. Gasilov, F. Blasco, *et al.*, in *Proceedings of the European Conference on Laser Interaction with Matter (ECLIM), 2002;* Proc. SPIE **5228**, 446 (2002).

Translated by V. Isaakyan

Technical Physics, Vol. 49, No. 4, 2004, pp. 396–404. Translated from Zhurnal Tekhnicheskoĭ Fiziki, Vol. 74, No. 4, 2004, pp. 18–26.

GAS DISCHARGES, PLASMA

Analysis of the Mechanisms for the Scattering of Plasma Particles by Non-Steady-State Fluctuations

V. I. Khvesyuk and A. Yu. Chirkov

Bauman Moscow State Technical University, Moscow, 105005 Russia

e-mail: khves@power.bmstu.ru

Received July 10, 2003

Abstract—Results of a numerical analysis of the interaction between plasma particles and the wave packets of electrostatic fluctuations are presented. The influence of the dynamic parameters of the particles and packets on the particle scattering is studied. It is shown that, in general, the electron scattering by such a kind of fluctuations differs qualitatively from the ion scattering. Estimates of the parameters of collisionless diffusion are proposed. © *2004 MAIK "Nauka/Interperiodica".*

INTRODUCTION

In [1, 2], a new approach to studying transport processes in tokamak plasmas was proposed. In those papers, a discrete set of the resonant surfaces was considered. For each of them, there is an infinite set of electrostatic wave modes. It is assumed that the amplitudes of all waves are the same, time-independent, and exponentially decrease with increasing distance from the resonant surface. The modes corresponding to the resonant surfaces overlap. Summation of the modes reduces the wave field pattern to a set of wave packets (fluctuations). In this model, the abnormal transport is governed by the scattering of charged particles by such a kind of fluctuations. We note that the authors of [1, 2] did not consider any specific type of oscillations and did not take into account the structure of the wave packets. They considered modes distributed uniformly over all frequencies (from $-\infty$ to $+\infty$) and possessing the same (in absolute value) phase velocity, which resulted in a set of infinitely narrow steady-state wave packets (δ functions).

In the general case, the interaction of particles with wave packets depends on the frequency range of the modes, their wavelengths, and the dispersion of the phase velocities. Therefore, it is of interest to analyze the particle interaction with wave packets formed according to the dispersion relations for certain types of plasma waves.

It is just such a problem of the interaction between particles and wave packets that is considered in the present paper. The calculations are performed for the frequency and wavelength ranges corresponding to low-frequency and lower hybrid drift instabilities [3–12]. The quantization conditions at the resonant surface lead to a finite set of discrete modes. It is assumed that the mode amplitudes decrease with increasing distance from the resonant surface, which corresponds to nonlocal solutions for drift waves propagating in a nonuniform plasma [10, 12]. Such a representation of the wave fields corresponds to non-steady-state two-dimensional wave packets.

The objective of this study is to investigate the influence of the parameters of particles and wave packets on the final result of their interaction. The main particle parameters are the energy, velocity relative to a wave packet, cyclotron radius, cyclotron frequency, and the phase of Larmor gyration at the interaction instant, while the main parameters of the wave packets are the frequencies, wavelengths, spatial dimensions, amplitudes, and the rates at which the amplitudes change.

1. NUMERICAL MODEL

We consider a cylindrical plasma configuration that is homogeneous along the z axis. In this model, the magnetic field B depends only on radius r and is directed along the z axis, while the waves propagates along the azimuthal coordinate θ. We also take into account a steady-state radial electric field $E_R(r)$.

The particle motion and particle fluxes are calculated in the model of collisionless diffusion across the magnetic field under the action of many modes of electrostatic drift oscillations [1, 2, 13, 14]. It is assumed that, many modes form localized nonsteady wave packets that propagate across the magnetic field and the plasma density gradient. The modes are assumed to be electrostatic, and the potential of each of the packets is described by the expression

$$\tilde{\varphi} = \sum_n \varphi_{0n} g_\perp(r) \cos(-\omega_n t + k_{\perp n} r\theta + k_{\parallel n} z + \psi_n), \quad (1)$$

where n is the mode number; $g_\perp(r)$ is the radial profile of the packet; φ_{0n} and ψ_n are the amplitudes and initial phases of the modes, respectively; ω_n is the frequency; $k_{\perp n} = 2\pi n r_s/\lambda_0 r$ is the azimuthal wavenumber; λ_0 is the

1063-7842/04/4904-0396$26.00 © 2004 MAIK "Nauka/Interperiodica"

maximum wavelength in the packet spectrum; $k_{\|n}$ is the longitudinal wavenumber, $k_{\|n} \ll k_{\perp n}$; and r_s is the value of the radial coordinate determining the parameters of the packet ($r = r_s$ approximately corresponds to the maximum of the profile $g_\perp(r)$). A set of discrete resonant surfaces $r = r_s$ ($s = 1, 2, 3, \ldots$) is introduced.

The quantities ω_n and $k_{\perp n}$ are related by the dispersion relation $\omega(k_\perp)$. The components of the electric field are defined by potential (1):

$$\tilde{E_r} = -\partial\tilde{\varphi}/\partial r,$$

$$\tilde{E_\theta} = -\frac{1}{r}\frac{\partial\tilde{\varphi}}{\partial\theta},$$

where tilde stands for the perturbations of the corresponding quantity.

Thus, wave packets of form (1) are non-steady-state two-dimensional formations.

We note that, according to the theory of drift instabilities [5, 6], the emergence of non-steady-state low-frequency drift waves is possible only at $k_\| \neq 0$, while high-frequency drift instabilities (lower hybrid and drift-cyclotron ones) may develop at $k_\| = 0$. When simulating cross-field transport both in high-frequency and low-frequency ranges, we do not take into account the influence of the longitudinal component $k_\|$ (note that low-frequency drift instability develops at $k_\| \ll k_\perp$ [6]). The maximum level of the potential fluctuations $\Delta\varphi_m$ in our calculations was determined by the relative amplitude

$$\varepsilon_m = \frac{e\Delta\varphi_m}{k_B T_e}, \tag{2}$$

where e is the electron charge, k_B is the Boltzmann constant, and T_e is the electron temperature.

It is assumed that the basic contribution to the wave fields comes from modes with the wavenumbers $k_\perp$ close to that at which the instability growth rate is maximum. This allows one to linearize the dispersion relation for each wave packet:

$$\omega(k_\perp) \approx \omega_0 + v_g(k_\perp - k_0), \tag{3}$$

where ω_0 and v_g are the frequency and group velocity of the packet, which are determined from the exact dispersion relation at $k_\perp = k_0$.

In principle, the wavenumber k_0 can be chosen rather arbitrarily in the instability range. For example, $k_\perp = k_0$ may correspond to the maximum of the instability growth rate. It should be noted that, in some cases, the maxima of the frequency $\omega(k_\perp)$ and growth rate $\gamma(k_\perp)$ of drift waves may correspond to close values of k [12]. Depending on the sign of the derivative $\partial\omega/\partial k_\perp$ of the exact dispersion relation, the group velocity in Eq. (3) may be directed either parallel to the phase velocity or opposite to it. In both cases, the wave packets in linear approximation (3) are periodical pulsed perturbations propagating at the velocity v_g with no spreading.

The radial electrostatic field E_R, which may arise in the plasma spontaneously or be applied externally, causes azimuthal rotation of the plasma. In this case, the group velocity depends on E_R as follows:

$$v_g = v_{g0} + V_E = v_{g0} - \frac{E_R}{B}, \tag{4}$$

where V_E is the velocity of azimuthal electric drift and v_{g0} is the group velocity in the reference frame rotating together with plasma.

It should be noted that v_{g0} may depend on the strength of the radial electrostatic field E_R (see, e.g., [9]) and also on its gradient dE_R/dr.

We also note that, approximate dispersion relation (3) ensures that wave packets are nonsteady, except for the case $\omega_0 = v_g k_0$. In this case, the dispersion relation has the form $\omega = v_g k_\perp$ and the wave packets have the form of solitonlike electrostatic perturbations whose shape does not change in time. In the applicability range of the drift approximation, such perturbations does not cause the displacement of the plasma particles electrons and ions across the magnetic field.

In our model, we consider localized fluctuations with $\delta_\| \ll \lambda_0$, where $\delta_\|$ is the length of a wave packet along its propagation direction. Packets with $\lambda_0 \gg \rho_{Ti}$ and $\omega \ll \omega_{ci}$ (where ρ_{Ti} is the ion Larmor radius in terms of the ion thermal velocity and ω_{ci} is the ion cyclotron frequency) correspond to low-frequency drift waves [6], while packets with $\lambda_0 \sim \rho_{Te}$ and $\omega_{ci} \ll \omega \ll \omega_{ce}$ (where ρ_{Te} is the electron Larmor radius in terms of the electron thermal velocity and ω_{ce} is the electron cyclotron frequency) correspond to lower hybrid drift waves [6]. In the intermediate range $\lambda_0 \sim \rho_{Ti}$ and $\omega \sim \omega_{ci}$, drift-cyclotron waves can exist [7].

In the given geometry, the trajectories of particles of kind α are determined by numerically solving the dynamic equations

$$m_\alpha \frac{dv_{r\alpha}}{dt} = q_\alpha[\tilde{E_r} + E_R(r) + v_{\theta\alpha}B], \tag{5}$$

$$m_\alpha \frac{dv_{\theta\alpha}}{dt} = q_\alpha(\tilde{E_\theta} - v_{r\alpha}B), \tag{6}$$

where m_α, q_α, $v_{r\alpha}$, and $v_{\theta\alpha}$ are the mass, charge, and the radial and azimuthal components of the particle velocity, respectively.

At $\delta_\| \gg \rho_\alpha$, $\omega \ll \omega_{c\alpha}$, and $v_g \ll v_{\alpha\perp}$ (where ρ_α is the cyclotron radius and $v_{\perp\alpha} = \sqrt{v_{r\alpha}^2 + v_{\theta\alpha}^2}$ is the velocity component normal to the magnetic field), the motion of a particle of kind α affected by a packet with given parameters ($\delta_\|$, ω_0, and v_g) can be considered in the drift approximation. In this case, the velocity of the par-

ticle guiding center relative to the wave packet is equal to

$$u_\alpha = |V_{dr} - v_g| = \left| -\frac{E_R}{B} + \frac{m v_{\perp\alpha}^2}{2 q_\alpha B^2}\frac{dB}{dr} - v_g \right| = \left| \frac{m v_{\perp\alpha}^2}{2 q_\alpha B^2}\frac{dB}{dr} - v_{g0} \right|. \quad (7)$$

Particle dynamic equations (5) and (6) follow from the Hamilton equations

$$\frac{dp_r}{dt} = -\frac{\partial H}{\partial r}, \quad \frac{dr}{dt} = \frac{\partial H}{\partial p_r},$$

$$\frac{dP_\theta}{dt} = -\frac{\partial H}{\partial \theta}, \quad \frac{d\theta}{dt} = \frac{\partial H}{\partial P_\theta},$$

where $H = H(t, r, \theta, p_r, P_\theta)$ is the Hamiltonian, $p_r = m v_r$, $P_\theta = m r v_\theta + q\Psi$, and Ψ is the function of the poloidal magnetic flux (the subscript α is omitted).

The Hamiltonian of a particle is equal to

$$H = \frac{p_r^2}{2m} + \frac{(P_\theta - q\Psi)^2}{2mr^2} + q\tilde{\varphi} + q\varphi_R, \quad (8)$$

where φ_R is the potential of the radial electrostatic field E_R.

The particles affected by the fluctuating fields are deflected in the radial direction, normally to the magnetic field.

The particle flux from a certain surface of radius ($r - |\Delta r| < r' < r + |\Delta r|$) through a given surface of radius r is

$$\Gamma'(r') = N(r')\Delta r \nu, \quad (9)$$

where N is the particle density, Δr is the displacement of the particle guiding center, and ν is the effective frequency of interaction between particles and fluctuations.

The total flux is equal to the sum of the oppositely directed fluxes through the given surface:

$$\Gamma(r) \approx -\frac{1}{3}\Delta r_m^2 \nu \frac{\partial N}{\partial r}, \quad (10)$$

where

$$D = \frac{1}{3}\Delta r_m^2 \nu$$

is the effective diffusion coefficient and Δr_m is the maximum displacement of the particle guiding center in a single interaction with a fluctuation.

When defining flux (10), we assumed that the radial displacement may take any value in the range $-\Delta r_m \le \Delta r \le \Delta r_m$ with the same probability and that $\Delta r_m \ll L_N$, where

$$L_N = \left(\frac{1}{N}\frac{\partial N}{\partial r}\right)^{-1}$$

is the characteristic scale on which the plasma density varies.

Expression (10) is usually employed to determine particle fluxes inside the plasma. When determining losses through the plasma boundary, it is more correct to use expression of form (9) for the convective flux

$$\Gamma^{\text{conv}} \approx \frac{1}{2}\Delta r_m \nu N.$$

The calculations performed in [13–16] showed that the motion of plasma particles in the field of many wave packets is stochastic. Then, the estimation of the particle fluxes associated with the collisionless transport mechanism under consideration is reduced to determining the values Δr_m and ν. We performed a series of calculations in order to reveal the basic relationships and characteristics of the interaction between a particle and a single wave packet.

The calculations were performed under a number of simplifying assumptions. The potential profile $\tilde{\varphi}$ in the direction of fluctuation propagation y (in cylindrical coordinates, $y = r\theta$) was approximated by a function

$$\tilde{\varphi} = \Delta\varphi_m \cos(-\omega_0 t + \psi_0) g_\parallel(\theta - \omega_g t) g_\perp(r), \quad (11)$$

where ω_0 accounts for the non-steady-state character of the wave packet, ψ_0 is the initial phase, and $\omega_g = v_g/r_{s0} = \text{const}$ is the angular velocity of the packet propagation in the azimuthal direction.

The value ω_g was calculated using the group velocity at the point $r = r_{s0}$ corresponding to the maximum of the radial profile $g_\perp$. In these calculations, the radial profile $g_\perp$ was chosen to be sufficiently wide, so that its characteristic width $\delta_\perp$ was certainly larger than the maximum displacement of the particle guiding center Δr_m. The function $g_\parallel$ was assumed to have a triangular shape.

Results of the calculations of the interaction between particles and wave packets (fluctuations) are presented in Sections 2 and 3. We performed calculations for both ions and electrons. The relationships obtained for ions and electrons are similar at the same ratios $\omega_{c\alpha}/\omega_0$, $\rho_\alpha/\delta_\parallel$, and $v_{\perp\alpha}/v_{g0}$ ($\alpha = i, e$). Therefore, for definiteness, all the results in Sections 2 and 3 are given for ions. The consideration for ions is limited to two regimes: a regime of drift motion ($\delta_\parallel \gg \rho_i$ and $\omega \ll \omega_{ci}$) and a regime of instantaneous interaction ($\delta_\parallel \ll \rho_i$ and $\omega \gg \omega_{ci}$).

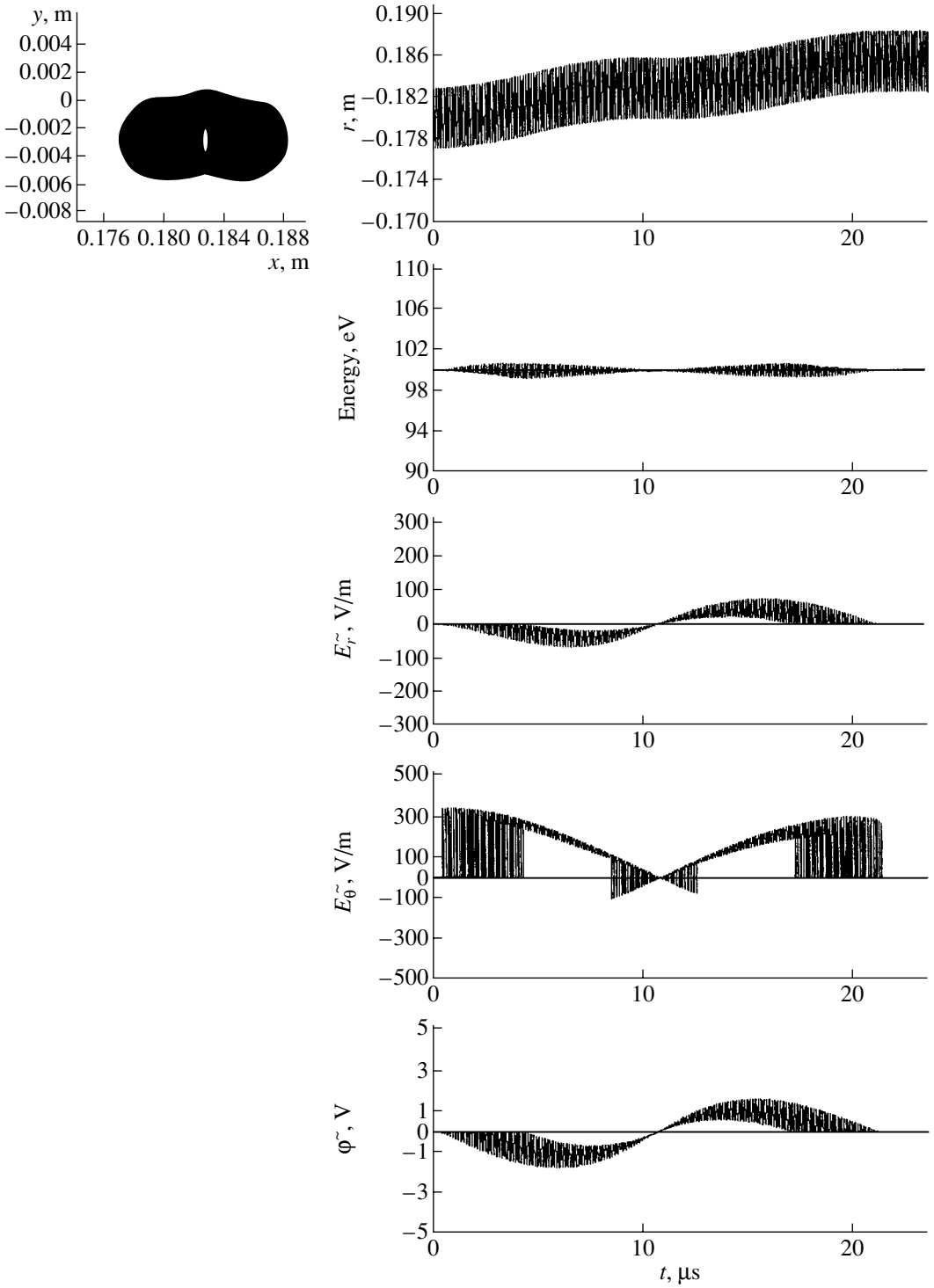

Fig. 1. Calculated dynamics of an ion (proton) influenced by a long-wavelength wave packet: $B = 0.5$ T, the plasma radius is $a = 0.2$ m, $T_i = 100$ eV, $T_e = 100$ eV, $\rho_i = 0.29$ mm, the initial ion energy is 100 eV, $r_{s0} = 0.18$ m, $\Delta\varphi_m = 4$ eV, $v_{g0} = -0.01 v_{Ti}$, $\delta_\parallel = 4\rho_{Ti} = 11.6$ mm, $\omega_0 = \omega_{mi} = 1.5 \times 10^5$ rad/s, and $\psi_0 = 0$.

2. INTERACTION BETWEEN PARTICLES AND FLUCTUATIONS AT $\delta_\parallel \gtrsim \rho$ AND $\omega \ll \omega_c$

Typical results of the calculations of the interaction between a particle and a long-wavelength fluctuation are presented in Fig. 1, which shows the particle trajectory in the plane (x, y) normal to the magnetic field, as well as the time evolution of the radial coordinate r and energy of the particle, the components $E_r^{\sim}$ and $E_\theta^{\sim}$ of

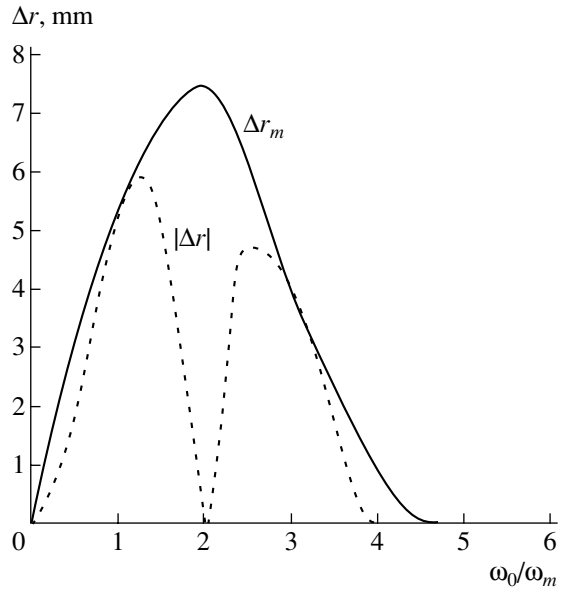

Fig. 2. Radial displacement of an ion (proton) at the initial phase of the wave packet $\psi_0 = 0$ (dashed line) and the maximum displacement over the entire range of ψ_0 (solid line) as functions of the wave frequency ω_0. The values of B, a, T_i, T_e, ρ_i, r_{s0}, $\Delta\varphi_m$, v_{g0}, $\delta_\parallel$ are the same as in Fig. 1.

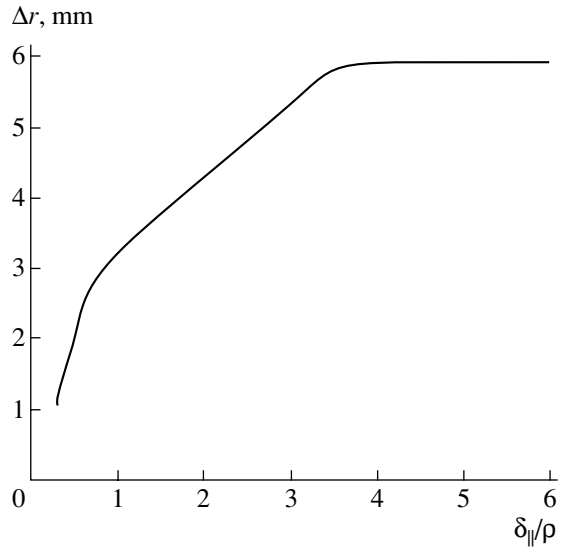

Fig. 3. Radial displacement of an ion (proton) as a function of the longitudinal size of the wave packet. The values of $\delta_\parallel$, B, a, T_i, T_e, ρ_i, r_{s0}, $\Delta\varphi_m$, v_{g0}, and ω_0 are the same as in Fig. 1.

the electric field of the packet, and the packet potential $\tilde{\varphi}$ along the particle trajectory.

The calculations showed that, as frequency ω_0 increases, the displacement increases until the time t_{int} of the interaction between a particle and a fluctuation becomes on the order of π/ω_0. The dependence of the displacement on the ratio ω_0/ω_m is shown in Fig. 2. In the case under consideration, the interaction time is $t_{\text{int}} = 2\delta_\parallel/u$ and, at $\omega_0 < \omega_m$ the displacement increases nearly in proportion to ω_0/ω_m, where

$$\omega_m = \frac{\pi|v_{g0}|}{2\delta_\parallel + 2\rho}. \tag{12}$$

When studying low-frequency drift waves, it is the range $\omega_0 < \omega_m$ that is of most interest because, for these waves, $\omega_m \gtrsim \omega_d = v_d/r$, where v_d and ω_d are the velocity and frequency of the diamagnetic drift. At $\omega_0 > 2\omega_m$, the displacement decreases sharply in magnitude. At $\delta_\parallel \sim \rho$, this decrease is monotonic (Fig. 2), while at $\delta_\parallel \gg \rho$, it is nonmonotonic.

According to the calculated results, the maximum particle displacement across the magnetic field lines at $\omega_0 < \omega_m$ can be evaluated by the formula

$$\Delta r_m = \frac{\langle \tilde{E_\theta} \rangle}{B} t_{\text{int}} = \eta_\delta \frac{\Delta\varphi_m}{Bu} \frac{\omega_0}{\omega_m}, \tag{13}$$

where the angular brackets stand for averaging along the particle trajectory over the time interval $0 \le t \le t_{\text{int}}$ and the coefficient η_δ accounts for the finiteness of the Larmor radius (as compared to the fluctuation size $\delta_\parallel$).

Figure 3 presents the calculated particle displacement as a function of the ratio $\delta_\parallel/\rho$. According to the calculated results, for $\delta_\parallel \gg 3.5\rho$, we have $\eta_\delta \approx 1$, while for $\delta_\parallel < 3.5\rho$, we have $\eta_\delta \approx \delta_\parallel/(3.5\rho) \approx 0.3\delta_\parallel/\rho$. We note that displacement (13) does not exceed the characteristic width of the packet radial profile $\delta_\perp$.

The frequency of interactions in the long-wavelength low-frequency range under consideration is equal to $\nu = u/\lambda_0$.

Low-frequency drift instability develops at relatively low β (β is the ratio of the plasma pressure to the magnetic field pressure); hence, the magnetic field dB/dr is weakly nonuniform in this case. Therefore, for most of the particles, we have $u \approx |v_{g0}|$ because the gradient-drift velocity entering in Eq. (7) can be ignored and, at $\omega_0 < \omega_m$, we can assume that

$$\Delta r_m = 2\varepsilon_m \frac{k_B T_e}{eB} \frac{\eta_\delta(\delta_\parallel + \rho)\omega_0}{\pi v_{g0}^2}. \tag{14}$$

Resonant particles with $u \approx 0$ should be considered separately because they are capable of making a significant contribution to the total flux. For a Maxwellian distribution, the density of the resonant particles is equal to $N^{\text{res}} \approx N\exp(-v_{\text{res}}^2/v_T^2)$, where v_{res} is the value of the transverse velocity component $v_\perp$ determined from the condition $u = 0$ and v_T is the particle thermal velocity.

The flux of resonant particles can be estimated as

$$\Gamma^{\text{res}} \approx \frac{1}{3} N^{\text{res}} \frac{\Delta\varphi_m}{\delta_\parallel B} = \frac{1}{3} N^{\text{res}} \varepsilon_m \frac{k_B T_e}{eB\delta_\parallel}. \tag{15}$$

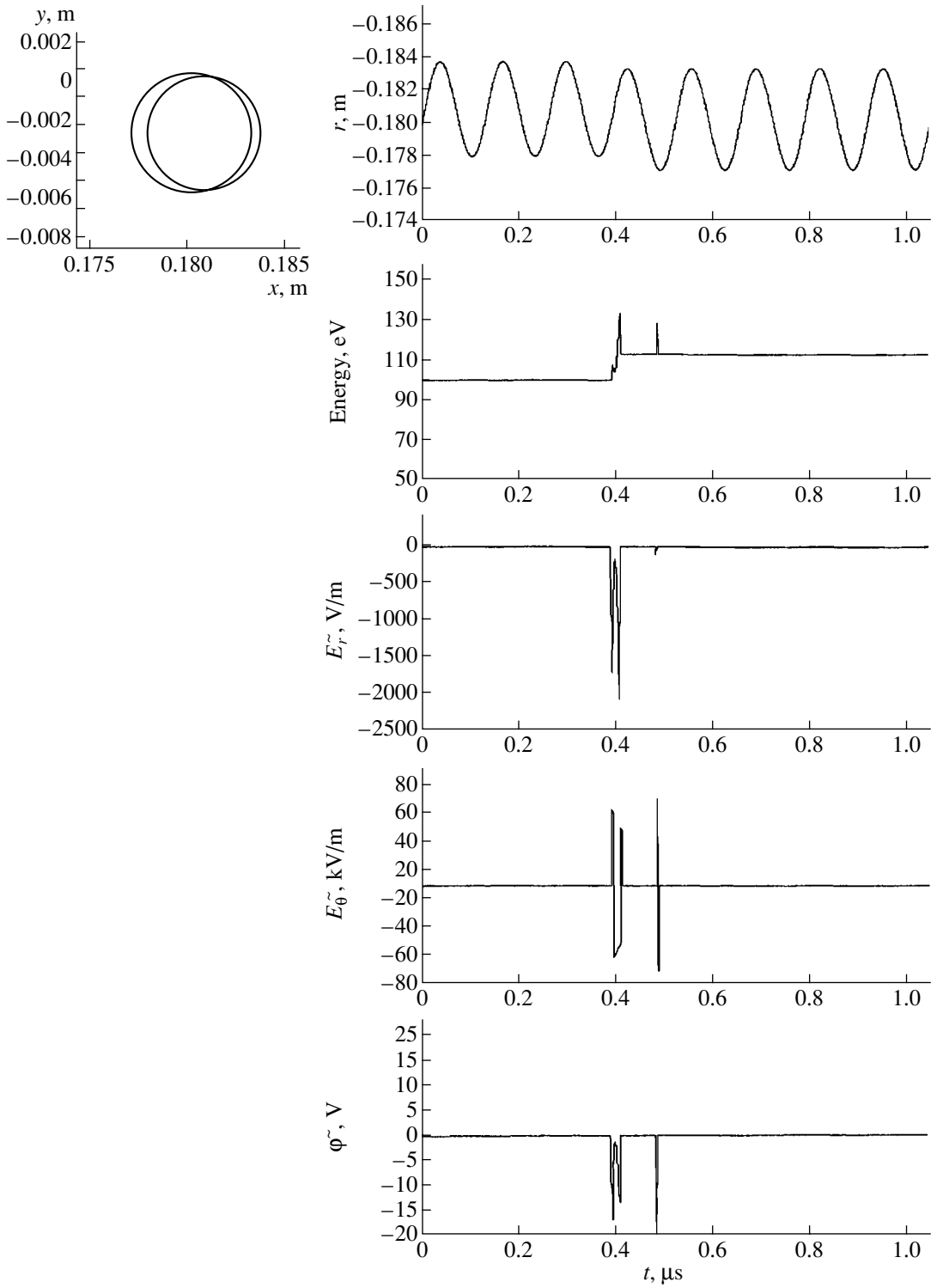

Fig. 4. Calculated dynamics of an ion (proton) influenced by a short-wavelength wave packet for $\Delta\varphi_m = 20$ eV, $v_{g0} = -0.3v_{Ti}$, $\delta_\parallel = 0.1\rho_{Ti}$, $\omega_0 = 0$, $\psi_0 = 0$, and $\zeta = \zeta_{res}$. The values of B, a, T_i, T_e, ρ_i, r_{s0} are the same as in Fig. 1.

3. INTERACTION BETWEEN PARTICLES AND FLUCTUATIONS AT $\delta_\parallel \ll \rho$ AND $\omega \lesssim \omega_c$

Typical results of the calculations of the interaction between a particle and a short-wavelength high-frequency fluctuation are presented in Fig. 4.

In the course of interaction between a particle and a short-wavelength packet ($\delta_\parallel \ll \rho$), the azimuthal component of the particle velocity changes by the value

$$\Delta v_\theta = -\frac{q\Delta\varphi}{m(v_\theta - v_g)}$$

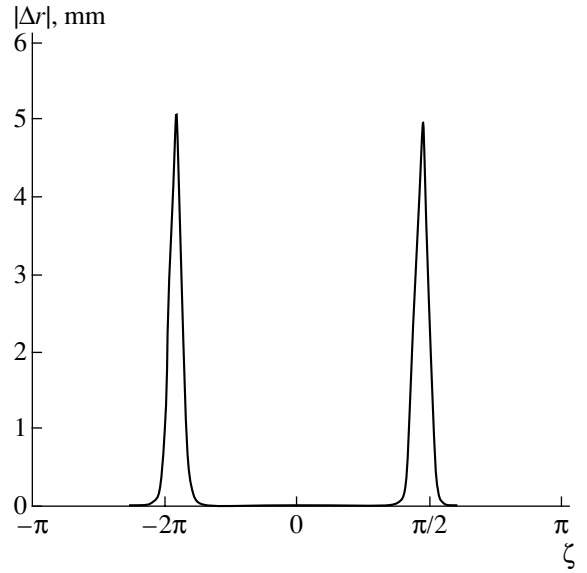

Fig. 5. Radial displacement of an ion (proton) as a function of the ion Larmor phase ζ for $v_{g0} = -0.1v_{Ti}$. The values of B, a, T_i, T_e, ρ_i, r_{s0}, $\delta_\parallel$, $\Delta\varphi_m$, ω_0, and ψ_0 are the same as in Fig. 4.

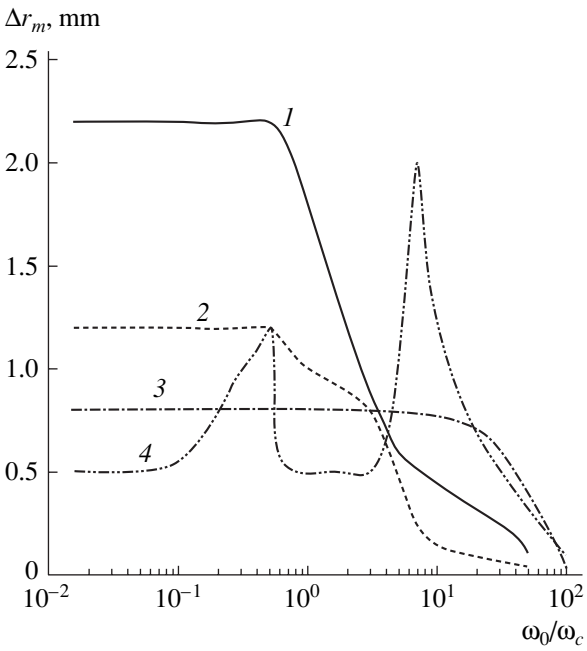

Fig. 6. Radial displacement of an ion (proton) as a function of the wave packet frequency ω_0 for v_{g0} = (*1*) $0.05v_{Ti}$, (*2*) $0.02v_{Ti}$, (*3*) $0.3v_{Ti}$, and (*4*) $0.01v_{Ti}$. The values of B, a, T_i, T_e, ρ_i, r_{s0}, $\delta_\parallel$, $\Delta\varphi_m$, ψ_0, and ζ are the same as in Fig. 4.

at $|\Delta v_\theta| \ll |v_\theta - v_g|$. Taking into account that the displacement of the guiding center along the radius is related to the change in the particle velocity by the relationship $\Delta r/\rho = \Delta v_\theta/v_\perp$, we obtain

$$\Delta r = \frac{m\Delta v_\theta}{qB} = \frac{\langle \tilde{E_\theta}\rangle t_{\rm int}}{B}. \qquad (16)$$

For $|v_\theta - v_g| \ll |v_\theta|$, assuming that

$$\langle \tilde{E_\theta}\rangle \sim -\frac{\Delta\varphi}{2\delta_\parallel}$$

and taking into account that $2\delta_\parallel \approx (v_\theta - v_g)t_{\rm int}$, we obtain from (14) that

$$\Delta r \sim -\frac{\Delta\varphi}{B(v_\theta - v_g)}.$$

The displacement of the particles with $v_\theta \approx v_g$ is maximum. The calculations show that it is these particles that make the main contribution to the total flux. The value of the Larmor phase ξ for these particles is close to the resonant value

$$\varsigma_{\rm res} = \pm\left[\frac{\pi}{2} + \arcsin\left(\frac{v_{g0}}{v_\perp}\right)\right]. \qquad (17)$$

The calculations show (Fig. 5) that the interaction is most efficient for particles with the Larmor phases $\varsigma_{\rm res} \pm 0.1\pi$.

The maximum interaction time of these particles with a fluctuation is

$$(t_{\rm int})_{\max} \approx 0.1\frac{2\pi}{\omega_c}.$$

For $\delta_\parallel \le 0.1\rho$, it follows from the relation

$$2\delta_\parallel = \frac{1}{2}v_\perp\omega_c t_{\rm int}^2$$

that the interaction time is

$$t_{\rm int} = \frac{2}{\omega_c}\sqrt{\frac{\delta_\parallel}{\rho}}.$$

The calculations show that a particle is displaced under the action of short-wavelength fluctuations even in the case of steady-state fluctuations, i.e., at $\omega_0 = 0$. Figure 6 presents the results of calculations demonstrating how the displacement depends on the frequency ω_0 of fluctuations. The displacement begins to appreciably decrease (approximately in proportion to ω_c/ω_0) at $\omega_0 \gg \omega_c$. Thus, at $|v_{g0}| \sim 0.3v_\perp$, the displacement begins to decrease starting from $\omega_0 \sim 50\omega_c$.

The influence of the group velocity is illustrated in Fig. 7. The calculations show that, as the absolute value of the group velocity increases to $|v_{g0}| \approx 0.1v_\perp$, the displacement increases approximately in proportion to $|v_{g0}|/(0.1v_\perp)$. This probably occurs because the nonsteady-state character of the interaction associated with the relative motion of an ion and a fluctuation becomes more pronounced. At $|v_{g0}| > 0.1v_\perp$ the displacement decreases approximately as $0.1v_\perp/|v_{g0}|$ because the time during which a fluctuation and a particle interact decreases.

Taking into account the aforesaid, the maximum ion displacement at $|v_{g0}| < 0.1v_\perp$ is

$$\Delta r_m = \frac{\langle \tilde{E_\theta} \rangle}{B} t_{\text{int}} \approx \frac{\Delta\varphi_m}{2\delta_\parallel B} \frac{|v_{g0}|}{0.1 v_\perp} t_{\text{int}} = 10 \frac{\Delta\varphi_m}{\delta_\parallel B\omega_c} \frac{|v_{g0}|}{v_\perp} \sqrt{\frac{\delta_\parallel}{\rho}} \quad (18)$$

while at $|v_{g0}| > 0.1v_\perp$, it is

$$\Delta r_m \approx \frac{\Delta\varphi_m}{10\delta_\parallel B\omega_c} \frac{v_\perp}{|v_{g0}|} \sqrt{\frac{\delta_\parallel}{\rho}}. \quad (19)$$

The calculations also show that, at relatively low particle energies ($v_\perp \lesssim v_T$), the displacement is almost independent of the energy and, at $v_\perp \gg v_T$, it rapidly decreases with energy.

In the case of short-wavelength fluctuations (in contrast to the case of long-wavelength fluctuations), formulas (18) and (19) for the displacement are applicable regardless of whether or not the condition $\Delta r_m < \delta_\perp$ is satisfied, because the displacement of the guiding center is related to a change in the particle energy in the course of practically instantaneous interaction with a packet, rather than to the particle drift (the position of a particle remains almost unchanged during the interaction).

Assuming that the particles obey a Maxwellian distribution, the averaging of the displacement squared (formulas (18) and (19)) over the particle velocities $v_\perp$ gives

$$\langle \Delta r_m^2 \rangle = \varepsilon_m^2 \left(\frac{k_B T_e}{eB} \right)^2 \frac{\eta_v}{\omega_c^2 \rho_T \delta_\parallel}, \quad (20)$$

where $\eta_v \approx 0.035 v_T/|v_{g0}|$ at $|v_{g0}| \le 0.07 v_T$ and $\eta_v \approx 0.5$ at $0.07 v_T < |v_{g0}| < 1.5 v_T$.

In the short-wavelength limit, we have $\lambda_0 \ll \rho$; i.e., over one cyclotron period, the particles interact with many packets. We note, however, that in this case, only interactions occurring at Larmor phases close to the resonant value ζ_{res} are to be taken into account. Therefore, the effective interaction frequency can be set equal to $\nu = \omega_c/\pi$.

4. DISCUSSION

In the present paper, we have investigated the behavior of plasma particles under the action of electric-field fluctuations with allowance for their finite width and non-steady-state character for various kinds of plasma oscillations (in the calculations, the characteristic wavelengths and frequencies of the fluctuations were varied). The results obtained allow us to evaluate the radial displacements of the plasma particles and the characteristic frequencies of the particle–fluctuation interaction that are necessary for calculating the diffusive and convective particle and energy fluxes from the plasma.

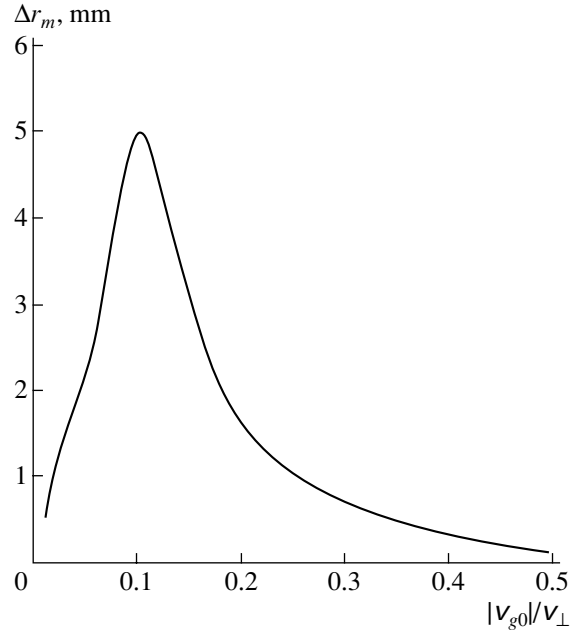

Fig. 7. Maximum radial displacement of an ion (proton) as a function of the group velocity of the wave packet v_{g0}. The values of B, a, T_i, T_e, ρ_i, r_{s0}, $\delta_\parallel$, $\Delta\varphi_m$, ω_0, ψ_0, and ζ are the same as in Fig. 4

According to the calculated results, a particle turns out to be displaced along the radius after the interaction with a fluctuation only when the fluctuation is non-steady. Thus, in the long-wavelength low-frequency limit, it is necessary that the fluctuation shape vary appreciably during the interaction between a particle and a fluctuation. In the short-wavelength high-frequency limit, a fluctuation should propagate with a sufficiently high velocity relative to a particle. It should be noted that in both these cases, the mean azimuthal electric field along the particle trajectory is nonzero, $\langle \tilde{E_\theta} \rangle \neq 0$. When this condition is satisfied, fluctuations can cause anomalous cross-field transport.

The calculations show that the results obtained for ions ($\rho = \rho_i$, $\omega_c = \omega_{ci}$, and $v_\perp = v_{\perp i}$) can also be applied to electrons by setting $\rho = \rho_e$, $\omega_c = \omega_{ce}$, and $v_\perp = v_{\perp e}$ in formulas (12)–(20). It should be noted that the interaction parameters for electrons, $(\Delta r_m)_e$ and ν_e, may differ from the interaction parameters for ions, $(\Delta r_m)_i$ and ν_i, at the same parameters of fluctuations.

Thus, in the case of fluctuations corresponding to low-frequency drift instability [3, 6, 12], we can assume the following parameter values: $\delta_\parallel \approx 0.1\lambda_0$, $\lambda_0 \approx L_N \approx r$, $\omega_0 \approx v_d/r$, $u_i \approx u_e \approx |v_{g0}| \approx 0.1 v_d$, and $v_d = k_B T_e/eBL_N$. In this case, the drift approximation is valid for both electrons and ions. The diffusion coefficients and convective ion and electron fluxes can then be estimated using formulas (12)–(14), which give the follow-

ing values:

$$D_i \approx D_e \approx \varepsilon_m^2 \frac{k_B T_e}{eB}, \quad (21)$$

$$\Gamma_i^{\text{conv}} \approx \Gamma_e^{\text{conv}} \approx 0.3\varepsilon_m \frac{k_B T_e}{eB} \frac{N_e}{L_N}. \quad (22)$$

In the case of lower hybrid drift instability [6–8], the conditions of the low-frequency limit $\omega \ll \omega_{ce}$ and $\delta_\parallel \sim \rho_e$ are satisfied for electrons, while for ions, in contrast, we have $\omega \gg \omega_{ci}$ and $\delta_\parallel \ll \rho_i$. In this case, we can assume $\delta_\parallel \approx \rho_{Te}$, $\lambda_0 \approx 10\rho_{Te}$, $v_{g0} \approx 0.2v_{Ti}$, and $\omega_0 \approx \sqrt{\omega_{ce}\omega_{ci}}$. Then, according to formulas (12)–(14), the diffusion coefficient and the convective flux of electrons are equal to

$$D_e \approx 20\varepsilon_m^2 \frac{k_B T_e}{eB}\left(\frac{T_e}{T_i}\right)^{\frac{3}{2}}, \quad (23)$$

$$\Gamma_e^{\text{conv}} \approx 10\varepsilon_m \frac{k_B T_e}{eB} \frac{N_e}{\rho_{Ti}}. \quad (24)$$

To derive the corresponding expressions for ions, it is necessary to use formulas (18)–(20) for the short-wavelength limit, which give

$$D_i \approx \varepsilon_m^2 \frac{k_B T_e}{eB}\left(\frac{T_e}{T_i}\right)^{\frac{1}{2}}, \quad (25)$$

$$\Gamma_i^{\text{conv}} \approx \varepsilon_m \frac{k_B T_e}{eB}\left(\frac{T_i}{T_e}\right)^{\frac{1}{4}} \frac{N_i}{\rho_{Ti}}. \quad (26)$$

It can be seen that, in this case, the ion and electron transport parameters differ drastically. The difference in the transport parameters may result in the different ion and electron fluxes. Therefore, mechanisms providing ambipolarity (the formation of a static electric field and a change in the density profile) must operate in the plasma.

We also note that there is a range of amplitudes ε_m within which the ion displacement may be negligibly small as compared to their cyclotron radius ($(\Delta r_m)_i \ll \rho_i$), whereas the electrons can substantially deviate from their undisturbed orbits ($(\Delta r_m)_e \gg \rho_e$). Hence, when the ion transport is suppressed down to the classical (or neoclassical) level, the electron transport may remain anomalously high, as has been observed in many experiments [17].

A natural consequence of the above model is the possibility of the existence of three transport regimes in a magnetized plasma at different fluctuation amplitudes: anomalous transport of both ions and electrons, anomalous transport of electrons and collisional (classical or neoclassical) transport of ions, and neoclassical transport of both ions and electrons at a certain minimum level of fluctuations.

The first of the above regimes corresponds to the conventional anomalous transport in a magnetized plasma. The second regime corresponds to the conditions under which anomalous transport is suppressed in the regions of internal transport barriers (see, e.g., [17]).

We note that, in the present paper, we did not consider the excitation mechanisms of the corresponding instabilities, and the wave amplitudes, which are necessary for the analysis of anomalous transport, were prescribed. To develop a self-consistent model, it is necessary to estimate the saturation level of the wave mode amplitudes with allowance for the anomalous transport of the particles resulting in the onset of instabilities.

ACKNOWLEDGMENTS

This work was supported in part by the International Science and Technology Center (project no. 1260) and the Russian Foundation for Basic Research (grant no. 03-02-16631).

REFERENCES

1. W. Horton, H.-B. Park, J.-M. Kwon, *et al.*, Phys. Plasmas **5**, 3910 (1998).
2. J.-M. Kwon, W. Horton, P. Zhu, *et al.*, Phys. Plasmas **7**, 1169 (2000).
3. B. B. Kadomtsev and A. V. Timofeev, Dokl. Akad. Nauk SSSR **146**, 581 (1962) [Sov. Phys. Dokl. **7**, 826 (1962)].
4. B. B. Kadomtsev, *Issues of Plasma Physics* (Gosatomizdat, Moscow, 1964), Vol. 4, p. 188.
5. A. B. Mikhaĭlovskiĭ, *Theory of Plasma Instabilities*, Vol. 2: *Instabilities in Inhomogeneous Plasma* (Atomizdat, Moscow, 1977) [in Russian].
6. R. C. Davidson and N. A. Krall, Nucl. Fusion **17**, 1313 (1977).
7. R. C. Davidson, N. T. Gladd, C. S. Wu, and J. D. Huba, Phys. Fluids **20**, 301 (1977).
8. J. D. Huba, J. F. Drake, and N. T. Gladd, Phys. Fluids **23**, 552 (1980).
9. Y.-J. Chen and C. K. Birdsall, Phys. Fluids **26**, 180 (1983).
10. R. D. Ferrato, H. Sanuki, R. G. Littlejohn, and B. D. Fried, Phys. Fluids **28**, 2181 (1985).
11. N. A. Krall, Phys. Fluids B **1**, 1811 (1989).
12. A. V. Timofeev and S. E. Tupikov, Fusion Technol. **35**, 253 (1999).
13. V. I. Khvesyuk and A. Yu. Chirkov, Fusion Technol. **39**, 398 (2001).
14. V. I. Khvesyuk, A. Yu. Chirkov, and A. V. Kovalev, Fiz. Plazmy **28**, 854 (2002) [Plasma Phys. Rep. **28**, 787 (2002)].
15. V. I. Khvesyuk, A. Yu. Chirkov, and A. A. Pshenichnikov, J. Plasma Fusion Res. **3**, 150 (2000).
16. A. Yu. Chirkov, V. I. Khvesyuk, and S. V. Ryzhkov, in *Proceedings of the 29th EPS Conference on Plasma Physics and Controlled Fusion, Montreux, 2002*, Vol. 26B, p. 5.066.
17. R. C. Wolf, Plasma Phys. Controlled Fusion **45**, R1 (2003).

Translated by N. Mende

Technical Physics, Vol. 49, No. 4, 2004, pp. 405–408. Translated from Zhurnal Tekhnicheskoĭ Fiziki, Vol. 74, No. 4, 2004, pp. 27–30.

GAS DISCHARGES, PLASMA

Study of a DC Magnetron Discharge by Using a Movable Grid Anode

A. V. Rogov and I. Yu. Burmakinskiĭ

Russian Research Centre Kurchatov Institute, pl. Kurchatova 1, Moscow, 123182 Russia

e-mail: alex-rogov@yandex.ru

Received September 18, 2003

Abstract—A method is proposed for determining the density of the ionizing electron component in a dc magnetron discharge in the region where the magnetic field is strong and highly nonuniform. The method is based on the analysis of the measured dependence of the discharge current on the distance between the cathode and the grid anode. The method was used to study the parameters of a magnetron discharge in a process magnetron operating in the regime with a narrow discharge region localized close to the cathode surface. © *2004 MAIK "Nauka/Interperiodica".*

INTRODUCTION

DC magnetron discharges used in magnetron sputtering systems [1, 2] are characterized by a narrow discharge region localized close to the cathode surface and a relatively strong (0.04–0.12 T) and highly nonuniform magnetic field with an arched configuration in both the vertical (150–350 T/m) and radial directions. For this reason, conventional diagnostics (such as probe measurements) are very difficult to apply to dc magnetron discharges. To examine the structure of a magnetron discharge by an electric probe [3], either special model magnetic systems with a reduced magnetic field are used [4] or a discharge is studied at a relatively large distance from the cathode, where the magnetic field is low [4, 5].

In the present paper, we propose a method for determining the spatial distribution of the density of the ionizing electrons by analyzing the measured dependence of the magnetron discharge current on the distance between the cathode and the grid anode and by examining the cathode erosion profile.

With this method, we have studied a dc magnetron discharge at ion-current densities at the cathode of ~400–700 A/m^2. In the experiments, we used a highly efficient small-sized magnetron developed by us for solving a wide class of problems of vacuum deposition.

DESCRIPTION OF THE EXPERIMENT

The experiments were carried out with a dc magnetron sputtering system. The axisymmetric magnetic system of the magnetron consisted of a cylindrical central magnet and a peripheral annular magnet made of the KS37 alloy. The magnets provided a magnetic field of $B_{cat} \approx 0.07$–0.08 T on the cathode surface in the region where the cathode erosion was maximum (Fig. 1). The magnetic field configuration over the cathode surface was preliminarily calculated (Fig. 1a). The calculations showed that the horizontal component of the magnetic field over the region where the cathode erosion was maximum was satisfactorily described by an exponential dependence with a decay length λ_β

$$B_R(x) = B_{cat}\exp\left\{-\frac{x}{\lambda_\beta}\right\}, \quad (1)$$

in our case, the decay length was $\lambda_\beta \approx 2.3$ mm.

The working gas was argon. To ensure uniform sputtering of the target, the experiments were carried with a 1.5-mm-thick graphite cathode, because of its small sputtering coefficient [6]. The magnetron anode was designed in the form of a circular diaphragm that was parallel to the cathode surface and had an aperture at its center. The aperture diameter was equal to the maximum diameter of the cathode erosion region. For the discharge to be localized between the anode and the cathode, the anode aperture was covered with a metal grid made of a 0.3-mm stainless-steel wire (Fig. 1a), the cell size being 1 mm. Preliminary measurements showed that the grid had no effect on the *I–V* characteristic of the discharge when the anode–cathode distance was longer than 7 mm.

The experiments included the measurements of the *I–V* characteristic for different values of the anode–cathode distance X^* at a fixed value of the argon pressure in the vacuum chamber ($P_{work} = 6.5 \times 10^{-3}$ torr). The anode–cathode distance was varied from 7.8 to 1.8 mm with a step of 0.5 mm. The largest distance was determined by the structural features of the magnetron, whereas at distances shorter than 1.8 mm, steady-state magnetron discharges could not be achieved because of the onset of anode–cathode microarcs.

The maximum erosion of the graphite cathode in the course of the experiments did not exceed 0.1 mm, so

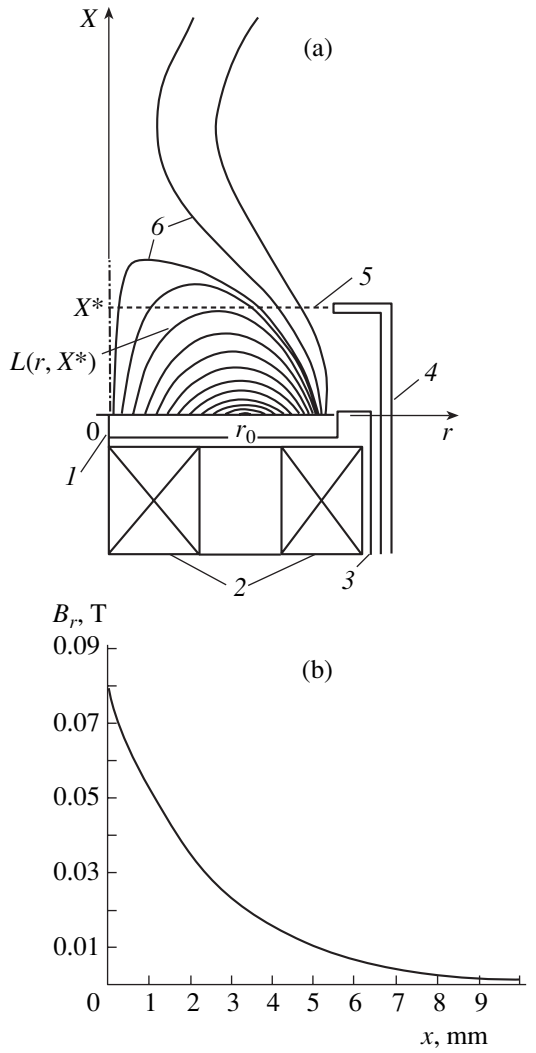

Fig. 1. (a) Magnetron ion sputtering system used in the experiments (half of the system is depicted) and (b) the radial component of the magnetron magnetic field as a function of the distance from the cathode: (*1*) cathode, (*2*) magnetic system (the central and peripheral magnets), (*3*) magnetron casing, (*4*) anode, (*5*) anode grid, and (*6*) magnetic field lines.

that the experiments were carried with the same cathode. Since the profile of the erosion region is independent of the cathode material, we performed special measurements of the erosion profile with a copper cathode of the same thickness (1.5 mm) until it was completely eroded; the measurements were performed for several anode–cathode distances. Comparisons of the erosion regions for two distances $X^* = 7.0$ and 2.8 mm showed that the observed difference in the profile of the erosion region correlates well with the change in the discharge volume bounded by a magnetic field line touching the anode grid (the boundary field line). The boundary of the erosion region is determined by the intersection of this magnetic line with the cathode surface (Fig. 2b).

From the experimental data (see Fig. 2), we deduced the dependences of the magnetron-discharge current on the distance X^* for several fixed values of the discharge voltage. These dependences were then recalculated to the dependences of the ion-current density by using the results of measurements of the erosion profiles.

PROCESSING OF EXPERIMENTAL DATA

The proposed method for measuring the density of the ionizing electrons in a magnetron discharge is based on a one-to-one correspondence between the change in the magnetron-discharge current and the change in the plasma volume limited by the boundary field line. The discharge current, which was measured directly, was a sum of two currents: the current of ions generated in the discharge plasma and the current of secondary electrons produced due to the ion bombardment of the cathode,

$$I_d = I_i(1 + \gamma_e), \tag{2}$$

where γ_e is the coefficient of secondary emission.[1] This allows us to calculate the ion current from the measured values of the discharge current.

For a fixed voltage and a given cathode–grid distance, the ion current at the cathode in a steady-state discharge can be represented as

$$I_i(X^*) = \int_{S\text{cat}} J_i(r, X^*)dS = e\int_{S\text{cat}}\int_0^{L(r, X^*)} n_e^{\text{hot}}(r, x, X^*)\nu_{\text{ion}}(r, x)dxdS, \tag{3}$$

where e is the ion charge, $J_i(r, X^*)$ is the ion current density at the cathode point with the coordinate r, $n_e^{\text{hot}}(r, x, X^*)$ is the density of ionizing electrons, and $\nu_{\text{ion}}(r, x)$ is the ionization frequency.

Integration is performed over the sputtered cathode area $S_{\text{cat}}(X^*)$ ($dS = 2\pi rdr$) and over the normal (to the cathode surface) coordinate x from 0 to the point $L(r, X^*)$ specifying the boundary field line for a given distance X^*.

The distribution of the ion current density on the cathode is axisymmetric and corresponds in structure to the erosion profile $h(r, X^*)$ [10], which can be either measured directly (Fig. 2b) or calculated. Relating the current density to the known erosion profile and total discharge current (2), we find

$$J_i(e, X^*) = \frac{h(r, X^*)}{\langle h\rangle(X^*)}\frac{I_d(X^*)}{(1 + \gamma_e)S_{\text{cat}}(X^*)}, \tag{4}$$

where

$$\langle h\rangle(X^*) = \frac{1}{S_{\text{cat}}(X^*)}\int_{S\text{cat}} h(r, X^*)dS, \tag{5}$$

[1] The secondary emission coefficient γ_e may be considered constant in the range of ion energies typical of magnetron ion sputtering systems [7–9].

is calculated numerically for every value of X^*.

Using relation (3) for the quantity $J_i(r, X^*)$ at a fixed coordinate ($r = r_0$), assuming that the ions move along vertical lines [10], and introducing the height-averaged ionization frequency

$$\langle \nu_i \rangle (r_0) = \frac{\int_0^{L(r_0, X^*)} n_e^{\text{hot}}(r_0, x, X^*)\nu_i(r_0, x)dx}{\int_0^{L(r_0, X^*)} n_e^{\text{hot}}(r_0, x, X^*)dx}, \quad (6)$$

we find the ion current density at the cathode at a fixed coordinate,

$$J_i(r_0, X^*) = e\langle \nu_i \rangle (r_0) \int_0^{L(r_0, X^*)} n_e^{\text{hot}}(r_0, x, X^*)dx. \quad (7)$$

Differentiating Eq. (7) with respect to the upper integration limit, we obtain

$$n_e^{\text{hot}}(r_0, x, X^*) = \frac{1}{e}\left[\frac{1}{\langle \nu_{\text{ion}} \rangle (r_0)} \frac{\partial J_i(r_0, X^*)}{\partial L^*(r_0, X^*)}\right]_{U = \text{const}}. \quad (8)$$

Assuming that the ionizing electrons are produced due to secondary electron emission and that their flux density is directly proportional to the ion current at the cathode, the spatial distribution of the density of the ionizing electrons can be represented as a product in which the first multiplier depends only on the ion current at the cathode, whereas the second (normalized) multiplier describes the coordinate dependence,

$$n_e^{\text{hot}}(r_0, x, X^*) = n^{\text{abs}}(J_i(r_0, X^*))n_e(r_0, x). \quad (9)$$

To determine the value of $n_e^{\text{abs}}(J_i(r_0, X^*))$, we use the quasineutrality condition for the discharge plasma. Then, from the measured *I–V* characteristics, we find the value of the discharge voltage as a function of the cathode–grid distance at a fixed discharge current. In this case, we have

$$\begin{aligned} U_d &= -\int_0^{X^*} E(x)dx = -[xE(x)]_0^{X^*} + \int_0^{X^*} \frac{\partial E(x)}{\partial x} x dx \\ &\approx \int_0^{X^*} \frac{\partial E(x)}{\partial x} x dx = \frac{e}{\varepsilon_0}\int_0^{X^*} (n_i - n_e)x dx, \end{aligned} \quad (10)$$

and, consequently,

$$(n_i - n_e) = \frac{\varepsilon_0}{e}\frac{1}{x}\left[\frac{\partial U_d}{\partial x}\right]_{I = \text{const}}. \quad (11)$$

Numerical estimates performed according to Eq. (11) show that the difference between the electron and ion densities is no larger than 2.4%; the profile of this difference is presented in Fig. 3a. Hence, the quasineutrality condition holds. Taking into account that $n_e \approx n_e^{\text{hot}}$ at small distances from the cathode, we define the quantity $n_e^{\text{abs}}(J_i(r_0, X^*))$ as

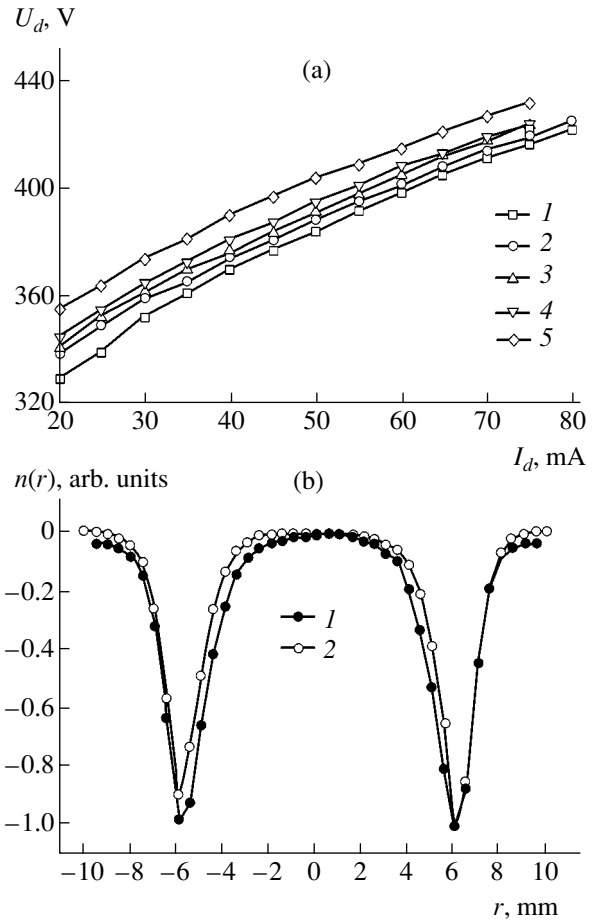

Fig. 2. (a) Measured *I–V* characteristics for different cathode–grid distances: X^* = (*1*) 7.8, (*2*) 5.8, (*3*) 4.8, (*4*) 3.8, and (*5*) 2.8 mm; (b) cathode erosion profiles for two different cathode–grid distances: X^* = (*1*) 7.8 and (*2*) 2.8 mm.

$$n_e^{\text{abs}}(J_i(r_0, X^*)) \approx n_i^{\text{cat}} \approx \frac{1}{\langle V_i \rangle e} J_i(r_0, X^*). \quad (12)$$

Then, from expressions (8), (9), and (12), we find

$$n_e(r_0, x) = \left[\frac{1}{\langle \nu_{\text{ion}} \rangle (r_0)} \frac{\partial J_i(r_0, X^*)}{\partial L(r_0, X^*)} \frac{\langle V_i \rangle}{J_i(r_0, X^*)}\right]_{U = \text{const}}. \quad (13)$$

In expressions (12) and (13), the average ion velocity is calculated for ions with the mass M_i and averaged energy $\langle E_i \rangle$ on the cathode surface [11]

$$\langle V_i \rangle \approx \sqrt{\frac{2\langle E_i \rangle}{M_i}}. \quad (14)$$

From expression (13), using a normalization condition for $n_e(r_0, x)$, we can also determine the average ionization frequency $\langle \nu_{\text{ion}} \rangle (r_0)$.

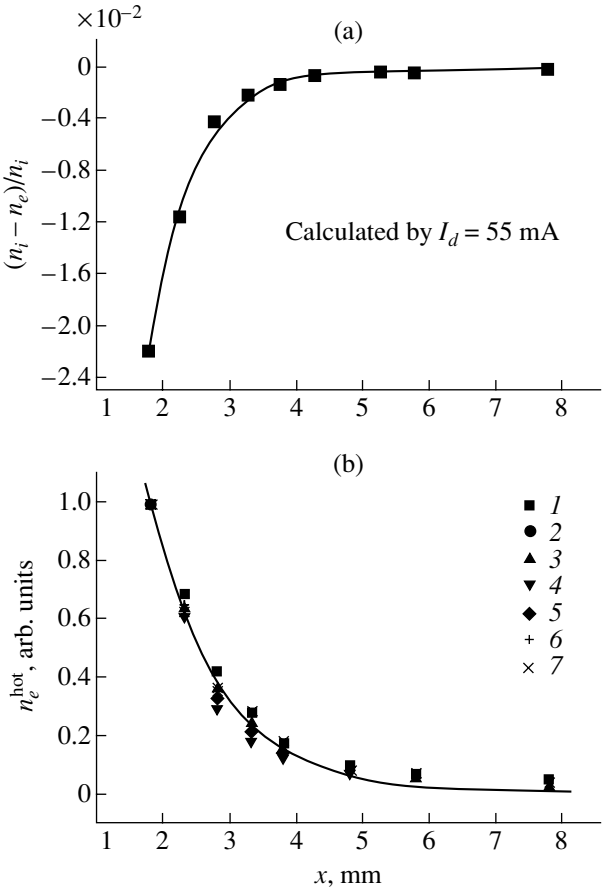

Fig. 3. (a) Relative difference between the electron and ion densities, calculated by formula (11); (b) the spatial distribution of the ionizing electrons at different discharge voltages: U_d = (*1*) 395, (*2*) 400, (*3*) 405, (*4*) 410, (*5*) 415, (*6*) 420, and (*7*) 425 V (the solid curve shows the approximation by a formula $n_e(x) \propto \exp\{-x/\lambda_e\}$ with $\lambda_e \approx 1.1$).

It is of great interest to determine the density of the ionizing electrons above the region where the cathode erosion is maximum (the profiles of this density for different discharge voltages are shown in Fig. 3b).

In the range of distances $X_0^* \le X \le X_{\max}^*$, in which the measurements were performed, the dependence of the electron density on the distance from the cathode is satisfactorily described by an exponential function with a decay length λ_e

$$n_e^{\text{hot}}(x) \propto \exp\left\{-\frac{x - X_0^*}{\lambda_e}\right\}, \qquad (15)$$

where λ_e varies only slightly over the entire range of the magnetron discharge voltages: $1.0 < \lambda_e < 1.2$. The latter circumstance allows us to conclude that the density distribution of the ionizing component is mainly determined by the x dependence of the magnitude of the horizontal component of the magnetic field in the discharge,

$$n_e^{\text{hot}}(x) \propto \{B_R(x)\}^{\alpha}, \qquad (16)$$

where α is defined as $\alpha = \lambda_\beta/\lambda_e$ and is in the range $1.8 < \alpha < 2.2$.

4. CONCLUSIONS

The electron density distribution is one of main discharge characteristics. The method described above allows one to determine the spatial parameters of the ionizing electron component in a magnetron, namely, the distribution of the electron density and the average ionization frequency as a function of the distance from the cathode. We have shown that the quasineutrality condition holds well in a magnetron discharge. When a grid anode is used in the magnetron, the discharge localization is determined by the position of the boundary field line. The main factors governing the distribution of the ionizing electrons in a magnetron discharge are the magnitude and configuration of the magnetic field of the permanent magnets. In view of the fact that the spatial electron distribution is related to the magnetic configuration, the operating parameters of an ion sputtering system can be predicted in its design phase, because this relation presents a way of estimating the ion currents and, as a consequence, the sputtering efficiency of the target material.

REFERENCES

1. P. J. Kelly and R. D. Arnell, Vacuum **56**, 159 (2000).
2. B. S. Danilin, *Low-Temperature Plasma for Thin Film Deposition* (Énergoatomizdat, Moscow, 1989) [in Russian].
3. F. F. Chen, in *Plasma Diagnostic Techniques*, Ed. by R. H. Huddlestone and S. L. Leonard (Academic, New York, 1965; Mir, Moscow, 1967).
4. T. E. Sheridan, M. J. Goecker, and J. Goree, J. Vac. Sci. Technol. A **9**, 688 (1991).
5. F. F. Elakshar, M. A. Hassouba, and A. A. Garamoon, Fiz. A **9** (4), 177 (2000).
6. W. Eckstein, C. Garcia-Rosales, *et al.*, in *Sputtering Data, Max-Planck-Inst. Plasmaphys., Garching, 1993.*
7. H. S. W. Massey and E. H. S. Burhop, *Electronic and Ionic Impact Phenomena* (Clarendon, Oxford, 1952; Inostrannaya Literatura, Moscow, 1958).
8. U. A. Arifov, *Interaction of Atomic Particles with Metal Surface* (Tashkent, 1961) [in Russian].
9. M. Kaminsky, *Atomic and Ionic Impact Phenomena on Metal Surfaces* (Springer-Verlag, Berlin, 1965; Mir, Moscow, 1967).
10. I. Yu. Burmakinskiĭ and A. V. Rogov, Zh. Tekh. Fiz. **73** (10), 46 (2003) [Tech. Phys. **48**, 1264 (2003)].
11. M. Touzeau, M. Prioul, *et al.*, Plasma Phys. Controlled Fusion **42**, B323 (2000).

Translated by N. Larionova

Technical Physics, Vol. 49, No. 4, 2004, pp. 409–412. Translated from Zhurnal Tekhnicheskoĭ Fiziki, Vol. 74, No. 4, 2004, pp. 31–34.

SOLIDS

Solubility of Gases in Uniaxially Strained Crystals

V. A. Volkov, G. S. Masharov, and S. I. Masharov

Ural State Technical University, ul. Mira 19, Yekaterinburg, 620002 Russia

Received July 21, 2003

Abstract—The solubility of gases in uniformly strained bcc crystals is calculated. As a result of straining, interstices occupied by interstitial atoms become nonequivalent and the temperature dependence of the solubility changes. The effect of deformation depends substantially on the sign of energy of interaction v_{AC} between dissolved atoms and host-crystal atoms. For elastic uniaxial tension, the solubility decreases linearly with strain at $v_{AC} > 0$; at $v_{AC} < 0$, it increases with strain. The amount of this effect is 1–10%. The effect of complexes consisting of two nearest dissolved atoms is studied. Conditions at which the role of the complexes is substantial are found. The complexes increase the solubility and change its dependence on the gas pressure. © *2004 MAIK "Nauka/Interperiodica".*

INTRODUCTION

Gas absorption by crystals is a complex physicochemical process that includes gas molecule dissociation at the gas–crystal interface followed by diffusion of atoms into the solvent volume. Since this process is reversible, the gas–crystal system comes into equilibrium in time, and the equilibrium concentration of atoms dissolved in the crystal specifies the solubility of the gas.

In this work, we calculate the solubility of a gas in bcc crystal A that is uniaxially strained (ε) along the *z* axis. In this crystal, the length a_0 of the unit cell edge in the *z* direction changes by $\Delta a = \varepsilon a_0$, and the changes in the lengths of the edges that are normal to the *z* axis are given by

$$\Delta a' = -\frac{\lambda}{2(\lambda+\mu)}a_0\varepsilon,$$

where λ and μ are the Lamé constants [1].

Absorbed atoms are assumed to occupy octahedral interstices in the undeformed crystal; that is, they are placed at the middles of the unit cell edges and at the centers of the unit cell faces. In the strained crystal, however, these positions are no longer equivalent. The distances between crystal atoms and interstices change, and the latter are subdivided into two types. Interstices of type I have two nearest crystal atoms at a distance $a_1/2$ ($a_1 = a_0 + \Delta a$), and interstices of type II have two nearest atoms at a distance $a_2/2$ ($a_2 = a_0 + \Delta a'$). It is obvious that the number N_1 of type-I interstices is half the number N_2 of type-II interstices. Since the total number of interstices of both types is $3N$ (N is the number of atoms in the crystal), we have

$$N_1 = N, \quad N_2 = 2N. \tag{1}$$

SOLUBILITY IN THE CASE OF THE UNIFORM DISTRIBUTION OF INTERSTITIALS

We will calculate the solubility of a gas in a crystal when interstitials are uniformly distributed over interstices. Let $v_{AC}(r)$ and $v(r)$ be the energy of interaction between host-crystal atoms and interstitials *C* and the energy of interaction of interstitials *C* between each other, respectively (the energies are taken with the minus sign). Then, the free energy of the crystal–gas system is

$$\begin{aligned} F = {} & -2v_{AC}\left(\frac{a_1}{2}\right)N_C^{(1)} - 2v_{AC}\left(\frac{a_2}{2}\right)N_C^{(2)} \\ & - 2v\left(\frac{a_2}{2}\right)\frac{N_C^{(1)}N_C^{(2)}}{N} - \frac{1}{2}v\left(\frac{a_1}{2}\right)\frac{N_C^{(2)^2}}{N} \\ & - kT\{N(\ln N - 1) + 2N(\ln 2N - 1) \\ & - N_C^{(1)}(\ln N_C^{(1)} - 1) - (N - N_C^{(1)})(\ln(N - N_C^{(1)}) - 1) \\ & - N_C^{(2)}(\ln N_C^{(2)} - 1) - (2N - N_C^{(2)}) \\ & \times(\ln(2N - N_C^{(2)}) - 1)\} + F_{\text{gas}}^{(\nu)}, \end{aligned} \tag{2}$$

where $F_{\text{gas}}^{(\nu)}$ is the free energy of a ν-atomic gas. For mono- and diatomic gases [2],

$$F_{\text{gas}}^{(\nu)} = \begin{cases} -N_g kT\ln\left[\dfrac{eV}{N_g}\left(\dfrac{2\pi mkT}{h^2}\right)^{3/2}\right], & \nu = 1, \\ -N_g kT\ln\left[\dfrac{eV}{N_g}\left(\dfrac{4\pi mkT}{h^2}\right)^{3/2}\right] & \\ + N_g\left[\dfrac{kT_C}{2} + kT\ln\dfrac{T_C^0}{T} - \dfrac{kT_C^0}{3} + \varepsilon_0\right], & \nu = 2. \end{cases} \tag{3}$$

1063-7842/04/4904-0409$26.00 © 2004 MAIK "Nauka/Interperiodica"

In formulas (2) and (3), $N_C^{(i)}$ is the number of interstitials in interstices of an *i*th type (i = I, II); N_g is the number of molecules in the gas phase; V is the gas volume; m is the weight of a gas atom; T_C and T_C^0 are the characteristic temperatures for vibrational and rotational degrees of freedom of a molecule, respectively; and ε_0 is the binding energy in a molecule.

Let $N_C^{(1)}$ and $N_C^{(2)}$ be thermodynamic variables. Then, using the extremeness condition for F with respect to $N_C^{(1)}$ and $N_C^{(2)}$ and taking into account that

$$N_C^{(1)} + N_C^{(2)} + \nu N_g = \text{const} \tag{4}$$

we can write equilibrium equations in the form

$$\begin{aligned} &-2\nu_{AC}\left(\frac{a_1}{2}\right) - 2\nu\left(\frac{a_2}{2}\right)\frac{N_C^{(2)}}{N} \\ &- kT[-\ln N_C^{(1)} + \ln(N - N_C^{(1)})] + \frac{\partial F_{\text{gas}}}{\partial N_C^{(1)}} = 0, \\ &-2\nu_{AC}\left(\frac{a_2}{2}\right) - 2\nu\left(\frac{a_2}{2}\right)\frac{N_C^{(1)}}{N} - \nu\left(\frac{a_1}{2}\right)\frac{N_C^{(2)}}{2} \\ &- kT[-\ln N_C^{(2)} + \ln(2N - N_C^{(2)})] + \frac{\partial F_{\text{gas}}}{\partial N_C^{(2)}} = 0. \end{aligned} \tag{5}$$

Solving system (5) under the assumption that $N_C^{(i)} \ll N_i$ and neglecting all terms except for those that are logarithmic in $N_C^{(i)}/N_i$, we come to

$$\begin{aligned} N_C^{(1)} &= N\left(\frac{p}{p_0^{(\nu)}}\right)^{1/\nu}\exp\left(\frac{2\nu_{AC}(a_1/2)}{kT}\right), \\ N_C^{(2)} &= 2N\left(\frac{p}{p_0^{(\nu)}}\right)^{1/\nu}\exp\left(\frac{2\nu_{AC}(a_2/2)}{kT}\right), \end{aligned} \tag{6}$$

where p is the gas pressure and

$$p_0^{(\nu)} = \begin{cases} kT\left(\dfrac{2\pi mkT}{h^2}\right)^{3/2}, & \nu = 1, \\ \dfrac{kT^2}{T_C}\left(\dfrac{4\pi mkT}{h^2}\right)^{3/2} & \\ \times \exp\left[-\dfrac{1}{2T}\left(T_C - \dfrac{2}{3}T_C^0\right) - \dfrac{\varepsilon_0}{kT}\right], & \nu = 2. \end{cases} \tag{7}$$

Using (6), we can write the solubility R as

$$R = \frac{N_C^{(1)} + N_C^{(2)}}{3N} = \frac{1}{3}\left(\frac{p}{p_0^{(\nu)}}\right)^{1/\nu}\left\{\exp\left(\frac{2\nu_{AC}(a_1/2)}{kT}\right) + 2\exp\left(\frac{2\nu_{AC}(a_2/2)}{kT}\right)\right\}. \tag{8}$$

At small strains ($\varepsilon \ll 1$) and high temperatures,

$$\begin{aligned} \exp\left(\frac{2\nu_{AC}(a_1/2)}{kT}\right) &\approx \exp\left(\frac{2\nu_{AC}^0}{kT}\right)\left(1 + \gamma\frac{a_0\varepsilon}{kT}\right), \\ \exp\left(\frac{2\nu_{AC}(a_1/2)}{kT}\right) &\approx \exp\left(\frac{2\nu_{AC}^0}{kT}\right)\left(1 - \gamma\frac{\lambda a_0}{\lambda + \mu}\frac{\varepsilon}{kT}\right), \end{aligned} \tag{9}$$

where

$$\nu_{AC}^0 = \nu_{AC}^0\left(\frac{a_0}{2}\right), \quad \gamma = \left.\frac{\partial \nu(r)_{AC}}{\partial r}\right|_{a_0}.$$

Then,

$$R = R_0\left\{1 + \frac{1}{3}\frac{\gamma a_0\varepsilon}{kT}\left(1 - \frac{\lambda}{\lambda + \mu}\right)\right\}, \tag{10}$$

where

$$R_0 = \left(\frac{p}{p_0^{(\nu)}}\right)^{1/\nu}\exp\left(\frac{2\nu_{AC}^0}{kT}\right) \tag{11}$$

is the solubility of the gas in the undeformed crystal.

According to (10), the solubility varies linearly with strain. Assuming that interstitial atoms are attracted by solvent atoms ($\nu_{AC} > 0$), we have $\gamma < 0$. Thus, the solubility of the gas in the crystal decreases under uniaxial tension and increases under compression. At temperatures such that

$$\frac{1}{3}\frac{\gamma a_0}{kT} = 1\text{–}10,$$

the uniaxial tension on the order of $\varepsilon \sim 0.01$ changes the solubility of the gas by 1–10%.

The interaction between atoms C can be taken into account in terms of the perturbation theory. In the first order of smallness in ν/kT, we find from equilibrium equation (5) that

$$\begin{aligned} \Delta N_C^{(1)} &= \frac{2\nu(a_2/2)}{kT}N_C^{(2)}, \\ \Delta N_C^{(2)} &= \frac{2\nu(a_2/2)N_C^{(1)} + \nu(a_1/2)N_C^{(2)}}{kT}. \end{aligned} \tag{12}$$

According to (10) and (11), uniaxial tension of the crystal does not change the pressure and temperature

dependences of the solubility: it obeys the Arrhenius law with a slightly modified preexponential.

EFFECT OF INTERSTITIAL COMPLEXES ON THE SOLUBILITY

As is known, interaction between point defects in crystals can cause their aggregation into various complexes [3]. In dilute interstitial alloys A–(C), the simplest complexes are pairs of nearest interstitials. Let us consider the effect of complexation on the solubility of gases in deformed crystals under the assumption that the number of complexes is small and they do not overlap with each other.

Obviously, there are two types of such complexes in uniformly strained bcc crystals. Those of the first type are formed by atoms C that occupy nearest interstices of different types. Their number is n_1, and their energy is

$$E_k^{(1)} = -v\left(\frac{a_2}{2}\right)n_1. \tag{13}$$

In complexes of the second type, neighboring atoms C occupy nearest interstices of type II. Accordingly, their number is n_2 and their energy is

$$E_k^{(2)} = -v\left(\frac{a_1}{2}\right)n_2. \tag{14}$$

Let us determine the thermodynamic probability of the state with n_1 complexes of the first type. It equals the number of distinguishable permutations of n_1 complexes taken the number of type-I interstice–type-II interstice pairs at a time. Since the number of these pairs is $4N$, this probability is given by

$$W_k^{(1)} = \frac{(4N)!}{n_1!(4N-n_1)!}. \tag{15}$$

Similarly, for complexes of the second type, we have

$$W_k^{(2)} = \frac{(2N)!}{n_2!(2N-n_2)!}. \tag{16}$$

To accommodate isolated atoms C, a solution containing nonoverlapping complexes of both types has $N - n_1 - 2n_2$ interstices of type I and $2N - 4n_1 - 3n_2$ interstices of type II. Then, the thermodynamic probability of the state with $N_C^{(1)}$ and $N_C^{(2)}$ isolated atoms C can be written as

$$W = \frac{(N-n_1-2n_2)!}{N_C^{(1)}!(N-n_1-2n_2-N_C^{(1)})!} \times \frac{(2N-4n_1-3n_2)!}{N_C^{(2)}!(2N-4n_1-3n_2-N_C^{(2)})!}. \tag{17}$$

In view of (15)–(17), the free energy is expressed as

$$\begin{aligned} F = &-\left[v\left(\frac{a_2}{2}\right) + 2v_{AC}\left(\frac{a_1}{2}\right) + 2v_{AC}\left(\frac{a_2}{2}\right)\right]n_1 \\ &-\left[v\left(\frac{a_1}{2}\right) + 2v_{AC}\left(\frac{a_1}{2}\right) + 2v_{AC}\left(\frac{a_2}{2}\right)\right]n_2 \\ &-2v_{AC}\left(\frac{a_1}{2}\right)N_C^{(1)} - 2v_{AC}\left(\frac{a_2}{2}\right)N_C^{(2)} - 2v\left(\frac{a_2}{2}\right)N_C^{(1)} \\ &\times\frac{N_C^{(2)}}{2N-4n_1-3n_2} - \frac{1}{2}v\left(\frac{a_1}{2}\right)\frac{N_C^{(2)^2}}{2N-4n_1-3n_2} \\ &-kT\{(N-n_1-2n_2)(\ln(N-n_1-2n_2)-1) \\ &+4N(\ln 4N-1) + 2N(\ln 2N-1) - N_C^{(1)}\ln(N_C^{(1)}-1) \\ &-(N-n_1-2n_2-N_C^{(1)})(\ln(N-n_1-2n_2-N_C^{(1)})-1) \\ &-N_C^{(2)}\ln(N_C^{(2)}-1) - (2N-4n_1-3n_2-N_C^{(2)}) \\ &\times\ln(N-4n_1-3n_2-N_C^{(2)}-1)\} + F_{\text{gas}}. \end{aligned} \tag{18}$$

We now construct equilibrium equations, using the extremeness condition for F with respect to $N_C^{(1)}$, $N_C^{(2)}$, n_1, and n_2 and also the relation

$$N_C^{(1)} + N_C^{(2)} + 2n_1 + 2n_2 + N_{\text{gas}} = \text{const}. \tag{19}$$

Next, we solve these equations, neglecting all concentration terms except for logarithmic ones and obtain

$$n_1 = 4N\left(\frac{p}{p_0^{(v)}}\right)^{2/v} e^{\frac{v\left(\frac{a_2}{2}\right)+2\left(v_{AC}\left(\frac{a_1}{2}\right)+v_{AC}\left(\frac{a_2}{2}\right)\right)}{kT}}, \tag{20}$$

$$n_2 = 2N\left(\frac{p}{p_0^{(v)}}\right)^{2/v} e^{\frac{v\left(\frac{a_1}{2}\right)+2\left(v_{AC}\left(\frac{a_1}{2}\right)+v_{AC}\left(\frac{a_2}{2}\right)\right)}{kT}}. \tag{21}$$

For $N_C^{(1)}$ and $N_C^{(2)}$, we arrived at expression (6), which was derived earlier.

According to (6), (20), and (21), the concentrations of complexes, $c_1 = n_1/4N$ and $c_2 = n_2/2N$, are related to the concentrations of isolated interstitials by the relationship

$$c_i = c_C^{(i)^2} e^{\frac{v}{kT}}; \quad i = 1, 2, \tag{22}$$

where $c_C^{(i)} = N_C^{(i)}/N_i$.

Whence, it follows that the concentration of complexes is significant only if $v > 0$ (atoms C are attracted to each other), because $c_C^{(i)} \ll 1$; at $v < 0$, we can neglect the presence of complexes.

Allowing for complexation, we find that the solubility R of the gas is given by

$$R = \frac{1}{3N}(N_C^{(1)} + N_C^{(2)} + 2(n_1 + n_2)) = R_1 + R_2, \quad (23)$$

where R_1 is defined by Eq. (8) and contributes to the solubility of isolated atoms and

$$R_2 = \frac{2}{3}\left(\frac{p}{p_0^{(\nu)}}\right)^{2/\nu}\left[2e^{\frac{v_{CC}\left(\frac{a_2}{2}\right)}{kT}} + e^{\frac{v_{CC}\left(\frac{a_2}{2}\right)}{kT}}\right]e^{\frac{v_{CC}\left(\frac{a_2}{2}\right)+v_{CC}\left(\frac{a_2}{2}\right)}{kT}} \quad (24)$$

is the solubility due to complexes. In the undeformed crystal,

$$R = R_0\left\{1 + 2\left(\frac{p}{p_0^{(\nu)}}\right)^{1/\nu} e^{\frac{v_0 + 2v_{AC}^0}{kT}}\right\}, \quad (25)$$

where R_0 is the solubility in the absence of complexes and $v^0 = v(a_0/2)$.

As follows from (24), complexation changes the dependence of the solubility on the gas pressure. For a monatomic gas, R can be represented as

$$R = ap + bp^2, \quad (26)$$

where a and b are functions of temperature.

For a diatomic gas, we have

$$R = a\sqrt{p} + bp. \quad (27)$$

Using Eqs. (26) and (27), one can determine the presence of complexes from experimental data on the solubility (from a deviation of $R(p)$ from the linear or parabolic dependences). The ratio b/a characterizes the fraction of complexes with respect to the number of isolated interstitials.

Let us find the strain dependence of R. As was shown above, R_1 is a linear function of ε: it decreases under tension and decreases under compression. Expanding v_{CC} and v_{AC} into series in Δa_1 and Δa_2, we have

$$R_2 = R_2^0\left\{1 + \frac{a_0\varepsilon}{3kT}\frac{\lambda + 2\mu}{2(\lambda + \mu)}\left[\frac{1}{3}e^{-\frac{v^0}{kT}}\beta + \gamma\right]\right\}, \quad (28)$$

where R_2^0 is the contribution of complexes to the solubility in the undeformed crystal and

$$v^0 = v\left(\frac{a_0}{2}\right), \quad \beta = \left.\frac{\partial v(r)}{\partial r}\right|_{a_0/2}.$$

The sign of the bracketed term is uncertain; therefore, a strain-induced change in R_2 can be both positive and negative.

COMPARISON WITH EXPERIMENT

In experiments, interaction of hydrogen with metals has been studied most extensively. The solubility has been found to obey the Sieverts law $R \sim \sqrt{p}$ in many cases. This indicates that the gas absorbed by a metal is in the form of isolated atoms in the solution. However, this law sometimes fails. For example, the solubility of hydrogen in palladium is a nonlinear function of $\sqrt{p}$ [4, Chap. 8], which may be explained by the presence of interstitial complexes.

In [4], the effect of elastic stresses on the solubility in Pd_3Ag was studied. It was found that strain changes the solubility and that the change correlates with the sign of strain. The amount of this effect (about 1%) agrees with theoretical estimates.

Thus, we conclude that our results agree with experimental data.

REFERENCES

1. L. D. Landau and E. M. Lifshitz, *Course of Theoretical Physics*, Vol. 7: *Theory of Elasticity* (Nauka, Moscow, 1987; Pergamon, New York, 1986).
2. R. Kubo, *Statistical Mechanics: An Advanced Course with Problems and Solutions* (North-Holland, Amsterdam, 1965; Mir, Moscow, 1967).
3. A. A. Smirnov, *Theory of Interstitial Alloys* (Nauka, Moscow, 1979) [in Russian].
4. G. G. Alefeld and J. Voekl, *Hydrogen in Metals* (Springer, New York, 1978; Mir, Moscow, 1981), Vol. 2.

Translated by K. Shakhlevich

Technical Physics, Vol. 49, No. 4, 2004, pp. 413–419. Translated from Zhurnal Tekhnicheskoĭ Fiziki, Vol. 74, No. 4, 2004, pp. 35–41.

SOLIDS

Simulation of Pulsed Magnetic Molding of Long Powdered Products

S. V. Dobrov and V. V. Ivanov

Institute of Electrophysics, Ural Division, Russian Academy of Sciences, ul. Amundsena 106, Yekaterinburg, 620016 Russia

e-mail: stas@iep.uran.ru

Received November 20, 2002; in final form, June 19, 2003

Abstract—A numerical model of radial (*Z*-pinch-based) pulsed magnetic molding of nanometer-grain powders is developed and thoroughly investigated. The essence of the model is use of a compression adiabat measured experimentally. With this model, one can select optimal sets of the initial parameters of the process depending on the parameters of workpieces being molded, predict the density and homogeneity of compacts, and the efficiency of using the storage energy. *© 2004 MAIK "Nauka/Interperiodica".*

INTRODUCTION

Long products, specifically, ceramic tubes with improved mechanical and service properties, are used in various fields of present-day technology. Ceramic materials with a fine submicrometer structure, which offer a unique set of operating parameters, are especially promising in this respect [1, 2]. Jet-forming heads of hydroabrasive cutters, as well as tubes made of YSZ (yttrium-stabilized zirconia) high-temperature electrolytes and used in electrochemical energy sources, are known examples of using critical parts in the form of tubes. In the former case, a thick-walled tube must have a high hardness and wear resistance; in the latter, a thin-walled tube must be very dense and offer a high oxygen-ion conductivity and mechanical strength.

Pulsed magnetic molding (PMM) seems to be a promising technique for producing long fine-structure ceramic products. It has a number of advantages over the conventional techniques of producing ceramic tubes such as slip casting and hydrostatic extrusion. In this method, powders are subjected to dry intense compaction by a radially compressed metallic cylindrical sheath. This provides chemical purity, as well as a higher density and homogeneity, of compacts. Earlier, the PMM method was used for making long tubular compacts from micrometer-grain powders of metals and cermets [3, 4]. Much experience in electromagnetic compression of sheaths and in numerically simulating this process has been gained (see, e.g., [5, 6]). However, this method of molding needed refinement, since production of strong compacts from such nanometer-grain powders, featuring a high hardness and toughness, was difficult. The essence of uniaxial pulsed molding and synthesis of ceramics from nanograin powders of simple oxides and their mixtures has been described elsewhere [7, 8].

Optimal parameters of cylindrical compacts are usually found from a number of resource-intensive experiments, which, however, do not provide answers to all questions. Moreover, the process of radial compression of powders is difficult to monitor in practice. To considerably cut the expenses and extract more information about the process, we performed a computer simulation, using a real (experimentally measured) compression adiabat (for the procedure of taking the adiabat, see [9]). The results of such an approach are reported in this work.

1. STATEMENT AND SOLUTION OF THE PROBLEM

Axisymmetric compaction of powders is carried out by radial compression of a thin-walled fixed-edge cylindrical metallic sheath subjected to the magnetic pressure of the current passing through the sheath. Our aim is to simulate compaction of a powder by describing the time evolution of the density fields and kinematic parameters (radii, as well as the velocities and accelerations of grains).

The sheath is assumed to be so long that edge effects may be neglected. At the same time, it must not be too long so as not to violate the quasi-stationarity condition for electrodynamic processes. Let the inner and outer radii of the sheath be r_{in} and r_{out}, respectively. The specific heat, conductivity, and melting point are assumed to be given. Inside the sheath, there is a concentric hard rod of radius R, which produces the inner channel of a workpiece being molded. The space between the rod and sheath is filled with a powder with a given compression adiabat (the dependence of the density of the

1063-7842/04/4904-0413$26.00 © 2004 MAIK "Nauka/Interperiodica"

medium on its density, $p = p(D)$). To the sheath, a current pulse

$$J = J_0 e^{-t/\tau} \sin \omega t$$

is applied (t is the time measured from the beginning of the process, τ is the current decay time, and ω is the cyclic frequency).

The depth δ of penetration of the current into the sheath does not depend on time; that is, transients ion the sheath are ignored. This approximation will be justified in Sect. 3.

Let the material of the sheath be described in terms of the Saint Venant model of ideal rigid–plastic body [10]. As applied to the cylindrical (essentially planar axisymmetric) geometry of the problem, this means that (i) the sheath is incompressible; (ii) if $|\sigma_\phi - \sigma_r| < k$ (where σ_ϕ and σ_r are the $\phi\phi$ and rr components of the stress tensor written in the cylindrical coordinates and k is the yield stress), the body remains rigid; that is, the strain rate equals zero (stresses are not given and it is assumed that k is a linear function temperature: $k = k_0(T_m - T)$, where T is the temperature of the sheath, T_m is the melting point of the sheath, and k_0 is a constant); and (iii) if the strain rate deviator is other than zero in any area of the sheath, then

$$|\sigma_\phi - \sigma_r| = k, \quad (1)$$

in this area; in other words, relationship (1) is valid throughout the sheath wall under uniform compression.

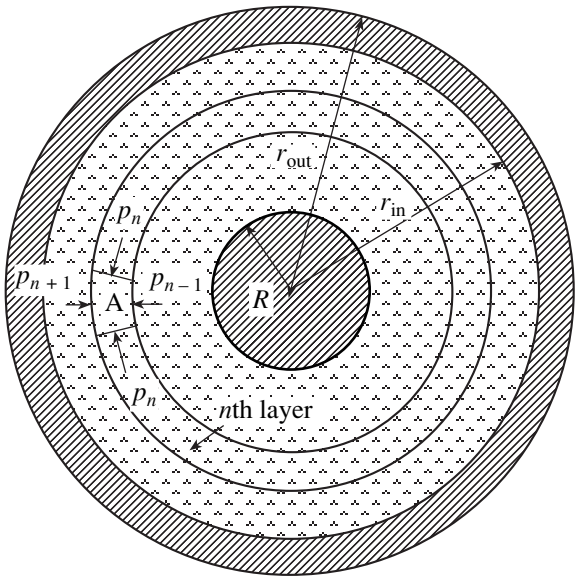

Fig. 1. Cross-sectional view of the sheath filled with a medium to be compacted.

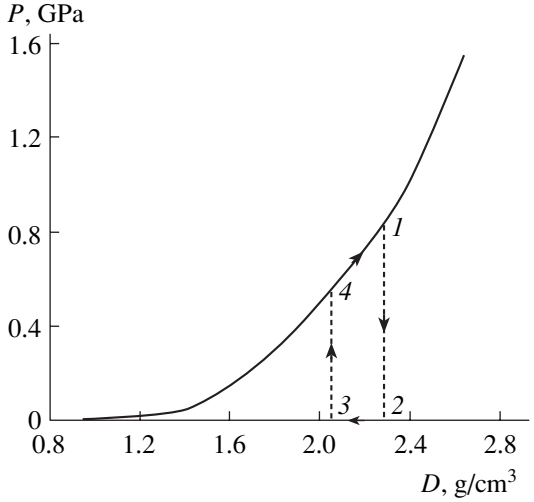

Fig. 2. Compression adiabat. Loading–unloading cycle is shown by dashed lines with arrows.

At this step, we suppose that the process considered is adiabatic (this assumption is justified in Sect. 3). The motion of the powder will be described in terms of the model of ideal compressible isotropic fluid. Since we simulate the process numerically, it is convenient to write the equations of motion directly for finite elements of the medium without invoking the Euler differential equation. Let us divide the volume occupied by the powder into N thin cylindrical layers (see Fig. 1). The density and pressure within each of the layers are assumed to be constant, and under compression they are related by the equation of compression adiabat.[1] If a layer is incompressible, we assume that the pressure in it is zero, thereby effectively taking into account pressure relaxation in the medium. If the expansion of the layer is followed by compression, the pressure experiences a step to point *4* of the adiabat. This point corresponds to the density at this time (Fig. 2).

Here, we study the compression of the sheath without stress relief. To consider the latter, additional measurements and the refinement of the model are necessary. This will be the subject of subsequent investigation.

2. BASIC EQUATIONS

Let us write the equation of motion for an nth layer. We separate out a small sector (letter A in Fig. 1) and sum all forces acting on it, designating the pressures in $(n-1)$th, nth, and $(n+1)$th layers as p_{n-1}, p_n, p_{n+1}, respectively. The equation of motion for the medial line of the nth layer (on this line, the center of mass of sector A is placed) has the form

$$m_n \frac{d^2 r_{0n}}{dt^2} = 2r_n(p_n - p_{n+1}) + 2r_{n-1}(p_{n-1} - p_n). \quad (2)$$

Here, m_n is the weight of the nth layer divided by π, r_n is

[1] Certainly, the form of the adiabat depends on the process parameters, such as the process rate. This circumstance will be regarded in further investigations.

the radius of the outer surface of the nth layer, and

$$r_{0n} = \frac{2}{3}\frac{r_n^3 - r_{n-1}^3}{r_n^2 - r_{n-1}^2} \tag{3}$$

is the radius of its medial line.

Substituting (3) into (2) yields the equation of motion for the outer surface of the nth layer:

$$a_n = \frac{1}{r_n(r_n + 2r_{n-1})}\left[\frac{3(r_n + r_{n-1})^2}{m_n}(r_n(p_n - p_{n+1}) + r_{n-1}(p_{n-1} - p_n)) - \frac{2}{r_n - r_{n+1}}(r_{n-1}v_{n-1} - r_n v_n)^2 - r_{n-1}(r_{n-1} + 2r_n)a_{n-1}\right], \tag{4}$$

where a_n and v_n are the velocity and acceleration of the outer surface of the nth layer. Also, we have $r_0 = R$, $a_0 = v_0 = 0$, $r_N = r_{\text{in}}$, $p_0 = p_1$, and $P_{N+1} = \sigma_r(r_{\text{in}})$.

Now let us consider the sheath. In the cylindrical coordinates, the equation of motion for a small particle of the sheath (in the case of axial symmetry and without strains along the z axis) has the form

$$\rho\frac{dV}{dt} = \frac{\sigma_\phi - \sigma_r}{r} - \frac{\partial\sigma_r}{\partial r} - f_{\text{m}}. \tag{5}$$

Here, ρ is the density of the sheath material; V is the radial (and the only) component of the particle velocity; and

$$f_{\text{m}}(r, t) = j(r, t)B(r, t)$$

is the Lorentz magnetic force, where

$$j(r, t) = j_0(t)\exp\frac{r - r_{\text{out}}}{\delta}$$

is the current density,

$$j_0 = \frac{J}{2\pi\delta[(r_{\text{in}} - \delta)(1 - \exp(-h/\delta)) + h]},$$

$$B(r, t) = \mu_0 j_0(t)\frac{\delta}{r} \times\left[(r - \delta)\exp\frac{r - r_{\text{out}}}{\delta} - (r_{\text{in}} - \delta)\exp\left(-\frac{h}{\delta}\right)\right]$$

is the magnetic field intensity distribution over the sheath, and $h = r_{\text{out}} - r_{\text{in}}$ is the sheath wall thickness.

Immediately before plastic deformation, $\sigma_\phi - \sigma_r = k$ throughout the sheath but $dV/dt = 0$. Integrating Eq. (5) over r and taking into consideration that the stress tensor is continuous at the interfaces ($\sigma_r(r_{\text{in}}) = \sigma_r(r_{\text{out}}) = 0$) yields an equation for the critical current density J_{c} at which the sheath starts to plastically deform. Its solution has the form

$$J_{\text{c}}^2 = \frac{4\pi^2\delta k\log(1 + h/r_{\text{in}})[(r_{\text{in}} - \delta)(1 - \exp(-h/\delta)) + h]^2}{\mu_0 Y(r_{\text{in}}, h, \delta)}, \tag{6}$$

where

$$Y(r_{\text{in}}, h, \delta) = \exp\left(-\frac{2h}{\delta}\right) \times\int_{r_{\text{in}}}^{r_{\text{in}}+h} dr\left[\left(1 - \frac{\delta}{r}\right)\exp\frac{r - r_{\text{in}}}{\delta} - \frac{r_{\text{in}} - \delta}{r}\right]\exp\frac{r - r_{\text{in}}}{\delta}.$$

Below, we give the equation of motion for the inner surface of the sheath, which coincides with the outer surface of the powder:

$$a_N = \left\{\frac{1}{r_N(r_N + 2r_{N-1})}\left[\frac{3(r_N + r_{N-1})^2}{m_N}((r_N - r_{N-1})p_N + r_{N-1}p_{N-1}) - \frac{2}{r_N + r_{N-1}}(r_{N-1}v_{N-1} - r_N v_N)^2 - r_{N-1}a_{N-1}(r_{N-1} + 2r_N)\right] - \frac{3(r_N + r_{N-1})^2}{(r_N + 2r_{N-1})m_N} \times\left[(\rho v_N^2 - k)\log\left(1 + \frac{h}{r_N}\right) - \frac{\rho v_N^2}{2}\frac{S}{(r_N + h)^2} + \frac{\mu_0 J^2 Y(r_N, h, \delta)}{4\pi^2\delta[(r_N - \delta)(1 - \exp(-h/\delta)) + h]^2}\right]\right\} \times\left\{1 + \frac{3(r_N + r_{N-1})^2}{(r_N + 2r_{N-1})m_N}\rho r_N\log\left(1 + \frac{h}{r_N}\right)\right\}^{-1}, \tag{7}$$

where

$$S = r_{\text{out}}^2 - r_{\text{in}}^2.$$

Equation (7) follows from Eq. (4), where p_{N+1} is the normal pressure on the inner surface of the sheath. It is found by integrating both sides of Eq. (5) from r_{in} to r_{out} in view of the fact that $\sigma_r(r_{\text{in}}) = p_{N+1}$ and $\sigma_r(r_{\text{out}}) = 0$ and that the velocity distribution over the wall of the tube is given by

$$V(r, t) = \frac{r_{\text{in}}(t)}{r}V_{\text{in}}(t),$$

where $V_{\text{in}}(t)$ is the velocity of the inner surface of the tube.

Finding p_{N+1} from the resultant expression and substituting it into (4), we arrive at an equation for a_N. It

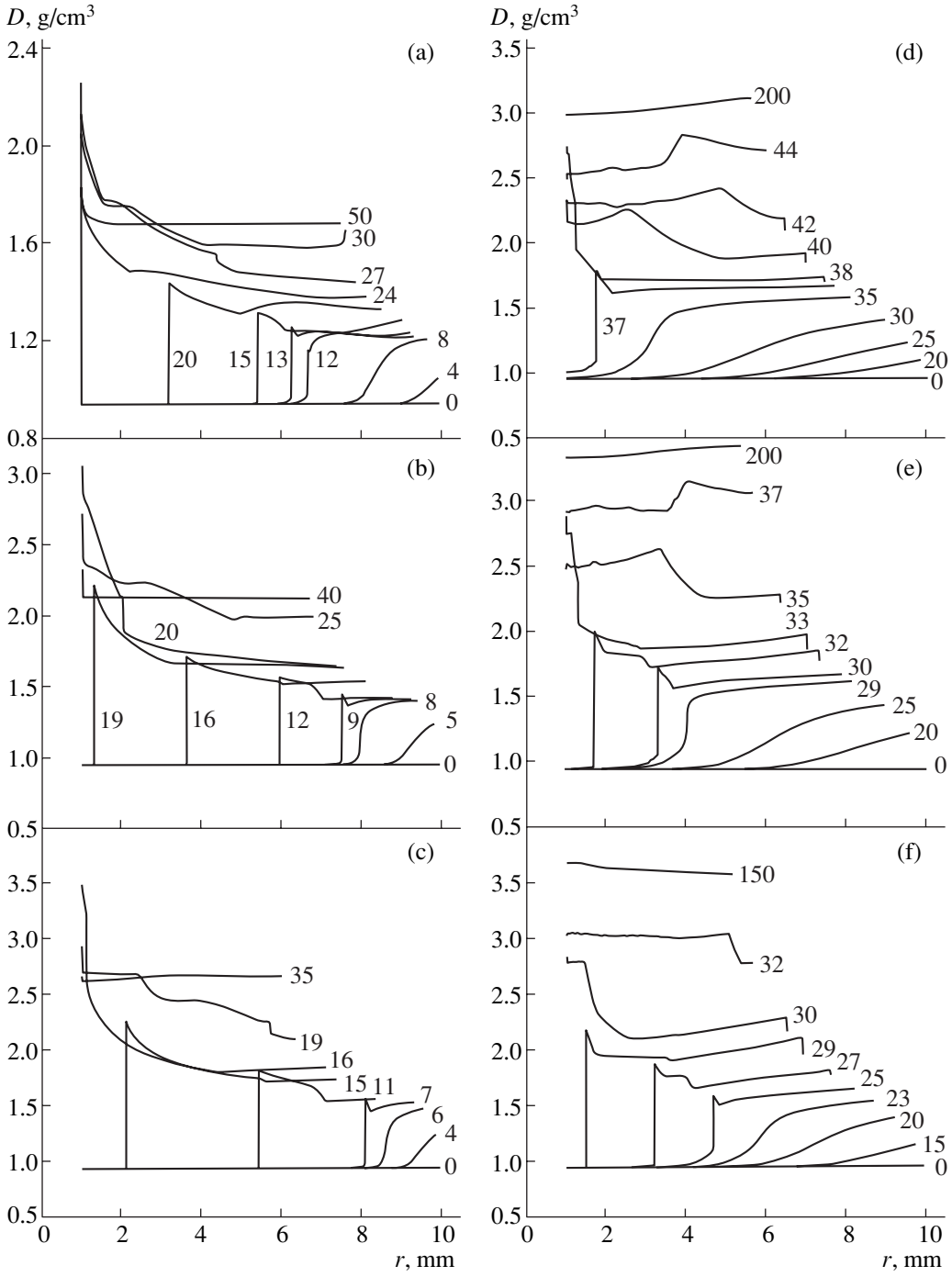

Fig. 3. Density field at various time instants (figures by the curves in microseconds) for two values of the current half-period, $T_{1/2}$ = (a–c) 9.76 and (d–f) 100 μs, and for a first-pulse amplitude of (a, d) 1.2, (b, e) 1.6, and (c, f) 2.0 MA.

solution is (7). Equations (4) ($n = 1, 2, \ldots, N-1$) form the basis for numerical simulation of molding. We will also use an expression for the work of pressure ΔW_p per unit tube length that is done on the powder when the inner surface of the tube is shifted by Δr_{in}:

$$\Delta W_P = 2\pi r_{in} p_N \Delta r_{in}. \quad (8)$$

3. RESULTS AND DISCUSSION

In this section, we discuss the results of simulation for several sets of the parameters and justify the assumption that the process is adiabatic. In calculations, the number of layers was taken to be equal to 1000 and $k = 100$ MPa at 293 K. The slopes of the conductivity and specific heat versus sheath temperature

curves were assumed to be the same as for copper [11]. As a compression adiabat, we used that for nanograin Al_2O_3 powder [12].

Figure 3 shows the time evolution of the compact-density fields for various pulse lengths and first-pulse amplitude. From these curves, one can determine the formation conditions for a powder-compressing shock. It is known that shock wave (SW) compression of powders frequently produces cracked and variable-density compacts [13]. Therefore, SW conditions are unfavorable especially as applied to powders of brittle materials. In the case of a longer pulse, the SW is seen to form at the final stage of the process, while in the case of a shorter pulse the SW conditions are set early in the process. The appearance of SWs is explained as follows. Behind the wave front, the velocity of a perturbation generated by the shrinking sheath is higher than ahead of the front, since the density of the medium behind the front is higher. Therefore, if the rate of compression is sufficiently high, the front steepens with time and a discontinuity in the density field arises in a time. The cylindrical geometry of the medium encourages such a scenario.

A practically important result of soft (SW-free) pulsed compaction of Al_2O_3 powder is shown in Fig. 4 (here, J_1 is the first-pulse amplitude). In the case of a longer pulse, a compact density as high as 2.5 g/cm^3 is achievable throughout the process without generating SWs. For a shorter pulse, the same density is reached at a much higher amplitude of the first pulse (Fig. 3c) and the compaction wave front steepens drastically.

A critical parameter of molding is the compacting pressure, i.e., the pressure exerted on the powder by the compressing sheath. The evolution of this parameter in time is demonstrated in Fig. 5. Sharp steps in the compacting pressure are a consequence of the loading–unloading model adopted (Fig. 2). As an actual pressure, one should take the envelope of the peaks, which is related to the density of the subsurface layer through the equation of adiabat. Figure 5 also shows the evolution of the density in the subsurface layer, which represents a relatively smooth curve (without high steps). This indicates that the process is steady and, hence, the model is adequate.

Comparing the compacting pressure and the pressure of the magnetic field (also shown in Fig. 5), one can notice that the former may exceed the maximal value of the latter by as much as one order of magnitude. This means that the compacting pressure may be kept at a sufficiently high level even if a moderate voltage is applied to the fixture of the equipment (the deforming sheath experiencing very high stresses is not a part of the fixture). This effect is inertial: at the initial stage of the process, where the pressure in the medium is low and the medium exhibits no resistance to compression, the major part of the magnetic field energy is converted to the kinetic energy of the shrinking sheath. Subsequently, as the pressure in the medium rises, the kinetic energy passes to the compacting energy.

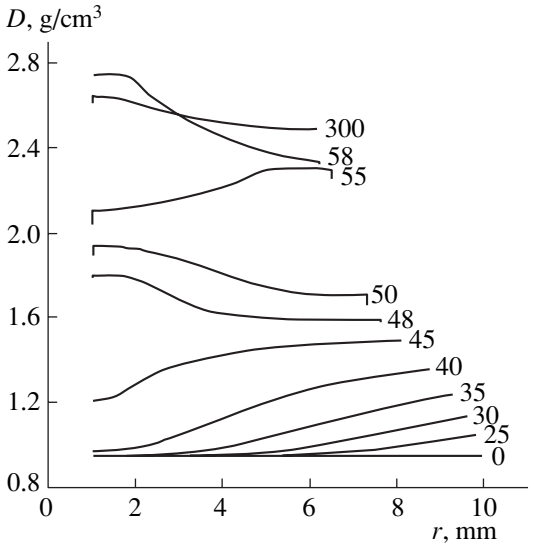

Fig. 4. Density field at various time instants (figures by the curves in microseconds) for $T_{1/2}$ = 100 μs, τ = 3000 μs, J_1 = 0.85 MA, and h = 1 mm.

Another important parameter characterizing the efficiency of compacting is the specific compacting energy mentioned above. Calculation of this parameter by formula (8) was also included in the computer program. Figure 6 plots this energy against the first-pulse amplitude for various thicknesses of the charge (internal-rod radii). For the shorter pulse, the thinner the initial layer of the powder, the higher the specific compacting energy. For the longer pulse, the situation is reversed. One more fact deserves attention: the specific compacting energy for the processes characterized by Figs. 3c and 4c equals 149.8 and 75.6 J/g, respectively. As was noted above, both processes provide nearly the same density of compacts. However, the processes considered here are adiabatic: the compacting energy is entirely converted to the internal energy of the medium being compacted, causing a temperature variation. Therefore, by controlling the width of compacting pulses, one can vary the temperature of the powder during compression.

Let us substantiate the assumptions made earlier, starting from the assumption that compacting is an adiabatic process. To do this, we compare the size l of the diffusion of an initially point temperature perturbation after a time Δt (the time of compacting) with the thickness of the powder layer. The expression for l has the form [14]

$$l \approx \sqrt{\frac{\lambda \Delta t}{\rho C_p}}, \tag{9}$$

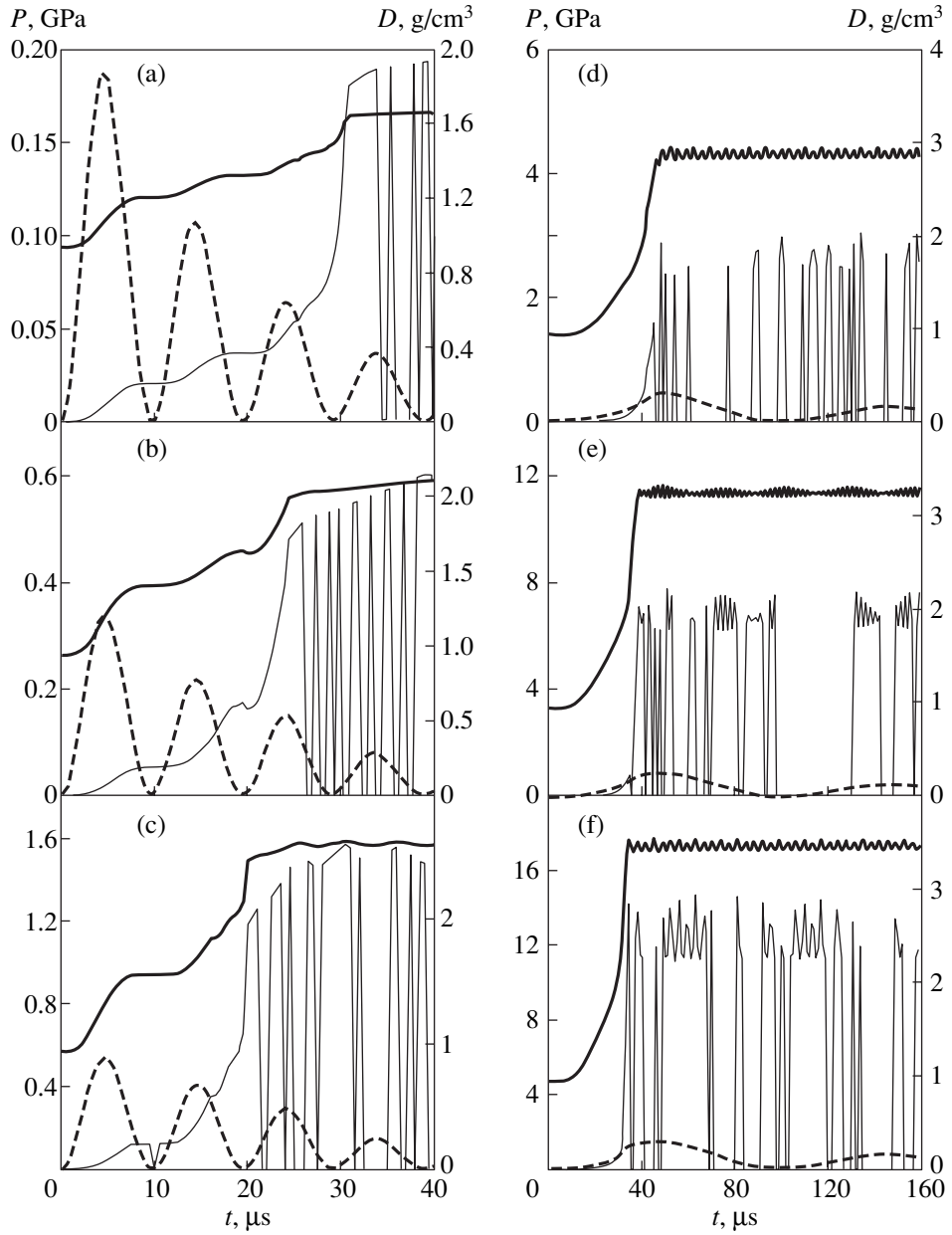

Fig. 5. Variation of the compacting pressure (thin continuous curve), magnetic pressure, and compact density (thick continuous curve) at the inner surface of the sheath for the same parameters as in Fig. 3.

where λ is the thermal conductivity, ρ is the density of the material, and C_p is the heat capacity at constant pressure.

Since relevant data for Al_2O_3 nanopowder are lacking, we take the values $\lambda = 2.4$ W/(m K) and $\rho = 2.7$ g/cm^3 for a mullite–corundum refractory with an Al_2O_3 content from 72 to 90% and a porosity of 16–20% under atmospheric pressure in a wide temperature range [15]. For C_p, we take 800 J/(kg K). This value is typical of pure alumina modifications at 298.15 K [16]. Substituting these values into (9) and putting $\Delta t = 50$ μs, we obtain $l \approx 8 \times 10^{-6}$ m $\ll 10^{-2}$ m. This proves that the process is adiabatic.

Now let us see whether we have the right to ignore electromagnetic transients in the sheath. Figure 7 reproduces Fig. 3a and compares it with the same process where the skin depth is four times smaller. Qualitatively, the curves run identically; as for a quantitative discrepancy, it is very small and of no practical significance. Thus, this discrepancy may be neglected and there is no need to consider electromagnetic processes in the sheath more accurately.

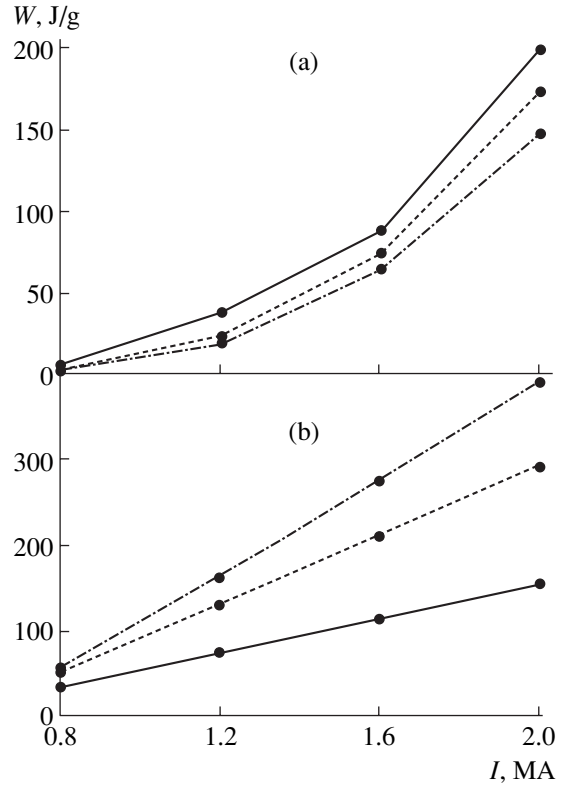

Fig. 6. Specific compacting energy vs. the first-peak amplitude for pulses of various lengths ($T_{1/2}$ = (a) 9.76 and (b) 100 μs) and an internal rod radius (compact thickness) R = 8 (continuous line), 4.5 (dashed line), and 0 mm (dash-and-dot line). The symbols are calculation by (9).

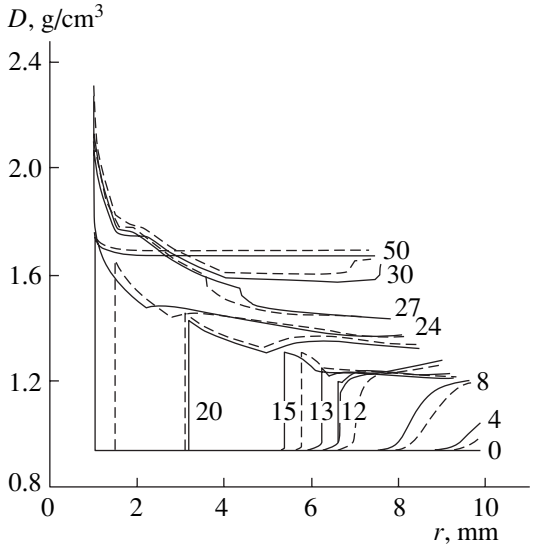

Fig. 7. The process shown in Fig. 3a (continuous line) vs. the same process where the skin depth of the sheath is four times smaller (dashed line).

CONCLUSIONS

A model of pulsed magnetic molding of long compacts is developed. It is based on using an actual (experimentally measured) adiabat of high-rate compression. The model allows one to (i) evaluate the time evolution of the density field, the field of kinematic parameters, and the compacting work; (ii) predict conditions under which a shock wave does not arise; and (iii) find sets of parameters that provide high compacting pressure pulses far exceeding the fixture strength.

ACKNOWLEDGMENTS

The authors thank Yu.A. Kotov and N.B. Volkov for the valuable discussion.

REFERENCES

1. G. Dell'Agli and G. Mascolo, in *Proceedings of the 7th European Conference on Advanced Materials, Rimini, 2001*; cdEUROMAT.273.doc.
2. A. V. Ustyugov, A. P. Tkachenko, and V. F. Chukharev, in *Proceedings of the 5th All-Russia Conference on Physical Chemistry of Ultradisperse Systems, Yekaterinburg, 2000* (Inst. Fiz. Met., Ural. Otd. Ross. Akad. Nauk, Yekaterinburg, 2000), pp. 341–342.
3. D. J. Sandstrom, Metal Prog. **86**, 215 (1964).
4. V. A. Mironov, *Pulsed Magnetic Molding of Powders* (Zinatne, Riga, 1980), pp. 79–118 [in Russian].
5. B. É. Fridman and F. G. Rutberg, Zh. Tekh. Fiz. **66** (2), 123 (1996) [Tech. Phys. **41**, 181 (1996)].
6. J. Peti, Yu. A. Alekseev, S. P. Anan'ev, and M. N. Kazeev, in *Proceedings of the 7th International Conference on Megagauss Magnetic Field Generation and Related Issues (MG-VII), Sarov, 1997*, pp. 579–586.
7. V. V. Ivanov, S. N. Paranin, A. N. Vikhrev, and A. A. Nozdrin, Materialovedenie, No. 5, 49 (1997).
8. V. V. Ivanov, S. Yu. Ivin, A. I. Medvedev, *et al.*, Neorg. Mater. **37**, 248 (2001).
9. V. V. Ivanov and A. A. Nozdrin, Pis'ma Zh. Tekh. Fiz. **23** (13), 76 (1997) [Tech. Phys. Lett. **23**, 527 (1997)].
10. A. A. Il'yushin, *Mechanics of Continuous Medium* (Izd. Mosk. Gos. Univ., Moscow, 1990) [in Russian].
11. *Handbook of Physical Quantities*, Ed. by I. S. Grigoriev and E. Z. Meilikhov (Énergoatomizdat, Moscow, 1991; CRC, Boca Raton, 1997) [in Russian].
12. V. V. Ivanov and A. A. Nozdrin, in *Proceedings of the 4th All-Russia Conference on Physics and Chemistry of Ultradisperse Systems, Moscow, 1999*, pp. 277–280.
13. R. A. Graham and A. B. Sawaoka, *High Pressure Explosive Processing of Ceramics*, Ed. by R. A. Graham and A. B. Sawaoka (Trans. Tech. Publ., 1987), pp. 17–27.
14. L. D. Landau and E. M. Lifshitz, *Course of Theoretical Physics*, Vol. 6: *Fluid Mechanics* (Nauka, Moscow, 1986; Pergamon, New York, 1987).
15. R. E. Krzhizhanovskiĭ and Z. Yu. Shtern, *A Handbook of Thermophysical Properties of Nonmetallic Materials* (Énergiya, Leningrad, 1973).
16. *A Handbook of Thermodynamic Properties of Elementary Substances*, 4 vols., Ed. by V. P. Glushko (Nauka, Moscow, 1977–1982).

Translated by V. Isaakyan

Technical Physics, Vol. 49, No. 4, 2004, pp. 420–425. Translated from Zhurnal Tekhnicheskoĭ Fiziki, Vol. 74, No. 4, 2004, pp. 42–47.

SOLID-STATE ELECTRONICS

Equilibrium States and Quasi-Static Magnetization Switching of a Multilayer Structure

D. I. Sementsov and A. M. Shutyĭ

Ul'yanovsk State University, Ul'yanovsk, 432700 Russia

e-mail: sementsov@ulsu.ru

Received June 30, 2003

Abstract—The equilibrium orientations of magnetic moments that correspond to various values and directions of the biasing field are found in a set of magnetic films with cubic crystalline anisotropy and uniaxial induced anisotropy. The films are coupled by exchange interaction of the antiferromagnetic type. Field intervals are established where noncollinear and bistability states causing orientational phase transitions and hysteresis exist. Ninety degree magnetization switching (per switching cycle) of the magnetic moments of the films, as well as an orientational phase transition of bifurcation character, is discovered. Hysteresis loops for 180° in-plane magnetization switching are constructed. © *2004 MAIK "Nauka/Interperiodica".*

INTRODUCTION

The static and dynamic properties of multilayer magnetically coupled structures have been the subject of intensive research over many years [1–7]. Interest in these structures stems from the fact that they offer much promise for a variety of devices. Today, one can distinguish designs with weak interlayer coupling due to dipole–dipole magnetostatic interaction [1, 2] and with strong coupling due to indirect exchange interaction [3–7]. The former are structures based on polycrystalline magnetic films separated by a thick nonmagnetic spacer. The thickness d_s of this spacer must satisfy the condition $d_s > \sqrt{2A/\pi M^2}$, where A is the exchange interaction constant and M is the saturation magnetization. For permalloy-like films, $A \simeq 10^{-6}$ erg/cm, $4\pi M \simeq 10^4$ Oe, and $d > 10^{-6}$ cm. To strongly coupled structures, one can refer magnetically ordered superlattices: thin-film structures consisting of nanocrystalline magnetic metal films separated by nonmagnetic metal spacers of thickness $d_s \simeq 10^{-7}$ cm. Extensive research on exchange-coupled films is dictated by present-day requirements of microelectronics. The unique physical properties of these objects, the most typical of which are $(Fe/Cr)_n$ periodic structures (n is the number of periods) are defined primarily by the type of coupling between the magnetic moments of adjacent layers. In the absence of a biasing field, ordinary (bilinear) exchange interaction causes either ferromagnetic or antiferromagnetic ordering, while biquadratic exchange interaction produces noncollinear arrangement of the magnetic moments of adjacent layers [8–10]. To analyze the establishment of dynamic regimes responding to small variations of structure parameters and switching fields, it is necessary to know for the first place the equilibrium states of the system [10–12]. In this work, we consider a periodic structure consisting of ferromagnetic layers separated by nonmagnetic spacers, which provide antiferromagnetic exchange coupling between the layers. Our aim is to study the equilibrium orientations of coupled magnetic moments and quasi-static switching of the magnetizations of the layers in a magnetic field of given direction. This type of coupling is of great interest, since it provides an opportunity to realize many equilibrium orientations and dynamic regimes.

FREE ENERGY

To exclude the effect of the top layers, we will assume that the structure being studied consists of a great number ($n \gg 1$) of layers (films) with a magnetization $\mathbf{M}_i$ and thickness d_i that are separated by nonmagnetic spacers. The thickness of the latter provides antiferromagnetic exchange coupling of the magnetic layers. Following available experimental data [13], it is adopted that magnetic anisotropy of the layers is the superposition of induced uniaxial (easy-axis) anisotropy and crystalline cubic anisotropy such that the [100] and [010] crystallographic axes lie in the plane of the layers and the easy magnetic axis runs normally to the layers. In this case, the free energy of the system per unit surface area is given by

$$E = \sum_{i=1}^{n} d_i \Big[-\mathbf{H}\cdot\mathbf{M}_i + \frac{K_{1i}}{4}(\sin^2 2\psi_i + \cos^4\psi_i \sin^2 2\varphi_i) + \frac{K_{2i}}{16}\sin^2 2\psi_i \cos^2\psi_i \sin^2 2\varphi_i \qquad (1)$$

1063-7842/04/4904-0420$26.00 © 2004 MAIK "Nauka/Interperiodica"

$$+ (K_{ui} - 2\pi M_i^2)\cos^2\psi_i \Big] + J\sum_{i=1}^{n} \frac{\mathbf{M}_i \cdot \mathbf{M}_{i+1}}{M_i M_{i+1}}.$$

Here, J is the constant of bilinear coupling due to indirect exchange interaction between the magnetic moments of adjacent layers (in general, this constant depends on the thickness, material, and structure of the spacer), $K_{1,2i}$ are the first and second cubic anisotropy constants, K_{ui} is the growth induced anisotropy constant, **H** is the static biasing field, φ_i is the azimuth angle that is measured from the [100] axis and specifies the orientation of the magnetic moment of a related layer, and ψ_i is the angle between the magnetization vector $\mathbf{M}_i$ and the film surface.

The magnetic layers are assumed to be identical; that is, $M_i = M$, $d_i = d$, $K_{ui} = K_u$, and $K_{1,2i} = K_{1,2}$. The coupling constant J is taken to be positive in order to provide antiferromagnetic coupling between the magnetic moments in adjacent layers, i.e., opposite directions of the moments in the absence of the biasing field. Then, the entire set of the magnetic layers is divided into two subsystems ($j = 1, 2$) and the layers in either of the subsystems are assumed to behave in a similar manner.

IN-PLANE MAGNETIZATION SWITCHING

First consider the quasi-static magnetization switching of the structure when the biasing field **H** lies in the plane of the films. With regard to high demagnetizing fields ($4\pi M \gg 2K_u/M$, JM) used in practice, the magnetic moments lie in the plane of the layers; therefore, equilibrium $\psi_j = 0$. Equilibrium azimuth angles $\varphi_j(H)$ can be found from the equilibrium conditions $\partial E/\partial\varphi_j = 0$ and $\partial^2 E/\partial\varphi_j^2 > 0$, which yield a set of equations for two adjacent layers (in view of (1)):

$$\begin{aligned} &2HM\sin(\varphi_j - \varphi_H) + K_1\sin 4\varphi_j \\ &\quad - 2\bar{J}\sin(\varphi_j - \varphi_{3-j}) = 0, \\ &HM\cos(\varphi_j - \varphi_H) + 2K_1\cos 4\varphi_j \\ &\quad - \bar{J}\cos(\varphi_j - \varphi_{3-j}) > 0; \quad j = 1, 2, \end{aligned} \tag{2}$$

where φ_H is the azimuth angle that is measured from the [100] axis and defines the direction of the field **H** in the plane and $\bar{J} = 2J/d$ (doubling of the coupling constant in comparison with a two-layer system is due to interaction of the magnetic moment of each of the layers with those of two nearby layers).

According to (2), in the initial state (i.e., in the absence of an external field), the magnetic moments of two adjacent layers are directed parallel and antiparallel to the [100] crystallographic direction, respectively.

Let us numerically analyze the equilibrium directions of the magnetizations of the layers for $\varphi_H = 0$, i.e., when the biasing field is parallel to the magnetization of layers with $j = 2$ and antiparallel to that of layers with $j = 1$. In calculations, we will use parameter values that are close to those of the $(Fe/Cr)_n$ system: $M = 1620$ G for iron layers; the anisotropy constants $K_1 = 4.6 \times 10^5$ erg/cm^3, $K_2 = 1.5 \times 10^5$ erg/cm^3, and $K_u = 2.06 \times 10^6$ erg/cm^3; and the thickness $d = 21.2 \times 10^{-8}$ cm. These parameters for chromium do not appear in (2) in explicit form, but they define the value of the coupling constant J [5]. Figure 1a plots the equilibrium azimuth angles φ_1 (continuous lines) and φ_2 (dotted lines) of the magnetic moments of two adjacent films against the biasing field for J = (*1*) 0.15 and (*2*) 0.25 erg/cm^2. For the initial orientations of the magnetic moments $\varphi_{10} = \pi$ and $\varphi_{20} = 0$ and for $\varphi_H = 0$, the starting state is equilib-

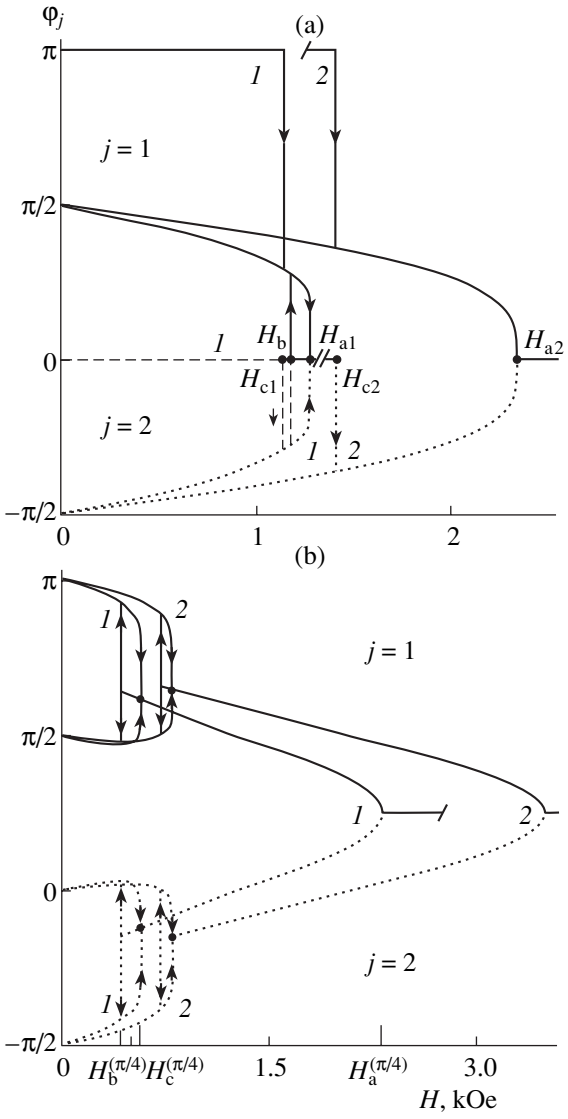

Fig. 1. Field dependences of the equilibrium angles φ_1 (solid curves) and φ_2 (dotted curves) under in-plane (a) 180° and 90° and (b) 45° magnetization switching. J = (*1*) 0.15 and (*2*) 0.25 erg/cm^2.

rium when the field varies from $H = 0$ to $H = H_c$. At $H = H_c$, the step orientational phase transition occurs throughout the system. As a result of antiferromagnetic coupling between adjacent magnetic moments, the magnetization of films with $j = 1$ switches by an angle other than 180°. An angular repulsion of the magnetic moments also changes the magnetization direction in films with $j = 2$ so that $\varphi_2(H_c) = -\varphi_1(H_c)$. As the field increases further, the angle between the magnetization vectors of adjacent layers decreases and reaches a minimal value $\varphi_1 - \varphi_2 = 2\varphi_a(J)$ at $H = H_a$ (the minimal value of this angle inversely varies with the coupling constant). At the field H_a, the second phase transition, causing the magnetic moments to be codirected with the field, is observed.

As the biasing field decreases from values of $H > H_a$, at which the state with the codirected moments of adjacent layers is an equilibrium state, this state persists down to $H_b < H_a$ for $J = 0.15$ erg/cm^2 (curve *1*). At $H = H_b$, the reverse orientational phase transition takes place, at which the vectors $\mathbf{M}_1$ and $\mathbf{M}_2$ diverge sharply up to the angles $\varphi_1(H_b) = -\varphi_2(H_b)$. With a further decrease in the biasing field, the angle between the magnetizations grows smoothly, reaching π at $H = 0$. However, each of the individual magnetic moments does not return to its initial state. Thus, switching a biasing field $H > H_c$ on and off causes the magnetic moments to rotate through an angle of $\pi/2$; that is, the initial configuration with the angles $\varphi_{10} = \pi$ and $\varphi_{20} = 0$ turns into the configuration with $\varphi_{10} = \pi/2$ and $\varphi_{20} = -\pi/2$. The latter configuration is equivalent to the initial one in terms of anisotropy of magnetic layers and direction of crystallographic axes.

In the case of in-plane 90° magnetization switching, which is observed at $\varphi_{10} = -\varphi_{20} = \pi/2$ and $\varphi_H = 0$, an increase in the field to H_a causes the magnetic moments to gradually converge. As in the case considered above, the orientational phase transition occurs at $H = H_a$, as a result of which only the state with codirected magnetic moments is equilibrium. When the biasing field declines, the noncollinear configuration is restored because of the reverse phase transition, at which $H = H_b$. Thus, at small J, we observe an orientational hysteresis loop, which narrows with increasing the coupling constant. When J is high (curve *2*), $H_b = H_a$ and the hysteresis loop disappears.

When the field differs from $H = H_c$, the branches of the equilibrium orientations of the magnetic moments $\mathbf{M}_{1,2}$ are the same for the cases of transverse and longitudinal in-plane magnetization switching (see above). As follows from (1) and (2), this is associated with the fact that, at the critical field, the energy minimum is absent for the angles $\varphi_1 = \pi$ and $\varphi_2 = 0$ and is present for noncollinear magnetic moments down to the zero field, when $\varphi_{j0} = \pm\pi/2$. As a result, having passed from the state with opposite orientations to the equilibrium-angle branches corresponding to noncollinear orientations, the magnetic moments cannot return to the initial configuration in the absence of the field.

Exact expressions for the critical field values are found from (2):

$$H_a = \frac{4}{3M}\sqrt{\frac{\bar{J} + K_1}{6K_1}}(\bar{J} + K_1), \quad H_b = \frac{2}{M}(\bar{J} - K_1), \qquad H_c = \frac{2}{M}\sqrt{K_1(\bar{J} + K_1)}. \tag{3}$$

The minimal angle between the magnetic moments for the noncollinear configuration is found from set (2) in view of (3):

$$\cos\varphi_a = \sqrt{\frac{\bar{J} + K_1}{6K_1}}. \tag{4}$$

As the coupling constant grows, the hysteresis loop narrows and the angle φ_a decreases and goes to zero (the loop collapses) at $J = J_{ab} \approx 0.24$ erg/cm^2 ($H_a = H_b$).

Consider now the important case of in-plane magnetization switching when the field **H** is aligned with the [110] axis, i.e., when $\varphi_H = \pi/4$. For this situation, equilibrium azimuth angles versus the biasing field are shown in Fig. 1b for $J = 0.15$ and 0.25 erg/cm^2 and magnetic moments oriented along the [100] direction ($\varphi_{10} = \pi$, $\varphi_{20} = 0$) and the [010] direction ($\varphi_{10} = \pi/2$, $\varphi_{20} = -\pi/2$). As the field grows, the magnetic moments of the films gradually approach each other up to a critical value $H_c^{(\pi/4)}$ where the orientational phase transition takes place. Upon this transition, both magnetic moments take on equilibrium initial (symmetric about the [110] direction) positions. With a further increase in biasing field, the magnetic moments approach closer to each other and become codirected at $H = H_a^{(\pi/4)}$. The branches of equilibrium orientations, which are symmetric relative to the [110] direction, can be constructed by using the expression

$$H = \frac{2}{M}(\bar{J} \mp K_1 \sin 2\varphi_j)\cos\left(\varphi_j \pm \frac{\pi}{4}\right), \tag{5}$$

which follows from (2). Here, the upper and lower signs refer to layers with $j = 1$ and 2, respectively.

The critical field $H_a^{(\pi/4)}$ corresponds to angles $\varphi_j = \pi/4$ and is given by

$$H_a^{(\pi/4)} = \frac{2}{M}(\bar{J} + K_1). \tag{6}$$

If the initial equilibrium orientation of the magnetic moments is symmetric about the [110] axis, a decrease in the biasing field to $H_b^{(\pi/4)} < H_c^{(\pi/4)}$ causes them to gradually diverge. The field $H_b^{(\pi/4)}$ is a field of bifurcation: as the field reaches this value, the set of two cou-

pled magnetic moments has two possible directions of magnetization switching. Eventually, equilibrium angles may be close to either the [100] or the [010] direction.

Figure 2a plots the field of bifurcation, the hysteresis loop width $\Delta_{bc}^{(\pi/4)} = H_c^{(\pi/4)} - H_b^{(\pi/4)}$, and the field of saturation magnetization $H_a^{(\pi/4)}$ in the [110] direction versus the coupling constant (curves *1*–*3*). In Fig. 2b, the angular steps $\Delta\varphi_{cj}^{(\pi/4)}$ and $\Delta\varphi_{bj}^{(\pi/4)}$ that occur at the points $H = H_c^{(\pi/4)}$ and $H = H_b^{(\pi/4)}$ of the phase transitions are plotted versus J (curves *1*, *2*). Large steps (continuous lines) are typical of the magnetic moment of the first layer when $\varphi_{10} = \pi$ and $\varphi_{20} = 0$ and of the magnetic moment of the second layer when $\varphi_j = \pm\pi/2$. It is seen that the critical field grows monotonically while the hysteresis loop narrows as the constant of interlayer interaction increases (for $J = 0.4$ erg/cm^2 (Fig. 1b, curve *2*), the loop has a width $\Delta_{bc}^{(\pi/4)} \approx 21$ Oe). The large angular steps also decrease monotonically. Small steps in the range of J considered (the dotted curves) exhibit a distinct maximum at the point of phase transition ($J \approx 0.2$ erg/cm^2, $H = H_b^{(\pi/4)}$) (that is, when the biasing field decreases) and grow monotonically with increasing field starting from $H = H_c^{(\pi/4)}$. It should be noted that, in the structure under study (specifically, at $M_1 = M_2$) both equilibrium configurations of the magnetic sublattices that result from the bifurcational phase transition at $H = H_b^{(\pi/4)}$ are identical in terms of total magnetization.

Magnetization switching to one of the two equilibrium states due to the phase transition at $H = H_b^{(\pi/4)}$ depends on parameter fluctuations and on the parameters responsible for the decay of the biasing field. Figure 3 shows (at $J = 0.2$ erg/cm^2) the time dependences of the angles φ_j tending to the equilibrium positions of the magnetic moments that set up after the orientational phase transition. The transition proceeds when the field decays (is switched off) by the law

$$H(t) = H_0 \exp(-t/\tau), \qquad (7)$$

where the time constant $\tau = 1$ ns. Two values of the initial field that are higher than the critical field $H_b^{(\pi/4)} = 576$ Oe, $H_0 = 580$ (curve *1*) and 579 Oe (curve *2*), are considered. We see that which of the two equilibrium states will be realized depends on the initial value of the biasing field. Such curves can also be obtained at the same H_0 but different decay rates.

The hysteresis loop observed under magnetization reversal in a magnetic sample (this loop is easy to observe in experiments) is an important characteristic of the sample. For multilayer systems, the hysteresis

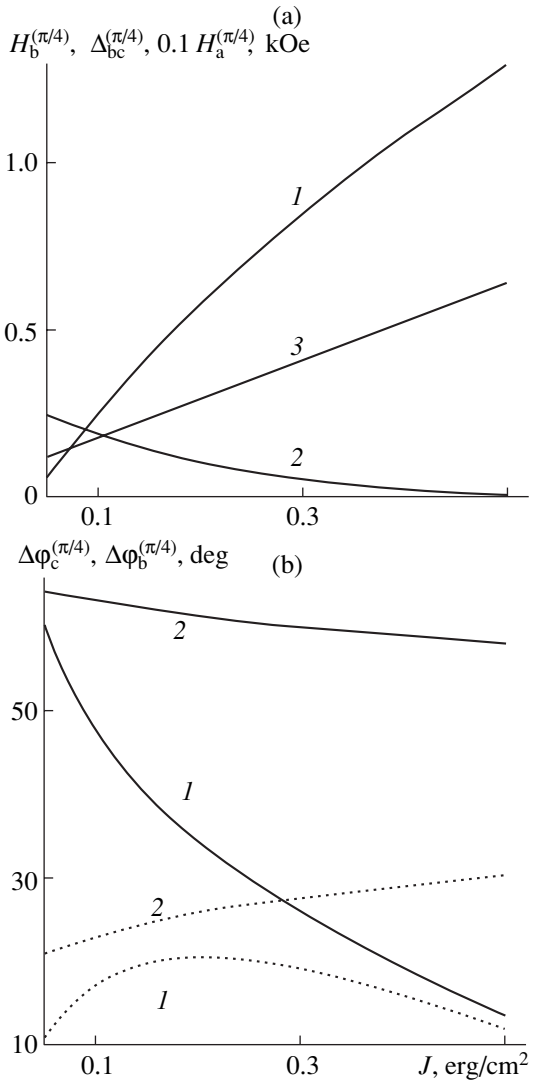

Fig. 2. (a) (*1*) Bifurcational field $H_b^{(\pi/4)}$, (*2*) hysteresis loop width $\Delta_{bc}^{(\pi/4)} = H_c^{(\pi/4)} - H_b^{(\pi/4)}$, and (*3*) saturation field $H_a^{(\pi/4)}$ in the [110] direction vs. coupling constant J. (b) Angular steps (*1*) $\Delta\varphi_{cj}^{(\pi/4)}$ and (*2*) $\Delta\varphi_{bj}^{(\pi/4)}$ vs. J ($j = 1$, solid curve; $j = 2$, dotted line).

loop is defined by the behavior of the total magnetization $\sum \mathbf{M}_i$ in a magnetization-reversing field. Figure 4 shows the field dependence of the normalized projection of the total magnetic moment of both sublattices, $(\mathbf{M}_1 + \mathbf{M}_2)/M$, onto the reversing field direction. The initial orientation of the magnetic moments are $\varphi_j = \pm\pi/2$; those of the external field are $\varphi_H = 0$, $\pi/4$, and $\pi/8$; and the coupling constants $J = 0.05$, 0.15, and 0.25 erg/cm^2. Since the functions are odd, only halves of the curves are depicted. It is seen that the hysteresis loops collapse, as a rule, under low fields. As the cou-

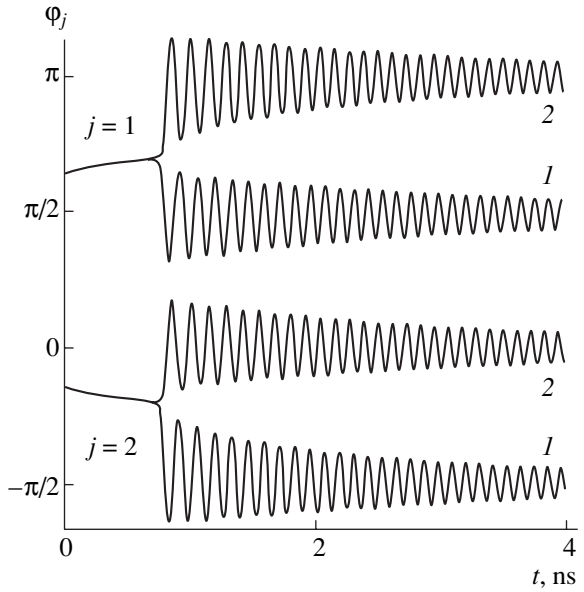

Fig. 3. Time dependences of the angles $\varphi_{1,2}$ near the phase transition field $H_b^{(\pi/4)}$. H_0 = (*1*) 580 and (*2*) 579 Oe, respectively.

pling constant grows, the loop narrows, the collapse range expands, and the loop turns into the magnetization reversal curve at $J > J_{ab}$ (or $J > J_{bc}^{(\pi/4)}$, where $J_{bc}^{(\pi/4)}$ meets the equality $H_b^{(\pi/4)} = H_c^{(\pi/4)}$). The loop has only one collapse point at $H = 0$ if $J = J_b$, where J_b is the value of the coupling constant at which H_b (or $H_b^{(\pi/4)}$) vanishes. For low coupling constants, $J < J_b$, the loop does not collapse. When the field is aligned with the [100] direction, the loops disappear at coupling constants lower than in the case of the field aligned with the [110] axis, since $J_{ab} > J_{ab}^{(\pi/4)}$. If the field makes an angle with the [100] or [110] direction, specifically at $\varphi_H = \pi/8$, the loop exhibits an additional bend, which is smooth or sharp, depending on the coupling constant value. Furthermore, as the field grows, the magnetization tends to a maximum asymptotically. However, the loops observed in this case are basically the same as when the field is parallel to the [100] axis. The shape of the loops depicted in Fig. 4 closely approximates the shape of the loops taken of actual film structures in experiments [13, 14].

PERPENDICULAR MAGNETIZATION SWITCHING

Let a biasing field **H** be parallel to the normal to the film surface. Then, if oppositely directed magnetic moments are initially aligned with the [100] or [010] axis, the equilibrium angle between the magnetic

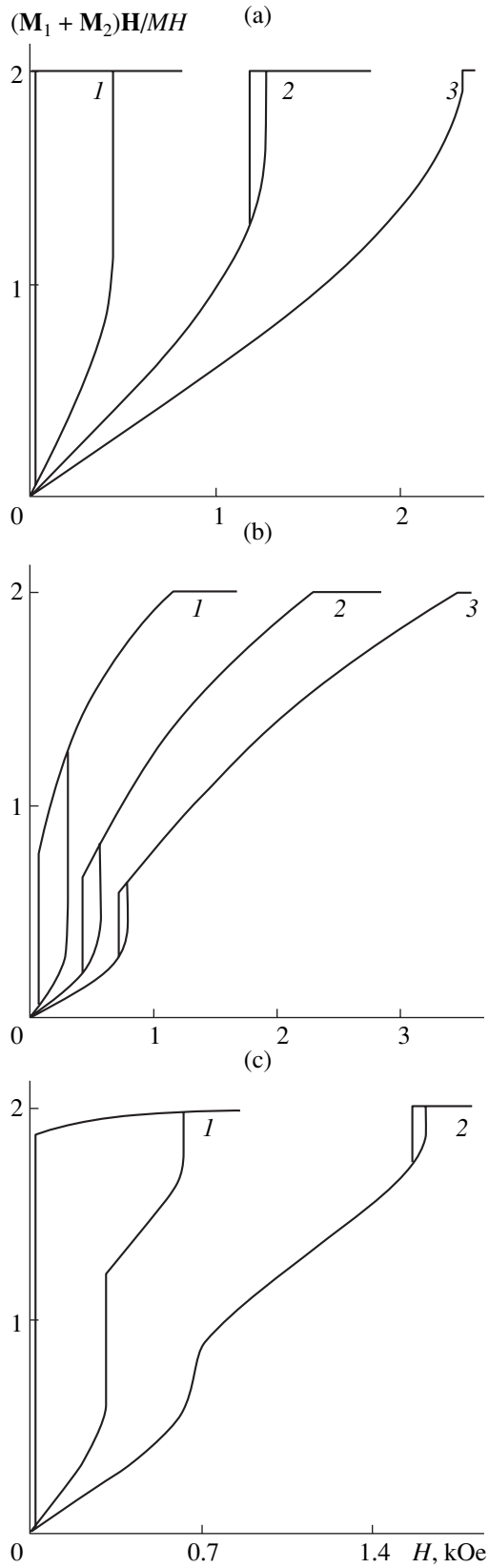

Fig. 4. Hysteresis loops in the multilayer structure for the initial orientations $\varphi_j = \pm\pi/2$ of the magnetic moments. The external field orientation φ_H = (a) 0, (b) $\pi/4$, and (c) $\pi/8$; J = (*1*) 0.05, (*2*) 0.15, and (*3*) 0.25 erg/cm^2.

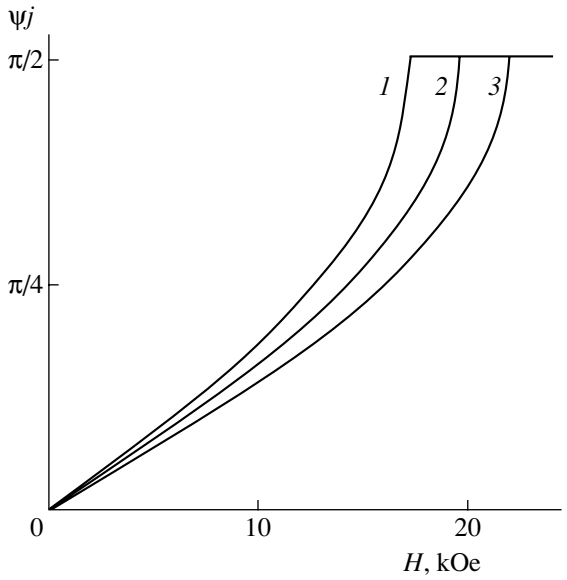

Fig. 5. Field dependences of the equilibrium angle ψ_j between the magnetic moments and the surface of the film for J = (*1*) 0, (*2*) 0.1, and (*3*) 0.2 erg/cm^2.

moments and the film surface is given by

$$-HM\cos\psi_j + \frac{K_1}{2}\sin 4\psi_j + (\bar{J} - K_u + 2\pi M^2)\sin 2\psi_j = 0. \quad (8)$$

From (8), it follows that magnetization switching in both layers proceeds symmetrically; i.e., the angles ψ_1 and ψ_2 remain equal to each other during their increase with biasing field. Once the field has reached a value

$$H_s = \frac{2}{M}(\bar{J} - K_1 - K_u + 2\pi M^2) \quad (9)$$

the magnetization saturates ($\psi_1 = \psi_2 = \pi/2$) and a further increase in the field does not change the orientation of the magnetic moments. Here, a decrease in the field does not cause orientation hysteresis: the forward and backward branches coincide. The dependences $\psi_j(H)$ for J = 0, 0.2, and 0.4 erg/cm^2 (curves *1*–*3*) are shown in Fig. 5. The saturation field H_s is a linear function of the coupling constant. This fact may be used for experimental determination of the latter.

CONCLUSIONS

Thus, multilayer structures like $(Fe/Cr)_n$ with antiferromagnetic coupling due to indirect exchange interaction may exhibit orientational phase transitions resulting in both collinear and noncollinear orientations of the magnetic moments of the films. At low values of the coupling constant, in-plane 90° magnetization switching causes an orientational hysteresis loop. If a biasing field of intensity $H > H_c$ aligned with the magnetic layers is turned on and off, the structure undergoes 90° switching (the hysteretic switching effect). If magnetization switching takes place along the [110] axis, the point of bifurcation arises. From this point, the magnetic moments may run nearly parallel to either the [100] or [010] axis. In the case of in-plane magnetization reversal, hysteresis loops of the system's total magnetization may collapse in a wide range of the interlayer coupling constant.

ACKNOWLEDGMENTS

This work was supported by the Ministry of Education of the Russian Federation (project no. PD02-1.2-72).

REFERENCES

1. *Physics of Thin Films: Advances in Research and Development*, Ed. by G. Haas, M. H. Francombe, and R. W. Hoffman (Academic, New York, 1974; Mir, Moscow, 1977), Vol. 6.
2. V. M. Fedosyuk, G. V. Makutin, and O. N. Kasyutin, Zarubezhn. Élektron., No. 415, 42 (1992).
3. V. A. Seredkin, D. I. Frolov, and V. Yu. Yakobchuk, Pis'ma Zh. Tekh. Fiz. **9**, 1446 (1983) [Sov. Tech. Phys. Lett. **9**, 621 (1983)].
4. Z. Zhang, L. Zhou, and P. E. Wigen, Phys. Rev. B **50**, 6094 (1994).
5. V. V. Ustinov, M. M. Kirillova, I. D. Lobov, *et al.*, Zh. Éksp. Teor. Fiz. **109**, 477 (1996) [JETP **82**, 253 (1996)].
6. V. V. Kostyuchenko and A. K. Zvezdin, Phys. Rev. B **57**, 5951 (1998).
7. A. M. Zyuzin, A. G. Bazhanov, and V. V. Radaĭkin, Zh. Tekh. Fiz. **69** (11), 97 (1999) [Tech. Phys. **44**, 1351 (1999)].
8. A. Schreyer, J. F. Ankner, Th. Zeidler, *et al.*, Phys. Rev. B **52**, 16066 (1995).
9. G. S. Patrin, N. V. Volkov, and V. P. Kononov, Pis'ma Zh. Éksp. Teor. Fiz. **68**, 287 (1998) [JETP Lett. **68**, 307 (1998)].
10. N. G. Bebenin and V. V. Ustinov, Fiz. Met. Metalloved. **84** (2), 29 (1997).
11. D. I. Sementsov and A. M. Shutyĭ, Pis'ma Zh. Tekh. Fiz. **27** (21), 19 (2001) [Tech. Phys. Lett. **27**, 897 (2001)].
12. D. I. Sementsov and A. M. Shutyĭ, Pis'ma Zh. Éksp. Teor. Fiz. **75**, 287 (2002) [JETP Lett. **75**, 242 (2002)].
13. M. A. Milyaev, L. N. Romashev, V. V. Ustinov, *et al.*, in *Proceedings of the 18th International Seminar, Moscow, 2002*, Part 1, pp. 102–104.
14. P. N. Statsenko, S. D. Antipov, G. E. Goryunov, *et al.*, in *Proceedings of the 18th International Seminar, Moscow, 2002*, Part 1, pp. 510–512.

Translated by V. Isaakyan

Technical Physics, Vol. 49, No. 4, 2004, pp. 426–430. Translated from Zhurnal Tekhnicheskoĭ Fiziki, Vol. 74, No. 4, 2004, pp. 48–52.

SOLID-STATE ELECTRONICS

Effect of Low-Energy Ion Bombardment on the Crystal Structure and Superconductivity of Niobium Films

V. V. Naumov*, V. F. Bochkarev*, A. A. Goryachev*, A. S. Kunitsyn*, E. I. Il'yashenko, P. E. Goa**, and T. H. Johansen****

** Institute of Microelectronics and Information Science, Russian Academy of Sciences, Yaroslavl, 150007 Russia*
e-mail: vvnau@rambler.ru
*** University of Oslo, N-0316 Oslo, Norway*
Received May 5, 2003

Abstract—The effect of ion bombardment on the growth of Nb films and their crystal structure is investigated. Epitaxial niobium films with the (001) orientation are grown on (01*i*2) Al_2O_3 substrates heated to 600°C and biased at –20 V. Niobium films with pronounced axial texture in the [110] direction are grown on water-cooled Sitall (devitrified glass such as Pyroceram) substrates. In Nb films biased at –50 V, which are in the superconducting state, the motion of individual magnetic vortices is observed with a magnetooptic indicator. © *2004 MAIK "Nauka/Interperiodica".*

Stimulated low-temperature ordered growth of films continues attracting considerable interest. During growth, a film is exposed to electromagnetic radiation [1] or particle fluxes [2–7]. Stimulation of ordered film growth by ion bombardment seems a promising growth technique because of a high locality of action in the subsurface layer, a wide interval of energies used, and the possibility of controlling the process over a wide range of parameters. Interest in radiation-assisted growth also stems from the fact that ion bombardment modifies the structure and, hence, properties of the film. In [2], the temperature of Si homoepitaxial growth was reduced by using low-energy ion bombardment. Ion stimulation was reported [3] to improve the properties of ohmic contacts. Ion-beam-assisted deposition (ion–plasma sputtering combined with ion bombardment at an angle to the surface) has also gained wide recognition [4]. A feature of this method is the formation of a biaxial (constrained) texture irrespective of the substrate material and properties. The ion–plasma method of film application (cathodic, magnetron, etc., sputtering) allows the researchers to realize growth with bias (when the substrate is under a negative potential) [5–7]. To the favorable effects inherent in the ion–plasma method and mentioned in [7], one can add an increase in the grain size [8] and a higher smoothness of the film surface [9]. Unfortunately, defect-induced stresses building up in the films limit the applicability of the method. However, the formation of defects goes in parallel with atomic structure ordering; that is, the crystal structure of films obtained under low-temperature ion bombardment at low substrate temperatures is much more perfect than that of films grown under the same conditions but without ion assistance. For fcc materials (such as yttria-stabilized zirconia [6] and nickel [7]), it has been shown that bombardment by ions with energies of 40–100 eV greatly improves (111) axial texture, which is less pronounced without bombardment. The (111) plane in the fcc lattice is known to be the closest packed. It is therefore natural to expect that ion bombardment will enhance (110) axial texture in bcc niobium films. In this work, we study the crystal structure of niobium films as a function of the substrate bias. Our aim was (i) to experimentally show that ion assistance causes (in a certain energy range) the growth of axially textured films with the closest packed plane running normally to the bombardment direction, (ii) to qualitatively estimate to what extent ion bombardment and substrate type (polycrystalline, single-crystalline, etc.) are responsible for the orientation of the film, and (iii) to demonstrate that atomic ordering goes in parallel with the formation of defects during ion bombardment. Where necessary, the results obtained are compared with experimental data for nickel films [7].

First, we will mention the results for niobium film growth on amorphous ST 501-10.6 Sitall substrates. Pure (99.95%) niobium films were applied by rf (13.56 MHz) magnetron sputtering. The residual pressure in the chamber and the operating pressure of argon were 10^{-4} and 0.5 Pa, respectively. The power at the target 100 mm in diameter was 200 W. During growth, the substrate was cooled by water. The substrate–target distance was 100 mm. During sputtering, the substrate and target were under the same rf potential. Because of different surface areas of the target (the first electrode) and substrate (the second electrode) and different mobilities of electrons and ions, the substrate was kept under a constant negative bias voltage [10]. A series of films was grown at substrate biases from 0 to –150 V. The ion energy was estimated with regard to the plasma poten-

1063-7842/04/4904-0426$26.00 © 2004 MAIK "Nauka/Interperiodica"

tial, which was measured with a Langmuir probe and was equal to +20 V relative to the chamber. The crystal structure of the films was studied with a DRON-3M diffractometer using CuK_α radiation.

The orientation of grains in the substrate plane was determined by constructing pole figures [7]. It was found that ion bombardment due to a bias applied to the substrate favors axial texturing in the [110] direction. In the absence of ion bombardment, the films have the same, though less pronounced, texture. The degree of crystallinity, as determined from the intensity of the (110) diffraction peak, grows as the bias rises from 0 to –50 V (Fig. 1). With a further increase in the bias, the degree of crystallinity varies in an irregular manner but its mean value remains higher than at low biases. Such a crystallinity versus bias dependence is, in general, similar to that observed in Ni films (texture in the (111) plane) [7]. These results indicate that ion bombardment favors the growth of those grains oriented in the direction that is preferential without bombardment and depends on the substrate orientation. It should be emphasized that this statement is valid for film growth that is considerably nonequilibrium, i.e., for growth that proceeds at low substrate temperatures. The relative density of niobium films, $\rho_{3Nb} = 0.966$ ($\rho_3 = \rho_2/\rho_1$, where ρ_1 is the density of a bulk sample, ρ_2 is the density of a film, and ρ_3 is the relative density), which have a high degree of crystallinity, is lower than that of similar Ni films ($\rho_{3Ni} = 1$). The density of the bulk samples and films were calculated from the values of interplanar spacings ((222) planes for Ni and (220) planes for Nb). This difference seems to be associated with different types of chemical bonds in niobium and nickel. Another distinction is that the crystallinity of Nb films varies irregularly at biases from –60 to –100 V, while the same dependence for Ni films is smooth and peaks near –90 V. This discrepancy is probably a result of a competing process, e.g., the participation of Nb ions in the process of bombardment. The atomic mass of Ni (58.7 u) is roughly twice as lower as that of Nb (92.9 u); therefore, this effect in the case of Ni is negligible. Moreover, the atomic mass of Ni is close to that of Ar (40 u); accordingly, the effect of Ni and Ar on a growing film is nearly the same.

These data suggest that ion bombardment may significantly decrease the temperature of epitaxial growth of films on a single-crystal substrate but only if the films have the preferential orientation mentioned above, which depends on the lattice type. For example, MBE-grown Nb(110) epitaxial films on $Al_2O_3(11i0)$, where i equals the sum of first two indices taken with opposite sign, were studied in [11]. The substrate was heated to 800°C, and the growth rate was 0.075 nm/s. We argue that low-energy ion bombardment would have reduced appreciably (by 100–200°C) the epitaxy temperature in that experiment. Both inert gas ions and ions of a material being deposited (e.g., niobium) may be used as bombarding particles.

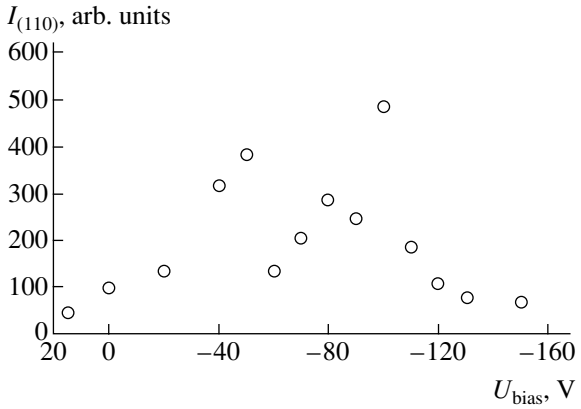

Fig. 1. (110) diffraction peak intensity for Nb/Sitall structures vs. bias voltage at the substrate during growth.

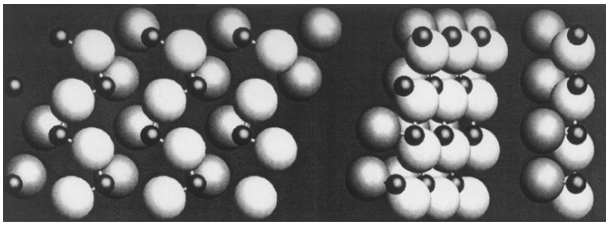

Fig. 2. Three views of the same fragment of the $Al_2O_3(01i2)$ plane. From left to right: top view, at an angle of 60°, and at an angle of 90°. The direction [11i0] in Al_2O_3 is parallel to the horizontal line on the left. Small dark balls, aluminum; large bright balls, oxygen. Two oxygen layers differ by color.

In this work, we studied the effect of low-temperature ion bombardment on the epitaxial growth of niobium on (01i2) sapphire substrates. Below, it will be shown that such an orientation of sapphire is the most suitable for the growth of Nb(001). In our opinion, the effect of ion bombardment consists in disordering the crystal lattice of the film. The higher the ion bombardment intensity, the more disordered the growth.

Figure 2 illustrates the (01i2) plane of sapphire. Aluminum atoms in this plane produce an almost rectangular network of sites with parameters close to those of the planar network of Nb(001). In Fig. 3, the networks are compared by superposition. Aluminum atoms in the (01i2) plane of Al_2O_3 produce a rhombus with minor and major diagonals of 0.477 and 0.5146 nm. Niobium atoms in the plane (001) create a square with a diagonal of 0.467 nm. Thus, if the (001) plane of Nb is rotated through an angle of 22° about the minor diagonal of Al_2O_3, the projection of the rhombus made of aluminum atoms onto this plane gives a square. The lattice mismatch between Nb and Al_2O_3 is 2.1%.

Films on the Al_2O_3 substrates were applied by magnetron sputtering at an argon pressure of 0.2 Pa, a magnetron power of 200 W (the growth rate 0.33 nm/s), and a substrate temperature of 600°C. Before the substrates

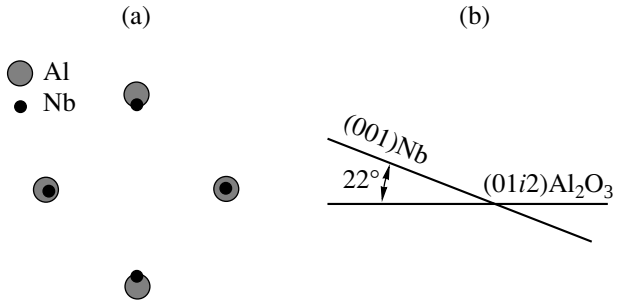

Fig. 3. (a) Arrangement of Al and Nb atoms when the (001) plane of Nb is parallel to the (01*i*2) plane of Al_2O_3 and (b) arrangement of the (001) plane of Nb and the (01*i*2) plane of Al_2O_3 in the case of epitaxial match (misorientation 2.1%).

were placed in the chamber, they had been cleaned by the standard chemical technique and dried in isopropyl alcohol vapor. The films were grown on substrates that were preprocessed by ion bombardment and biased at 0, –20, –40, –60, and –90 V (for convenience, they are numbered 0, 20, 40, 60, and 90, respectively). The substrate preprocessing by ions was performed at a bias voltage of –20 V for 5 min. Substrate no. 1 was not preprocessed and was used as a reference sample.

X-ray analysis data showed that sample no. 1 is axially textured in the (110) plane. Its (110) pole figure is shown in Fig. 4a. The angle α in the pole figure is the angle of rotation of the sample in the diffractometer about the line of intersection between the equatorial plane of the goniometer and the plane of the sample; the angle β, the angle of rotation of the sample about the normal to its surface. Two peaks making an angle α = 45° correspond to (11*i*1) reflections from the substrate, since their Bragg angle is close to that for the (110) reflection from the Nb film (this reflection was used to construct the pole figures). Such a result suggests that chemical rinsing alone is insufficient for good cleaning of the substrate surface. Figures 4b and 4c demonstrate pole figures for samples no. 0 and 20. It is seen that these films are epitaxial with the (100) plane of the niobium running nearly parallel to the substrate surface. All the pole figures are shown on an enlarged scale in order to reveal few grains of another orientation. The total intensity of the Nb peaks at α = 45° reaches 200 (in arbitrary units). However, only the interval from 0 (white color) to 3 arb. units (black color) is shown in the pole figures. The pole figure for sample no. 0 (Fig. 4b) exhibits a weak peak at α = 15°. It indicates that this film contains a small amount (1.5%, as follows from comparison between the intensities) of crystalline blocks whose orientation differs from that of the major portion of crystallites. This means that the temperature 600°C is insufficient for epitaxial growth. At the same time, the pole figure for sample no. 20 (Fig. 4c), as well as those for samples no. 40 and 60, does not contain other peaks; in other words, the pole figures are similar to each other. In the pole figure for sample no. 90, an additional peak appears again now at α = 5°. As the bias voltage rises, the (002) diffraction peak varies in intensity and half-width (in terms of the angle β) (see the table).

As follows from the table, the misorientation between the (001) plane of Nb and the Al_2O_3 surface increases, approaching the situation shown in Fig. 4b. The relative arrangement of crystallographic planes in the film and substrate are presented in Fig. 5. Here, γ is the angle between the (001) plane and the substrate surface (see the table).

As the bias rises from 0 to –20 V, the (002) peak intensity somewhat increases and the half-peak in terms of β decreases, indicating that the crystal structure of the niobium film is improved. However, as the bias grows further, the crystal structure of the film degrades again, as demonstrated by the fact that the intensity of the (002) peak decreases and its half-width increases. It is noteworthy that, at a bias of –90 V, the (110) pole figure shows a peak that corresponds to grains oriented in the [110] direction much closer to the substrate surface

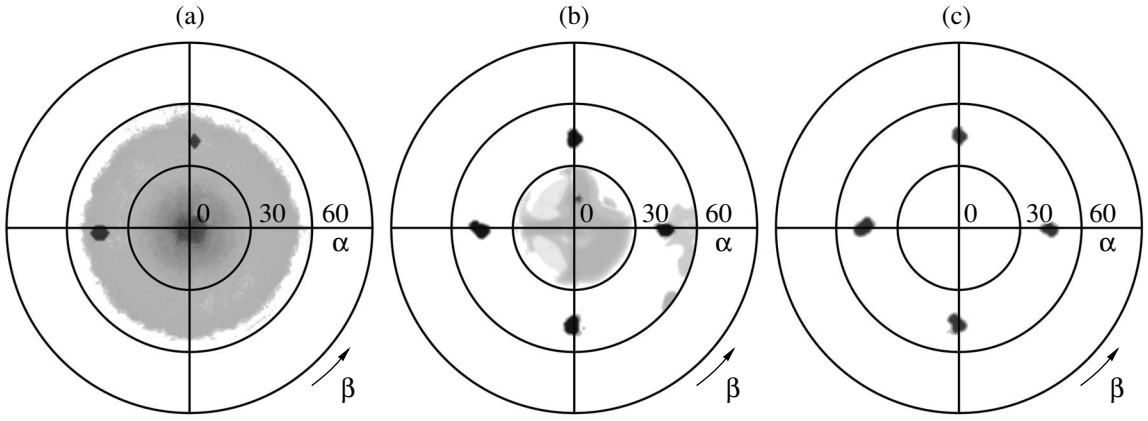

Fig. 4. (110) pole figures for Nb/Al_2O_3 films obtained (a) without ion cleaning and biasing (sample no. 1), (b) with ion cleaning without biasing (sample no. 0), and (c) with ion cleaning at a bias of –20 V (sample no. 20).

(the misorientation is 5°) than in sample no. 0. This fact supports our assumption that ion bombardment favors the growth of grains in the [110] direction. However, unlike the films obtained on the amorphous substrate, grains with such an orientation arise in a small amount, demonstrating that the effect of the substrate is much stronger than the effect of ion bombardment. The most ordered epitaxial film is the one grown at a bias of –20 V.

We studied the superconducting properties of the Nb films grown on the Sitall substrates biased at 0, –20, –40, and –50 V. The superconducting transition with T_c = 9 K was detected only in the film grown at –50 V. This film was used for the observation of individual vortices by the magnetooptic method [12]. This method (for details, see [13]) allows one to visualize the magnetic field distribution in a magnetooptic indicator, which is in contact with a film in the superconducting state. In this work, a 0.8-μm-thick Bi-substituted ferrite garnet (BFG) film grown by liquid phase epitaxy on a gadolinium gallium garnet (GGG) substrate served as a magnetooptic indicator. Plane-polarized light from the illumination source of a microscope reflects from a planar specular surface of the superconducting sample, passing through the BFG film two times. The higher the magnetic field at this point of the BFG film (the Faraday coefficient is 0.66° μm^{-1}A/m for a radiation wavelength of 546 nm), the larger the rotation of the plane of polarization. In crossed polarizer and analyzer, this effect shows up in an increase in the image brightness.

In our experiments, we applied a 0.5-μm-thick Nb film directly on a BFG film at a substrate bias of –50 V. The Nb film was also deposited on Sitall. To observe the dynamics of magnetic vortices, the Nb/BFG/GGG multilayer structure was cooled to 5 K, after which a magnetic field of 1590 A/m was applied normally to the surface of the structure. The motion of magnetic vortices was observed when the magnetic field changed by 79.6 A/m (Fig. 6). In Fig. 6, the initial and final positions of the vortices appear as dark and bright spots, respectively. The image in Fig. 6 was obtained by subtracting the initial positions from the final ones. The time interval between the initial and final positions of the vortices is 1 s.

A high velocity of the vortices, about 10 μm/s, is noteworthy. It seems, however, that their velocity depends in this case on the rate of change on the magnetic field, since a vortex (flux line) lattice is still absent; hence, interaction between the vortices is weak. Yet, there must be many pinning centers in the Nb film (recall that this film is polycrystalline with a grain size of about 10 nm). One may then expect that grain boundaries in the axial Nb film grown under ion bombardment have a higher-than-usual atomic order in the direction parallel to the film surface. That is why the film exhibits the superconducting property and the velocity of the vortices is high.

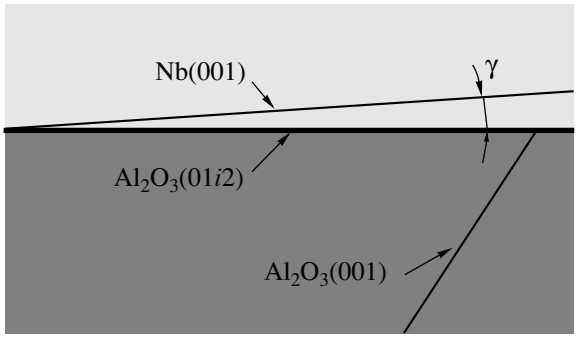

Fig. 5. Relative arrangement of crystallographic planes in the Nb film and Al_2O_3 substrate.

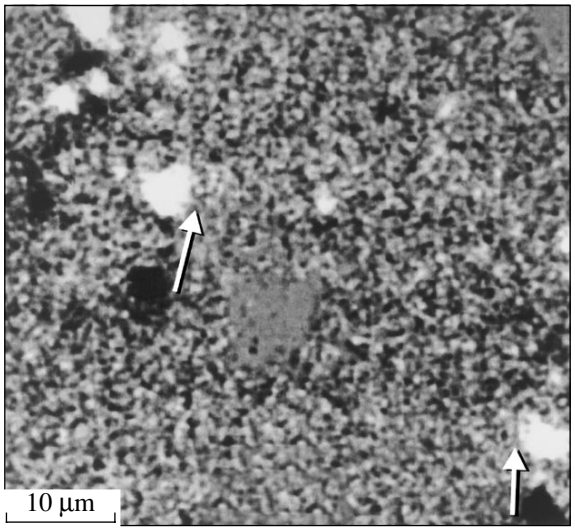

Fig. 6. Magnetic vortex dynamics in the Nb/BFG/GGG multilayer structure that is visualized with a magnetooptic indicator. The direction of vortex motion is indicated by arrows.

Thus, it is demonstrated experimentally that low-energy ion bombardment of Nb films during their deposition favors the growth of grains oriented parallel to the closest packed plane ((110) in our case). If the lattice parameters and orientation of a single-crystalline substrate differ from those of the film, the epitaxy tem-

Table

Sample no.	Misorientation γ between the (001) plane of Nb and substrate surface, deg	(002) reflection peak intensity for Nb at given γ, counts/s	Half-width of peak in terms of angle of rotation β, deg
0	3	21450	10
20	3	22370	7.4
40	4.2	14930	8.4
60	4.8	9590	11

perature may be somewhat reduced by using low-energy (≈30 eV) ion bombardment.

If the substrate orientation coincides with that favored by ion bombardment, the process temperature may be decreased appreciably (by 200°C in our experiments). Today, the selection of materials used in conventional semiconductor technology is limited by a number of factors, including the substrate temperature. As a rule, it must not exceed 200–300°C. Taking advantage of the orienting effect of low-energy ion bombardment, one may reduce the temperature of epitaxial growth of materials growing at high temperatures and apply them in the standard process steps of semiconductor technology.

REFERENCES

1. H. Akazawa, J. Appl. Phys. **79**, 9396 (1996).
2. W. Shindo and T. Ohmi, J. Appl. Phys. **79**, 2347 (1996).
3. S. P. Morgan and D. V. Morgan, Thin Solid Films **272**, 107 (1996).
4. K. G. Ressler, N. Sonnenberg, and M. G. Cima, J. Electron. Mater. **25**, 35 (1996).
5. A. Misra and N. Nastasi, Appl. Phys. Lett. **75**, 3123 (1999).
6. V. V. Naumov, V. F. Bochkarev, O. S. Trushin, *et al.*, Neorg. Mater. **34**, 57 (1998).
7. V. V. Naumov, V. F. Bochkarev, O. S. Trushin, *et al.*, Zh. Tekh. Fiz. **71** (8), 92 (2001) [Tech. Phys. **46**, 1020 (2001)].
8. J. Shi, D. Kojima, and M. Hashimoto, J. Appl. Phys. **88**, 1679 (2000).
9. X. L. Peng, Z. H. Barber, and T. W. Clyne, Surf. Coat. Technol. **138**, 23 (2001).
10. Yu. P. Raĭzer, M. N. Shneĭder, and N. A. Yatsenko, *High-Frequency Capacitive Discharge* (Mosk. Fiz.-Tekh. Inst., Moscow, 1995), pp. 123–131 [in Russian].
11. A. R. Wildes, R. A. Cowley, R. C. C. Ward, *et al.*, J. Phys.: Condens. Matter **10**, L631 (1998).
12. A. V. Antonov, M. U. Gusev, E. I. Il'yashenko, *et al.*, in *Proceedings of the International Symposium on Magnetooptics, Kharkov ISMO-91, 1991*, p. 70.
13. P. E. Goa, H. Hauglin, M. Baziljevich, *et al.*, Supercond. Sci. Technol. **14**, 729 (2001).

Translated by V. Isaakyan

Technical Physics, Vol. 49, No. 4, 2004, pp. 431–434. Translated from Zhurnal Tekhnicheskoĭ Fiziki, Vol. 74, No. 4, 2004, pp. 53–57.

SOLID-STATE ELECTRONICS

Perpendicular Magnetic Anisotropy in Single-Crystal $Co_{50}Pt_{50}$/MgO(100) Films

P. D. Kim*, I. A. Turpanov*, S. V. Stolyar, R. S. Iskhakov*, V. I. Yushkov***, A. Ya. Beten'kova*, L. A. Li*, E. V. Bondareva*, T. N. Isaeva*, and M. M. Karpenko***

** Kirenskiĭ Institute of Physics, Siberian Division, Russian Academy of Sciences, Krasnoyarsk, 660036 Russia*
e-mail: kim@iph.krasn.ru
*** Krasnoyarsk State University, Krasnoyarsk, 660041 Russia*
**** Krasnoyarsk State Technical University, Krasnoyarsk, 660074 Russia*
Received August 4, 2003

Abstract—The crystal structure and hysteretic magnetic properties of equiatomic single-crystal CoPt films applied on MgO substrates by magnetron sputtering, as well as modification of these properties by thermal annealing, are studied. Heat-treated films of thickness in the range $2 < d \le 16$ nm exhibit perpendicular magnetic anisotropy. A correlation between the crystalline anisotropy constant of the CoPt films and the order parameter of the LI_0 superstructure in these alloys is found. The effect of a single-crystalline MgO substrate on the structure and magnetic properties of equiatomic CoPt films is revealed. © *2004 MAIK "Nauka/Interperiodica".*

Upon ordering of type Al ⟶ LI_0, CoPt alloys with a near-equiatomic composition acquire the tetragonal magnetically uniaxial superstructure LI_0. In this crystallogeometrical state, the alloys are characterized by the saturation magnetization M_s = 800 G and the crystalline anisotropy field H_a = 125 kOe [1]. These values satisfy the condition $H_a \gg 4\pi M_s$, which makes it possible to produce perpendicular magnetic anisotropy in thin films of this equiatomic alloy provided that the films have (001) texture. Therefore, $Co_{50}Pt_{50}$ (like $Fe_{50}Pt_{50}$ and $Fe_{50}Pd_{50}$) alloys are currently viewed as candidates for a high-density planar magnetic data-storage medium.

The magnetic properties of ordered equiatomic CoPt alloys, such as the anisotropy field H_a, the coercive field H_c, and the rectangularity $S = M_r/M_s$ (where M_r is the remanent magnetization) of the hysteresis loop, depend on their microstructure, namely, on the grain size, the density of defects, and the order parameter η of the superstructure LI_0. Upon Al ⟶ LI_0 ordering, any of three ⟨010⟩ axes of the fcc matrix may be taken as the tetragonal axis. Therefore, there exist three types of nuclei C_i (C_1, C_2, and C_3) of the ordered superstructure LI_0 if external actions are absent. As a result, the alloy experiences structural self-organization, causing a complicated microstructure hierarchy [2]. Thus, in fabricating film media with desired magnetic properties, it is necessary to select appropriate methods for forming the microstructure of ordered (or partially ordered) $Co_{50}Pt_{50}$ (as well as $Fe_{50}Pt_{50}$ and $Fe_{50}Pd_{50}$) alloys.

The aim of this work is to study the hysteretic magnetic properties of single-crystal films of equiatomic CoPt alloys applied on single-crystal MgO(100) substrates and reveal the effect of the substrate on the magnetic properties of these ferromagnetic films.

EXPERIMENTAL

The samples used were grown by magnetron sputtering in Ar at a pressure of 2×10^{-4} Torr. In order to avoid chemical inhomogeneity, Co and Pt layers were applied in succession. The application time per metal layer τ_i was taken such that a monomolecular layer of the metal was deposited [3]. The thickness d of the films was varied between 2 and 100 nm and was checked (as well as the chemical composition of the films) by X-ray fluorescence analysis. Isothermal annealing was carried out in a vacuum chamber under a pressure of no higher than 5×10^{-6} Torr.

Hysteresis loops were recorded at room temperature with a vibrational magnetometer at fields $H < 12$ kOe. Measurements were performed in two configurations: $H \parallel n$ and $H \perp n$, where n is the normal to the film surface. The structure of the samples was examined on a DRON-4 diffractometer at room temperature in CuK_α radiation (λ = 0.154 nm).

STRUCTURE OF THE SAMPLES

Figure 1 shows X-ray diffraction spectra of the films. The diffraction pattern from the as-prepared $Co_{50}Pt_{50}$/MgO(100) structure with d = 19 nm (Fig. 1a) indicates that the $Co_{50}Pt_{50}$ alloy with the fcc lattice is initially single-crystalline. Here, only the (200) reflection from the film is detected. The lattice constant of the alloy calculated from the interplanar spacing d_{200} was

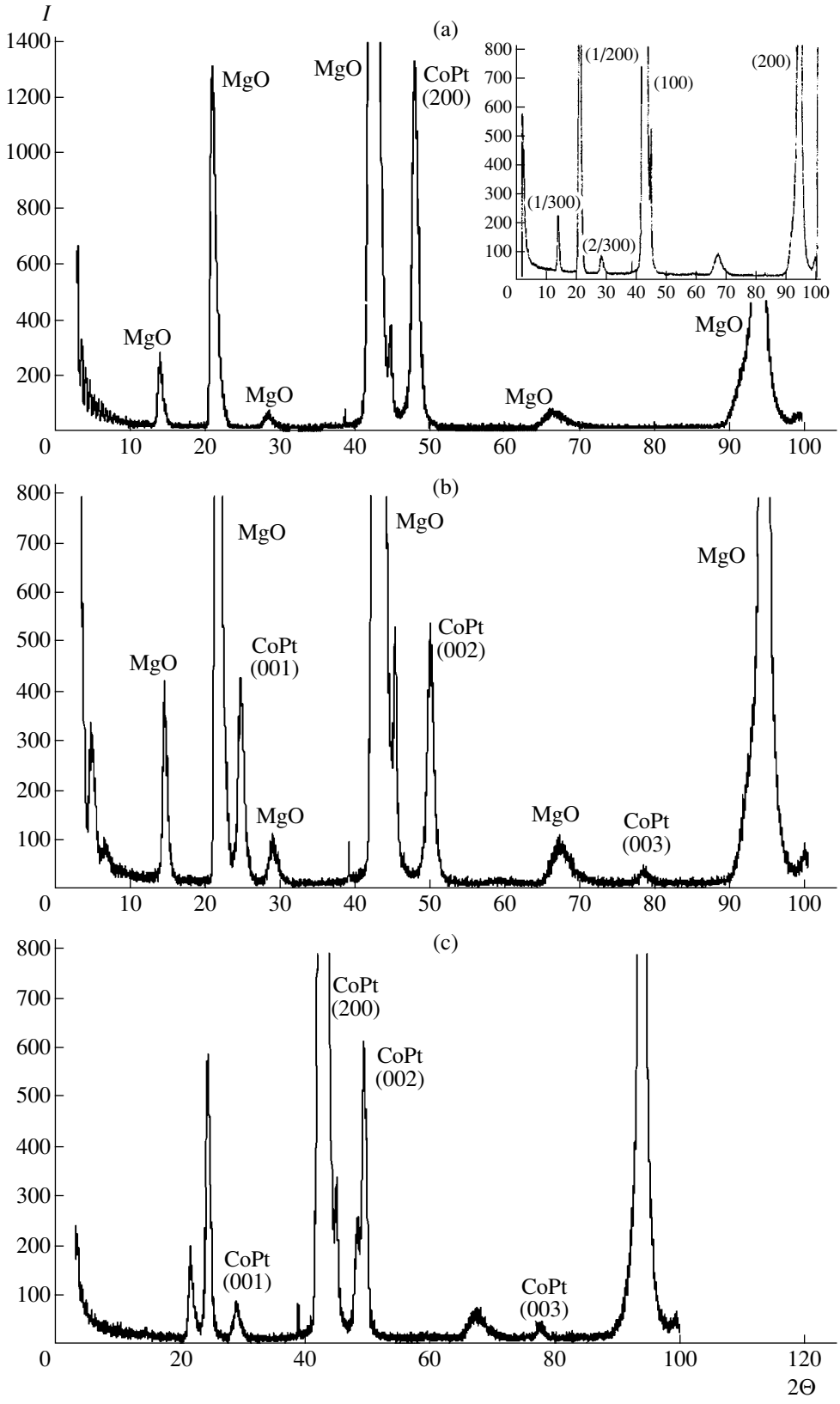

Fig. 1. X-ray diffraction patterns taken from the $Co_{50}Pt_{50}$ films on MgO substrates: (a) as-prepared film with d = 19 nm, (b) heat-treated film with d = 7 nm, and (c) heat-treated film with d = 15 nm. The inset to (a) shows the diffraction pattern from the MgO substrate.

found to be $a = 0.377$ nm. Other peaks in this diffraction pattern are associated with reflections from the MgO substrate. The inset to Fig. 1a shows the spectrum of the substrate. Reflections (1/200), (1/300), (2/300), etc., is likely to indicate that impurity atoms in the MgO are arranged regularly and the MgO substrate has a block structure. Figure 1b demonstrates the diffraction pattern from the 7-nm-thick single-crystal $Co_{50}Pt_{50}$/MgO(100) film annealed at 600°C for 3 h. Reflections (001) and (003) observed suggest that the alloy has the tetragonal superstructure LI_0 after annealing. The tetrad axis runs parallel to the normal n to the film. For the superstructure LI_0 the tetrad axis of which is parallel to the normal, the intensity ratio $I_{(001)}/I_{(002)}$ may be used to estimate the order parameter η [4]. The parameter η turned out to grow with increasing thickness of the $Co_{50}Pt_{50}$/MgO(100) film subjected to annealing. The dependence of η versus the film thickness is presented in Fig. 2. Figure 1c shows the X-ray diffraction pattern taken from the $Co_{50}Pt_{50}$/MgO(100) film with $d = 15$ nm. Here, the (200) reflection intensity is lower than the intensity of the (002) reflection. For the given sample, the ratio $c/a = 0.978$. The presence of the (200) reflection indicates that the $Co_{50}Pt_{50}$/MgO(100) film under study has such regions of the superstructure LI_0 where the tetrad axis lies in the plane of the film. In fact, as the film becomes thicker than 150 nm with the annealing conditions remaining the same, the (200) reflection intensity grows. This means that the fraction of LI_0 regions with the tetrad axis lying in the plane of the film increases.

MAGNETIC PROPERTIES OF THE FILMS

In the as-prepared state, the CoPt films had two easy magnetic axes, lying in the plane of the film orthogonally to each other. The rectangularity S of the hysteresis loop for the as-prepared films was 0.6–0.8 throughout the range $2 < d < 100$ nm. The coercive field for these films, about 500 Oe, also did not depend on the thickness d. Heat treatment of the as-prepared films at $T = 600$°C for 3 h radically changes the hysteretic magnetic properties. For the films with $d \le 16$ nm, such a heat treatment produces an easy magnetic axis that is aligned with the normal to the film. For $d > 16$ nm, the easy magnetic axis lay in the plane of the film as before. The hysteresis loop rectangularity measured in the easy direction was found to be 0.9–1.0. Figure 3 shows the normalized dependences $M(H)$ ($H \parallel n$, $H \perp n$) for the annealed film with $d = 10$ nm. The dependences imply the presence of perpendicular magnetic anisotropy. Isothermal annealing is seen to make the film magnetically hard. The coercive field H_c for the films thicker than 16 nm varied between 6 and 10 kOe. For the annealed films with $d < 16$ nm, the value of H_c depends the film thickness: $H_c = H_c(d)$. The experimental dependence $H_c(d)$ for these films, which are characterized by $S = 1$, is given in Fig. 4.

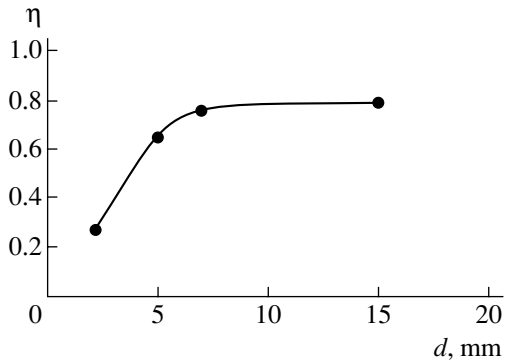

Fig. 2. Order parameter η of the heat-treated $Co_{50}Pt_{50}$/MgO films vs. d.

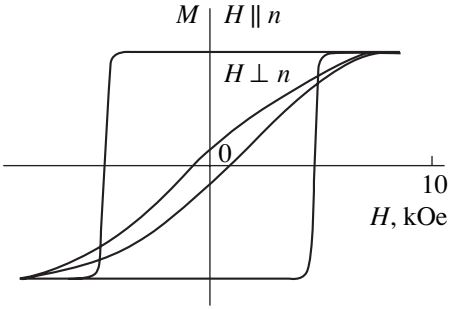

Fig. 3. Normalized dependences $M(H)$ obtained in two configurations ($H \parallel n$, $H \perp n$) for the heat-treated $Co_{50}Pt_{50}$/MgO film with $d = 10$ nm.

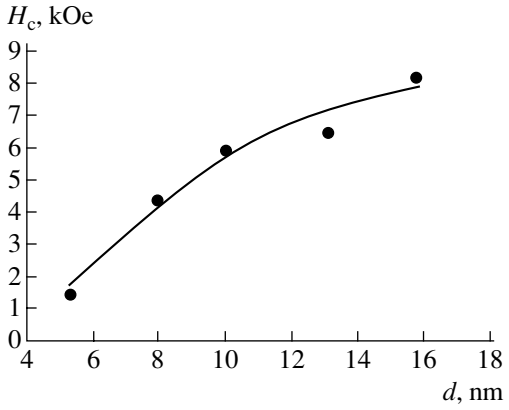

Fig. 4. Coercive field $H_c(d)$ vs. thickness d measured in the easy magnetic direction for heat-treated $Co_{50}Pt_{50}$/MgO films.

The coercive field H_c for single-crystal heat-treated $Co_{50}Pt_{50}$/MgO(100) films with $d < 16$ nm and $S = 1$ is measured as the difference between the crystalline anisotropy field H_a and the demagnetizing field of the film: $H_c = H_a - 4\pi M$ [5]. Therefore, our experimental dependence $H_c(d)$ may be used to calculate H_a and, hence, the crystalline anisotropy constant $K = H_a M/2$ ($M = 800$ G), a fundamental parameter of a ferromagnet. In this way, for single-crystal ordered (or partially

ordered) 2- to 16-nm-thick $Co_{50}Pt_{50}$/MgO(100) films with the structure LI_0, which exhibit perpendicular magnetic anisotropy, we found that the constant K varies in the interval 4×10^6–8×10^6 erg/cm^3.

RESULTS AND DISCUSSION

Heat treatment of disordered thin films of the $Co_{50}Pt_{50}$ solid solution on single-crystal MgO(100) substrates produces the ordered superstructure LI_0. Analysis of the hysteretic magnetic properties of these alloys shows that (i) the heat-treated films with thicknesses $d \leq 16$ nm exhibit perpendicular magnetic anisotropy and (ii) the coercive field H_c measured along the easy magnetic axis depends on the film thickness (Fig. 4).

It is known that a film of an alloy differs in properties from its bulk state. First, thin films have an elevated concentration of defects. Second, a film is essentially a 2D object. Third, the state of the film is greatly influenced by the substrate.

Perpendicular anisotropy discovered in $Co_{50}Pt_{50}$/MgO(100) thin films with $d \leq 16$ nm results from lattice match between the ferromagnetic alloy and substrate. The tetrad axis along ⟨100⟩ and ⟨010⟩ directions is difficult to form because of a rise in the elastic strain energy in the thin ferromagnetic film. The fact that only one ⟨001⟩-directed nucleus of the ordered structure LI_0 (Fig. 1b) originates is a consequence of self-organization, which minimizes the elastic strain energy. As the $Co_{50}Pt_{50}$ film gets thicker, the effect of the single-crystal MgO substrate weakens; therefore, all three types of ordered domains C_i (C_1, C_2, C_3) (Fig. 1c) may arise in thick annealed films. Accordingly, the easy magnetic axis becomes parallel to the plane of the magnetic film and isotropic over its plane.

Let us now discuss the dependence $H_c(d)$ (Fig. 4). The increase in the coercive field with the thickness of the $Co_{50}Pt_{50}$ ferromagnetic film means the growth of the crystalline anisotropy constant K. In our opinion, such a behavior reflects the variation of the order parameter η in the ordered superstructure LI_0 (Fig. 3). In fact, in the films with this superstructure, the dependences $H_c(d)$ (Fig. 4) and $\eta(d)$ (Fig. 2) found experimentally correlate when the thickness varies between 2 and 16 nm. As η of the CoPt alloy increases, so does H_c (and hence K). We suppose that the dependence of η on the thickness of the film with partially ordered superstructure LI_0 also follows from a high lattice match between the ferromagnetic single-crystal $Co_{50}Pt_{50}$ film and single-crystal MgO(100) substrate. Our reasoning is as follows. In the case of the fcc $\longrightarrow$ LI_0 phase transition, the volume of the alloy must remain unchanged: $V_{fcc} \longrightarrow V_{LI_0}$ or $a^3 = a'^2c$, where a' and c are the parameters of the tetragonal lattice of the LI_0 phase. Upon ordering, c decreases. For the completely ordered superstructure LI_0 ($\eta = 1$), $c/a = 0.972$ [2]. Consequently, a' in such films is bound to increase. However, in the thin single-crystal films studied, a' cannot change because of a film–substrate lattice match; in other words, the substrate in thin-film single-crystal $Co_{50}Pt_{50}$/MgO(100) structures prevents ordering in the range of small d mentioned above. As the $Co_{50}Pt_{50}$ film thickens, the effect of the MgO(100) substrate weakens, since the elastic strain drops as $1/d$ and the order parameter η of the alloy grows.

Thus, we investigated the hysteretic magnetic properties of single-crystal $Co_{50}Pt_{50}$ films on MgO(100) substrates. In ordered 2- to-16-nm-thick films with the LI_0 superstructure, the presence and degree of perpendicular magnetic anisotropy are shown to be totally controlled by the single-crystal MgO structure. The substrate influences the formation of the crystal lattice of the ordered ferromagnetic alloy twofold: it (i) favors the appearance of the tetrad axis in the alloy along the normal to the film and (ii) prevents ordering in the alloy.

REFERENCES

1. A. E. Ermakov and V. V. Maĭkov, Fiz. Met. Metalloved., No. 5, 201 (1990).
2. N. I. Vlasova, G. S. Kandaurova, and N. N. Shchegoleva, Fiz. Met. Metalloved. **90** (3), 31 (2000).
3. P. D. Kim, in *Proceedings of the 17th International Seminar on New Magnetic Materials of Microelectronics, Moscow, 2000*, pp. 537–539.
4. M. M. Umanskiĭ and Z. K. Zolina, *Book of Problems on X-ray Analysis* (Mosk. Gos. Univ., Moscow, 1975).
5. N. M. Salanskiĭ and M. Sh. Erukhimov, *Physical Properties and Application of Magnetic Films* (Nauka, Novosibirsk, 1975) [in Russian].

Translated by V. Isaakyan

Technical Physics, Vol. 49, No. 4, 2004, pp. 435–442. Translated from Zhurnal Tekhnicheskoĭ Fiziki, Vol. 74, No. 4, 2004, pp. 58–65.

SOLID-STATE ELECTRONICS

Effect of Clustering in LaCa(Sr)MnO Epitaxial Films on Their Magnetic, Electron, and Optical Properties

Z. A. Samoilenko*, V. D. Okunev*, E. I. Pushenko*, T. A. D'yachenko*, O. P. Cherenkov*, R. Szymczak, H. Szymczak**, S. J. Lewandowski**, M. Baran**, and P. Gierlowski****

** Galkin Physicotechnical Institute, National Academy of Sciences of Ukraine, Donetsk, 83114 Ukraine*

*** Institute of Physics, Polish Academy of Sciences, 02-668 Warsaw, Poland*

Received August 12, 2003

Abstract—This work is aimed at finding a correlation between the magnetic properties, conductivity, and crystal structure of $La_{0.6}Sr_{0.2}Mn_{1.2}O_3$ and $La_{2/3}Ca_{1/3}MnO_3$ films prepared by pulsed laser (KrF) deposition in order to study the behavior of their $M(T)$ and $M(H)$ magnetizations. X-ray diffraction is used to investigate the cluster crystal structure of the manganites. It is shown that the variation of growth temperature and substrate type, along with laser irradiation, change not only the matrix structure (long-range order in ion arrangement) but also the cluster structure (mesoscopic order). The magnetic, electron, and optical properties revealed experimentally are explained by changes in the atomic and electron subsystems of the cluster structures, which provide magnetic interaction between clusters. © *2004 MAIK "Nauka/Interperiodica".*

LaSr(Ca)MnO manganites, which attract the researchers' attention because of the giant magnetoresistance effect, feature a flexible structure consisting of readily reconfigurable fragments, as a result of which the properties of the material vary in a wide range. Specifically, these manganites behave either as an insulator with metallic inclusions (solidified drops) or a metallic medium with insulating inclusions [1]. Similarly, in terms of magnetism, they represent a two-phase magnetic system where either ferromagnetic or antiferromagnetic interaction prevails [2].

The reason why the manganites readily respond to an external action (magnetic and electric field, temperature, etc.) is the superposition of different-scale structural elements. Namely, the basic crystalline matrix with long-range order (which is a paramagnet with insulating properties at temperatures above the Curie temperature) coexists with the mesoscopic cluster structure with nanometer-range atomic order (which is a ferromagnet with metallic conduction) [3]. The cluster size (30–200 Å) and concentration (2–25%) depend on film growth conditions. Fine isolated clusters play a role of quantum dots with a discrete energy spectrum [3]. If clusters are so large and their concentration is so high that the spacing Δ between size quantization levels satisfies the condition $\Delta \ll kT$, the material, despite its single-crystalline structure, is similar to a standard granular medium in electrical properties [4, 5].

The aim of this work is to find a correlation between the magnetic properties and fine features of atomic order in cluster Mn–O planes of LaCa(Sr)MnO films. The analysis of the integral intensity and widths of diffuse peaks, which bear information on the concentration and size of clusters, turned out to be insufficient, and we had to study the intensity distribution versus the angle of scattering within the diffuse peaks themselves. The dependences $I_{dif} = f(\theta)$, characterizing the occupancy of clusters by scatterers ($I_{dif} \sim N$), which are fragments of planes with an interplanar spacing d, were represented, according to the Bragg equation $2d\sin\theta = n\lambda$, as curves of the diffuse scattering intensity versus the interplanar distance: $I_{dif} = f(d)$. From the temperature dependences of the resistivity, we managed to reveal the nature of interaction between metallic-conduction clusters with the insulating matrix. Such an approach provided a more penetrating insight into a relation between the electromagnetic properties and atomic order in cluster areas of the manganite films.

EXPERIMENTAL

The films were obtained by pulsed sputtering of a $La_{0.6}Sr_{0.2}Mn_{1.2}O_3$ or $La_{2/3}Ca_{1/3}MnO_3$ target using a KrF excimer laser (the pulse width τ = 25 ns, the energy density at the target Φ = 3.0 J/cm^2, the oxygen pressure in the working chamber P_0 = 300 mtorr). The films were deposited on $SrLaGaO_4$, $Nd_3Ga_5O_{12}$, $Gd_3Ga_5O_{12}$, SiO_2/Si, SAT La-30, and SAT La-22 substrates at growth temperatures T_g = 600–730°C.

Irradiation was carried out by the same laser but with a lower energy density ($0.1 < \Phi < 0.15$ J/cm^2, which is below the scattering threshold for LaSr(Ca)MnO). The number of shots was varied between 5 and 500.

The film structure was examined by the photometric method (long-wave CrK_α radiation), which makes it easy to record diffuse scattering of X rays in the case of

cluster solid solutions which our objects are. Electric measurements were carried out by the standard technique in the temperature interval 4.2–300 K. The optical absorption spectra of the films were taken at room temperature in the energy range $\hbar\omega$ = 0.5–5.0 eV by using an SP 700C spectrophotometer. Magnetic measurements of the thin films were performed with a SQUID magnetometer.

RESULTS AND DISCUSSION

Magnetic order with and without external magnetic field. The magnetization of as-prepared (as-pr) and laser-processed (LP) $La_{2/3}Ca_{1/3}MnO/SiO_2/Si$ samples (the growth temperature T_g = 625°C) was measured upon heating in an external magnetic field of 100 Oe. The samples were precooled to a cryogenic temperature of 5 K in the absence (zero-field cooling, ZFC and LP + ZFC curves) and presence (field cooling, FC and LP + FC curves) of the magnetic field (Fig. 1).

Consider the domain below the Curie temperature T_C. Here, the curves FC and ZFC diverge. The discrepancy may be related to a difference in domain structure or to the presence of clusters. The experimentally observed fact that the curves diverge starting from the Curie temperature (the temperature of onset of magnetic ordering) T_C = 215 K for the as-prepared sample and from 210 K for the LP sample (Fig. 1) suggests that clustering is a more plausible mechanism. It is noteworthy that the transition of the LP films to the magnetically ordered state in the interval 125–225 K is more extended compared with the unprocessed samples (curves FC/as-pr, FC-LP and ZFC/as-pr, ZFC-LP in Fig. 1).

In a magnetic system with ferromagnetic (FM) clusters, the clusters may interact with the antiferromagnetic (AFM) matrix and with each other. At cryogenic temperatures (5 K), the magnetization of the FC samples (cooled in magnetic field of 100 Oe) exceeds that of the ZFC samples (i.e., cooled in the absence of the field) by a factor of 8.75. For the irradiated samples, the magnetizations differ by a factor of 11.75; i.e., the difference is 27% higher. This means that laser irradiation extends the range of the magnetic state of the cluster structure. Such an effect may be associated with an increase in the FM cluster size upon irradiation. For example, in the as-prepared and LP (400 shots) $LaSrMnO/Gd_3Ga_5O_{12}$ films with T_g = 600°C, the cluster size is 70 and 160 Å, respectively.

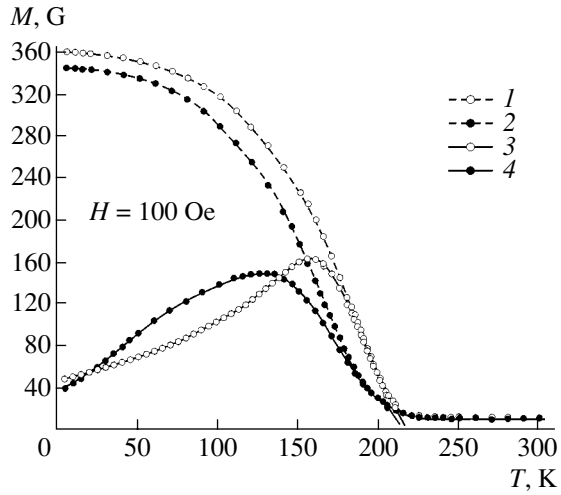

Fig. 1. Temperature dependence of the magnetization in the LaCaMnO film (the growth temperature 625°C) measured in a field of 100 Oe: (*1*, *3*) as-prepared and (*2*, *4*) irradiated state. (*1*, *2*) FC and (*3*, *4*) ZFC conditions.

From the temperature dependence of magnetization, $M(T)$, it follows that laser irradiation shifts the "freezing" temperature from T_f = 165 K (for the ZFC samples) to 120 K (for the ZFC + LP samples). The measurements were made in a weak magnetic field of 100 Oe (Fig. 1). As the temperature decreases (ZFC measurements), $M(T)$ goes through a maximum ($T_{max} = T_f$) and declines (Fig. 1). Such a run of the curves is due to freezing of the magnetic moments of clusters: the external magnetic field influences the orientation of local magnetic moments only slightly, magnetic disorder builds up because of their random orientation, and the magnetization of the samples eventually diminishes. The curves $M(T)$ taken under the ZFC conditions are similar to those for cluster spin glasses or magnetically hard magnets [2, 6].

Hysteresis loop for nonirradiated and laser-irradiated samples at 5 K. Different degrees of order in the irradiated and nonirradiated samples are better visualized by taking the hysteresis loop (Fig. 2). Upon laser processing, the loop narrows by 20%, which indicates that magnetic order in the LP sample and its magnetic homogeneity are improved. The effect of clusters shows up as frustration (magnetic moment freezing) even in high (800–2600 Oe) fields: in fields where the loop closes, the LP sample has a higher magnetization than the nonirradiated one (Fig. 2).

Magnetizations of films grown at different temperatures. Magnetic measurements also reveal the dependence of the cluster state on T_g. For H = 100 Oe and T = 5–300 K, the different run of the curves in Fig. 3 is explained largely by the different structures of films grown at different temperatures. The higher family of curves with a high $M(T)$ (335–350 G) refers to films obtained by low-temperature synthesis (T_g = 625°C); the lower family ($M(T)$ = 130–190 G at 5 K), to films grown at 725°C. However, the former have a higher Curie temperature (205–215 K versus 235–260 K). The distinction is also associated with transformations in the cluster structure: according to [3], as T_g grows, the $R\bar{3}c$ rhombohedral structure (R) passes into the *Pnma* orthorhombic (O) structure, so that the material becomes two-phase ($R + O$) at T_g = 650–670°C or one-phase (R at T_g < 650°C or O at T_g > 670°C).

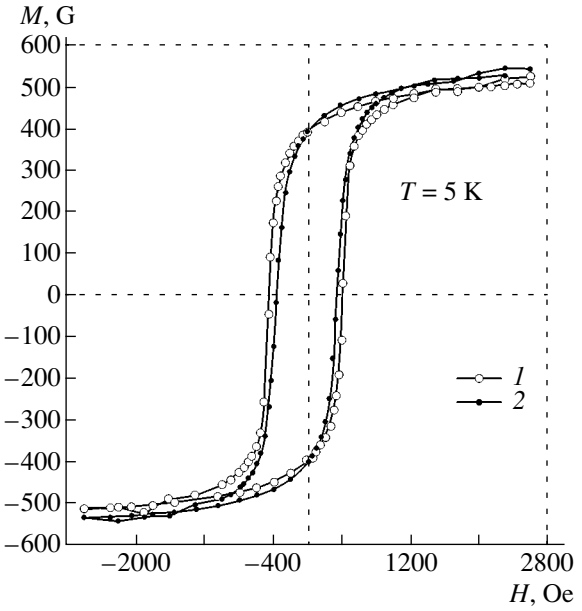

Fig. 2. Hysteresis loop (*1*) before and (*2*) after laser irradiation for the sample grown at 625°C.

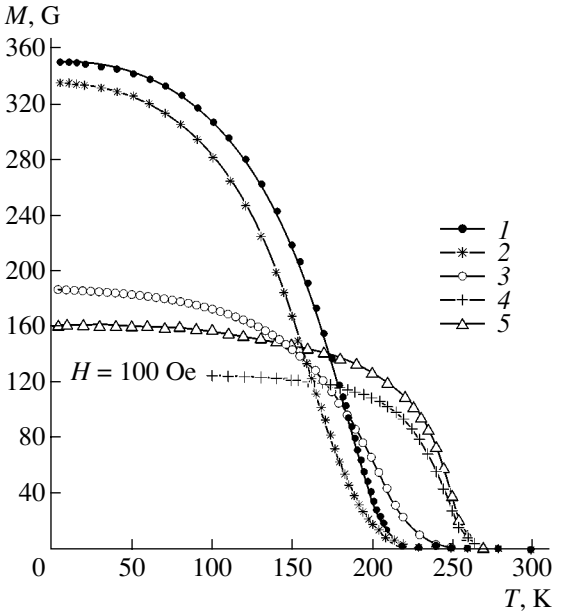

Fig. 3. Temperature dependences of the magnetization in the LaCaMnO films grown at (*1, 2*) 625 and (*3–5*) 725°C (the curves were taken in a magnetic field of 100 Oe). (*1–3*) SiO_2/Si substrate, (*4*) SAT La-30 substrate, and (*5*) SAT La-22 substrate.

As follows from X-ray diffraction patterns, FM clusters in the samples are fragments of Mn–O planes of the *R* and *O* phases. These fragments generate diffuse peaks of various shape and intensity in the angular range $\theta = 30–36°$ (in accordance with the Mn–O bond length in manganites) (Figs. 4, 5). FM clusters with metallic conduction are basic constituents of these fragments. Clustering stems from large-scale fluctuations of the Mn–O bond concentration [7–9] and takes place when the internal energy of the LaCa(Sr)MnO multicomponent system decreases as a result of local ordering like chemical layering [7].

The effect of growth temperature on the distribution of planes in cluster areas. To shed light on the nature of the diffuse maxima, we studied the fine structure of two diffraction peaks, A_1 (30°–33°) and A_0 (33°–36°), corresponding to large (A_1) and small (A_0) interplanar spacings. According to the Bragg equation $2d\sin\theta = n\lambda$ we have $d \sim 1/\sin\theta$ at λ = const. LaCa(Sr)MnO films grown at 625 and 725°C have the rhombohedral and orthorhombic structure, respectively [3]. A major contribution to diffuse peak A_1 comes from rhombohedral clusters ((203) and $20\bar{3}$) reflections with a peak at $\theta = 31.5°–32.0°$) and orthorhombic clusters ((202) reflection with a peak at 30.5°). For range A_0, the metallic state of the structure at T_g = 625 and 725°C is due to rhombohedral clusters reflecting from the (400) plane at 35° and orthorhombic clusters reflecting from the (004) plane at 36.5°. Cluster areas in these films differ not only in atomic order in related planes but also in lattice distortion, which grows when the orthorhombic ($a \neq b \neq c$; $\alpha = \beta = \gamma = 90°$) phase turns into the rhombohedral phase ($a = b = c$; $\alpha = \beta = 90°$, $\gamma \neq 90°$). Comparing the diffraction maxima from cluster areas of the samples differing in T_g (Fig. 5) reveals the following.

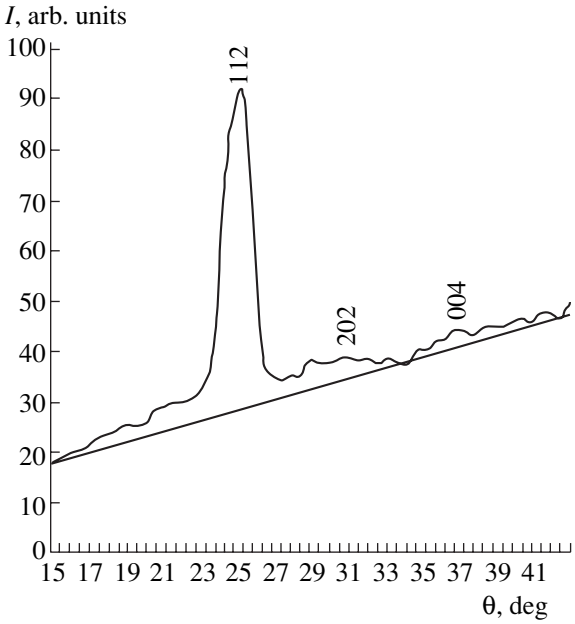

Fig. 4. X-ray diffraction pattern taken of the single-crystal LaCaMnO film.

(i) In area A_1, different shapes of the diffuse maxima indicate different contributions from either of the phases to the integral intensity.

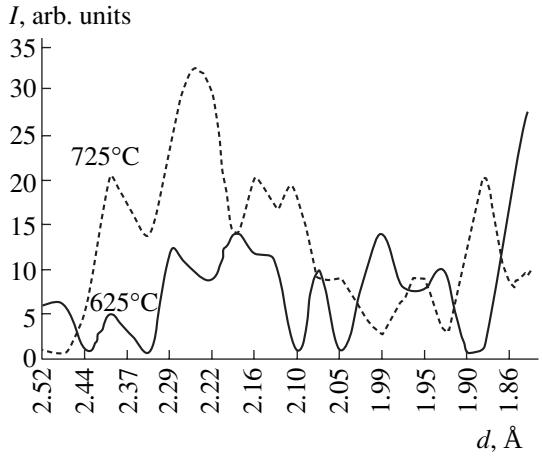

Fig. 5. Diffraction patterns in the vicinity of diffuse maxima taken of clusters in the LaCaMnO films grown on the same substrate (SiO_2/Si) at 625 and 725°C.

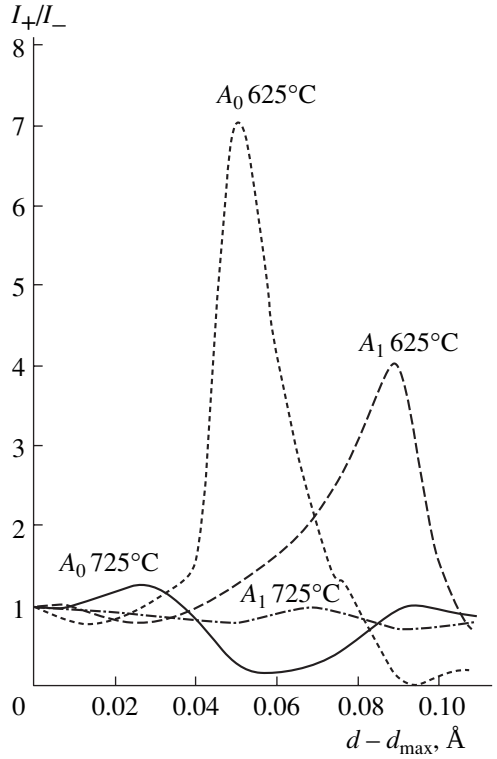

Fig. 6. Intensity ratio I_+/I_- at points symmetric about d_{max} ($d_>/d_<$) for the diffraction areas A_0 and A_1 in the LaCaMnO/SiO_2/Si films grown at 625 and 725°C.

(ii) While the integral intensities of the areas A_1 and A_0 (these intensities reflect a relationship between the concentrations of scatterers with different interplanar spacings) are nearly the same, $I(A_0)/I(A_1) = 0.9$, for T_g = 625°C, they differ greatly for T_g = 725°C: $I(A_0)/I(A_1)$ = 0.43.

(iii) For the films synthesized at the high temperature (725°C), the integral intensities of the areas A_1 and A_0 far exceed those from the low-temperature (625°C) films. This supports the fact that the fraction of Mn–O clusters in the films grown at 725°C exceeds that in the films with T_g = 625°C (12.4 versus 6.7%). It should be noted, however, that not all clusters are responsible for metallic conduction and ferromagnetism but only those containing Mn^{3+} and Mn^{4+} ions in comparable amounts. In view of the higher intensity of the area A_1 and taking into account the Mn–O bond lengths in different charge states of manganese (Mn^{2+}, Mn^{3+}, or Mn^{4+}), we may argue, starting from the curves in Fig. 5, that the cluster structure in the films grown at 725°C has noticeably different amounts of different-valence manganese ions (the planes with smaller d in the area A_0 correspond to higher charged ions; those with larger d in the area A_1, to lower charged ions).

Consider the difference between the cluster areas A_1 and A_0 in terms of the skewness in the diffuse maximum intensity distributions in the areas, i.e., the distributions of d skewed to the left ($d > d_{max}$) and to the right ($d < d_{max}$) with respect to the predicted values: $d(A_1)$ = 2.25 Å and $d(A_0)$ = 1.94 Å. These values agree with experimentally observed positions of diffuse maxima for the overlapping reflections $(202)_O$ and $(203, 20\bar{3})_R$ from the *O* and *R* phases, respectively (these reflections form the area A_1), and for the reflections $(400)_R$ and $(004)_O$, which form the area A_0. Tracing the intensities to the left (I_+) and to the right (I_-) from the center with a step of 0.01 Å, we compared the concentrations of scattering ions in the fragments of planes with $d > d_{max}$ and $d < d_{max}$ for either of the cluster areas in different samples (see Fig. 6).

First, we draw the reader's attention to different ranges of the ratio I_+/I_- (the narrow range from 0.2 to 0.3 for T_g = 725°C and the wide range from 0 to 7 for T_g = 625°C). Second, the curves qualitatively differ: they either slightly fluctuate about the mean value (T_g = 725°C) or are skewed largely to the right, $I_+/I_- > 1$ (T_g = 625°C).

Since the intensity of diffuse scattering is proportional to the concentration of scatterers, $I_{dif} \sim N$, it follows from the ranges of the ratio I_+/I_- (Fig. 6) that the low-temperature films (T_g = 625°C) exhibit atomic order with a step periodic variation in the occupation of the cluster areas by planes with different d. The relative intensity from widely spaced planes, $d = (d_{max} + 0.06)$ Å, is seven times higher than from symmetrically arranged narrow-spaced planes with $d = (d_{max} - 0.06)$ Å in the area A_0. For the area A_1, the relative intensity from the planes with $d = (d_{max} + 0.09)$ Å is four times higher than from the planes with $d = (d_{max} - 0.09)$ Å. In the case of the high-temperature films (725°C), the periodic variation of the microstructure is smoother and the narrow-spaced ($d < d_{max}$) planes slightly prevail (mostly $I_+/I_- < 1$).

The results presented in Figs. 5 and 6 allow us to come with proposals for the effect of cluster structures (appearing as the areas A_0 and A_1 in the diffraction patterns) on magnetic ordering. Based on the dependences $(I_+/I_-) = f(d_{max} - d)$ for diffuse scattering from the films with $T_g = 625$°C (Fig. 6), which suggest that the atomic structure of Mn–O planes in both areas (A_0 and A_1) is heavily strained and highly anisotropic, one can argue that the cluster structure of the rhombohedral phase (625°C) is favorable for magnetic ordering in both the ZFC and FC cases (Fig. 1). In the orthorhombic films (725°C), the difference in the density of scatterers in the planes compared is smaller but here the curve $I(d - d_{max})$ runs in the opposite manner. Therefore, when one of the structure groups (say, A_1) experiences tensile stresses, while the other (A_0) is compressed, magnetic ordering in an external field may start at higher temperatures. As a consequence, the Curie temperature in the films grown at 725°C (where like stresses prevail (Fig. 1) but the saturation magnetization $M(H)$ = const is lower than in those with $T_g = 625$°C: 250 G for the films with $T_g = 725$°C against 500 G for the films with $T_g = 625$°C) is higher than in the films with $T_g = 625$°C. The strong discrepancy between the curves in Fig. 7 substantiates the cluster nature of magnetic interaction.

An external magnetic field induces magnetic order of various orientation in the cluster areas A_1 and A_0 (which appears, at least, as crystallographically misoriented families of {202} and {004} planes giving unequal diffraction intensities, as follows from the diffraction patterns in Fig. 5). This fact is supported by the lower saturation magnetization in the films with T_g = 725°C compared with the films with T_g = 625°C (Fig. 7), although the concentration of the metallic phase in the films grown at low temperatures (<650°C) is lower.

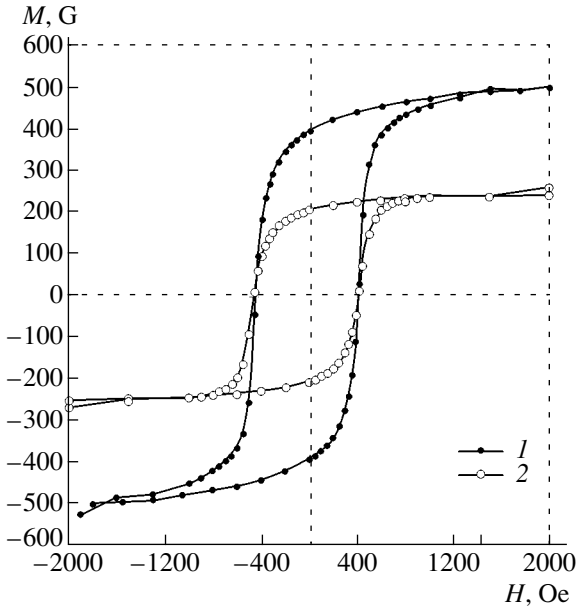

Fig. 7. Hysteresis loops for the LaCaMnO films grown at (*1*) 625 and (*2*) 725°C.

ELECTRICAL PROPERTIES OF THE FILMS

Depending on the growth temperature for LaSrMnO and LaCaMnO films, two types of the resistivity versus temperature dependence are observed. In the case of rhombohedral films (fine metallic-conduction clusters embedded in the insulating matrix) at $T < T_{crit} = 130$–160 K, the dependence $1/\rho \sim \exp(-(T_0/T)^{1/n})$ with $n = 4$ (the Mott law) or $n = 2$ (granular systems) changes to the dependence $\rho(T)$ that has saturation portions, which is typical of LaSrMnO, PrCaMnO, and other manganites [10, 11]. In these portions, the temperature coefficient of resistance approaches zero; that is, $\rho(T)$ = const.

The portions where $\rho(T) \approx$ const appear at low temperatures ($T < T_{crit}$), at which fine metallic-conduction clusters turn into a set of tunnel-coupled quantum dots with discrete (atomlike) energy spectrum [10–17]. The most plausible mechanism of conduction seems to be elastic tunneling between quantum dots under the condition of the Kondo effect, which provides a window in Coulomb blockade [4]. The amount of the effect $\rho(T)$ = const depends on the cluster size D; free hole concentration p, which specifies the energy spacing Δ between size quantization levels; and cluster spacing L. The parameters Δ and D are related to the density of states $N(E_F)$ at the Fermi level by the formula

$$\Delta = [D^3 N(E_F)] \approx [D^3 p/E_F]^{-1}.$$

Earlier, we calculated the parameters of quantum dots using available data for the metallic phase fraction C_m and mean cluster size D in the films grown at $T_g <$ 625°C. For $C_m = 0.02$–0.05, $D = 20$–50 Å, and $p = 3 \times 10^{21}$ cm^{-3}, we have $\Delta = 0.01$–0.10 eV, which explains the value $T_{crit} = 160$ K [10].

Let us consider the appearance of the portion $\rho(T)$ = const in terms of a simple model according to which the temperature dependence of the resistance tends to saturation when the thermal energy becomes lower than the spacing between size quantization levels:

$$\Delta \approx [D^3 N(E_F)]^{-1} \approx [D^3 p/E_F]^{-1} > kT.$$

Then, the critical temperature is bound to decrease with increasing cluster size. If clusters are fine, the critical temperature may be high (≈180 K) even in low-resistivity $La_{2/3}Ca_{1/3}MnO_3$ films ($\rho \approx 0.2$ Ω cm in the portion $\rho(T)$ = const) grown at 625°C (Fig. 8a).

At the growth temperature 725°C, the dependence $R(T)$ changes qualitatively: the saturation portion at $T <$ 180 K disappears and the curve takes the conventional form with a peak at $T = 180$ K and a dip at $T = 28$–30 K (Fig. 9). Also, when the growth temperature rises to

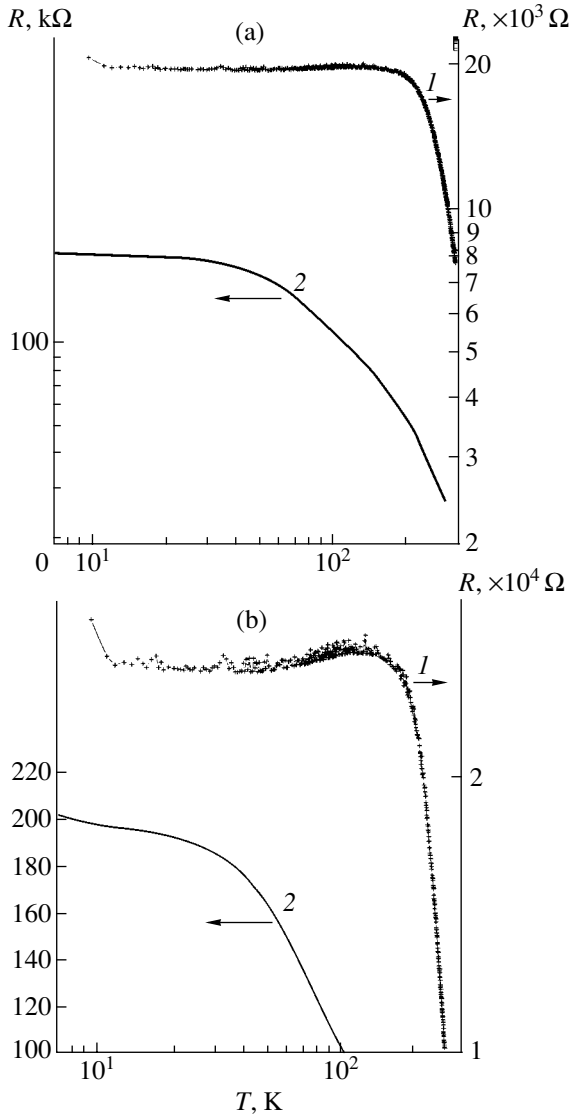

Fig. 8. (a) Temperature dependence of the resistance for the (*1*) LaCaMnO film grown at 625°C and (*2*) YBaCuO film after irradiation by five laser shots with an energy density of 135 mJ/cm^2. (b) The portions $R(T)$ = const of curves *1* and *2* on an enlarged scale.

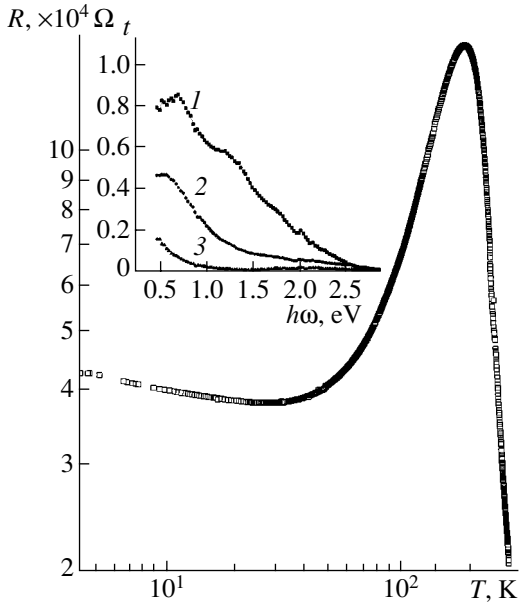

Fig. 9. Temperature dependence of the resistance for the LaCaMnO film grown at 725°C. The inset shows the optical transmission spectra for the LaSrMnO film (T_g = 600°C) in the (*1*) as-prepared and (*2*) irradiated state. (*3*) The optical transmission spectrum for the orthorhombic structure (T_g = 730°C).

725°C, the resistance of the films increases by a factor of 2–8 according to the measurement temperature. It is known that the insulator–metal transition near the Curie temperature is usually absent in manganites, so that similarity between the dependences $R = R(T)$ in manganites with magnetic order and in metals is formal and the conductivity in the former case is much lower than the minimal metallic conductivity σ_{min} [18, 19]. Since the conductivity is governed by *p* and *d* hybridization, σ_{min} must lie between 10^2 and 10^3 $(\Omega\ \text{cm})^{-1}$. For our films at T = 290 K, σ = 15 $(\Omega\ \text{cm})^{-1}$ (T_g = 625°C) and 5 $(\Omega\ \text{cm})^{-1}$ (T_g = 725°C), i.e., is one to two orders of magnitude lower than σ_{min}.

For the films grown at 625°C, σ is 2.7 and 2.3 times that for the films grown at 725°C at measurement temperatures of 290 and 5 K, respectively. This means that the concentration of metallic clusters in the former films is higher, providing a higher low-temperature magnetization under magnetic ordering (Fig. 3). At the same time, the rhombohedral structure has a lower Curie temperature.

For all the films, tunneling is the basic mechanism of conductivity at both moderate and low temperatures. This statement is confirmed by the run of the magnetoresistance versus temperature curve [3]: it decreases monotonically with temperature, which is typical of spin-dependent tunneling [20, 21]. When electrons tunnel between metallic clusters separated by high-resistivity spacers in an insulating matrix, the resistivity is given by

$$\rho = \rho_0 \exp(L/L_0),$$

where L is the mean intergranular spacing.

In the case of planar clusters (the thickness is one-third of the linear size D), the cluster spacing can be found using the cluster concentration C_m determined from the integral intensity ratio I_{clust}/I_{coh}:

$$L = D(3C_m^{-1/3} - 1).$$

The parameters of the $La_{2/3}Ca_{1/3}MnO_3$ films for various cluster sizes D are listed in the table.

One may assume that magnetic ordering in inhomogeneous samples results from tunneling between FM

clusters ion an AFM matrix. The coupling energy W decreases with distance between the clusters:

$$W = W_0 e^{-(L/L_1)}.$$

The probability of electrons tunneling between clusters to a great extent depends on Coulomb-blockade-related effects, which control the conductivity of granular systems [4], and also exponentially depends on the charge energy

$$E_c = e^2/\varepsilon D,$$

where e is the electron charge and ε is the permittivity.

Upon irradiation, the concentration of the metallic phase increases roughly twofold, which would have to improve the magnetic properties of the samples. However, as follows from the table, the mean spacing between clusters increases by 30% and magnetic coupling between them weakens. At the same time, the increase in L is compensated for by the decrease in E_c and loosening of Coulomb blockade. Eventually, the energy of exchange interaction between clusters rises (in particular, because of an increase in the density of states when the fraction of the orthorhombic phase exceeds that of the rhombohedral one upon irradiation [3]).

The portion $R(T)$ = const for the LaCaMnO film (T_g = 625°C) is shown on an enlarged scale in Fig. 8b (the full curve is shown in Fig. 8a). It is seen that the relationship $R(T)$ = const is an approximation: the curve has a peak at T = 119.5 K and a dip at 34.5 K. However, the extreme resistances differ by only 1.5% (for the films grown at 725°C, the difference is 500%). In the vicinity of the peak, the thermal energy and the energy W of tunnel coupling between clusters equal each other: $kT_{max} = W$.

Thus, magnetic ordering influences the conductivity of tunnel-coupled quantum dots, as indicated by the extrema in the curves $R(T)$. When clusters behave as quantum dots, as in manganites grown at 625°C, the energy spectrum is discrete and this influence is weak while experimentally observable. It was shown [15] that LaSr(Ca)MnO films with magnetic clusters, for which the dependence $\rho(T)$ is nonmonotonic and has portions $\rho(T)$ = const, behave in a radically different manner than YBaCuO nonmagnetic films, for which the related dependence is monotonic (Fig. 8, curve *2*).

The optical transmission (t) spectra for the as-prepared and LP films (inset to Fig. 9) exhibit qualitative and quantitative discrepancies. Portions where the charge is absorbed by free carriers (t decreases as $\hbar\omega$ becomes lower than 0.8 eV) are immediately apparent for both the as-prepared and irradiated rhombohedral films (T_g = 600°C). For the orthorhombic phase (T_g = 730°C) this portion is invisible, because absorption by free carriers appears only at $\hbar\omega < 0.2$ eV in this case [22].

As follows from the value of t in the range $\hbar\omega <$ 0.8 eV (the range of metallic conduction), the density of states in the rhombohedral phase is lower than in the orthorhombic phase. The Fermi energy for the R phase (E_F = 0.8 eV) is much higher than for the O phase ($E_F \le$ 0.2 eV). The narrow hysteresis loop described above and the increase in the saturation magnetization of the films upon laser processing (Fig. 2), causing the $R \longrightarrow O$ phase transition [3], may be related to an increase in the density of electronic states, which are responsible for metallic conduction and ferromagnetism.

Table

T_g, °C	State	D, Å	C_m, %	L, Å
625	As-prepared	70	6.7	49.5
625	LP	150	11.24	65.5
725	As-prepared	110	12	44.6

CONCLUSIONS

Our study of the magnetization, conductivity, and structure of single-crystal LaCa(Sr)MnO manganite films shows that the differences in the dependences $M(T)$, $M(H)$, and $R(T)$ are due to various types of magnetic order in Mn–O planes of metallic clusters embedded in an insulating matrix.

Analysis of X-ray diffuse scattering revealed two groups of clusters: with a large (d = 2.05–2.52 Å) and small (d = 1.86–2.05 Å) interplanar spacing (the orthorhombic and rhombohedral phases, respectively).

Detailed study of X-ray diffuse scattering shows that, in the rhombohedral phase grown at T_g = 625°C, the number of planes with interplanar spacings $d > d_{mean}$ five to seven times exceeds the number of planes with other spacings in either of the groups. In the orthorhombic phase (T_g = 725°C), the number of states with $d > d_{mean}$ and $d < d_{mean}$ fluctuates in both groups of clusters.

In manganites grown at different temperatures, both groups of clusters behave in a radically different manner. In the films grown at 625°C, clusters at low temperatures ($T < T_C$) behave as tunnel-coupled quantum dots with a discrete energy spectrum (which shows up in the constant-resistance portion in the curves $R(T)$. In the films grown at 725°C, they are characterized by a continuous spectrum (which shows up as a decrease in the resistance in the range where the electronic and magnetic subsystems interact intensely, $R(T) = R_{max} - R_{min}$). For magnetic interaction, tunnel coupling between Mn–O clusters are of crucial importance.

REFERENCES

1. É. L. Nagaev, Usp. Fiz. Nauk **166**, 833 (1996) [Phys. Usp. **39**, 781 (1996)].
2. R. V. Demin, L. I. Koroleva, R. Szymszak, and H. Szymszak, Pis'ma Zh. Éksp. Teor. Fiz. **75**, 402 (2002) [JETP Lett. **75**, 331 (2002)].

3. Z. A. Samoĭlenko, V. D. Okunev, E. I. Pushenko, *et al.*, Zh. Tekh. Fiz. **73** (2), 118 (2003) [Tech. Phys. **48**, 250 (2003)].
4. B. Abeles, Sheng Ping, M. D. Coutts, and Y. Arie, Adv. Phys. **24**, 407 (1975).
5. Sheng Ping and J. Klafter, Phys. Rev. B **27**, 2583 (1983).
6. I. O. Troyanchuk, O. S. Mantytskaya, A. N. Chobot, and G. Shimchak, Zh. Éksp. Teor. Fiz. **122**, 347 (2002) [JETP **95**, 300 (2002)].
7. M. A. Krivoglaz, *Electronic Structure and Electron Properties of Metals and Alloys: A Collection of Scientific Works* (Naukova Dumka, Kiev, 1998), pp. 3–30 [in Russian].
8. M. V. Krasin'kova, Zh. Tekh. Fiz. **72** (5), 30 (2002) [Tech. Phys. **47**, 543 (2002)].
9. A. I. Mitsek, Metallofiz. Noveishie Tekhnol. **21** (10), 3 (1999).
10. V. D. Okunev, N. N. Pafomov, V. A. Isaev, *et al.*, Fiz. Tverd. Tela (St. Petersburg) **44**, 150 (2002) [Phys. Solid State **44**, 157 (2002)].
11. V. G. Prokhorov, G. G. Kaminsky, V. S. Flis, and Y. Pak Lee, Fiz. Nizk. Temp. **25**, 1060 (1999) [Low Temp. Phys. **25**, 792 (1999)].
12. O. Yu. Gorbenko, R. V. Demin, A. R. Kaul', *et al.*, Fiz. Tverd. Tela (St. Petersburg) **40**, 290 (1998) [Phys. Solid State **40**, 263 (1998)].
13. V. S. Gaviko, V. E. Arkhipov, A. V. Korolev, *et al.*, Fiz. Tverd. Tela (St. Petersburg) **41**, 1064 (1999) [Phys. Solid State **41**, 969 (1999)].
14. V. D. Okunev, Z. A. Samoilenko, V. M. Svistunov, *et al.*, J. Appl. Phys. **85**, 7282 (1999).
15. V. D. Okunev, Z. A. Samoilenko, V. A. Isaev, *et al.*, Pis'ma Zh. Tekh. Fiz. **28** (2), 12 (2002) [Tech. Phys. Lett. **28**, 44 (2002)].
16. L. I. Glazman and M. É. Raĭkh, Pis'ma Zh. Éksp. Teor. Fiz. **47**, 378 (1988) [JETP Lett. **47**, 452 (1988)].
17. K. Kikoin and Y. Avishai, Phys. Rev. Lett. **86**, 2090 (2001).
18. N. F. Mott, *Metal–Insulator Transformations* (Taylor & Fransis, London, 1974; Nauka, Moscow, 1979).
19. N. F. Mott and E. A. Davis, *Electronic Processes in Non-Crystalline Materials* (Clarendon, Oxford, 1979; Mir, Moscow, 1982), Vol. 1.
20. J. S. Helman and B. Abeles, Phys. Rev. Lett. **37**, 1429 (1976).
21. S. Lee, H. Y. Hwang, B. I. Shraiman, *et al.*, Phys. Rev. Lett. **82**, 4508 (1999).
22. N. N. Loshkareva, Yu. N. Sukhorukov, E. V. Mostovshchikova, *et al.*, Zh. Éksp. Teor. Fiz. **182**, 412 (2002) [JETP **94**, 350 (2002)].

Translated by V. Isaakyan

Technical Physics, Vol. 49, No. 4, 2004, pp. 443–446. Translated from Zhurnal Tekhnicheskoĭ Fiziki, Vol. 74, No. 4, 2004, pp. 66–69.

OPTICS,
QUANTUM ELECTRONICS

Electric-Discharge He/Xe/I_2 Excimer–Halogen UV Lamp

A. K. Shuaibov and I. A. Grabovaya

Uzhhorod National University, vul. Pidgirna 46, Uzhhorod, 88000 Ukraine
e-mail: ishev@univ.uzhgorod.ua

Received July 18, 2003

Abstract—The characteristics of a low-size low-pressure UV lamp operating on the atomic iodine resonant line (λ = 206 nm) and xenon iodide (λ = 253 nm) and dimer iodine (λ = 342 nm) bands are investigated. A lamp with an interelectrode distance of 19 cm was pumped by a longitudinal dc glow discharge. The working gas mixtures were He/I_2 and He/Xe/I_2 mixtures with a total pressure of 50–1500 Pa. The output parameters of the electric-discharge excimer–halogen lamp were optimized in terms of the gas mixture pressure and composition and the power deposited in the discharge. It is shown that the total UV power emitted from the entire aperture of the lamp in the spectral range 200–350 nm attains 5–7 W with an efficiency of ≤5%. © *2004 MAIK "Nauka/Interperiodica".*

INTRODUCTION

At present, optical techniques employing high-power sources of spontaneous or laser radiation are widely used in microelectronics, ecology, and medicine [1, 2]. This has inspired studies of the emission characteristics of different types of electric discharges in mixtures of noble gases with halogen-containing agents at low and moderate pressures. The most powerful and efficient excimer–halogen lamps were pumped by dc glow discharges, and their emission spectra partially or totally covered the spectral range from 160 to 353 nm [3–15]. These lamps, however, were thoroughly studied only when working with mixtures of heavy noble gases with Cl_2 or HCl. These working mixtures are rather corrosive, and the lifetime of lamps with bare electrodes operating in a static-gas mode is no longer than 50–100 h [3]. At discharge currents higher than 20–30 mA, the concentration of the chlorine-containing agents sharply decreases because of their absorption by the hot electrodes. For this reason, to increase the lifetime of a sealed-off excimer–halogen lamp to 1000 h and more, one has to use less efficient and more complicated pumping techniques employing capacitive or barrier discharges [15–17]. Therefore, it seems attractive to use Br_2 and I_2 molecules, which are less corrosive than chlorine. This enables one to increase the lifetime of dc excimer–halogen lamps; moreover, besides excimer and halogen molecular bands, the emission spectrum of such lamps contains a 206-nm resonance line of I*. In a recent paper [18], the lifetime of a sealed-off iodine lamp pumped by a glow discharge was reported to be as high as 1000 h. In that study, the main attention was paid to the emission of the 206-nm resonant line of atomic iodine, whereas conditions for the formation of XeI* and I_2^* molecules and their contribution to the total emission intensity of a dc lamp were not studied.

This paper is devoted to studying the output characteristics of an excimer–halogen lamp with He/I_2 and He/Xe/I_2 working mixtures pumped by a glow discharge.

EXPERIMENTAL SETUP

A dc longitudinal discharge was ignited in a quartz tube transparent down to 190 nm. The inner diameter of the discharge tube was 1.4 cm. The distance between the hollow cylindrical nickel electrodes with an outer diameter of 1.4 cm and a length of 1.5 cm was 19 cm. Iodine crystals were placed in a special socket behind the anode (see Fig. 1).

The optical characteristics of the glow discharge were studied using an FÉU-106 photomultiplier and MDR-2 monochromator with a 1200-grove/mm grating. The spectral sensitivities of the photomultiplier and monochromator were relatively calibrated in the spectral range 190–400 nm. The glow discharge was supplied from a high-voltage rectifier with a rated average current of ≤50 mA and voltage of ≤25 kV. Before being filled with noble gases, the discharge tube was pumped out to a residual pressure of 5–7 Pa. During a discharge,

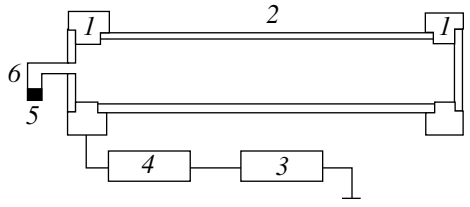

Fig. 1. Schematic of an excimer–halogen lamp: (*1*) electrodes, (*2*) quartz tube, (*3*) high-voltage power supply, (*4*) ballast resistor, (*5*) iodine crystals, and (*6*) socket for iodine crystals.

1063-7842/04/4904-0443$26.00 © 2004 MAIK "Nauka/Interperiodica"

the tube was cooled with a fan so that the temperature of the socket with iodine crystals was close to room temperature and exceeded the room temperature by no more than 10–15°C even at the highest energy deposition in the discharge. In the experiment, the iodine vapor pressure in the coldest part of the discharge tube was no higher than 100–200 Pa [19]. The electric characteristics of the discharge and the total power of the UV emission were measured by the method described in [20, 21].

LAMP CHARACTERISTICS

A uniform dc glow discharge in mixtures of noble gases with iodine vapor was observed at He and Xe pressures of ≤150–200 Pa and average currents of ≥30–40 mA. As the discharge current was decreased from 50 to 3–5 mA, the diameter of the bright plasma column that was observed against the background of a low-intensity diffuse discharge decreased from 10 to 2 mm. At noble gas pressures higher than 1 kPa, the discharge had the form of a plasma column against the background of a uniform low-current glow discharge throughout the entire current range under study. Such behavior corresponds to the regime of dynamic contraction.

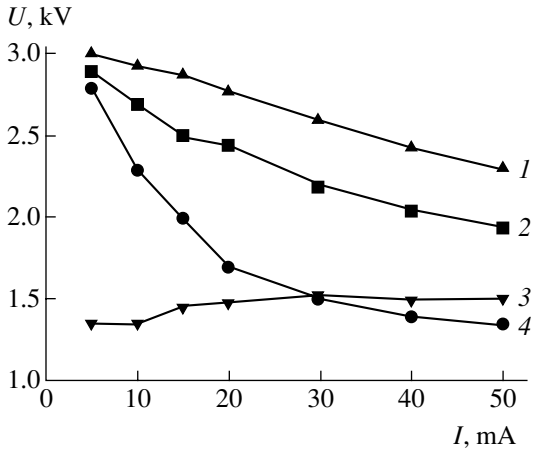

Fig. 2. Current–voltage characteristics of dc glow discharges in He/I_2 mixtures (curves *1*, *2*, *4*) at $P(He)$ = (*1*) 130, (*2*) 400, and (*4*) 1600 Pa and $He/Xe/I_2$ mixture (curve *3*) at $P(He)/P(Xe)$ = 400/120 Pa.

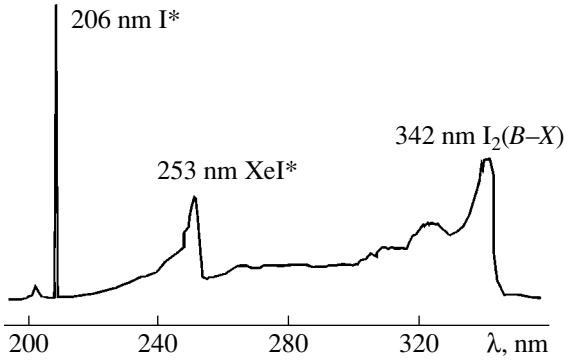

Fig. 3. UV emission spectrum of glow discharge in a $He/Xe/I_2$ mixture at $P(He)/P(Xe)$ = 400/120 Pa.

The current–voltage characteristics of glow discharges in He/I_2 and $He/Xe/I_2$ mixtures are shown in Fig. 2. The current–voltage characteristics of discharges in a He/I_2 mixture correspond to a subnormal regime, whereas in the case of a $He/Xe/I_2$ mixture, they correspond to the weakly-pronounced anomalous stage of a glow discharge. As the pressure $P(He)$ in a He/I_2 mixture increases, the discharge passes to the regime of dynamic contraction, the ignition voltage decreases, and the voltage decreases with increasing discharge current at a progressively increasing rate. Due to the presence of a large number of negative ions in the discharge plasma and because of the different radial diffusion velocities of the electrons and negative iodine ions, an ion–ion plasma forms in the central part of the discharge tube. For this reason, the current–voltage characteristics of electronegative and electropositive gases are quite different. When a glow discharge operated in Xe/I_2 mixtures with $P(Xe)$ = 130–1600 Pa, the current–voltage characteristics varied with $P(Xe)$ in a similar way; however the rate at which the voltage decreases with increasing discharge current was two to three times lower (at discharge currents of $I_d \geq 20$ mA, the current–voltage characteristics were more flat and close to the current–voltage characteristic of a normal glow discharge). A minor additive of xenon to a He/I_2 mixture led to a decrease in the discharge ignition voltage by a factor of 2 (Fig. 2, curve *3*) and the formation of a plateau in the current–voltage characteristic at discharge currents of I_d = 20–50 mA.

The spectrum of UV emission from the glow discharge plasma in $He/Xe/I_2$ mixtures is shown in Fig. 3. In the case of the He/I_2 mixture, the spectrum contains the resonant line of atomic iodine (λ = 206 nm) and the system of $I_2(B–X)$ molecular bands within the spectral range 320–342 nm, whereas in the case of a $He/Xe/I_2$ mixture, there is also the XeI(*B–X*) band with λ = 253 nm. When a glow discharge operated in a He/I_2 mixture with $P(He)$ = 400 Pa, the spectral distribution of the UV emission intensity was $I(206\text{ nm})/I(342\text{ nm})$ = 52/48%, whereas in a $He/Xe/I_2$ mixture with $P(He)/P(Xe)$ = 400/120 Pa, it was $I(206\text{ nm})/I(253\text{ nm})/I(342\text{ nm})$ = 54/9/37%. Due to a rather large spectral width of the emission of XeI* and I_2^* molecules, a significant fraction of the total UV power was emitted in the form of molecular bands.

The dependences of the emission intensity of the iodine resonant line on the power deposited in a discharge are shown in Fig. 4. These dependences (except for the curve corresponding to the pronounced regime of dynamic contraction of a glow discharge in a He/I_2 mixture) show that the emission intensity increases

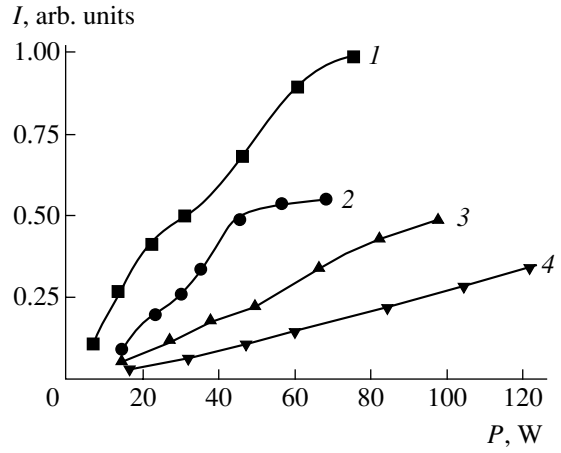

Fig. 4. Emission intensity of the 206-nm resonant line of atomic iodine vs. power deposited in a glow discharge in a He/Xe/I_2 mixture (curve *1*) at P(He)/P(Xe) = 400/120 Pa and He/I_2 mixtures (curves *2–4*) at P(He) = (*2*) 1600, (*3*) 400, and (*4*) 130 Pa.

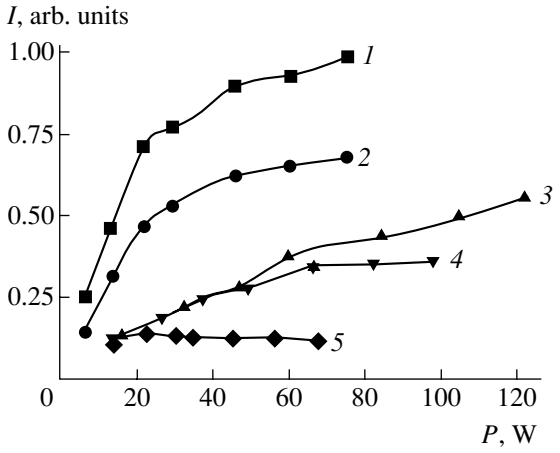

Fig. 5. Intensities of the 342-nm I_2^* (*B–X*) (curves *1, 3–5*) and 253-nm XeI*(*B–X*) (curve *2*) emission bands vs. power deposited in a glow discharge in He/Xe/I_2 mixtures (curves *1, 2*) at P(He)/P(Xe) = 400/120 Pa and He/I_2 mixtures (curves *3–5*) at P(He) = (*3*) 130, (*4*) 400, and (*5*) 1600 Pa.

nearly in proportion with the deposited power. The increase in P(He) and, especially, addition of xenon to the working mixture result in a steeper dependence of the emission intensity of the 206-nm line on the deposited power. Such behavior can be attributed to an increase in the temperature of the coldest part of the discharge tube and an increase in the partial pressure of iodine vapor. It can also be seen in Fig. 4 that the increase in the pressure of a He/I_2 mixture (which is accompanied by the transition to the contraction regime) leads to the increase in the production efficiency of the excited iodine atoms in the plasma column.

Figure 5 shows the emission intensities of the XeI* and I_2^* molecular bands versus the power deposited in a glow discharge. In a He/Xe/I_2 mixture, the I_2^* (*B–X*) 342-nm band is the most intense. The band intensities are seen to increase linearly with power. The slopes of the curves are different within the current ranges I_d = 5–20 and 25–50 mA (the slope is larger at lower discharge currents). When a discharge operated in a He/I_2 mixture, the intensity of the 342-nm band was maximum at P(He) = 130 Pa and the slope of the dependence of the emission intensity on the deposited power decreased with the helium partial pressure.

The maximum total UV power emitted from the entire aperture of the excimer–halogen lamp was 5–7 W with an efficiency of ≤5%. The lamp lifetime in a static-gas mode was as high as 400–500 h.

Thus, the study of the output characteristics of a low-size He/Xe/I_2 excimer–halogen lamp pumped by a dc glow discharge has shown that, in addition to the I* 206-nm emission line, the XeI*(*B–X*) 253-nm and I_2^* (*B–X*) 342-nm bands also significantly contribute to the total UV emission. The maximum total UV power is 7 W with an efficiency of ≤5%. The lamp lifetime in a static-gas mode is ≤500 h.

REFERENCES

1. I. W. Boyd and J.-Y. Zhang, Mater. Res. Soc. Symp. Proc. **617**, J4.4.1 (2000).
2. G. S. Polunin, V. V. Kourenkov, and E. G. Polunina, J. Refract. Surg. **14**, S230 (1998).
3. A. P. Golovitskiĭ and S. N. Kan, Opt. Spektrosk. **75**, 604 (1993) [Opt. Spectrosc. **75**, 357 (1993)].
4. M. I. Lomaev, A. N. Panchenko, and É. A. Sosnin, Zh. Tekh. Fiz. **68** (2), 64 (1998) [Tech. Phys. **43**, 192 (1998)].
5. A. N. Panchenko and V. F. Tarasenko, Opt. Spektrosk. **84**, 389 (1998) [Opt. Spectrosc. **84**, 337 (1998)].
6. A. K. Shuaibov, A. I. Dashchenko, and I. V. Shevera, Kvantovaya Élektron. (Moscow) **31**, 371 (2001).
7. A. K. Shuaibov, A. I. Dashchenko, and I. V. Shevera, Zh. Tekh. Fiz. **71** (8), 121 (2001) [Tech. Phys. **46**, 1049 (2001)].
8. A. K. Shuaibov, Zh. Tekh. Fiz. **72** (10), 138 (2002) [Tech. Phys. **47**, 1341 (2002)].
9. A. K. Shuaibov, A. I. Dashchenko, and I. V. Shevera, Opt. Spektrosk. **92**, 753 (2002) [Opt. Spectrosc. **92**, 690 (2002)].
10. A. K. Shuaibov, L. L. Shimon, I. V. Shevera, and A. I. Dashchenko, Fiz. Plazmy **28**, 1147 (2002) [Plasma Phys. Rep. **28**, 1060 (2002)].
11. A. K. Shuaibov, L. L. Shimon, I. V. Shevera, and A. I. Dashchenko, Ukr. Patent No. 53509A (20 June 2002), Byull. Isobret., No. 1 (2003).
12. A. K. Shuaibov, L. L. Shimon, I. V. Shevera, and A. I. Dashchenko, Ukr. Patent No. 55724 A (24 May 2002), Byull. Isobret., No. 4 (2003).

13. A. K. Shuaibov, A. I. Dashchenko, and I. V. Shevera, Teplofiz. Vys. Temp. **40**, 337 (2002).
14. A. K. Shuaibov, I. V. Shevera, and A. I. Dashchenko, Zh. Prikl. Spektrosk. **70**, 129 (2003).
15. M. I. Lomaev, V. S. Skakun, É. A. Sosnin, *et al.*, Usp. Fiz. Nauk **173**, 201 (2003).
16. Z. Falkenstein, J. J. Coogan, and Y. Sakai, J. Phys. D **30**, 2704 (1997).
17. A. Oda, H. Sugawara, Y. Sakai, and H. Akashi, J. Phys. D **33**, 1507 (2000).
18. M. I. Lomaev and V. F. Tarasenko, Proc. SPIE **4747**, 390 (2002).
19. *Properties of Inorganic Compounds: A Handbook* (Khimiya, Leningrad, 1983) [in Russian].
20. A. K. Shuaibov, L. L. Shimon, A. I. Dashchenko, and I. V. Shevera, J. Phys. Stud. **5**, 131 (2001).
21. A. K. Shuaibov, L. L. Shimon, A. I. Dashchenko, and I. V. Shevera, Prib. Tekh. Éksp., No. 1, 104 (2002).

Translated by N. Ustinovskiĭ

Technical Physics, Vol. 49, No. 4, 2004, pp. 447–453. Translated from Zhurnal Tekhnicheskoĭ Fiziki, Vol. 74, No. 4, 2004, pp. 70–76.

ACOUSTICS, ACOUSTOELECTRONICS

Ultrasonic Engine Based on Traveling Waves in a Plate

A. B. Nadtochiy, A. N. Gorb, and O. A. Korotchenkov

Shevchenko National University, Vladimirskaya ul. 64, Kiev, 03022 Ukraine

e-mail: nadt@gala.net

Received July 18, 2003

Abstract—Velocity dispersion curves and phase relationships between the surface displacement components are calculated in the case of waves propagating in *XZ*-, *YZ*-, and *ZY*-cut $LiNbO_3$ plates. The dispersion curves agree with experimental frequency dependences of the excitation efficiency for various modes in the plates. The displacements of ZnS microparticles placed on the surface of the plates qualitatively agree with the analytical phase relationships between the displacement components. Results obtained indicate that the plate may be used as an ultrasonic engine capable of transferring microparticles in various physical and industrial processes.

INTRODUCTION

The transfer of microobjects is a basic process in many physical and industrial automated systems, which is accomplished by different methods. In particular, micromechanical systems use electrostatic [1–3] and magnetic [4] engines. Ultrasonic engines offer substantial advantages [5]. First, ultrasonic waves may be excited far away from the guiding channel, allowing one to spatially separate the electric and mechanical systems. Second, the use of a piezoelectric acoustic line made, for example, of $LiNbO_3$ or quartz, provides a mobile electric potential near its surface. This opens up possibilities for transfer of charged microparticles, including biological objects.

Ultrasonic engines are based largely on traveling surface acoustic waves and standing waves in rods and plates. Investigations into traveling waves in plates consider the effect of acoustic flow. Such an approach is strictly valid for hydrodynamic systems [6, 7]. An important property of an ultrasonic engine is that the normal and tangential (relative to the surface) components of the force may be controlled independently. In view of a variety of wave modes in the plates and, correspondingly, a variety of phase relationships between the displacement components on the surface, the use of waves in the plates for implementing an ultrasonic engine seems to be reasonable. Such a possibility was first indicated in [7]. Note that an ultrasonic engine of this type can be used in modern semiconductor nanotechnology. For example, the transfer of charge carriers in quantum wells that occurs in composite piezoelectric substrate–multilayer semiconductor systems modifies significantly the luminescent characteristics of the semiconductor [8].

The goal of this study is to find phase relationships between the surface displacement components at the excitation of waves in the plates. Theoretical results for *X*-, *Y*-, and *Z*-cut $LiNbO_3$ plates are reported. Experimental results for transfer of microparticles over the plate surface are given as tentative data. Mechanisms behind charged object transfer in the piezoelectric field of the wave will be discussed in a special paper.

1. OPERATION OF THE ENGINE

A standard ultrasonic engine that employs resonance oscillations in the plate contains an array of ridges separated by a distance comparable to the standing wave wavelength [9, 10]. The principle of operation of an ultrasonic engine implies that, when the plate oscillates, the motion of the ridges is imparted to an extended object placed on them. A change in the resonance oscillation mode of the plate changes the vibration phase of the ridges, which may change the direction of object displacement.

A traveling-wave ultrasonic engine considered in this paper combines transfer mechanisms typical of a resonant engine and the effect of acoustic flow, which entrains the object in the direction of wave propagation. Note that, in plates, backward waves with oppositely directed phase and group velocities may coexist [11]. As a consequence, the direction of object transfer may be varied not only by varying the phase relationships between the components of elastic displacements along and perpendicularly the plate according to the wave frequency, but also via forward-to-backward wave switching.

2. THEORETICAL MODEL

Wave propagation in lithium niobate plates has been covered in most detail for the zeroth-order Lamb modes s_0 and a_0 [12]. Our goal is to find phase relationships between the surface displacement components for higher order modes in *XZ*-, *YZ*, and *ZY*-cut plates and use these results for designing ultrasonic engines. In the

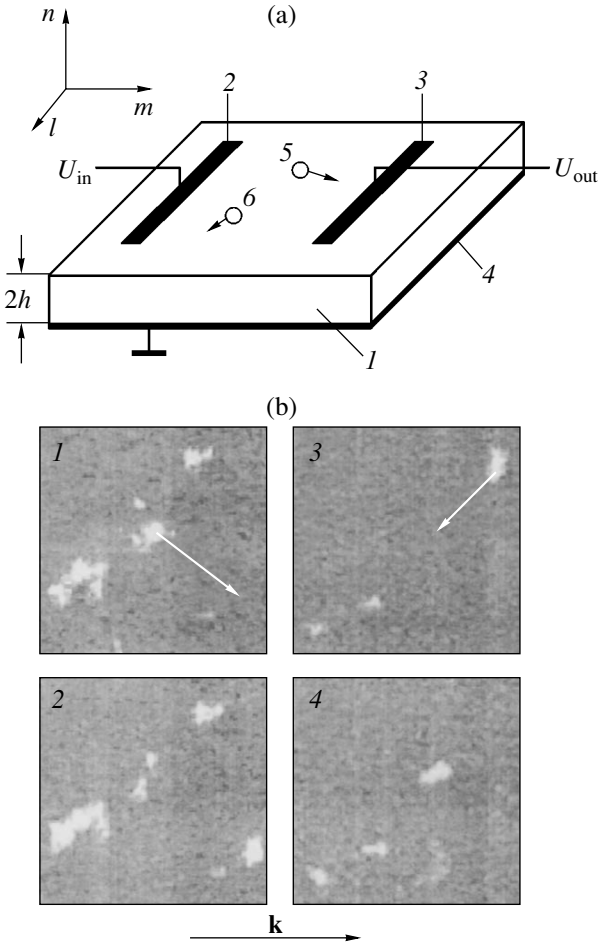

Fig. 1. (a) Geometry of the experiment: (*1*) $LiNbO_3$ plate, (*2*) electrode of the input transducer, (*3*) output electrode, (*4*) metallic substrate, and (*5*, *6*) ZnS microparticles transferred by the wave excited in the plate. (b) Micrographs of 280×280-μm areas showing the positions of microparticles on the *YZ*-cut $LiNbO_3$ plate that are taken (*1*, *3*) before and (*2*, *4*) after jerky motion of one particle (*2*) in the direction of the wavevector **k** and (*4*) in the opposite direction. The arrows in panels *1* and *3* show particle displacements.

designation of the cuts, the first letter means the normal to the surface and the second indicates the wave propagation direction.

2.1. Dispersion of wave propagation velocity in $LiNbO_3$ plates. Consider waves propagating in a plate of thickness 2*h* (Fig. 1a). The orientation of the plate in the crystallographic coordinates is specified by two vectors: $\mathbf{m} = m_x x + m_y y + m_z z$ (aligned with the wave propagation direction) and $\mathbf{n} = n_x x + n_y y + n_z z$ (directed normally to the plate). Since these vectors are orthogonal to each other, $\mathbf{n} \cdot \mathbf{m} = 0$. We also introduce the vector product of **m** and **n**: $\mathbf{l} = \mathbf{n} \times \mathbf{m}$. The components l_i are given by $l_i = \delta_{ijk} m_i n_j$, where δ_{ijk} is the Levi-Civita symbol. The problem is solved in the electrostatic approximation. To this end, we write the wave equation

$$\rho \frac{\partial^2 u_i}{\partial t^2} = \frac{\partial T_{ij}}{\partial x_j}, \tag{1}$$

the Poisson equation

$$\frac{\partial D_i}{\partial x_i} = 0 \tag{2}$$

and the equations for piezoelectric effect

$$T_{ij} = c^E_{ijkl} \frac{\partial u_k}{\partial x_l} + e_{mij} \frac{\partial \varphi}{\partial x_m}, \tag{3}$$

$$D_i = e_{ikl} \frac{\partial u_k}{\partial x_l} - \varepsilon^S_{ij} \frac{\partial \varphi}{\partial x_j}. \tag{4}$$

Here, ρ is the density, u_i are the acoustic displacement components, T_{ij} are the mechanical stress tensor components, φ is the electric potential, *t* is the time, D_i is the electric induction, c^E_{ijkl} are the elastic modulus tensor components at a constant electric field, e_{mij} are the piezoelectric coefficient tensor components, and ε^S_{ij} are the permittivity tensor components at a constant strain. Below, the superscripts *E* and *S* at the elastic moduli and permittivity are omitted.

In order to simplify the equations, we use the designation $\varphi = u_4$ and represent solutions to the set of Eqs. (1) and (2) as plane inhomogeneous waves:

$$u_i = a_i \exp[ik(Vt - (m_x x + m_y y + m_z z) - \beta(n_x x + n_y y + n_z z))], \tag{5}$$

where a_i is the complex amplitude, *V* is the phase velocity, β is the transverse-to-longitudinal wavenumber ratio, and $i = 1$–4.

Substituting (5) into Eqs. (1) and (2) in view of (3) and (4) yields a set of four homogeneous Christoffel equations for the displacements components and potential:

$$[\Gamma_{pq} - \delta_{pq} \rho V^2][u_k] = 0, \tag{6}$$

where $\Gamma_{pq} = c_{ipqj} R_{ij}$, $\Gamma_{p4} = \Gamma_{4p} = e_{ijp} R_{ij}$, $\Gamma_{44} = -\varepsilon_{ij} R_{ij}$, and $R_{ij} = \beta^2 n_i n_j + \beta(n_i m_j + n_j m_i) + m_i m_j$ (i, p, q, $j = 1$–3 and $k = 1$–4).

Set (6) has nonzero solutions when its determinant is zero. The determinant of this set has the form of an eighth-degree polynomial in β, thus specifying eight independent solutions. Then, the general solution for the displacements and potential takes the form

$$u_p = \sum_{q=1}^{8} b_q B_{pq} \exp[ik(Vt - (m_x x + m_y y + m_z z) - \beta_q(n_x x + n_y y + n_z z))], \tag{7}$$

where $p = 1$–4 and $q = 1$–8.

In (7), the coefficients B_{pq} establish a relationship between the potential φ_q and the partial components of the displacements u_{xq}, u_{yq}, and u_{zq} for each β_q. They can be taken as algebraic complements of one row of the matrix of set (6).

The eight coefficients b_q are found from the boundary conditions. Six of them equate the normal and tangential stresses on the plate surface to zero,

$$T_{ij}n_in_j(\pm h) = T_{ij}n_im_j(\pm h) = T_{ij}n_il_j(\pm h) = 0, \quad (8)$$

and the remaining two require that the electric induction be continuous on the nonmetallized side of the plate. On the metallized surface, the potential is constant:

$$D_in_i(+h) = -\varepsilon_0\frac{\partial\varphi}{\partial x_i}n_i, \quad \varphi(-h) = 0. \quad (9)$$

The symbols $+h$ and $-h$ in Eqs. (8) and (9) refer, respectively, to the upper and lower sides of the plate. Since the equations of these surfaces have the form $n_xx + n_yy + n_zz = \pm h$, the sum $n_xx + n_yy + n_zz$, appearing in Eq. (7), is replaced by $+h$ or $-h$ in (8) and (9). In this paper, we will consider plates with metallized lower sides and, therefore, use electric boundary conditions (9). In free space above the surface, the electric potential satisfies the Laplace equation $\nabla^2\varphi = 0$.

Substituting (7) into boundary conditions (8) and (9), we obtain a homogeneous system of eight equations in eight unknown coefficients b_q. Upon mathematical transformation, the components of the matrix $[M]$ of this system can be represented as

$$\begin{aligned}
M(1,q) &= \exp(-kh\beta_q)[c_{ijkp}(n_in_jn_k\beta_q + n_in_jm_k)B_{pq} \\
&\quad + e_{ijk}(n_in_jn_k\beta_q + m_in_jn_k)B_{4q}], \\
M(2,q) &= \exp(2kh\beta_q)M(1,q), \\
M(3,q) &= \exp(-kh\beta_q)[c_{ijkp}(n_im_jn_k\beta_q + n_im_jm_k)B_{pq} \\
&\quad + e_{ijk}(n_in_jm_k\beta_q + m_in_jm_k)B_{4q}], \\
M(4,q) &= \exp(2kh\beta_q)M(3,q), \\
M(5,q) &= \exp(-kh\beta_q)[c_{ijkp}(n_il_jn_k\beta_q + n_il_jm_k)B_{pq} \\
&\quad + e_{ijk}(n_in_jl_k\beta_p + m_in_jl_k)B_{4q}], \\
M(6,q) &= \exp(2kh\beta_q)M(5,q), \\
M(7,q) &= \exp(-kh\beta_q)[e_{ijp}(n_in_j\beta_q + n_im_j)B_{pq} \\
&\quad - (\varepsilon_{ij}(n_in_j\beta_q + n_im_j) + i\varepsilon_0)B_{4q}], \\
M(8,q) &= \exp(kh\beta_q)B_{4q},
\end{aligned} \quad (10)$$

where $i, j, k, p = 1$–3 and $q = 1$–8.

Nonzero solutions to the system of Eqs. (8) and (9) are determined by the condition

$$\det[M] = 0. \quad (11)$$

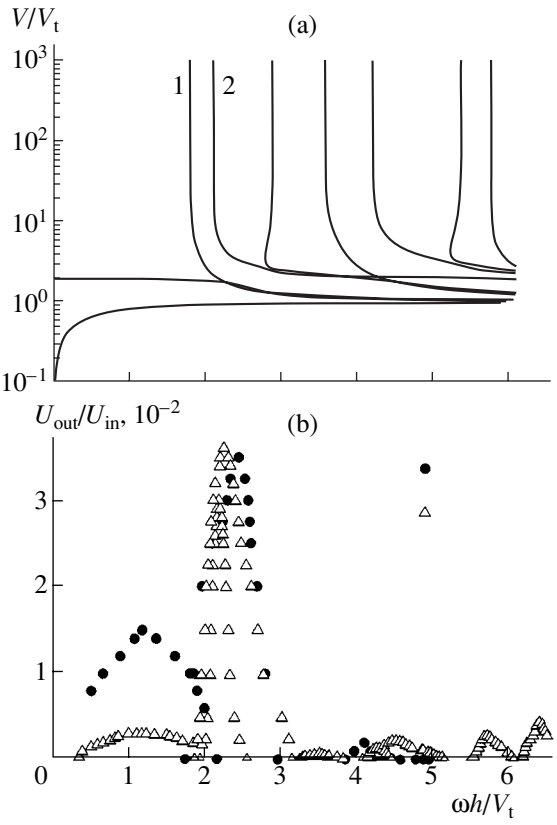

Fig. 2. (a) Theoretical dispersion curves and (b) excitation spectrum for the modes excited in the *XZ*-cut $LiNbO_3$ plates. The figures by the curves are the numbers of the modes that are analyzed in Figs. 5–7. The symbols refer to different samples. V_t is the velocity of the transverse wave.

Solving Eq. (11), we arrive at a relationship between the velocity V and the wavenumber k (or the frequency $\omega = kV$), i.e., the dispersion relation. To numerically solve Eq. (11), one should find zeroes of the expression $\mathrm{Im}(\det[M]) + \mathrm{Re}(\det[M])$ in a certain frequency range at a given velocity V. Given the elastic moduli, piezoelectric moduli, and permittivity of lithium niobate [12], dispersion curves for the *XZ*, *YZ*, and *ZY* cuts can be obtained (Figs. 2a, 3a, 4a). Equation (7) allows one to calculate the displacement components at an arbitrary point on the surface or inside the plate accurate to a constant multiplier. To do this, the coefficients b_q and B_{pq} are substituted into (7), where b_q are taken as algebraic complementary subsets of one row of the matrix of system (10).

It can be shown that, for the *XZ* cut and symmetric boundary conditions, the solution can be represented as the superposition of symmetric and antisymmetric Lamb modes. In our case, the boundary conditions are asymmetric (the upper surface of the plate is free, while the lower one is short-circuited) and the solution cannot be represented in this manner. This is also supported by the fact that the dispersion curves do not intersect. For the *YZ* cut, the solution is the superposition of piezo-

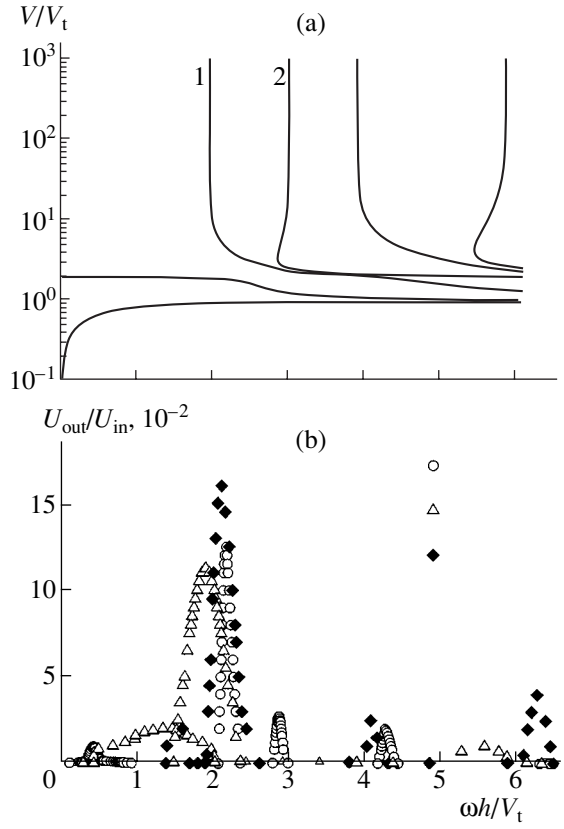

Fig. 3. Same as in Fig. 2 for modes in the *YZ*-cut plates. The symbols refer to different samples.

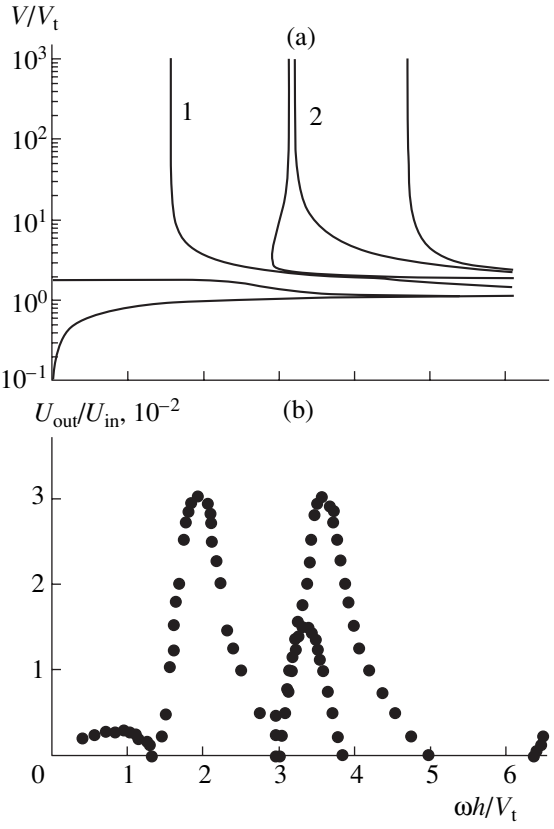

Fig. 4. Same as in Fig. 2 for modes in the *ZY*-cut plates.

electrically inactive transverse waves (displacement along the *x* axis) and Lamb waves (displacement along the *y* and *z* axes). For the *ZY* cut, as for the *YZ* cut, the solution is the superposition of piezoelectrically inactive transverse waves (displacement along the *x* axis) and Lamb waves causing displacements along the *y* and *z* axes.

Note that the positive slope of the dispersion curve, which is observed in a number of curves in Figs. 2a–4a near the frequency where a mode originates, indicate that this mode is a backward wave with oppositely directed phase and group velocities [11].

2.2. Phase relationships for the displacement components on the surface of $LiNbO_3$ plates. Consider by way of example the amplitude and phase relationships between the displacement components on the surface of the *YZ*-cut plate. For Lamb waves, the component u_x is zero and Eq. (7) yields relationships for the displacement components u_y and u_z:

$$\begin{aligned} u_y &= |u_y| \exp(i(\omega t + \phi_y)), \\ u_z &= |u_z| \exp(i(\omega t + \phi_z)), \end{aligned} \tag{12}$$

where $|u_y|$ is the magnitude of the displacement along the *y* axis and ϕ_y is the initial phase.

The quantities $|u_z|$ and ϕ_z have the same meaning. The real part of (12) defines the displacement vector on the surface. Let $\Delta\phi = \phi_z - \phi_y$ be the phase shift between the displacement components u_z and u_y. Then,

$$\begin{aligned} \mathrm{Re}u_y &= |u_y| \cos(\omega t), \\ \mathrm{Re}u_z &= |u_z| \cos(\omega t + \Delta\phi). \end{aligned} \tag{13}$$

Formulas (13) constitute the parametric equation of an ellipse. Therefore, at any point on the surface, the end of the displacement vector describes an ellipse for the time $T = 2\pi/\omega$. The sense of rotation of the displacement vector depends on the phase shift $\Delta\phi$ between the displacement components. When $-\pi < \Delta\phi < 0$, the vector rotates counterclockwise. When $0 < \Delta\phi < \pi$, the rotation is reverse.

The phase relationships between the displacement components for all three cuts are graphically illustrated in Figs. 5–7. These relationships are seen to depend significantly on the type of mode excited and on the direction of a cut. For example, changeover from mode 1 (curve 1 in Fig. 6) to mode 2 (curve 2) in the *YZ*-cut plate decreases markedly the surface displacement component u_z because of an increase in the component u_y. As a consequence, the relationship between the tangential and normal components of the force acting on

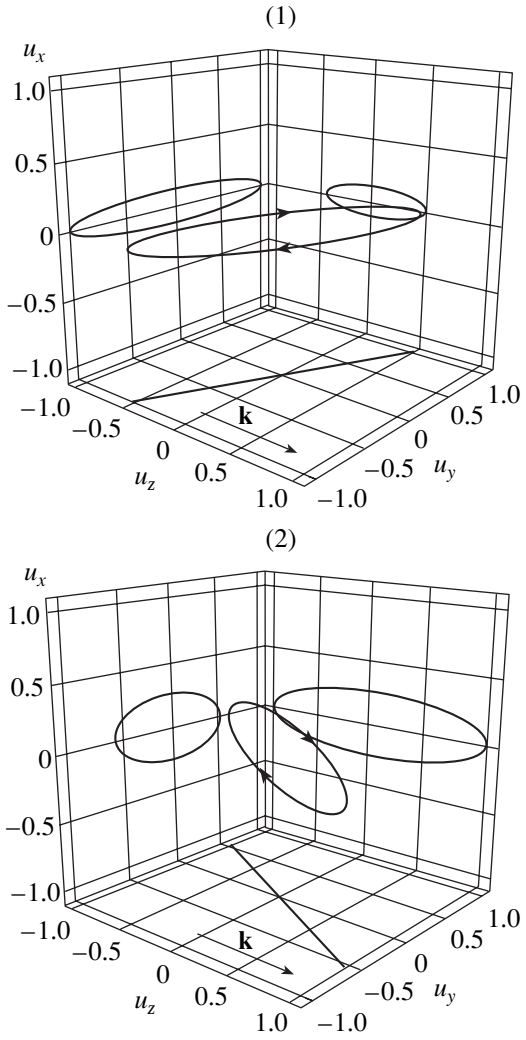

Fig. 5. Elliptic trajectories of the particles on the surface of the *XZ*-cut $LiNbO_3$ plate and their projections onto three mutually orthogonal planes when modes 1 and 2 (Fig. 2) are excited. The arrows show the directions of particle motion.

objects to be transferred over the surface changes. In addition, the rotation of the resultant displacement vector, being initially clockwise (Fig. 6, curve 1), becomes counterclockwise (curve 2). Moreover, mode 2 in Fig. 3a is a backward wave. The last two facts imply that backward (with respect to the vector **k**) displacements of the objects will prevail when the engine operates using mode 2 (in comparison with mode-1 operation). It is also expected that backward displacements will prevail when the engine with the *YZ* cut operates using mode 2 compared with the case when the engine has the *ZY* cut and operates on the same mode. For the latter, the modes excited (1 and 2 in Fig. 4a) are forward waves and the resultant displacement vector rotates clockwise (Fig. 7). The dependences found above were checked experimentally.

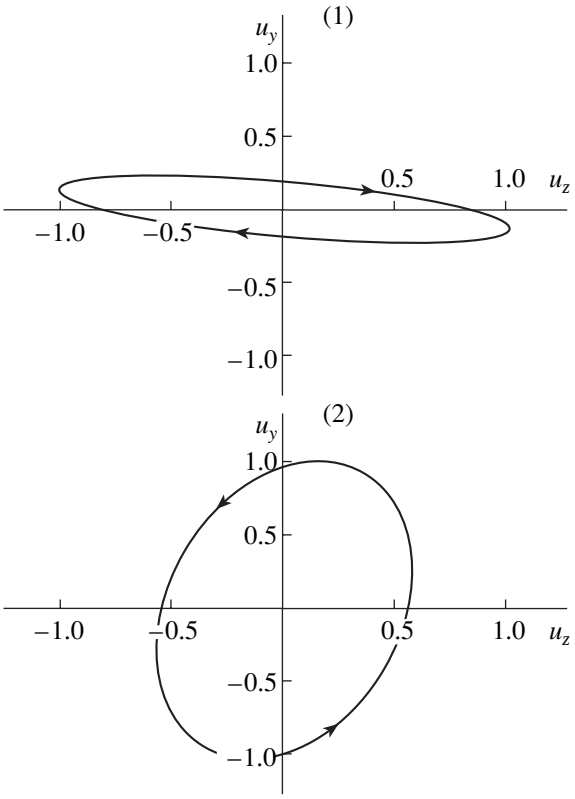

Fig. 6. Elliptic trajectories of the particles on the surface of the *YZ*-cut plate for modes 1 and 2 in Fig. 3. The arrows show the directions of particle motion.

3. EXPERIMENTAL TECHNIQUE

In experiments, we studied the excitation efficiency for various modes and the performance of the engine operating using modes 1 and 2 excited in the *XZ*-, *YZ*-, and *ZY*-cut $LiNbO_3$ plates. The plates were 210 to 1010 μm thick and 1 to 4 cm long. Two identical ≈0.5-mm-thick electrodes (*2*, *3* in Fig. 1a) were applied to the upper surface of the $LiNbO_3$ plate (*1* in Fig. 1). The $LiNbO_3$ plate resided freely on grounded metal surface *4*. The input electric voltage U_{in}, which excited ultrasonic waves, was applied between electrode *2* and the metal surface. Electrode *3* was used to detect the waves excited. The signal U_{out} picked up from electrode *3* was displayed on an oscilloscope. Radio-frequency pulses applied to the electrodes were approximately 5 μs wide. The frequency was varied in the range 1–17 MHz. We studied the signal amplitude U_{out} on the output electrode versus the frequency of the input signal, with its amplitude U_{in} being constant.

The efficiency of the engine and the validity of our theoretical results were checked by placing ZnS microparticles on the $LiNbO_3$ plates under study. The microparticles were approximately 13 μm in diameter, and their weight was $\approx 5 \times 10^{-9}$ g (*5*, *6* in Fig. 1a). When the voltage U_{in} was increased, the microparticles on the surface execute a jerky motion (shown by arrows *5* and *6*

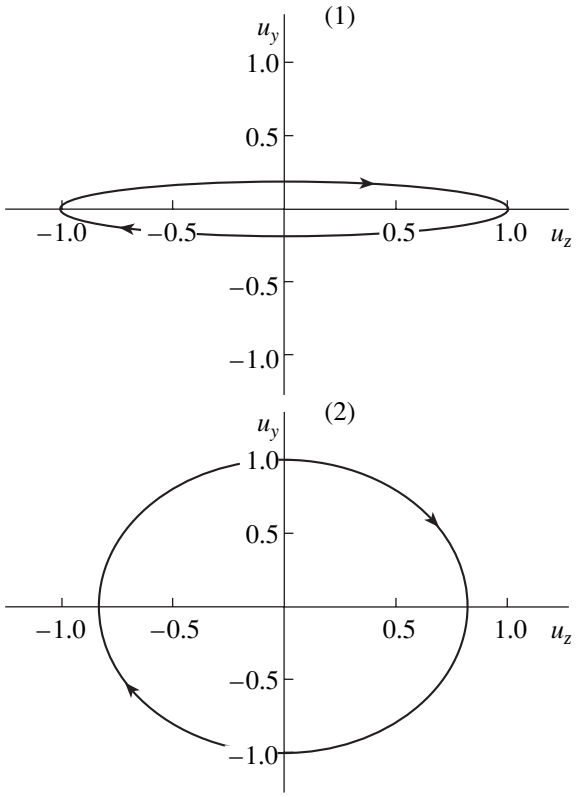

Fig. 7. Elliptic trajectories of the particles on the surface of the *ZY*-cut plate for modes 1 and 2 in Fig. 4. The arrows show the directions of particle motion.

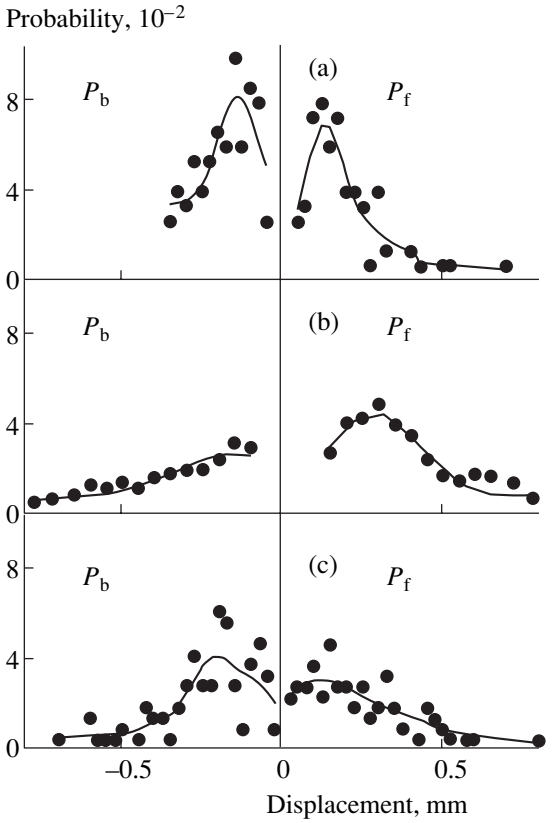

Fig. 8. Probabilities of forward, P_f, and backward, P_b, displacements of ZnS particles placed on the surface of the (a) *XZ*-, (b) *ZY*-, and (c) *YZ*-cut $LiNbO_3$ plates: (a) mode 2 in Fig. 2a, (b) mode 2 in Fig. 4a, and (c) mode 2 in Fig. 3a. The applied voltage is U_{in} = 55 V.

in Fig. 1a) in all directions with respect to the wavevector **k**. This may be due to the limited dimensions of the plate and the curved (nonplanar) phase front. Jerks were observed both visually (under an optical microscope) and by photographing the surface at regular time intervals (Fig. 1b). It was found that the displacement distribution has maxima in the direction of wave propagation and in the opposite direction, while the number of jerks perpendicular to the vector **k** is negligible. The amplitudes of these maxima depend on both the cut and the type of the mode excited in the plate. Below, we will consider the probability distributions for displacements in the direction of the wavevector **k** (forward direction), $P_f = N_f/N$, and in the opposite (backward) direction, $P_b = N_b/N$, versus the displacement. Here, N_f and N_b are the numbers of jerks in the direction of **k** and in the opposite direction, respectively, and N is the total number of jerks (which was typically about 200).

4. COMPARISON OF EXPERIMENTAL AND THEORETICAL RESULTS

The results for the excitation efficiency of various modes in the plates are presented in Figs. 2b–4b. They show that the configuration of the transducer electrodes that was adopted in the experiment excites most efficiently modes 1 and 2 indicated in Figs. 2a–4a. The zeroth-order symmetric mode is also fairly intense [13].

The most intense modes specify the operating frequency of the engine; therefore, the amplitude and phase relationships between the displacement components (Figs. 5–7) were calculated only for these modes. It should be noted that the displacement components in each of the plots in Figs. 5–7 are normalized to their maximum value. Proportions between the resultant amplitudes of different modes excited in variously cut plates can be approximated by proportions between the maximal intensities of the modes in Figs. 2b–4b.

From Figs. 5–7, it follows that, in the ultrasonic engine based on the *XZ*-cut $LiNbO_3$ plate, displacements in the direction of the wavevector **k** are bound to prevail over displacements in the –**k** direction. Also, in the plate thus cut, the number of jerks sideways relative to the **k** vector is bound to be greater than in the *YZ*- and *ZY*-cut plates (because $u_x \neq 0$ in Fig. 5). Such is indeed the case in the experiment. Figure 8a shows the probabilities P_f and P_b (for forward and backward displacements), and P_f is seen to be really much greater than P_b in the *XZ*-cut plates.

In the *ZY*-cut plates, the jumps of the microparticles in the direction of –**k** are longer (Fig. 8b), suggesting that in Fig. 7 the fraction of displacements that are normal to the surface is greater than that in Fig. 5. As a consequence, the oscillating tangential component of the force acting on the microparticles causes their effective backward motion as shown in Fig. 8b.

Finally, when backward mode 2 (Fig. 3a) is excited in the *YZ*-cut plate, the backward motion probability P_b is greater than the probability of forward motion, P_f (Fig. 8c). This result fully agrees with the theoretical predictions in Sect. 2.2.

CONCLUSIONS

Our theoretical dispersion curves and phase relationships for the particle displacement components on *XZ*-, *YZ*-, and *ZY*-cut $LiNbO_3$ plates may serve as a basis for designing an ultrasonic-wave engine. The ZnS particle displacements produced by ultrasonic waves qualitatively agree with theoretical predictions.

REFERENCES

1. L. S. Fan, Y. C. Tai, and R. S. Muller, Sens. Actuators **20**, 41 (1989).
2. W. S. N. Trimmer and R. Jebens, Sens. Actuators **20**, 17 (1989).
3. K. Nakamura, H. Ogura, S. Maeda, *et al.*, in *Proceedings of the 8th IEEE International Workshop on Micro-Electro-Mechanical Systems, Amsterdam, 1995*, pp. 374–379.
4. T. Akaki and M. Okabe, in *Proceedings of the 8th IEEE International Workshop on Micro-Electro-Mechanical Systems, Amsterdam, 1996*, p. 244.
5. P. Gravesen, J. Branebjerg, and O. Jensen, J. Micromech. Microeng. **3** (4), 168 (1993).
6. R. M. Moroney, R. M. White, and R. T. Howe, Appl. Phys. Lett. **59**, 774 (1991).
7. A. N. Gorb and O. A. Korotchenkov, Pis'ma Zh. Tekh. Fiz. **28** (17), 67 (2002) [Tech. Phys. Lett. **28**, 740 (2002)].
8. A. B. Nadtochii, O. A. Korotchenkov, and H. G. Grimmeiss, Phys. Rev. B **67**, 125301 (2003).
9. T. Takano and Y. Tomikawa, Jpn. J. Appl. Phys. **28**, 164 (1989).
10. S. Y. He, W. S. Chen, and Z. L. Chen, IEEE Trans. Ultrason. Ferroelectr. Freq. Control **45**, 1133 (1998).
11. I. Tolstoy and E. Usdin, J. Acoust. Soc. Am. **29**, 37 (1957).
12. *Acoustic Crystals*, Ed. by M. P. Shaskol'skaya (Nauka, Moscow, 1982) [in Russian].
13. S. G. Joshi and Y. Jin, J. Appl. Phys. **70**, 4113 (1991).

Translated by A. Khzmalyan

Technical Physics, Vol. 49, No. 4, 2004, pp. 454–458. Translated from Zhurnal Tekhnicheskoĭ Fiziki, Vol. 74, No. 4, 2004, pp. 77–81.

ACOUSTICS, ACOUSTOELECTRONICS

Evolution of Compression–Tension Acoustic Pulses Generated by Intense Nanosecond Electron Beams in a Solid

V. I. Bykov, D. I. Vaisburd, M. I. Chebodaev, and A. V. Chernov

Tomsk Polytechnical University, pr. Lenina 30, Tomsk, 634050 Russia

e-mail: vaisburd@nlp.dfe.tpu.edu.ru

Received July 28, 2003

Abstract—This paper pursues the study of compression–tension acoustic pulses generated by nanosecond electron beams in a solid. In previous works, where the behavior of the acoustic pulses in the near wave zone is analyzed, the pulse shape is defined by the absorbed beam energy distribution. In this work, the evolution of acoustic pulses traveling large distances in thick samples and experiencing multiple reflections in thin samples is studied for the first time. It is demonstrated that diffraction is the basic factor governing the pulse shape.

INTRODUCTION

Studies of nonstationary acoustic fields generated by ionizing radiation in solids dates back to the 1950s. Before 1966, only low-intensity electron beams were used to excite sound. The pioneering investigation of acoustic pulses generated by high-current electron beams was made in [1, 2]. The test sample was irradiated throughout the surface by a uniform (over the cross section) beam. The duration τ_p of the radiation pulse was much less than the acoustic pulse duration R_e/V_l, where R_e is the mean path of electrons and V_l is the longitudinal sound velocity in the sample. In this case, one can assume that the energy deposition into the sample is instantaneous (the approximation of instantaneous energy delivery). The surface displacement was measured in absolute units using a laser interferometer. The measured time dependence of the displacement is adequately described by the one-dimensional wave equation of thermoelasticity, a solution to which is a plane wave. Early direct measurements of acoustic stresses generated by a high-current electron beam were carried out at the Nonlinear Physics Laboratory at the Tomsk Polytechnical University [3]. Acoustic waves were measured with piezoelectric transducers. Intense acoustic waves of the second type, i.e., those generated by a dense electron beam in a solid plate (bending waves), were first detected and studied in [4]. It was demonstrated that stresses associated with bending waves are comparable to those of a longitudinal pulse, while the surface displacement amplitude may be three orders of magnitude greater. The conditions under which longitudinal compression–tension pulses and intense bending waves are observed simultaneously were found.

Most of the previous studies of longitudinal waves dealt with pulses whose path in the sample is slightly greater than their spatial extent. In this work, we analyze the evolution of a compression–tension acoustic pulse that travels a distance much greater than the beam path.

EXPERIMENTAL

Figure 1 demonstrates the setup used to detect acoustic fields excited by nanosecond electron beams.

An electron beam generated by accelerator *1* is incident on sample *3*, which is attached to the housing of the interferometer and serves as a mirror in its measuring arm. The interaction of the electron beam with the sample causes its nonuniform heating and generates thermoelastic stresses, which cause a strain propagating as an acoustic pulse. The displacement of the back surface of the sample is detected with an optical system consisting of helium–neon laser *4*, Michelson interfer-

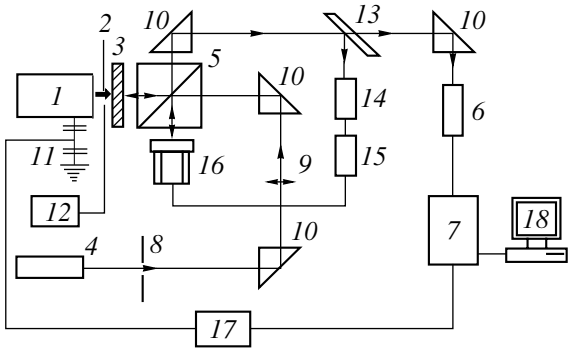

Fig. 1. Block diagram of the setup: (*1*) high-current electron accelerator, (*2*) collimator, (*3*) sample, (*4*) LGN-224 laser, (*5*) interferometer, (*6*) photodetector, (*7*) oscilloscope, (*8*) diaphragm, (*9*) lens, (*10*) rotary prism, (*11*) capacitive divider, (*12*) galvanometer, (*13*) glass plate, (*14*) automatic tuning photodetector, (*15*) automatic tuning amplifier, (*16*) piezoceramic transducer, (*17*) attenuator, and (*18*) personal computer.

ometer *5*, photodetector *6*, and oscilloscope *7*. The Michelson interferometer and the sample are placed in an experimental vacuum chamber. Photodetector *6* measures the intensity variation in the interference pattern when the surface of the sample is displaced. The electric signal amplified by a wide-band amplifier is applied to TDS3000B storage oscilloscope *7* interfaced with computer *18* (for a detailed description of the setup, see [5]).

A DZhIN small-size high-current accelerator serves as a source of electrons. The electron energy is no greater than 0.35 MeV, the pulse duration ranges from 5 to 30 ns, and the current density is within 0.1–1000 A/cm^2. The beam diameter is varied from 1.5 to 12 mm using a collimator. The samples were made of metals (copper and D16T aluminum alloy) and semiconductors (silicon and germanium) in the form of one-side-polished circular plates with a diameter of 8–62 mm and a thickness of 1–50 mm. Nonlinear optical elements based on beta barium borate (BBB) and potassium dihydrophosphate (PDP) crystals had the form of parallelepipeds measuring $12 \times 11 \times 6.45$ and $20.6 \times 20.6 \times 20.6$ mm, respectively. The back sides of the elements were coated by reflecting layers.

EXPERIMENTAL RESULTS

Figures 2 and 3 show the displacements of the back side of the samples irradiated by electron pulses. The curve was obtained by processing the interferograms. The pattern displays a series of longitudinal displacement pulses: the primary pulse and its reflections (echo pulses). Zero time corresponds to the time of beam injection into the target.

Comparing the primary acoustic signal with its echo pulses, one can see that the former changes the shape when propagating (Fig. 2). The initially unipolar displacement pulse becomes bipolar and symmetric (i.e., is differentiated), and its duration increases. Experiments show that the effect of differentiation is universal, showing up in various materials (Figs. 2–4). The time taken for the bipolar pulse to become perfectly symmetric depends on the longitudinal sound velocity and the size of the zone irradiated. This suggests that the phenomenon under consideration is of a 3D (diffraction) nature. The most illustrative are experiments with single crystals, in which the sound attenuation is low. Figure 4 shows a displacement pulse and its echo pulses experimentally observed in silicon. The scatter of the beam fluence is no greater than 10%, which provides a high reproducibility of the interferograms. Appropriately selecting the oscilloscope delay, we observed the detailed image of both the primary longitudinal acoustic pulse and its echo pulses.

WAVE EQUATION

The propagation of an acoustic pulse induced by a dense nanosecond electron beam (Fig. 5) is well

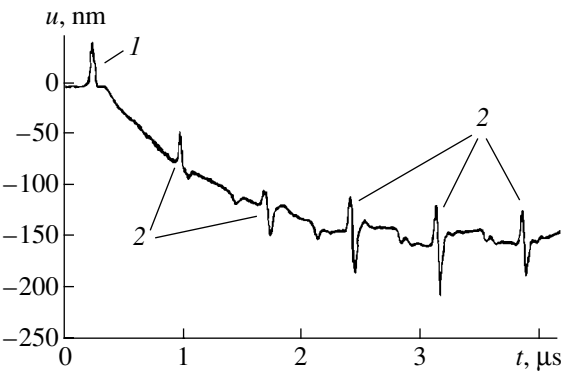

Fig. 2. Displacement of the back surface of the 2.35-mm-thick D16T aluminum alloy sample with a diameter of 29 mm. The collimator radius is 3.5 mm, and the electron fluence is 4.5×10^{12} cm^{-2} per pulse. (*1*) Primary longitudinal pulse and (*2*) a series of echo pulses.

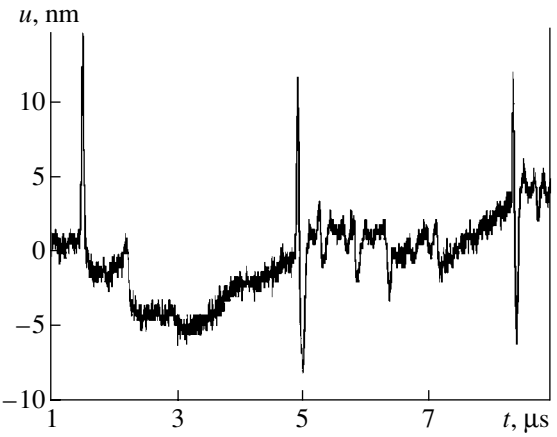

Fig. 3. Displacement of the back surface of the 9.70-mm-thick BBB crystal for a collimator radius of 2.5 mm and an electron fluence of 1.1×10^{13} cm^{-2} per pulse.

described by the one-dimensional equation of thermoelasticity if the distance h from the surface irradiated to the point of observation is comparable to the distance the electron beam travels in the target. An increase in the distance h leads to a significant discrepancy between the analytical acoustic fields and those found experimentally, so that the complete set of the equations of thermoelasticity should be analyzed.

Since the collimator diameter is much less than the target diameter and the target thickness is much greater than the beam penetration depth, we consider the infinite half-space $x > 0$. The acoustic pulse formation time is much shorter than the time of temperature relaxation. Therefore, the thermal conductivity entering into the equation is set equal to zero. The assumption that acoustic pulse propagation is an adiabatic process leads us to the coupled problem of thermoelasticity. Then, for an isotropic medium, the equation of thermoelasticity written in terms of the scalar potential and the trans-

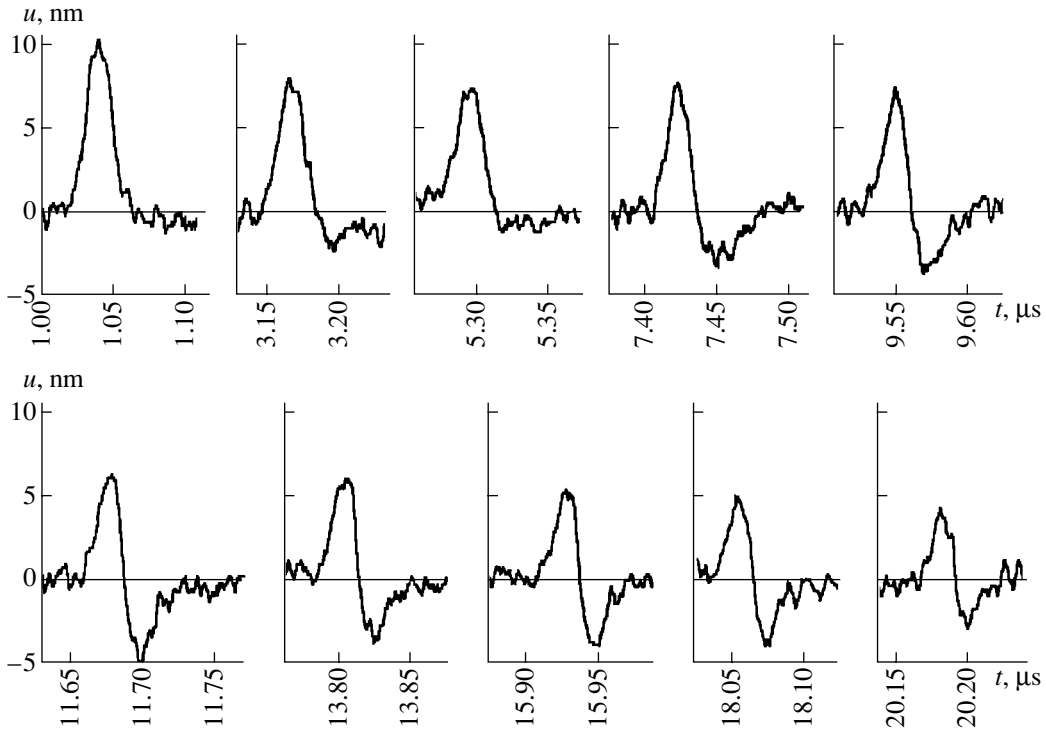

Fig. 4. Evolution of the acoustic displacement pulse for the (111) back surface of the 9.9-mm-thick silicon sample with a diameter of 29 mm at a collimator radius of 3.5 mm and an electron fluence of 2.75×10^{13} cm^{-2} per pulse.

verse component of the displacement has the form [6]

$$\begin{cases} \ddot{\Phi} - V_\mathrm{l}^2 \Delta\Phi = -\Gamma W \\ \ddot{\mathbf{u}}^{(\mathrm{t})} - V_\mathrm{t}^2 \Delta \mathbf{u}^{(\mathrm{t})} = 0. \end{cases} \quad (1)$$

Here, Φ is the scalar potential, $\mathbf{u}^{(\mathrm{t})}$ is the transverse component of the displacement vector, V_l and V_t are the velocities of the longitudinal and transverse acoustic waves, Δ is the Laplacian, Γ is the Grüneisen parameter,

$$W(\mathbf{r}, t) = \int_0^t d\tau M_\mathrm{d}(\mathbf{r}, \tau),$$

and $M_d(\mathbf{r}, t)$ is the absorbed dose rate.

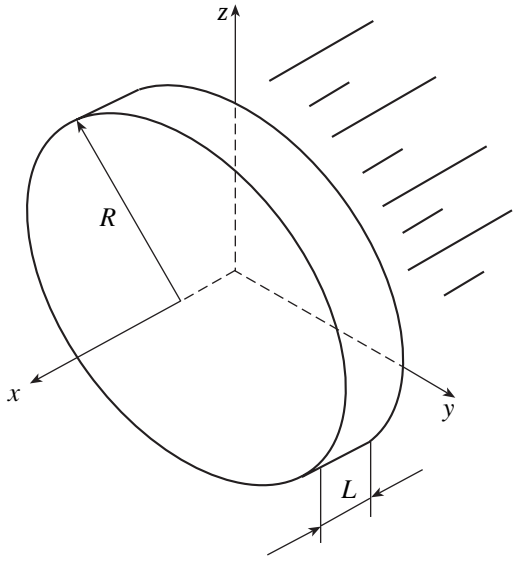

Fig. 5. Sample irradiation geometry.

At zero time, the sample is at rest (undeformed). The initial conditions are given by

$$\begin{cases} \Phi(\mathbf{r}, 0) = 0 \\ \dot{\Phi}(\mathbf{r}, 0) = 0, \end{cases} \quad \begin{cases} \mathbf{u}^{(\mathrm{t})}(\mathbf{r}, 0) = 0 \\ \dot{\mathbf{u}}^{(\mathrm{t})}(\mathbf{r}, 0) = 0. \end{cases} \quad (2)$$

The normal components of the stress tensor at the boundary equal zero, since the boundary is free. The boundary conditions at $x = 0$ have the form

$$\begin{cases} V_\mathrm{l}^2 u_{x,x} + (V_\mathrm{l}^2 + 2V_\mathrm{t}^2)(u_{y,y} + u_{z,z}) = \Gamma W \\ u_{x,y} + u_{y,x} = 0 \\ u_{x,z} + u_{z,x} = 0, \end{cases} \quad (3)$$

where $u_i = u_i^{(\mathrm{l})} + u_i^{(\mathrm{t})}$, $u_{ik} = \partial u_i / \partial x_k$, and $u_i^{(\mathrm{t})}$ is an ith component of the transverse component of the displacement vector.

The transverse component of displacements does not have a source and is due to the reflection of the longitudinal component of the displacement wave from the

boundary; hence, it is small and may be neglected. Since the mean magnitude of the absorbed dose rate gradient along the x axis is much greater than the mean magnitude of this gradient in the transverse direction, it follows from the first equation of system (1) that $u_x \gg u_y \approx u_z$.

Estimating the mean values of the second-order partial derivatives of the absorbed dose rate yields relationships for the derivatives of the longitudinal displacement pulse:

$$u_{x,x} \gg u_{x,y} \approx u_{x,z} \approx u_{y,x} \approx u_{z,x}$$
$$\gg u_{y,y} \approx u_{z,z} \approx u_{y,z} \approx u_{z,y}.$$

Finally, system of equations (1) is reduced to a single equation for the x component of longitudinal displacements:

$$\ddot{u} - V^2\Delta u = -\Gamma\partial W/\partial x, \quad (4)$$

where $u \equiv u_x^{(1)}$ and $V \equiv V_l$.

At $x = 0$, the boundary condition for the x component of longitudinal displacements is written as

$$\lim_{x\to 0}\left(\frac{\partial u(x,y,z,t)}{\partial x} - \frac{\Gamma}{V^2}W(x,y,z,t)\right) = 0. \quad (5)$$

The boundary-value problem given by (4) and (5) with the zero initial conditions can be replaced by the equivalent Cauchy problem with the zero initial conditions:

$$\ddot{u} - V^2\Delta u = -\Gamma\partial \tilde{W}/\partial x, \quad (6)$$

where $\tilde{W}$ is the antisymmetric extension of the function W into the left-hand half-space $x < 0$.

The solution to Eq. (6) with the zero initial conditions is known to have the form of a retarded potential:

$$u(\mathbf{r},t) = -\frac{\Gamma}{4\pi V^2}\frac{\partial}{\partial x}\int_{R^3} d\mathbf{r}'\frac{\tilde{W}(\mathbf{r}', t - V^{-1}|\mathbf{r}' - \mathbf{r}|)}{|\mathbf{r}' - \mathbf{r}|}. \quad (7)$$

ANALYSIS OF THE SOLUTION TO THE WAVE EQUATION

Let us analyze a solution to the wave equation for an acoustic displacement pulse at the symmetry axis of the system, $y = z = 0$, with the specific form of the absorbed dose rate function known. For a nanosecond electron beam, the absorbed dose rate can be represented as the product of the time-dependent longitudinal, $D(x, t)$, and transverse distributions of the dose. If the beam is homogeneous, the dose transverse distribution is well approximated by the Heaviside theta function $\theta(R - \rho)$, where R is the collimator radius and $\rho^2 = y^2 + z^2$. In this case, the absorbed dose rate is given by

$$M_d(x,y,z,t) = D(x,t)\theta(R - \rho). \quad (8)$$

In the near wave zone ($Vt < R$), the displacement is written as

$$u(x,t) = -\frac{\Gamma}{2V^2}\left[\int_{x-Vt}^{x} d\xi w\left(\xi, t - \frac{x-\xi}{V}\right) - \int_{x}^{x+Vt} d\xi w\left(\xi, t + \frac{x-\xi}{V}\right)\right], \quad (9)$$

where

$$w = \int_0^t D(x,\tau)d\tau.$$

Solution (10) coincides with the Zaker solution [7] to the one-dimensional wave equation (see, for example, [1]), which describes the propagation of acoustic signals in thin samples. For the far wave zone ($V \cdot t \gg R$), we have

$$u(x,t) = -\frac{\Gamma R}{4V^3}\frac{\partial}{\partial t}\left[\int_{x-Vt}^{x} d\xi w - \left(\xi, t - \frac{x-\xi}{V}\right) - \int_{x}^{x+Vt} d\xi w\left(\xi, t + \frac{x-\xi}{V}\right)\right]. \quad (10)$$

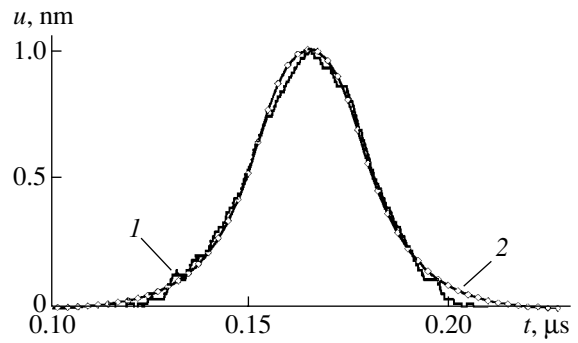

Fig. 6. (*1*) Measured and (*2*) calculated acoustic displacement pulses in the near wave zone for the 0.99-mm-thick D16T sample for a collimator radius of 3.5 mm.

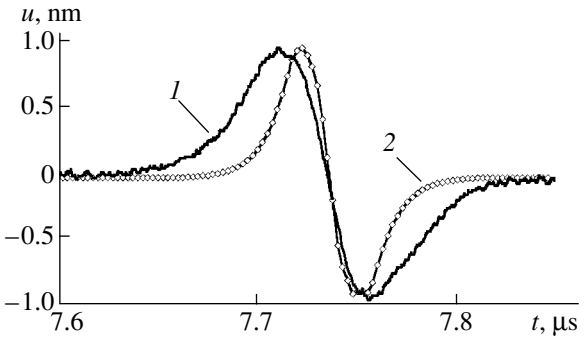

Fig. 7. (*1*) Measured and (*2*) calculated acoustic displacement pulses in the far wave zone for the 49.50-mm-thick D16T sample for a collimator radius of 3.5 mm.

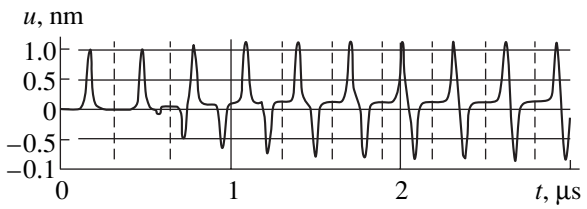

Fig. 8. Calculated evolution of the acoustic pulse for the back surface displacement in the case of the 1.0-mm-thick D16T sample for a collimator radius of 3.5 mm.

From expressions (9) and (10), it follows that the signal in the far wave zone is its derivative in the near wave zone.

EVOLUTION OF AN ACOUSTIC DISPLACEMENT PULSE

Computer simulation of an acoustic displacement pulse was based on formula (7) at the symmetry axis of the region irradiated. The absorbed dose rate $D(x, t)$ from (8) is given by

$$D(x, t) = D(x) \cdot f(t).$$

Here, $D(x)$ is the dose longitudinal distribution calculated by the procedure from [8] and $f(t)$ is the irradiating pulse taken in the form $f(t) = \theta(\tau_p - t)$, where $\tau_p = 25$ ns is the irradiating pulse duration.

Figures 6 and 7 demonstrate fairly good agreement between the experimental and computed data.

In contrast to the diffraction equation [9–11], expression (7) makes it possible to trace the evolution of an initially unipolar (in the near wave zone) acoustic displacement pulse to a bipolar signal in the far wave zone (Fig. 8). However, the model proposed ignores the acoustic wave attenuation in the sample and cannot explain the increase in the longitudinal pulse duration observed experimentally.

ACKNOWLEDGMENTS

This work was supported by INTAS (grant no. 01-458).

REFERENCES

1. R. B. Oswald, IEEE Trans. Nucl. Sci. **13** (6), 63 (1966).
2. R. B. Oswald, F. B. McLean, D. R. Schallhorn, and L. D. Buxton, J. Appl. Phys. **42**, 3463 (1971).
3. A. A. Bespal'ko and G. I. Gering, Pis'ma Zh. Tekh. Fiz. **3** (4), 152 (1977) [Sov. Tech. Phys. Lett. **3**, 373 (1977)].
4. A. L. Bardenshteĭn, V. I. Bykov, and D. I. Vaisburd, Pis'ma Zh. Éksp. Teor. Fiz. **61** (2), 96 (1995) [JETP Lett. **61**, 100 (1995)].
5. A. A. Bespal'ko and V. I. Bykov, Izv. Vyssh. Uchebn. Zaved. Fiz., No. 1, 82 (1997).
6. V. Novatskiĭ, *Dynamic Problems of Thermoelasticity* (Nauka, Moscow, 1970) [in Russian].
7. T. A. Zaker, J. Appl. Mech. **86**, 143 (1965).
8. T. Tabata and R. Ito, Nucl. Sci. Eng. **52**, 226 (1974).
9. V. E. Gusev and A. A. Karabutov, *Laser Optoacoustics* (Nauka, Moscow, 1991) [in Russian].
10. V. I. Bykov, M. I. Chebodaev, and A. V. Chernov, in *Proceedings of the 1st International Congress on Radiation Physics, High Current Electronics and Modification of Materials, Tomsk, 2000*, Vol. 1; in *Proceedings of the 11th International Conference on Radiation Physics and Chemistry of Condensed Matter, Tomsk, 2000* (Nauka, Novosibirsk, 2000), pp. 305–310.
11. V. I. Bykov, M. I. Chebodaev, and A. V. Chernov, Izv. Vyssh. Uchebn. Zaved. Fiz., No. 5, 77 (2001).

Translated by A. Chikishev

Technical Physics, Vol. 49, No. 4, 2004, pp. 459–465. Translated from Zhurnal Tekhnicheskoĭ Fiziki, Vol. 74, No. 4, 2004, pp. 82–88.

RADIOPHYSICS

Eigenmodes of an Anisotropic Dielectric Spherical Body

Yu. V. Prokopenko, T. A. Smirnova, and Yu. F. Filippov

Usikov Institute of Radiophysics and Electronics, National Academy of Sciences of Ukraine, Kharkov, 61085 Ukraine
e-mail: prokopen@ire.kharkov.ua

Received August 11, 2003

Abstract—Quasi-TE and quasi-TM oscillations of an anisotropic spherical body immersed in an isotropic medium are studied. An investigation of the set of Maxwell's equations within the spherical body shows that it reduces to two coupled differential equations, which are analyzed theoretically for small values of the anisotropy parameter. An approximate solution to these differential equations is obtained. A dispersion relation determining the frequencies of the resonant oscillations is derived for the boundary conditions imposed on the surface of the spherical body. The effect of anisotropy on the spectral characteristics of the resonant oscillations is examined. © *2004 MAIK "Nauka/Interperiodica".*

INTRODUCTION

At present, dielectric resonators are widely used to investigate physical phenomena occurring in different branches of science and technology. A homogeneous isotropic spherical body can execute two types of independent resonant oscillations, namely, TE oscillations (those for which $E_r = 0$) and TM oscillations (those for which $H_r = 0$) [1, 2]. The parameters of the dielectrics used to fabricate high-quality resonators are inherently anisotropic. The effect of anisotropy on the spectral characteristics of the resonant oscillations must be taken into account in manufacturing integrated circuits intended to operate in the millimeter and submillimeter wavelength ranges. The most widely used uniaxial monocrystals are those of ruby, sapphire, and quartz, which have low dielectric losses. The electric parameters of such crystals are described by the dielectric tensor $\hat{\varepsilon} = \varepsilon_{ik} d_{i,k}$, where $\varepsilon_{xx} = \varepsilon_{yy} = \varepsilon_\perp$ and $\varepsilon_{zz} = \varepsilon_\parallel$ are the tensor components in the directions perpendicular and parallel to the anisotropy axis, respectively, and $\delta_{i,k}$ is the Kronecker index. The resonant oscillations of a uniaxial dielectric spherical body whose fields are independent of the azimuthal coordinate were investigated earlier by Filippov and Eremenko [3, 4]. It is of great interest to generalize the theory to include the dependence of the fields on the azimuthal coordinate. Makkinejad and Ford [5] considered azimuthally nonuniform oscillations in a resonator filled with an anisotropic dielectric medium and bounded by a perfectly conducting spherical surface. They investigated the set of Maxwell's equations by the method of expansion in spherical vector functions and derived two infinite sets of algebraic equations. Solving them numerically, they were only able to calculate the frequencies of the lowest oscillations modes. However, this method does not allow the study of anisotropy-related effects occurring within a spherical body.

SUBJECT OF INVESTIGATION

We consider a spherical body immersed in an isotropic medium with the dielectric permittivity ε_b and magnetic permeability μ_b (Fig. 1). The body material is a uniaxial dielectric with the magnetic permeability μ_d. The spherical body possesses anisotropic properties that are described by the above dielectric tensor $\hat{\varepsilon}$. In spherical coordinates (r, Θ, φ), the components of the dielectric tensor have the form

$$\hat{\varepsilon} = \begin{pmatrix} \varepsilon_{rr} & -\varepsilon_{r\Theta} & 0 \\ -\varepsilon_{r\Theta} & \varepsilon_{\Theta\Theta} & 0 \\ 0 & 0 & \varepsilon_\perp \end{pmatrix}.$$

Here, $\varepsilon_{rr} = \varepsilon_+ + \varepsilon_- \cos 2\Theta$, $\varepsilon_{\Theta\Theta} = \varepsilon_+ - \varepsilon_- \cos 2\Theta$, and $\varepsilon_{r\Theta} = \varepsilon_{\Theta r} = \varepsilon_- \sin 2\Theta$, where $2\varepsilon_\pm = \varepsilon_\parallel \pm \varepsilon_\perp$. The fact that the tensor components depend on the polar coordinate makes

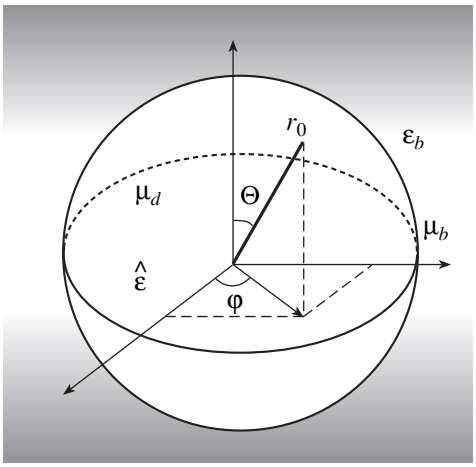

Fig. 1. Spherical dielectric resonator.

1063-7842/04/4904-0459$26.00 © 2004 MAIK "Nauka/Interperiodica"

the solution of the problem about the eigenmodes of a spherical dielectric resonator much more difficult.

THEORY

For electromagnetic oscillations whose amplitudes depend on time as $\exp(-i\omega t)$, we introduce the functions U^H and U^E through the relationships

$$H_r = l_x l_\Theta U^H; \quad E_r = l_x l_\Theta U^E.$$

Here, $l_x = \varepsilon_\perp k^2 + \partial^2/\partial r^2$ and $l_\Theta = \varepsilon_{\Theta\Theta} k^2 + \partial^2/\partial r^2$, where $k = \omega/c$, with ω being the complex eigenfrequency, and c, the speed of light.

It is easy to show that an arbitrary function Ψ satisfies the identities

$$l_\Theta\left(\varepsilon_{r\Theta}\mu k^2 r + \frac{\partial^2}{\partial r\partial\Theta}\right)\Psi = \left(\varepsilon_{r\Theta}\mu k^2 r + \frac{\partial^2}{\partial r\partial\Theta}\right) l_\Theta\Psi,$$

$$l_\Theta\left[\varepsilon_{\Theta\Theta}\frac{\partial}{\partial\Theta} + \varepsilon_{r\Theta}\left(1 - r\frac{\partial}{\partial r}\right)\right]\Psi = \left[\varepsilon_{\Theta\Theta}\frac{\partial}{\partial\Theta} - \varepsilon_{r\Theta}\frac{\partial}{\partial r}r\right] l_\Theta\Psi.$$

Using these identities, we reduce the set of Maxwell's equations within the spherical body to the following two coupled differential equations for the functions U^H and U^E:

$$\hat{L}_H U^H = 2i\varepsilon_- k\hat{\Lambda}\frac{\partial U^E}{\partial\varphi}, \quad \hat{L}_E U^E = 2i\varepsilon_-\mu_d k\hat{\Lambda}\frac{\partial U^H}{\partial\varphi}, \quad (1)$$

where

$$\hat{L}_H = (\Delta_\perp + r^2 l_x) l_\Theta - 2\varepsilon_-\mu_d k^2\frac{\partial^2}{\partial\varphi^2}, \quad \hat{L}_E = \hat{\Omega}_0 + \frac{\varepsilon_-}{\varepsilon_+}\hat{\Omega} l_x,$$

$$\Delta_\perp = \frac{1}{\sin\Theta}\frac{\partial}{\partial\Theta}\sin\Theta\frac{\partial}{\partial\Theta} + \frac{1}{\sin^2\Theta}\frac{\partial^2}{\partial\varphi^2},$$

$$\hat{\Lambda} = \left(r l_x - 2\frac{\partial}{\partial r}\right)\cos\Theta - \sin\Theta\frac{\partial^2}{\partial\Theta\partial r},$$

$$\hat{\Omega}_0 = \left[\Delta_\perp + r^2\frac{\partial^2}{\partial r^2} + \varepsilon_+\left(1 - \frac{\varepsilon_-^2}{\varepsilon_+^2}\right)\mu_d k^2 r^2\right] l_x + 2\varepsilon_-\left(1 - \frac{\varepsilon_-}{\varepsilon_+}\right)\mu_d k^2\frac{\partial^2}{\partial\varphi^2},$$

$$\hat{\Omega} = \cos 2\Theta\left[r^2\frac{\partial^2}{\partial r^2} - \Delta_\perp + 3\left(1 - r\frac{\partial}{\partial r}\right)\right] + \left(3 - 2r\frac{\partial}{\partial r}\right)\sin 2\Theta\frac{\partial}{\partial\Theta} + 1 - r\frac{\partial}{\partial r} - 2\frac{\partial^2}{\partial\varphi^2}.$$

The tangential components of the fields are expressed in terms of the functions U^E and U^H as follows:

$$rE_\varphi = \frac{l_\Theta}{\sin\Theta}\frac{\partial^2 U^E}{\partial r\partial\varphi} - ik\mu_d\frac{\partial}{\partial\Theta}(l_\Theta U^H),$$

$$rE_\Theta = \frac{ik\mu_d}{\sin\Theta}\frac{\partial}{\partial\varphi}(l_x U^H) + \left(\varepsilon_{r\Theta}\mu_d k^2 r + \frac{\partial^2}{\partial r\partial\Theta}\right) l_x U^E,$$

$$rH_\Theta = \frac{\partial^2}{\partial r\partial\Theta}(l_\Theta U^H) - \frac{ik\varepsilon_{xx}}{\sin\Theta}\frac{\partial}{\partial\varphi}(l_\Theta U^E), \quad (2)$$

$$rH_\varphi = \frac{l_x}{\sin\Theta}\frac{\partial^2 U^H}{\partial r\partial\varphi} + ik\left[\varepsilon_{\Theta\Theta}\frac{\partial}{\partial\Theta} + \varepsilon_{r\Theta}\left(1 - r\frac{\partial}{\partial r}\right)\right] l_x U^E.$$

Equations (1) with zero on the right-hand sides are independent of one another and describe two independent types of azimuthally uniform oscillations. For oscillations whose fields depend on the azimuthal coordinate, Eqs. (1) for the functions U^H and U^E are mutually coupled. We represent the solution to the equations in the form of the expansions

$$U^S(r, \Theta, \varphi) = \sum_p U_p^S(r, \Theta, \varphi) = \sum_p R_p^S(r) Y_{n,m}(\Theta, \varphi), \quad (3)$$

where the superscript S stands for E or H and the subscript p runs through the three parameters n, m, and s. The functions $Y_{n,m}(\Theta, \varphi) = P_n^m(\cos\Theta)\exp(im\varphi)$ are the eigenfunctions of the operator $\Delta_\perp$. Here, $P_n^m(\cos\Theta)$ are the associated Legendre functions, which are nonzero for azimuthal indices such that $m \le n$ and, as functions of the polar coordinate, have $n - m$ zeros [6]. The polar index n determines the number of field oscillations over the polar coordinate Θ for azimuthally uniform modes (those with $m = 0$). The azimuthal index m, in turn, characterizes the number of field oscillations over the azimuthal coordinate φ for modes with $m = n$. The radial index s gives the number of field oscillations over the radial coordinate r.

The above eigenfunctions satisfy the functional relationships [7]

$$\sin\Theta\frac{\partial Y_{n,m}(\Theta, \varphi)}{\partial\Theta} = f_n[n(n - m + 1)Y_{n+1,m}(\Theta, \varphi) - (n + 1)(n + m)Y_{n-1,m}(\Theta, \varphi)],$$
$$\cos\Theta Y_{n,m}(\Theta, \varphi) = f_n[(n - m + 1)Y_{n+1,m}(\Theta, \varphi) + (n + m)Y_{n-1,m}(\Theta, \varphi)], \quad (4)$$

where $f_n = 1/(2n + 1)$.

It can also be shown that

$$\sin 2\Theta \frac{\partial Y_{n,m}(\Theta,\varphi)}{\partial\Theta} = 2f_n[n(n-m+1)(n-m+2)f_{n+1}Y_{n+2,m}(\Theta,\varphi) - (n+1)(n+m)(n+m-1)f_{n-1}Y_{n-2,m}(\Theta,\varphi)] - 2[n(n+1)-3m^2]f_{n+1}f_{n-1}Y_{n,m}(\Theta,\varphi),$$

$$\cos 2\Theta Y_{n,m}(\Theta,\varphi) = f_n[(n-m+1)(n-m+2)f_{n+1}Y_{n+2,m}(\Theta,\varphi) - (n+m)(n+m-1)f_{n-1}Y_{n-2,m}(\Theta,\varphi)] + [2n(n+1)-2m^2-1]f_{n+1}f_{n-1}Y_{n,m}(\Theta,\varphi). \quad (5)$$

Since the dependence of the coefficients in Eqs. (1) on the polar angle changes only the polar index, we will omit the azimuthal and radial indices, *m* and *s*, to save space.

Substituting expansions (3) into Eqs. (1), using relationships (4) and (5), and equating the factors in front of the eigenfunctions $Y_{n,m}(\Theta,\varphi)$, we arrive at the following set of ordinary differential equations for the radial modes $R_n^E(r)$ and $R_n^H(r)$:

$$a_{1,n}^H R_n^H - a_{2,n-2}^H R_{n-2}^H - a_{3,n+2}^H R_{n+2}^H = -2\varepsilon_- mk[b_{1,n-1}R_{n-1}^E - b_{2,n+1}R_{n+1}^E],$$

$$a_{1,n}^E R_n^E - \frac{\varepsilon_-}{\varepsilon_+}(a_{2,n-2}^E R_{n-2}^H + a_{3,n+2}^E R_{n+2}^E) = -2\varepsilon_-\mu_d mk[b_{1,n-1}R_{n-1}^H - b_{2,n+1}R_{n+1}^H]/\varepsilon_+, \quad (6)$$

where

$$a_{1,n}^H = T_n[l_+ - (1-4m^2)g_- f_{n-1}f_{n+1}] + 2g_- m^2,$$

$$T_n = r^2 l_x - n(n+1),$$

$$a_{2,n}^H = 2g_-(n-m+1)(n-m+2)f_n f_{n+1}T_n,$$

$$b_{1,n} = (n-m+1)f_n\left[rl_x - (n+2)\frac{d}{dr}\right],$$

$$a_{3,n}^H = 2g_-(n+m)(n+m-1)f_n f_{n-1}T_n,$$

$$b_{2,n} = (n+m)f_n\left[rl_x + (n-1)\frac{d}{dr}\right],$$

$$a_{1,n}^E = \left\{\left[r^2\frac{d^2}{dr^2} - n(n+1)\right]\times\left[1+\frac{\varepsilon_-}{\varepsilon_+}(1-4m^2)f_{n-1}f_{n+1}\right] + \left(1-\frac{\varepsilon_-^2}{\varepsilon_+^2}\right)g_+ r^2\right\}l_x - 2m^2\left(1-\frac{\varepsilon_-}{\varepsilon_+}\right)g_-,$$

$$a_{2,n}^E = 2f_n f_{n+1}(n-m+1)(n-m+2)\times\left[r^2\frac{d^2}{dr^2} - (2n+3)r\frac{d}{dr} + n(n+1)\right],$$

$$a_{3,n}^E = 2f_n f_{n-1}(n+m)(n+m-1)\times\left[r^2\frac{d^2}{dr^2} + (2n-1)r\frac{d}{dr} + (n+1)(n-3)\right],$$

$$g_\pm = \varepsilon_\pm\mu_d k^2.$$

Because of the dependence of the components of the tensor $\hat{\varepsilon}$ on the polar coordinate, the modes with different polar numbers are mutually coupled to each other. For a nonzero azimuthal index *m* and for arbitrary values of the polar index *n*, it is impossible to obtain an exact solution to Eqs. (6). For ruby, sapphire, and quartz monocrystals, which are widely used in technology, the ratio $\varepsilon_-/\varepsilon_+$ is on the order of 0.1. That is why we will solve Eqs. (6) by the method of expansion in this small parameter.

Zeroth Approximation

We neglect the quantities proportional to $\varepsilon_-/\varepsilon_+$ to obtain the following two independent ordinary differential equations:

$$[l_+ - n(n+1)/r^2]l_+ R_n^S = 0, \quad (7)$$

where the operator has the form

$$l_+ = \frac{d^2}{dr^2} + g_+.$$

Inside the sphere, Eqs. (7) have the solutions $j_\nu(x) = \sqrt{\pi x/2}J_\nu(x)$, and outside the sphere, the solutions are $h_\nu^{(1)}(x) = \sqrt{\pi x/2}H_\nu^{(1)}(x)$. Here, $\nu = n + 1/2$ and $J_\nu(x)$ and $H_\nu^{(1)}(x)$ are the Bessel and Hankel functions of the first kind, respectively. The functions $j_\nu(x)$ and $h_\nu^{(1)}(x)$ satisfy the functional relationship

$$z_\nu'(x) = z_{\nu-1}(x) - \frac{n}{x}z_\nu(x) = \frac{n+1}{x}z_\nu(x) - z_{\nu+1}(x).$$

Here and below, the prime denotes the derivative of the function with respect to its argument.

At the spherical surface $r = r_0$, the tangential components of the fields, E_φ, H_φ, E_Θ, and H_Θ, are continuous. For this to hold, the following four functions should be

continuous at the surface of the spherical body:

$$\varepsilon_j l_+ R^E_{n,j};\quad \mu_j l_+ R^H_{n,j};\quad \frac{dl_+ R^E_{n,j}}{dr};\quad \frac{dl_+ R^H_{n,j}}{dr}, \tag{8}$$

where j runs through d and b. In this case, the set of basic equations (1) splits into independent subsets determining the resonance characteristics of the TE and TM oscillations. Under the continuous conditions for functions (8), we obtain

$$l_+ R^E_n(r) = \begin{cases} j_\nu(x_d r/r_0), & r \le r_0 \\ \dfrac{\varepsilon_b}{\varepsilon_d}\dfrac{j_\nu(x_d)}{h^{(1)}_\nu(x_b)} h^{(1)}_\nu(x_b r/r_0), & r \ge r_0, \end{cases}$$

$$l_+ R^H_n(r) = \begin{cases} j_\nu(x_d r/r_0), & r \le r_0 \\ \dfrac{\mu_b}{\mu_d}\dfrac{j_\nu(x_d)}{h^{(1)}_\nu(x_b)} h^{(1)}_\nu(x_b r/r_0), & r \ge r_0, \end{cases}$$

where $x_d = \sqrt{\varepsilon_+ \mu_d}\, kr_0$ and $x_b = \sqrt{\varepsilon_b \mu_b}\, kr_0$.

The components of the fields of TE oscillations are described by the relationships

$$E^H_r = 0,\quad rE^H_\Theta = \frac{ik\mu_j}{\sin\Theta}\frac{\partial l_+ U^H}{\partial\varphi},\quad rE^H_\varphi = -ik\mu_j\frac{\partial l_+ U^H}{\partial\Theta},$$

$$H^H_r = \frac{n(n+1)}{r^2} l_+ U^H,\quad rH^H_\Theta = -\frac{\partial^2 l_+ U^H}{\partial\Theta\partial r},$$

$$rH^H_\varphi = \frac{1}{\sin\Theta}\frac{\partial^2 l_+ U^H}{\partial\varphi\partial r}.$$

The eigenfrequencies of a ball are determined by the solutions to the dispersion relation

$$\sqrt{\varepsilon_d/\mu_d}\frac{j'_\nu(x_d)}{j_\nu(x_d)} = \sqrt{\varepsilon_b/\mu_b}\frac{h^{(1)}_\nu(x_b)}{h^{(1)}_\nu(x_b)}. \tag{9}$$

For the fields of the TM oscillations, we have

$$H^E_r = 0,\quad rH^E_\Theta = -\frac{ik\varepsilon_j}{\sin\Theta}\frac{\partial l_+ U^E}{\partial\varphi},\quad rH^E_\varphi = ik\varepsilon_j\frac{\partial l_+ U^E}{\partial\Theta},$$

$$E^E_r = \frac{n(n+1)}{r^2} l_+ U^E,\quad rE^E_\Theta = -\frac{\partial^2 l_+ U^E}{\partial\Theta\partial r},$$

$$rE^E_\varphi = \frac{1}{\sin\Theta}\frac{\partial^2 l_+ U^E}{\partial\varphi\partial r}.$$

The corresponding eigenfrequencies are determined from the dispersion relation

$$\sqrt{\mu_d/\varepsilon_d}\frac{j'_\nu(x_d)}{j_\nu(x_d)} = \sqrt{\mu_b/\varepsilon_b}\frac{h^{(1)'}_\nu(x_b)}{h^{(1)}_\nu(x_b)}. \tag{10}$$

To a first approximation, the solutions obtained describe the spectral characteristics of the oscillations of an isotropic spherical body with the dielectric permittivity ε_+. Each polar index n corresponds to $2n + 1$ angular modes $Y_{n,m}(\Theta, \varphi)$. However, dispersion relations (9) and (10) do not contain the azimuthal index m. Consequently, for a given value of the polar index n, $2n + 1$ resonant modes can be excited in an isotropic spherical body at the same frequency, each characterized by its particular dependence on the angular coordinates. We thus see that the oscillation frequency is degenerate, with an associated degeneracy of $2n + 1$. Note that, at a fixed polar number, the result of the azimuthal nonuniformity of the fields is that their distribution over the polar coordinate Θ depends on the azimuthal number m. Let us examine this point in more detail.

The associated Legendre function determines the field distribution over the polar angle Θ and has $n–m$ zeros in the interval $0 < \Theta < \pi$ [6]. For our purposes here, it is more convenient to calculate the Legendre function $P^m_n(\cos\Theta)$ from the series [7]

$$P^m_n(\cos\Theta) = \frac{(n+m)!\sin^m\Theta}{2^m m!(n-m)!}\left\{1 - \frac{(n-m)(n+m+1)}{1!(m+1)} \times\frac{1-\cos\Theta}{2} + \frac{(n-m)(n-m-1)(n+m+1)(n+m+2)}{2!(m+1)(m+2)} \times\left(\frac{1-\cos\Theta}{2}\right)^2 - \ldots\right\}. \tag{11}$$

Figure 2 shows how the parameter

$$\chi \equiv \frac{P^m_3(\cos\Theta)}{P^3_3(\Theta = \pi/2)}$$

depends on the polar angle Θ for the polar index $n = 3$. Since the functions $P^m_3(\cos\Theta)$ with the azimuthal indices $m > 3$ vanish, there can exist the following modes of oscillations of the isotropic spherical body under consideration.

(i) An azimuthally uniform mode with $n = 3$ and $m = 0$. The dependence of the field of this mode on the polar coordinate is determined by the Legendre polynomial $P_n(\cos\Theta) \equiv P^0_n(\cos\Theta)$, which has n zeros in the angular interval $0 < \Theta < \pi$.

(ii) An azimuthal mode with $m = n = 3$. The field of this mode depends on the azimuthal coordinate as $\exp(in\varphi)$ and is symmetric about the polar angle $\Theta = \pi/2$, at which it is maximum. Over the angular interval $0 < \Theta < \pi$, the field of the mode does not vanish and its amplitude is larger than the amplitudes of the fields of

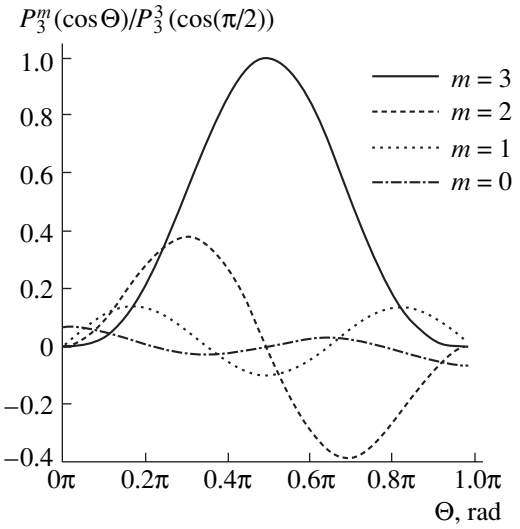

Fig. 2. Normalized Legendre functions vs. polar angle for the polar index $n = 3$ and different azimuthal indices such that $m \le n$.

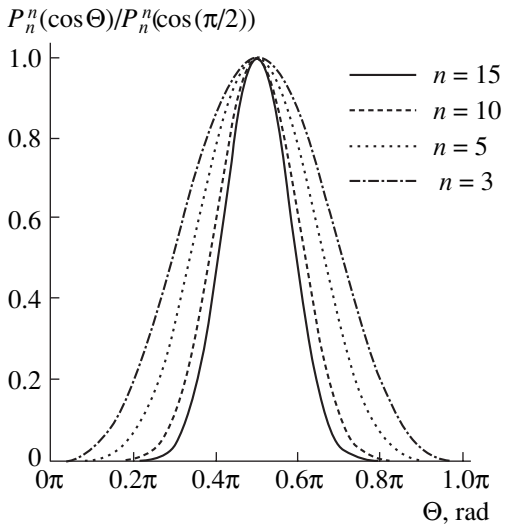

Fig. 3. Normalized Legendre functions vs. polar angle for $m = n$.

the modes with $m \neq n$. For arbitrary values of the polar index, formula (11) yields $P_n^n(\cos\Theta) = (2n - 1)!!\sin^n\Theta$. This oscillation mode was observed experimentally in [8, 9].

(iii) An asymmetric mode with $m = n - 1 = 2$. The field of this mode depends on the azimuthal coordinate as $\exp[i(n - 1)\varphi]$ and is asymmetric about the polar angle $\Theta = \pi/2$, at which it vanishes. For arbitrary values of n, we have $P_m^{n-1}(\cos\Theta) = (2n - 1)!!\sin^{n-1}\Theta\cos\Theta$.

(iv) A symmetric mode with $m = n - 2 = 1$. The field of this mode depends on the azimuthal coordinate as $\exp[i(n - 2)\varphi]$ and is symmetric about the polar angle $\Theta = \pi/2$, at which it has a minimum amplitude. The field amplitude is maximum at $\Theta = \pi/4$. For arbitrary values of n, we have $P_n^{n-2}(\cos\Theta) = (2n - 1)!!\sin^{n-2}\Theta[\cos^2\Theta - 1/(2n - 1)]$.

The distributions of the fields of eigenmodes with different azimuthal numbers and with arbitrary polar numbers over the polar coordinate can be analyzed in a similar way. Note only that the larger the polar number, the narrower the region near the surface of the spherical body where the fields of the oscillation modes are localized. The modes whose fields are maximum at the polar angle $\Theta = \pi/2$ are those with equal polar and azimuthal numbers. The larger the polar number, the larger the magnitude of the field and the narrower the region around this polar angle where the field is concentrated (Fig. 3). Azimuthal oscillations with large polar numbers n are of high quality; they are referred to as oscillations of the "whispering-gallery" type.

The results obtained above are also valid for a hemispherical resonator bounded by a perfectly conducting plane at $\Theta = \pi/2$. In this case, the oscillation frequency, too, is degenerate, with a degeneracy of $n = 1$. The degeneracy is partially lost because there are no TE oscillations for which the sum of m and n is even and no TM oscillations for which this sum is odd.

First Approximation

In Eqs. (6), we neglect the quantities proportional to $(\varepsilon_-/\varepsilon_+)^2$ to obtain

$$\begin{aligned}\alpha_n^H l_+ R_n^H &= -2\varepsilon_-\mu_d mkr[\beta_{1,n} l_+ R_{n-1}^E + \beta_{2,n} l_+ R_{n+1}^E],\\ \alpha_n^E l_+ R_n^E &= -2\varepsilon_- mkr[\beta_{1,n} l_+ R_{n-1}^H + \beta_{2,n} l_+ R_{n+1}^H]/\varepsilon_+,\end{aligned} \tag{12}$$

where

$$\alpha_n^H = \left[r^2\left(\frac{d^2}{dr^2} + \gamma_H^2\right) - n(n+1)\right],$$

$$\alpha_n^E = \left[r^2\left(\frac{d^2}{dr^2} + \gamma_E^2\right) - n(n+1)\right]; \quad l_+ = \frac{d^2}{dr^2} + \varepsilon_+ k^2,$$

$$\beta_{1,n} = (n-m) f_{n-1}\left[r - \frac{n+1}{n(n-1)}\frac{d}{dr}r^2\right],$$

$$\beta_{2,n} = (n+m-1) f_{n+1}\left[r - \frac{n}{(n+1)(n+2)}\frac{d}{dr}r^2\right],$$

$$\gamma_E^2 = 1 - \frac{\varepsilon_-}{\varepsilon_+}\left[(1-4m^2) f_{n-1} f_{n+1} + \frac{2m^2}{n(n+1)}\right],$$

$$\gamma_H^2 = 1 - \frac{\varepsilon_-}{\varepsilon_+}\left(1 - \frac{2m^2}{n(n+1)}\right).$$

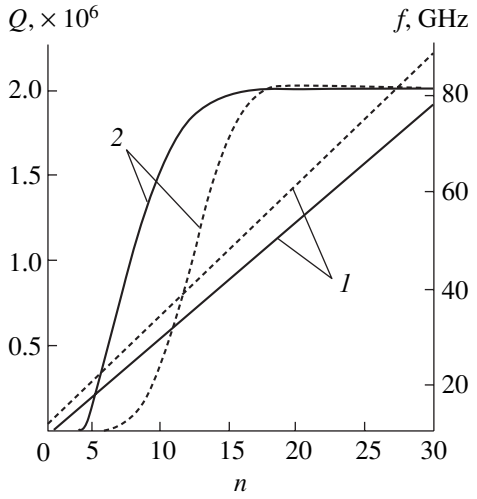

Fig. 4. (*1*) Eigenfrequencies and (*2*) quality factors of the quasi-TE$_{nn1}$ oscillations (solid curves) and quasi-TM$_{nn1}$ oscillations (dashed curves) of a leucosapphire spherical body of radius 0.66 cm.

Because of the anisotropy, the coefficients γ_E and γ_H depend on the azimuthal index m and there exist oscillation modes of the opposite kind with adjacent polar numbers; i.e., the fields of the TE (TM) oscillations have the components that are described by the solutions $R_{n\pm1}^{E(H)}(r)$. The contributions of these solutions to the functions $R_n^{H(E)}(r)$ are proportional to $(\varepsilon_-/\varepsilon_+)^2$ and, in the approximation at hand, can be ignored. As for the solutions to the equations with zero on the right-hand sides, they can be represented in the form $R_n^S(r) = A_n^S j_n(\sqrt{\varepsilon_+\mu_d}\,\gamma_S kr)$.

Using the continuity conditions for the tangential components of the electromagnetic fields at the spherical surface $r = r_0$, we obtain the dispersion relation for quasi-TM oscillations,

$$\frac{\sqrt{\varepsilon_+\mu_d}\gamma_E}{\varepsilon_\perp}\frac{j_n'(\sqrt{\varepsilon_+\mu_d}\gamma_E kr_0)}{j_n(\sqrt{\varepsilon_+\mu_d}\gamma_E kr_0)} = \sqrt{\frac{\mu_b}{\varepsilon_b}}\frac{h_n^{(1)'}(\sqrt{\varepsilon_b\mu_b}kr_0)}{h_n^{(1)}(\sqrt{\varepsilon_b\mu_b}kr_0)}, \quad (13)$$

and the dispersion relation for quasi-TE oscillations,

$$\frac{\sqrt{\varepsilon_+}\gamma_H}{\sqrt{\mu_d}}\frac{j_n'(\sqrt{\varepsilon_+\mu_d}\gamma_H kr_0)}{j_n(\sqrt{\varepsilon_+\mu_d}\gamma_H kr_0)} = \sqrt{\frac{\varepsilon_b}{\mu_b}}\frac{h_n^{(1)'}(\sqrt{\varepsilon_b\mu_b}kr_0)}{h_n^{(1)}(\sqrt{\varepsilon_b\mu_b}kr_0)}. \quad (14)$$

The solutions to these dispersion relations determine the frequencies of the resonant oscillations of a spherical uniaxial crystal immersed in an isotropic medium with the dielectric permittivity ε_b and magnetic permeability μ_b.

The above analysis does not apply to oscillations with large polar numbers $n \gg m$ or with $n \ll 1$. In these cases, the operators on the left-hand sides of ordinary differential equations (12) coincide, and it is necessary to take into account higher order terms in the expansions in the small parameter $\varepsilon_-/\varepsilon_+$. The only azimuthally uniform oscillations that are sensitive to the anisotropy are TM oscillations. In [3], it was shown that azimuthally uniform TM oscillations with large polar numbers split into ordinary and extraordinary modes, which

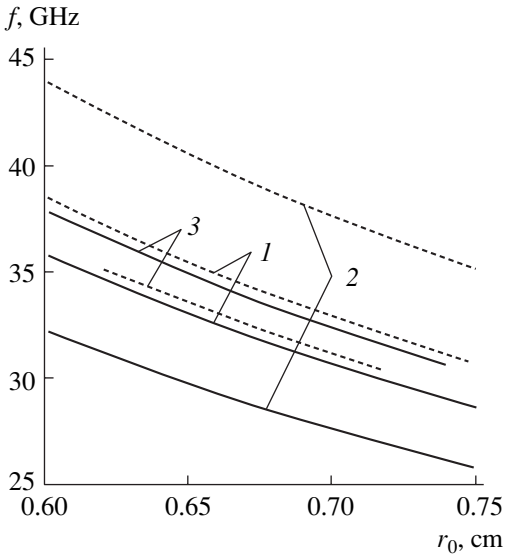

Fig. 5. Eigenfrequencies of the quasi-TE$_{1011}$ (solid curves) and quasi-TM$_{1011}$ (dashed curves) oscillations of a dielectric spherical body as functions of its radius. The calculations were carried out for an isotropic resonator with (*1*) $\varepsilon_d = 9.4$ and (*2*) $\varepsilon_d = 11.6$ and (*3*) for an anisotropic resonator with $\varepsilon_\perp = 9.4$ and $\varepsilon_\parallel = 11.6$.

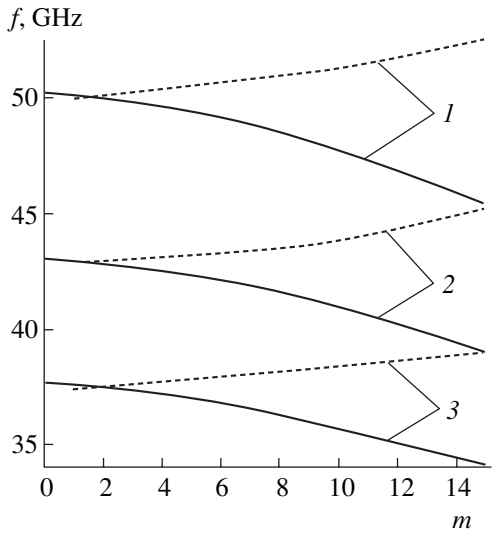

Fig. 6. Eigenfrequencies of the quasi-TE$_{15ml}$ (solid curves) and quasi-TE$_{15ml}$ (dashed curves) oscillations of a leucosapphire spherical body with radius r_0 = (*1*) 0.6, (*2*) 0.7, and (*3*) 0.8 cm.

have different resonant frequencies and whose wave vectors have different radial components.

NUMERICAL EXPERIMENT

Solutions (13) and (14) determine the eigenfrequencies of a spherical uniaxial crystal; the field structure of the eigenmodes of such a crystal depend on the azimuthal coordinate.

In numerical experiments, we simulated millimeter-wavelength eigenmodes of anisotropic and isotropic dielectric spherical bodies in vacuum.

The numerical results obtained for a leucosapphire spherical body with radius $r_0 = 0.66$ cm ($\varepsilon_\perp = 11.6$, the dissipation factor at a temperature of 77 K being $\tan\delta = 5 \times 10^{-7}$ [10]) are illustrated in Fig. 4, which shows (*1*) the eigenfrequencies *f* and (*2*) the quality factors *Q* of the quasi-TE and quasi-TM oscillations with $n = m$. The quality factors for all types of quasi-TE oscillations with $n > 10$ and of quasi-TM oscillations with $n \geq 15$ at different frequencies are the highest. This allows a dielectric spherical body to be used as a broadband multimode element in devices for microwave technology.

The effect of the anisotropy of a spherical body on its eigenfrequencies is illustrated in Fig. 5. It can be seen that the eigenfrequencies of an anisotropic spherical body are shifted with respect to those of an isotropic spherical body whose material is characterized by conventional values of the dielectric permittivity. The eigenfrequencies of the quasi-TE oscillations of an anisotropic resonator are higher than those of an isotropic resonator, and the eigenfrequencies of the quasi-TM oscillations are lower. The eigenfrequencies of small resonators ($r_0 < 0.4$ cm) increase sharply with decreasing radius, so that the resonant oscillations occur in the submillimeter wavelength range.

The anisotropy of a spherical body leads to a frequency splitting of the eigenmodes with different azimuthal numbers *m*. Figure 6 shows the eigenfrequencies of a resonator executing quasi-TE and quasi-TM oscillations with different azimuthal numbers *m*, the polar number ($n = 15$) and the radial number ($s = 1$) being fixed. As the azimuthal number increases, the eigenfrequency of the quasi-TM oscillations becomes higher and that of the quasi-TE oscillations becomes lower. The quality factor of the resonator is, as before, high and is weakly sensitive to both the resonator radius and the azimuthal mode number.

CONCLUSIONS

We have developed a theory of open resonators in the form of spherical uniaxial crystals (ruby, sapphire, and quartz). Owing to the anisotropy of such crystals, the components of the dielectric tensor in spherical coordinates depend on the polar angle. We have investigated for the first time azimuthally nonuniform eigenmodes of an anisotropic spherical body. We have shown that the anisotropy removes the degeneracy of the frequency of the resonant oscillations—a feature peculiar to an isotropic spherical body. In an anisotropic spherical body, the TE and TM oscillations transform into quasi-TE and quasi-TM oscillations.

ACKNOWLEDGMENTS

This work was supported in part by the Science and Technology Center of Ukraine, project nos. 1916 and 2051.

REFERENCES

1. J. A. Stratton, *Electromagnetic Theory* (McGraw-Hill, New York, 1941; Gostekhizdat, Moscow, 1948).
2. M. Gastine, L. Courties, and J. Dormann, IEEE Trans. Microwave Theory Tech. **15**, 694 (1967).
3. Yu. F. Filippov and Z. E. Eremenko, Zh. Tekh. Fiz. **70** (10), 8 (2000) [Tech. Phys. **45**, 528 (2000)].
4. Z. E. Eremenko and Yu. F. Filipov, Int. J. Infrared Millim. Waves **22**, 1065 (2001).
5. B. Makkinejad and G. W. Ford, Phys. Rev. B **44**, 8536 (1991).
6. A. N. Tikhonov and A. A. Samarskiĭ, *Equations of Mathematical Physics* (Gostekhteorizdat, Moscow, 1951; Pergamon, Oxford, 1964).
7. E. Jahnke, F. Emde, and F. Losch, *Tables of Higher Functions*, 6th ed. (McGraw-Hill, New York, 1960; Nauka, Moscow, 1977).
8. S. Kharkovsky, Yu. Filipov, and Z. Eremenko, Microwave Opt. Technol. Lett. **21**, 252 (1999).
9. A. N. Oraevskiĭ, Kvantovaya Élektron. (Moscow) **32**, 377 (2003).
10. V. N. Egorov and A. S. Volovikov, Izv. Vyssh. Uchebn. Zaved. Radiofiz. **44**, 960 (2001).

Translated by O. Khadin

Technical Physics, Vol. 49, No. 4, 2004, pp. 466–470. Translated from Zhurnal Tekhnicheskoĭ Fiziki, Vol. 74, No. 4, 2004, pp. 89–93.

RADIOPHYSICS

Transition Radiation of Nonrelativistic Electron Bunches Passing through Diaphragms

V. N. Bolotov, S. I. Kononenko, V. I. Muratov, and V. D. Fedorchenko

Karazin National University, Kharkov, 61007 Ukraine

e-mail: renic@iemr.vl.net.ua

Received June 27, 2003

Abstract—Experiments on generating electromagnetic pulses (EMPs) by using nonrelativistic electron bunches passing through diaphragms of various radii are described. Results obtained agree with the predictions of the transition radiation theory as applied to nonrelativistic charged particles passing through apertured conducting screens. They may also be used in designing devices for generating EMPs with tunable characteristics, as well as in developing a transition radiation theory for electrodynamic structures of complex geometries. © *2004 MAIK "Nauka/Interperiodica".*

INTRODUCTION

As is well known, electromagnetic radiation may be generated not only by charged particles being accelerated but also by those moving with a constant velocity. In the latter case, the presence of a material medium is essential for electromagnetic wave generation. A charged particle moving rectilinearly and uniformly either near or through a conducting medium generates time-varying currents in it. The currents induced produce electromagnetic radiation. Uniform motion of charged particles near insulators results in a local space–time polarization and, hence, in radiation of electromagnetic waves with intensities substantially lower that in the former case. Thus, electromagnetic radiation arises due to the reconfiguration of the field of a charged particle–medium system. The above electromagnetic phenomena give rise to definite types of radiation, such as transition radiation, diffraction radiation, and Smith–Purcell radiation [1, 2]. Cherenkov radiation, which is generated by charged particles moving rectilinearly and uniformly with velocities exceeding the phase velocity of light in a given medium, stands somewhat apart from these types of radiation.

Today, generation of short high-power EMPs is of considerable interest. Specifically, EMPs are generated by rapidly reconfiguring the field of a system where a charged electron bunch interacts with a conducting solid. Wide-band transition radiation is intended to be employed in pulsed radar. It should be noted that, to date, microwave generators employing diffraction radiation have been designed and found wide application [2].

In this paper, the influence of apertures of various configurations on electromagnetic wave generation by electron bunches passing through the apertures is studied.

EXPERIMENTAL

Experiments were carried out with the setup shown in Fig. 1. Two interpenetrating electron beams were injected through a metal tube 9 cm in diameter placed in a uniform magnetic field of 400 Oe. A lanthanum hexaboride pellet 0.3 cm in radius emitted the first beam; a flat tantalum spiral threaded by the electrons of the first beam generated the second electron beam. The beam velocities were 3.6×10^9 and 3.3×10^9 cm/s, respectively; the total current, 40–50 mA. A sinusoidal (50 Hz) accelerating voltage applied to the electron guns made it possible to observe high-frequency signals at any beam energies from minimum (threshold) to maximum (Fig. 2). The operating pressure in the chamber was 2×10^{-6} mm Hg. An initial perturbation was produced by applying a high-frequency voltage from an external generator to modulator *3* (Fig. 1), which is a 15-cm-long decelerating coil connected to the generator through an additional coil with counter winding. The modulating voltage at a frequency of 1 GHz was applied from a G4-37A generator with a power of 1 W. Cavity resonator *4* (Fig. 1) was placed some distance (≈40 cm) away from the modulator. The signal from the resonator was detected by coupling loop and applied to either an S1-69 oscillograph or a spectrum analyzer (the frequency range 40 GHz).

Electron bunches were formed by Bernstein–Green–Kruskal waves (BGK waves) [3, 4]. These are stationary nonlinear waves whose profile depends on the initial distribution function of trapped particles. At certain ratios between the velocities and densities of modulated beams, the potential of BGK waves may vary with time in the form of a short pulse. The initial stage of wave evolution is the most favorable for modifying the shape of the wave. Therefore, an electron bunch is formed before the amplitude of the first harmonic reaches a peak.

1063-7842/04/4904-0466$26.00

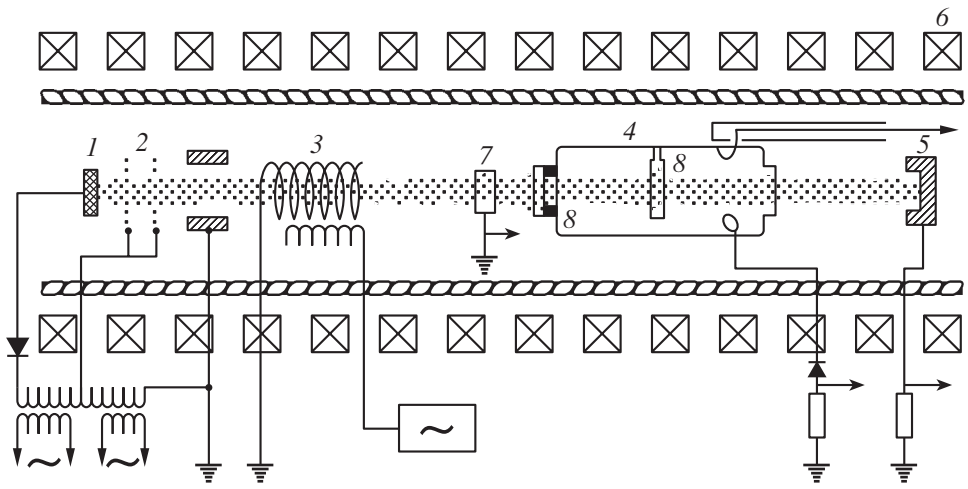

Fig. 1. Experimental setup: (*1*, *2*) electron guns, (*3*) modulator, (*4*) cavity resonator, (*5*) collector, (*6*) magnets, (*7*) capacitor probe, and (*8*) apertured diaphragm placed at either the center of the cavity or its input.

In experiments, electron bunches with supercritical velocities are used [5, 6]. Such bunches amplify only waves with a finite amplitude exceeding the threshold value, above which the wave traps the particles. That is why waves of smaller amplitudes are not amplified by a supercritical beam and, thus, do not generate noise distorting the evolution process. Thus, if the initial distribution function of trapped particles is constant along the particle paths, continuous electron waves may be generated. The profile of these waves was determined by capacitor probe *7* (Fig. 1). The harmonic structure of the signal was studied using the spectrum analyzer, which measures the amplitudes of eight harmonics normalized to the amplitude of the fundamental harmonic. Calibration of the high-frequency channel was performed by standard-frequency generators. Figure 3 shows the bunch waveform found by solving the inverse Fourier problem for a modulation frequency of 925 MHz. The bunch is seen to have the form of a short pulse with an FWHM on the order of 10^{-10} s. Knowing the velocity of the bunch, we determined its longitudinal size l, which equals 0.3 cm. The transverse size of the bunch depended on the cathode geometry and was equal to 0.6 cm. Similar results were found at other modulation frequencies.

It was found that electron bunches passing through metal diaphragms *8* (Fig. 1) of various sizes generate transition electromagnetic radiation [1, 7]. Cavity resonator *4* (Fig. 1) with a radius of 1.75 cm and length of 13.6 cm was used to detect this radiation. A copper diaphragm with a diameter of 16 mm and thickness d = 0.2 cm with an aperture (r_0 = 0.4 cm) was placed at the center of the cavity, where the electric field of the fundamental mode H_{11} is zero. The frequency spectrum of waves induced by the bunch is rather wide. The resonator selects only modes with frequencies coinciding with its eigenfrequencies. Figure 4 shows a characteristic frequency spectrum of electromagnetic radiation at a

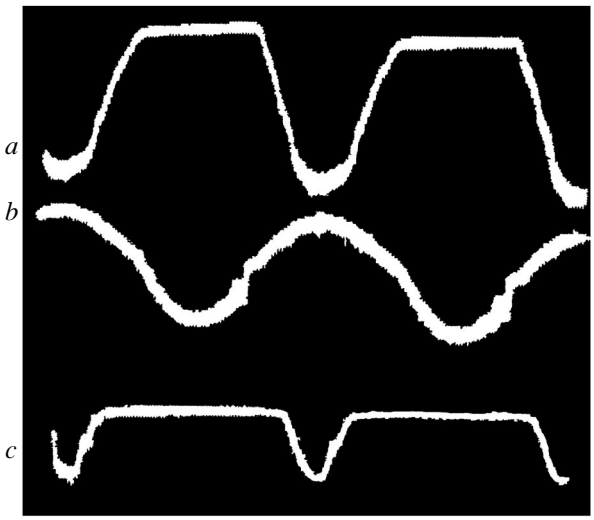

Fig. 2. Waveforms of the (*a*) current, (*b*) accelerating voltage, and (*c*) high-frequency signal from the cavity resonator.

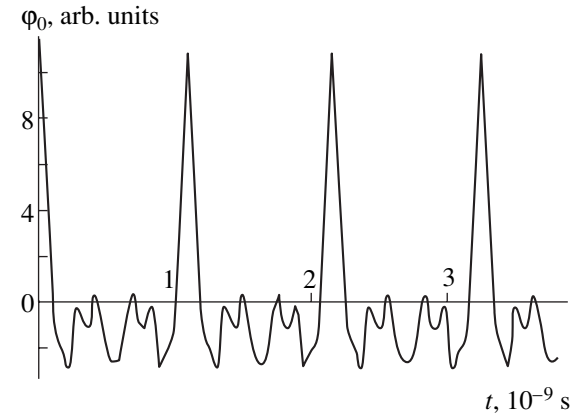

Fig. 3. Waveform of the potential generated by the electron bunches.

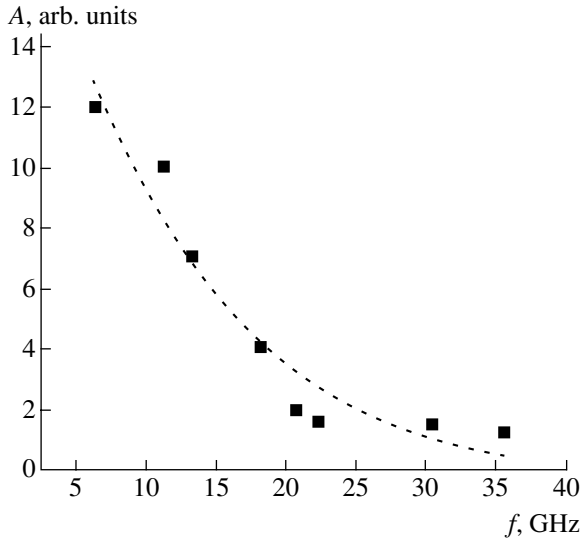

Fig. 4. Frequency spectrum for the diaphragm placed at the center of the cavity.

modulation frequency of 1.06 GHz. The peak power of 6.38-GHz radiation was measured with a thermistor bridge and was found to equal 80 mW.

The material of the diaphragm exerts a considerable influence on both the intensity and bandwidth of the spectrum. Comparison of geometrically identical copper and ceramic diaphragms shows that the spectrum in the latter case is limited by the lower eigenfrequency of the resonator and the radiation intensity in the former case is two orders of magnitude higher than that for the ceramic. For niobium–titanium alloy, the spectrum is similar to that for the copper diaphragm.

The diaphragm was placed at both the center and the input of the cavity resonator. In the latter case, the radiation intensity as a function of the aperture radius was studied for a thin diaphragm (d = 0.2 cm) at a beam radius of 0.3 cm (Fig. 5). The measurements were performed at the fundamental mode with a frequency of 6.38 GHz. As is seen, the radiation amplitude reaches a maximum when the aperture radii are close to the beam radius and decreases with increasing aperture radius. The radiation amplitude as a function of the diaphragm thickness d at the same frequency and optimal aperture radius is shown in Fig. 6. The transition radiation amplitude is maximal for $d < 1$ mm and decreases rapidly with increasing diaphragm thickness, tending to zero for thicknesses larger than the length of the electron bunch.

THEORETICAL MODEL OF TRANSITION RADIATION FROM NONRELATIVISTIC ELECTRON BUNCHES PASSING THROUGH A CONDUCTING SCREEN WITH AN APERTURE

Consider the radiation from a nonrelativistic electron bunch passing with a constant velocity through a circle aperture in a conducting screen. We assume that the screen thickness d is much smaller than the wavelength λ measured: $d \ll \lambda$. Following [8], we introduce the cylindrical coordinate system with the z axis passing through the aperture center perpendicularly to the screen plane. Let a be the aperture radius and S, S_1, and S_2 designate the plane $z = 0$ and plane areas coinciding with the screen and aperture, respectively.

The resulting field is represented in the form $\mathbf{E}^r = \mathbf{E}^0 + \mathbf{E}$ and $\mathbf{H}^r = \mathbf{H}^0 + \mathbf{H}$, where $\mathbf{E}^0$ and $\mathbf{H}^0$ are the fields generated by the beam in free space and $\mathbf{E}$ and $\mathbf{H}$ are the fields generated by the screen. If the screen is conducting, the electron bunch induces varying currents, which give rise to the $\mathbf{E}$ and $\mathbf{H}$ fields. If the electron beam

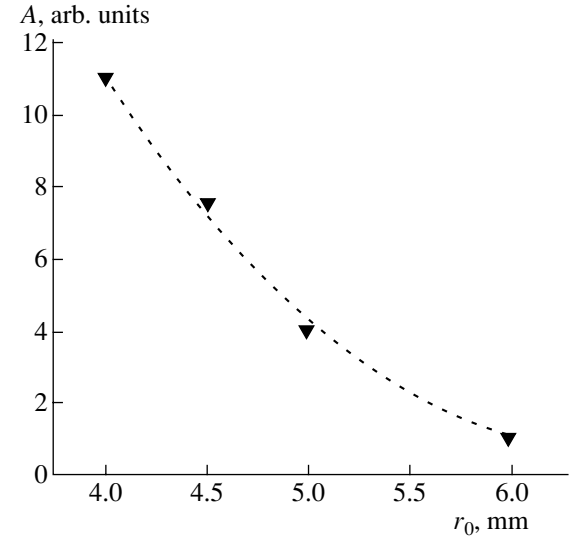

Fig. 5. Dependence of the radiation amplitude on the aperture radius.

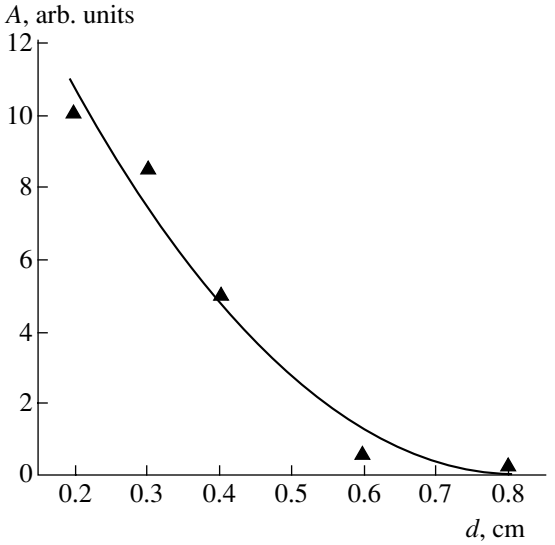

Fig. 6. Dependence of the radiation amplitude on the diaphragm thickness.

passes through an aperture in an insulating screen, it polarizes the insulator. Arising polarization currents also cause electromagnetic radiation but with substantially lower intensities. In view of the axial symmetry in the cylindrical coordinate system, the only nonzero components of all the fields are E_r, E_z, and H_φ. This is easy to realize if one bears in mind that the vector potential is aligned with the electron bunch velocity and, hence, has the only nonzero component A_z. The $\mathbf{E}^0$ and $\mathbf{H}^0$ fields exponentially decay at infinity and do not contribute to the radiation.

To be specific, we will seek a solution for a point charged particle in the half-space $z \geq 0$. In order to find $\mathbf{E}$ in the wave zone, one has to solve an inhomogeneous wave equation subject to inhomogeneous boundary conditions. Let us represent $\mathbf{E}$ as the sum

$$\mathbf{E} = \mathbf{E}_1 + \mathbf{E}_2, \quad (1)$$

where $\mathbf{E}_1$ is a solution to an inhomogeneous equation with homogeneous boundary conditions and $\mathbf{E}_2$ is a solution to a homogeneous equation with inhomogeneous boundary conditions.

The first problem is reduced to determining the radiation field of a point charge q appearing on the plane $z = 0$ and moving along the z axis with a constant velocity v. The tangential component of the field strength is $E_t = 0$ over the z plane. This corresponds to the case of the transition radiation from a charge escaping from a metal into a vacuum. Thus, at $v \ll c$, where c is the speed of light, the solution to the first problem has the form

$$\mathbf{E}_1(\omega) = -\frac{qv\sin\vartheta}{\pi c^2}\frac{e^{-ikR_0}}{R_0}\boldsymbol{\vartheta}_0, \quad (2)$$

where q is the electron charge, v is the electron velocity, ϑ is the angle between the z axis and the direction to the point of observation, $\boldsymbol{\vartheta}_0$ is the unit vector in the direction of increase in ϑ, k is the wavenumber, and R_0 is the distance between the aperture center and point of observation.

In order to solve the second problem, one has to find the radiation field from the known distribution of the field tangent components on the plane $z = 0$. On the surface, the fields are given in the following way: $E_t = 0$ for $r > a$ and $H_t = H_t^0$ for $r < a$. Here, H_t^0 is the field in the absence of the conducting screen. Such a statement means a mixed boundary-value problem. This problem is generally difficult to solve. However, in the case of nonrelativistic beams, the electric field of a moving charge may be considered the same as that of a static charge placed at the point where the moving charge is at the moment. Then, the field at the aperture is given by

$$\mathbf{E}_2(M) = \int_{S_2}\mathbf{E}''(M, P)\,dS_2, \quad (3)$$

where $\mathbf{E}_2$ is the field of interest at the point of observation M and $\mathbf{E}''$ is the field generated at the point M by a point magnetic dipole located at a point P on the surface S_2 ($P \in S_2$). The aperture S_2 is assumed to be perfectly conducting (the Babinet theorem for transition radiation [9]).

In [8], this problem was solved for the wave zone ($\lambda \gg 2\pi a$) and the field $\mathbf{E}_2(M)$ was found:

$$\mathbf{E}_2(M) = \frac{qv\sin\vartheta}{\pi c^2}\frac{e^{-ikR_0}}{R_0}\left[1 - e^{-\omega a/v}\left(1 + \frac{\omega a}{v}\right)\right]\boldsymbol{\vartheta}_0. \quad (4)$$

Summing up expressions (2) and (4), one can find the total radiation field:

$$\mathbf{E}(\omega) = -\frac{qv\sin\vartheta}{\pi c^2}\frac{e^{-ikR_0}}{R_0}e^{-\omega a/v}\left(1 + \frac{\omega a}{v}\right)\boldsymbol{\vartheta}_0. \quad (5)$$

Expression (5) shows that the presence of an aperture attenuates the transition radiation. The higher the radiation frequency, the stronger the attenuation.

The spectral density $W(\omega, \theta, a)$ of the energy emitted is proportional to $|\mathbf{E}|^2$. Thus, the normalized radiation intensity has the form

$$W(\omega, \theta, a) = Kv^2\left[e^{-\omega a/v}\left(1 + \frac{\omega a}{v}\right)\right]^2\sin^2\theta. \quad (6)$$

In the experiments, the frequency f related to the circular frequency ω by the well-known relationship $\omega = 2\pi f$ was measured. In all the calculations, $\beta = v/c$ was taken to be equal to 0.1. The radiation intensity was normalized to the transition radiation intensity without

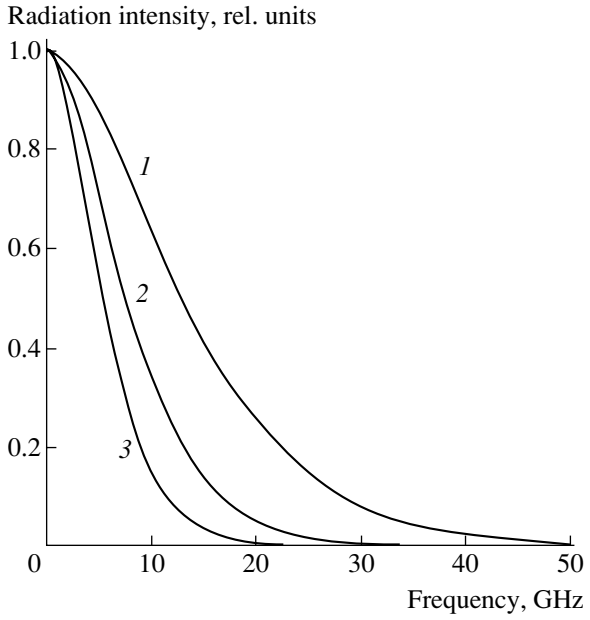

Fig. 7. Spectra of the transition radiation generated by electron bunches passing through apertures of radii a = (*1*) 0.4, (*2*) 0.7, and (*3*) 1 mm.

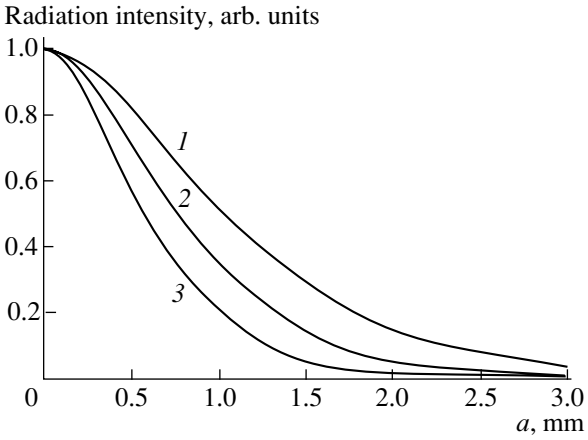

Fig. 8. Relative intensity of the transition radiation as a function of the aperture radius for frequencies f = (*1*) 5, (*2*) 6.823, and (*3*) 9 GHz.

the aperture. Figure 7 shows the transition radiation spectrum for the apertured conducting screen.

As is known, the total energy of transition radiation tends to infinity. Apertures in a screen suppress higher harmonics (Fig. 7); therefore, the total energy of transition radiation is finite in this case.

However, the transition radiation intensity at a given frequency decreases with increasing radius of apertures made in a conducting screen. These dependences are shown in Fig. 8 for various frequencies. The plots show that the transition radiation intensity at a given frequency decreases with increasing aperture radius.

CONCLUSIONS

In this paper, an experimental setup for producing nonrelativistic electron bunches by using BGK waves is described. The frequency of the electron bunches generated is on the order of 1 GHz. These bunches are stable objects with a length of 3 mm and a diameter of 6 mm. When passing through diaphragms made of different materials with apertures of various radii, the electron bunches produced in the experiment generate electromagnetic radiation. The results obtained are compared with the theory of transition radiation from charged particles passing through an apertured conducting plane [8]. Indeed, the radiation intensity versus the aperture radius curves obtained in our experiments (Fig. 5) agree qualitatively with those resulting from theoretical considerations (Fig. 8). Quantitative agreement is possible if an effective aperture radius one order of magnitude smaller than the radii used in the experiments is introduced into the theoretical model. This is because the theory was constructed for point particles, whereas the beam radius in our experiments approaches the aperture radius.

It should be noted that, in the case of relativistic beams, the theory of transition radiation is adequately developed for conducting screens with apertures [9]. Unfortunately, the results of [9] cannot be applied to nonrelativistic beams of charged particles. The reason is that the theory [9] is based on the scalar approximation of the diffraction theory; i.e., it is applicable only to ultrarelativistic particles. This approximation does not consider the limiting case of nonrelativistic beams.

Figure 7 shows the electromagnetic radiation spectra found theoretically for various aperture radii. As is seen, the high-frequency spectrum components tend to zero as the aperture radius grows. In this paper, this result is confirmed experimentally (Fig. 4).

Thus, we demonstrated the possibility of creating short (0.1 ns) electromagnetic pulses. The characteristics of the pulses (the intensity and pattern of the radiation, spectral composition, etc.) can be controlled by using diaphragms that may have different configurations and be made of different materials.

REFERENCES

1. V. L. Ginzburg and V. N. Tsytovich, *Transient Radiation and Transient Scattering* (Nauka, Moscow, 1984) [in Russian].
2. V. P. Shestopalov, *Diffraction Electronics* (Vysshaya Shkola, Khar'kov, 1976) [in Russian].
3. I. B. Bernstein, I. M. Green, and M. D. Kruskal, Phys. Rev. **108**, 546 (1957).
4. V. P. Kovalenko, Usp. Fiz. Nauk **139**, 223 (1983) [Sov. Phys. Usp. **26**, 116 (1983)].
5. A. S. Bakaĭ, V. D. Mazalov, and V. D. Fedorchenko, Zh. Éksp. Teor. Fiz. **76**, 107 (1979) [Sov. Phys. JETP **49**, 54 (1979)].
6. A. S. Bakaĭ, S. S. Krivulya, V. D. Fedorchenko, and V. I. Muratov, Pis'ma Zh. Éksp. Teor. Fiz. **21**, 226 (1975) [JETP Lett. **21**, 101 (1975)].
7. S. S. Kalmykova and V. I. Kurilko, *Physics of Collective Transition Instabilities in Charged Particle Fluxes* (Naukova Dumka, Kiev, 1989), pp. 162–175 [in Russian].
8. V. Bobrinev and V. Braginskiĭ, Dokl. Akad. Nauk SSSR **123**, 634 (1958).
9. B. M. Bolotovskiĭ and E. A. Galst'yan, Usp. Fiz. Nauk **170**, 809 (2000) [Phys. Usp. **43**, 755 (2000)].

Translated by M. Fofanov

Technical Physics, Vol. 49, No. 4, 2004, pp. 471–474. Translated from Zhurnal Tekhnicheskoĭ Fiziki, Vol. 74, No. 4, 2004, pp. 94–97.

RADIOPHYSICS

Millimeter-Wave Whispering Gallery Modes in an Ellipsoidal Dielectric Resonator with a Small Ellipticity

A. E. Kogut, Z. E. Eremenko, Yu. F. Filippov, and V. V. Kutuzov

Usikov Institute of Radiophysics and Electronics, National Academy of Sciences of Ukraine, ul. Akad. Proskura 12, Kharkov, 61085 Ukraine

e-mail: kogut@ire.kharkov.ua

Received July 17, 2003

Abstract—It is found that, when the shape of a dielectric sphere (hemisphere) operating under the whispering gallery mode conditions is perturbed by a surface curvature gradient (ellipticity), the unloaded Q factor of the sphere degrades and its resonance frequencies change. It is shown theoretically and experimentally that an elliptic irregularity removes frequency degeneracy of whispering gallery modes at millimeter waves. *© 2004 MAIK "Nauka/Interperiodica".*

Interest in resonance systems built around spherical or hemispherical dielectric resonators (DRs) is due mostly to the possibility of their wide practical use [1–3], including in thermonuclear fusion [4]. At millimeter waves, high-*Q* whispering-gallery-mode (WGM) dielectric resonators are currently applied in the oscillatory circuits of stable millimeter-wave oscillators and power combiners [3]. They can also be used as measuring devices in permittivity meters [2].

Hemispherical DRs support independent WGMs of the waveguide type: TM_{nml} ($E_r \neq 0$) and TE_{nml} ($H_r \neq 0$), where the indices *n*, *m*, and *l* indicate the numbers of field variations in the polar, θ, azimuthal, φ, and radial, *r*, coordinates, respectively. The eigenmodes of a hemispherical DR are described by the same dispersion relation as the modes of a dielectric sphere [5]:

$$\sqrt{\varepsilon}\frac{j_\nu'(x_d)}{j_\nu(x_d)} = \frac{h_\nu^{(1)'}(x_b)}{h_\nu^{(1)}(x_b)}\ (TE\ \text{modes}),$$
$$\sqrt{1/\varepsilon}\frac{j_\nu'(x_d)}{j_\nu(x_d)} = \frac{h_\nu^{(1)'}(x_b)}{h_\nu^{(1)}(x_b)}\ (TE\ \text{modes}), \quad (1)$$

where $j_\nu(x) = \sqrt{\pi x/2}\,J_{n+1/2}(x)$, $h_\nu^{(1)}(x) = \sqrt{\pi x/2}H_{n+1/2}^{(1)}(x)$, $x_d = \sqrt{\varepsilon}\,x_b$, $x_b = \omega r_0/c$, $J_\nu(x)$ and $H_\nu^{(1)}(x)$ are the cylindrical Bessel and Hankel functions of the first kind, *c* is the speed of light, ω is the resonant frequency, and r_0 is the radius of the hemisphere.

These equations do not contain the azimuthal index *m*, which causes $(n + 1)$-fold mode degeneracy in a dielectric hemisphere placed on a perfectly conducting plane metal surface [6].

Fabrication-induced distortions of the shape of hemispherical DRs, including of those with distributed parameters (ellipticity), significantly affect the spectral and power characteristics of the resonators [7] and devices built around them. Lowest order azimuthal WGMs with $m = 1$ in small ellipsoidal DRs in the absence of frequency-degenerate higher order azimuthal modes were studied in [7]. These degenerate modes exist in hemispherical DRs whose diameter *D* is much greater than the wavelength λ_d in the dielectric ($D \geq 10\lambda_d$) [6]. The order of degeneracy for eigenmodes is different from that for forced oscillations (in the latter case, the degeneracy is determined at the waveguide junction between the exciting waveguide and a curvilinear guiding channel arising on the spherical surface [6]).

The aim of our experiments is to study the effect of a slight ellipticity of a spherical DR on its spectral and power characteristics, as well as on the field distribution of frequency-degenerate WGMs. The behavior of a dielectric ellipsoid with its axes slightly differing in length is contrasted with the behavior of a spherical resonator. To minimize the effect of the radiator on the forced oscillation field, a small-aperture radiator was placed in the region where the WGM field decays.

The weak ellipticity of the surface removes degeneracy and produces hybrid oscillations. In this case, the dispersion relation has form (1) with the eigenfunction index ν given by [8]

$$\nu(j) = \left[(n + 1/2)^2 + \frac{(m^2 + \gamma_n)a_j}{n(n+1)}\right]^{1/2}.$$

Here,

$$\gamma_n = \frac{2n^2(n+1)^2 - m^2(2n^2 + 2n + 3)}{(2n-1)(2n+3)},$$

$$a_j = \varepsilon_j\omega^2\tau^2/c^2, \quad \varepsilon_j = \begin{cases}\varepsilon, & r \leq r_0\\ 1, & r \geq r_0,\end{cases}$$

1063-7842/04/4904-0471$26.00 © 2004 MAIK "Nauka/Interperiodica"

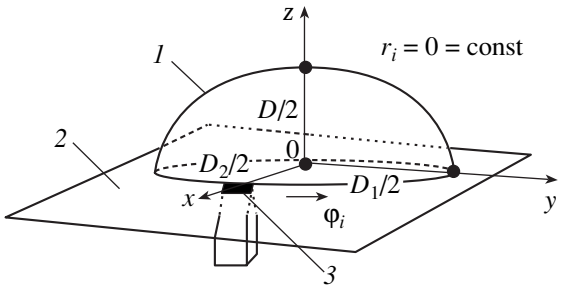

Fig. 1. Object and geometry of the experiment.

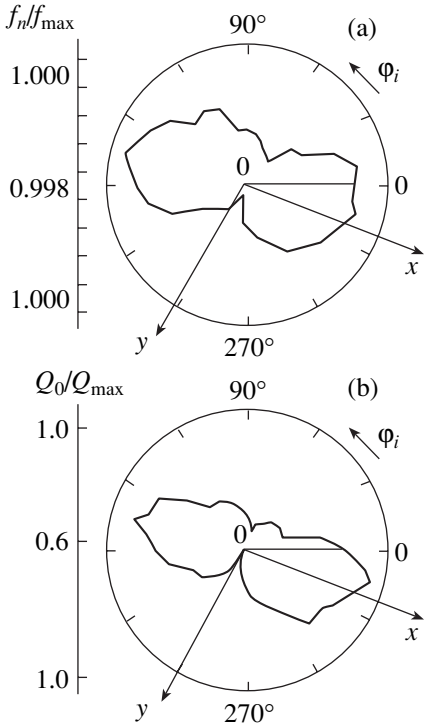

Fig. 2. Normalized (a) resonant frequency f_n and (b) unloaded Q factor of the degenerate WGMs vs. the azimuthal coordinate of the radiator.

and τ is the interfocal spacing. As in [9], the dependence of the indices $\nu(j)$ on the azimuthal index m, which is caused by the weak elliptical irregularity of the hemispherical dielectric resonator, removes the frequency degeneracy of resonant oscillations.

The experiments were performed with a DR that had the form of half a three-axial ellipsoid (designated *1* in Fig. 1) placed on plane metal surface *2*. The axes of the ellipsoid were D_1, $D_2 = \alpha_1 D_1$, and $D_3 = \alpha_2 D_1$ ($\alpha_1 = 1.006$, $\alpha_2 = 1.013$). The ellipsoid was cut by the plane containing its major and medium axes. The dielectric structure was made of Teflon ($\varepsilon = 2.08$), and the length of its minor axis was $D_1 = 77.2$ mm. WGMs were excited at the plane metallic base of the dielectric structure by means of a radiator in the form of the open end of a hollow rectangular metallic waveguide with the tapered wide wall. On the metallic surface, the radiator was terminated by coupling slot *3* measuring $7.2 \times d$ mm and centered at the edge of the dielectric structure ($r_1 = 0 = \text{const}$).

We studied the resonance frequencies of the modes and their unloaded Q factors, as well as the shapes and dimensions of field localization regions on the elliptical DR surface, versus the azimuthal coordinate of the radiator in the frequency range 30–36 GHz. The unloaded Q factor was evaluated from the measured value of the impedance [10]. The probe body method was used to identify oscillation modes by the number of field variations in a given direction and to locate the boundaries of field localization regions [11].

The mode characteristics obtained for this ellipsoid were compared with the properties of a Teflon hemispherical DR with diameter $D = 60$ mm placed on a plane metal surface.

The coupling slot was oriented so that the *TM* modes were excited for the first place. Since the eccentricity of the ellipsoidal DR is small, its modes may roughly be viewed as waveguide modes of a spherical DR. Along the frequency axis, the resonance responses of the oscillations in the resonators considered show up as almost periodic trains with an average frequency separation of 0.9 GHz for the ellipsoidal DR and 1.2 GHz for the hemispherical DR. The deviation from these average values, which is due to the different effect of the radiator on the oscillation fields at different frequencies, was within 15 MHz (±0.05%) over the frequency band of interest.

Figure 2 shows the normalized (a) resonant frequency f_n (which is close to 35 GHz) and (b) unloaded Q factor Q_0 versus the azimuthal coordinate φ_1 of the radiator.

This figure also shows the orientation of the ellipsoid axes relative to the radiator (0*x* and 0*y* are the minor and major axes, respectively). Note that oscillations along the DR axes are two extreme cases of our study. Modes excited in the 0*x* direction may roughly be regarded as the modes of a dielectric hemisphere, because WGMs propagate over the DR inner surface following trajectories (waveguide channels) with a minimal variation (gradient) of the curvature. Oscillations excited in the 0*y* direction are characterized by the highest gradient of the surface curvature, which provides a waveguide channel on the DR surface.

For the ellipsoidal DR, the above dependences are nonmonotonic and nearly periodic, unlike the spectral and power characteristics of the oscillations in the hemispherical DR. The latter are independent of the azimuthal coordinate of the radiator owing to the axial symmetry of the resonance structure. For the ellipsoidal DR, the azimuthal coordinates of the maxima and minima of the frequency and Q factor coincide with the directions of its major and minor axes. A change in the unloaded Q factor leads to a change in the width of the resonance curve. When the Q factor decreases, the res-

onance curve diffuses. In DRs whose electromagnetic properties are close to those of spherical DRs, this may be caused by two reasons: removal of resonant mode degeneracy and an increase in the power loss of degenerate oscillations.

A DR ellipticity, which is a distributed irregularity, may remove degeneracy of the forced oscillations. In other words, if the azimuthal coordinate of the radiator changes, so does the excitation direction in the ellipsoidal DR, altering the frequency separation between the resonances of modes with different azimuthal indices m. To enhance the effect of degeneracy removal in an ellipsoidal DR, a local irregularity (hole) is made on the metal surface opposite to the radiator [6].

When the radiator is placed between the axes of the ellipsoid ($\varphi_1 = 30°$) and the depth of the hole is h = 0.5 mm, the frequency degeneracy (which is twofold in our experiment) of the ellipsoidal DR disappears. The removal of degeneracy is accompanied by a decrease in the frequency of the higher azimuthal mode ($m = 2$). Near the operating frequency f = 36 GHz, the frequency separation between the split modes is Δf = 9 MHz. The frequency separation Δf varies with azimuthal coordinate of the radiator and attains a maximal value Δf = 16 MHz at $\varphi_1 = 75°$ and 255° (at these coordinates, WGMs and DR modes propagate in waveguide channels with the highest curvature gradient). Conversely, when the radiator is placed so that the waves propagate along trajectories with the lowest curvature gradient or with a constant curvature ($\varphi_1 = 165°$ and 245°), distinct splitting is absent and $\Delta f \approx 0$.

Figure 3 shows the normalized resonance frequencies of modes in the system with a local irregularity (a hole on the metal surface) versus the azimuthal coordinate φ_1 of the radiator. These plots allow one to trace the dynamics of degeneracy removal in the ellipsoidal DR on surface areas with variable curvature.

The dashed line that bounds the hatched region illustrates the behavior of the resonance frequency of the mode with the azimuthal index $m = 2$. The other curve refers to the degenerate mode frequency.

It is seen that there exist intervals of φ_1 where the splitting of modes with different azimuthal indices is most pronounced (20°–120° and 200°–290°) and intervals where the splitting is absent (120°–200° and 290°–20°).

Measurements of the unloaded Q factor at all coordinates φ_1 of the radiator require that the oscillations be nondegenerate. To this end, the effect of the local irregularity was enhanced by increasing the depth of the hole on the metal surface to 1.5 mm. At this depth, splitting of the modes is distinct even for φ_1 within the ranges 120°–200° and 290°–20°, where the waves are excited even in the channels with the lowest curvature gradient.

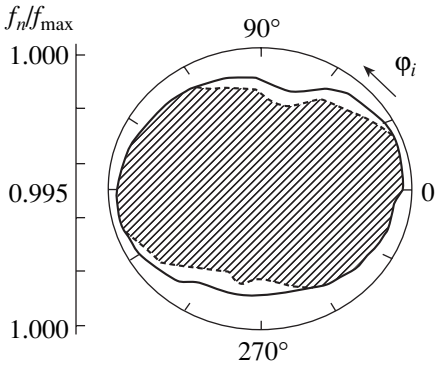

Fig. 3. Splitting WGMs in the ellipsoidal DR as a function of the azimuthal coordinate of the radiator.

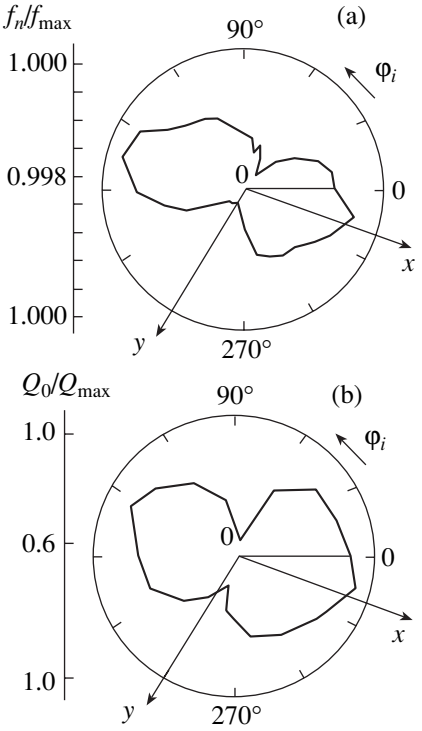

Fig. 4. Normalized (a) resonance frequency and (b) unloaded Q factor of the WGM with m = 2 vs. the azimuthal coordinate of the radiator.

Figure 4 shows the (a) resonance frequency and (b) unloaded Q factor normalized to their maxima for the mode with m = 2 at frequencies close to 36 GHz.

These functions are seen to be nonmonotonic and almost periodic. The highest unloaded Q factor is observed for WGMs that propagate through the waveguide channels with the lowest curvature gradient ($\varphi_1 \longrightarrow$ 165° and 345°). The lowest unloaded Q factor, which corresponds to the highest power losses, is observed for modes excited along the major axis of the ellipsoid, where the curvature gradient is the highest. It may be supposed that the curvature gradient makes a major contribution to the radiation power losses,

because the dielectric losses are almost constant and ohmic losses on the metal surface are low because of the high conductivity of the metal and small dimensions of the field spots near the radiator and its image [6]. The shift in the resonance frequency of the mode with $m = 2$ depends on φ_1 of the radiator and is attributed to a change in the waveguide channel length [7]. Therefore, when the number of field variations in the direction of wave propagation is fixed, the DR resonance frequency changes.

From the field distributions on the ellipsoidal DR surface, it follows that, like in hemispherical DRs [12], the field localization regions have the form of irregular belts, which narrow near the metal surface, the radiator, and the image of the radiator on the opposite side of the dielectric structure. Between these areas, the belts widen. The width of the belt in its narrowest part is almost constant and approaches the linear size of the wider wall of the waveguide (7.2 mm). At the circumference of the wider part of the belt, its width depends on the position of the radiator relative to the axes of the ellipsoid, because the waveguide channel curvature changes. The width of the belt here varies within 8–9%.

Thus, we showed that, unlike DRs with a spherical surface, the spectral and power characteristics of forced WGMs in ellipsoidal DRs depend on the azimuthal coordinate of the radiator, i.e., on its position relative to the geometrical axes of the dielectric structure. The shape and dimensions of WGM field localization regions also depend on the azimuthal coordinate of the radiator. In an ellipsoidal DR, the dependence of the mode properties on the direction relative to its axes removes degeneracy of the resonator modes.

REFERENCES

1. V. V. Vasiliev, V. L. Velichansky, V. L. Ilchenko, *et al.*, Opt. Commun. **158**, 305 (1998).
2. E. M. Ganapol'skiĭ, A. V. Golik, and A. P. Korolyuk, Fiz. Nizk. Temp. **19**, 1255 (1993) [Low Temp. Phys. **19**, 892 (1993)].
3. S. N. Khar'kovskiĭ, A. E. Kogut, V. V. Kutuzov, *et al.*, in *Proceedings of the 7th International Conference on Microwave Engineering and Telecommunication Technologies, Sevastopol, 1997,* Vol. 2, pp. 361–362.
4. V. P. Smirnov, Vestnik Ross. Akad. Nauk **73**, 305 (2003).
5. J. A. Stratton, *Electromagnetic Theory* (McGraw-Hill, New York, 1941; Gostekhizdat, Moscow, 1948).
6. A. E. Kogut, V. V. Kutuzov, Yu. F. Filippov, *et al.*, Izv. Vyssh. Uchebn. Zaved. Radioélektronika **40** (2), 19 (1997).
7. A. E. Kogut, Pis'ma Zh. Tekh. Fiz. **28** (23), 70 (2002) [Tech. Phys. Lett. **28**, 1007 (2002)].
8. Yu. F. Filippov and Yu. V. Prokopenko, in *Proceedings of the International Conference on Mathematical Methods in Electromagnetic Theory MMET-2002, Kiev, 2002,* Vol. 2, pp. 662–664.
9. H. M. Lai, P. T. Leung, K. Young, *et al.*, Phys. Rev. A **41**, 5187 (1990).
10. E. L. Ginzton, *Microwave Measurements* (McGraw-Hill, New York, 1957; Inostrannaya Literatura, Moscow, 1960).
11. R. A. Valitov, S. F. Dyubko, B. I. Makarenko, *et al.*, in *Millimeter and Submillimeter Measurements: Methods and Equipment*, Ed. by R. A. Valitov and B. I. Makarenko (Radio i Svyaz', Moscow, 1984) [in Russian].
12. S. N. Khar'kovskiĭ, A. E. Kogut, and V. A. Solodovnik, Pis'ma Zh. Tekh. Fiz. **21** (18), 38 (1995) [Tech. Phys. Lett. **21**, 741 (1995)].

Translated by A. Khzmalyan

Technical Physics, Vol. 49, No. 4, 2004, pp. 475–478. Translated from Zhurnal Tekhnicheskoĭ Fiziki, Vol. 74, No. 4, 2004, pp. 98–101.

SURFACES, ELECTRON AND ION EMISSION

Alkali Metal Adsorption on the Gallium Arsenide Surface: A Change in the Work Function

S. Yu. Davydov* and A. V. Pavlyk**

** Ioffe Physicotechnical Institute, Russian Academy of Sciences, Politekhnicheskaya ul. 26, St. Petersburg, 194021 Russia*

e-mail: sergei.davydov@mail.ioffe.ru

*** St. Petersburg State Electrotechnical University (LÉTI), ul. Prof. Popova 5, St. Petersburg, 197376 Russia*

Received September 17, 2003

Abstract—A change in the work function when Cs atoms are adsorbed on the GaAs(100) surface and K, Rb, and Cs atoms are adsorbed on the GaAs(110) surface is calculated with a simple model. The model includes both dipole–dipole interaction of adatoms and broadening of their quasi-levels due to exchange effects. The results of calculation are in good agreement with experimental data. © *2004 MAIK "Nauka/Interperiodica".*

Interaction of metal atoms with semiconductor surfaces is of interest most of all for Schottky-barrier formation [1]. It has been found that the barrier height is established even at the early stage of metal layer deposition [2]. Therefore, it is important to realize the effect of a submonolayer metal film on electronic states at the semiconductor surface. A change $\Delta\phi$ in the work function of an adsorptive system seems to be the simplest integral characteristics of this effect. In this study, we calculate $\Delta\phi$ upon adsorption of alkali metal (AM) atoms on the gallium arsenide surface.

The selection of this particular adsorptive system is not accidental. On the one hand, Group-I metals, having typical metallic properties, contain only one electron in the outer shell, and this electron is responsible for adsorption. On the other hand, the electronic and crystal structures of the gallium arsenide surface have been studied much more extensively than the surface of other III–V compounds [2].

The majority of calculations for the AM/GaAs system are based on a certain version of the density functional formalism [3]. Like all *ab initio* approaches, the density functional formalism has decisive advantages but faces difficulties when applied to calculating the $\Delta\phi(\Theta)$ function (where $\Theta = N/N_{\text{ml}}$ is the coverage, N is the adatom density, and N_{ml} is the adatom density in a monolayer). In particular, it is necessary to take into account the actual geometry of the adsorption layer, which changes stepwise with Θ due to structural transformations. Thus, one is forced to calculate $\Delta\phi$ for several characteristic coverage values, which makes comparison with experimental data difficult. Note that there are a number of model approaches to the problem [1, 4, 5] which allow for the parametric description of the $\Delta\phi(\Theta)$ function.

In [6, 7], we suggested a simple scheme making it possible to calculate the variation $\Delta\phi$ of the work function with Θ in an adsorptive system. The model was applied to AM adsorption on silicon and rutile. It is known [8] that basically adatoms interact via (i) dipole–dipole repulsion, causing their depolarization and a shift of their quasi-levels, as well as (ii) direct and (iii) indirect electron exchange between them, which causes quasi-levels to split and a quasi-two-dimensional surface band to arise. In [6, 7], all these channels were considered. However, while dipole–dipole interaction was considered directly, the diffusion of quasi-levels into the band was simulated. Namely, we assumed that the half-width Γ_0 of an isolated adatom quasi-level changes to $\Gamma = \Gamma_0(1 + \gamma\Theta)$ as the coverage increases (here, γ is a dimensionless parameter). According to the model [6, 7], both tunnel and Auger processes contribute to the broadening of the isolated adatom level.

It should be emphasized that the structure of the adsorption layer is ignored in our model: only the surface density of adatoms is of importance. Such a crude simplification is yet adequate (at least at low coverages) in the case of adsorption of alkali metals with a large atomic charge. Therefore, the basic channel of interaction between alkali adatoms is dipole–dipole repulsion, which is proportional to R_a^{-3} (R_a is the distance between neighboring adatoms) and has circular symmetry in the plane of the surface. Also, no consideration is given in the model to the question of which particular surface atom (Ga or As) an AM adatom binds to, because it suffices to know that the electron of the AM atom will be transferred to the conduction band of the substrate.

As was shown in [9, 10], the adatom charge Z is expressed as

$$Z(\Theta) = \frac{2}{\pi}\arctan\frac{\Omega - \xi\Theta^{3/2}Z(\Theta)}{\Gamma(\Theta)}, \quad \xi = 2e^2\lambda^2 N_{\text{ml}}^{3/2}A. \quad (1)$$

1063-7842/04/4904-0475$26.00 © 2004 MAIK "Nauka/Interperiodica"

Table 1. Model parameters for cesium adsorption on the (100) surface of gallium arsenide

Parameter	Ω, eV	Γ_0, eV	γ	Φ, eV	ξ, eV
I [11]	2.91	1.93	2.09 2.76	13.5	9.2
II [12]	2.91	1.26	2.84	13.5	9.2

Note: The upper and lower values of γ in the first row correspond to 300 and 200 K, respectively.

Table 2. Model parameters for alkali metal adsorption on the (110) surface of gallium arsenide [14]

Parameter	Ω, eV	Γ_0, eV	γ	Φ, eV	ξ, eV
K	2.74	2.83	0.52	19.1	12.7
Rb	2.75	2.35	0.64	17.0	11.0
Cs	2.81	2.40	0.15	17.4	12.1

Here, Ω is the energy of the adatom quasi-level relative to the Fermi level of the substrate, ξ is the constant of dipole–dipole repulsion between adatoms, 2λ is the arm of a surface dipole formed by the adatom and its image in the substrate (we neglect the dielectric correction factor $(\varepsilon_0 - 1)/(\varepsilon_0 + 1)$, where ε_0 is the static permittivity), and $A \approx 10$ is a dimensionless coefficient weakly dependent on the geometry of the adatom array. The change in the work function $\Delta\phi$ is expressed as [9, 10]

$$\Delta\phi(\Theta) = -\Phi\Theta Z, \quad \Phi = 4\pi e^2 N_{ml}\lambda. \qquad (2)$$

In order to determine the model parameters, we will use the procedure proposed in [6, 7], which consists in the following. First, we experimentally find the initial slope of the function $\Delta\phi(\Theta)$ (i.e., $d\Delta\phi/d\Theta$ at $\Theta \longrightarrow 0$) and the change $\Delta\phi_{ml}$ in the work function of the adsorptive system when the coverage equals one monolayer. These two quantities are taken as fitting parameters, because (i) the initial slope of $\Delta\phi(\Theta)$ determines the dipole moment $p_0 = 2Ze\lambda$ of an isolated adatom and (ii) from the closeness of $\phi + \Delta\phi_{ml}$ to the work function of the corresponding alkali metal, one can judge to what extent the properties of the first AM monolayer approach the properties of the bulk material.

Let us consider adsorption of cesium atoms on the GaAs(100) surface using experimental data from [11, 12]. We assume that $N_{ml} = 4 \times 10^{14}$ atoms/cm^2 (see, e.g., [12–14]) and that the time of growth of a monolayer in [11] (exposure time) is 500 s. Next, we set $\lambda = 2$ Å, which is somewhat lower than the half-sum of the atomic and ionic radii (2.24 Å), reflecting the fact that an adatom in a submonolayer film is mainly in the ionic state (see below). The energy of the quasi-level is given by

$$\Omega = \phi - I + e^2/4\lambda, \qquad (3)$$

where I is the ionization energy of an AM atom (3.89 eV for cesium [15]) and $\phi = 5$ eV is the work function of the GaAs(100) surface [11].

Note that, in the present model, the only direct characteristic of the semiconductor is the work function ϕ, which obviously varies with doping level. Theoretically, it would be more logical to use the electron affin-

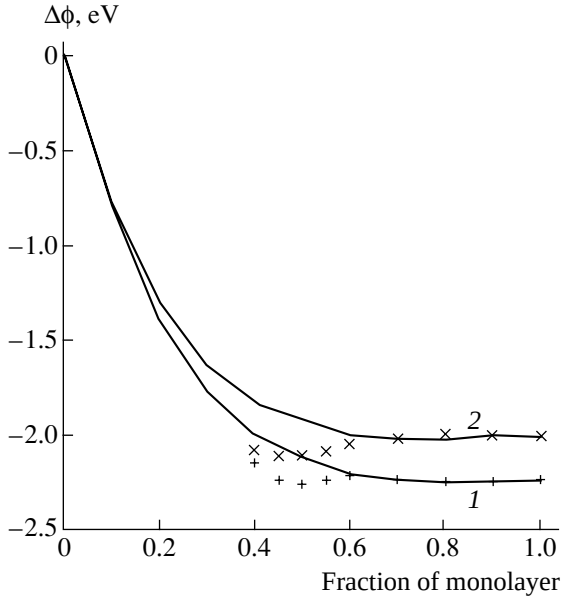

Fig. 1. Cesium adsorption on the (100) surface of gallium arsenide [11]. The solid lines were calculated at (*1*) 300 and (*2*) 200 K. The symbols are data points taken at (+) 300 and (×) 200 K.

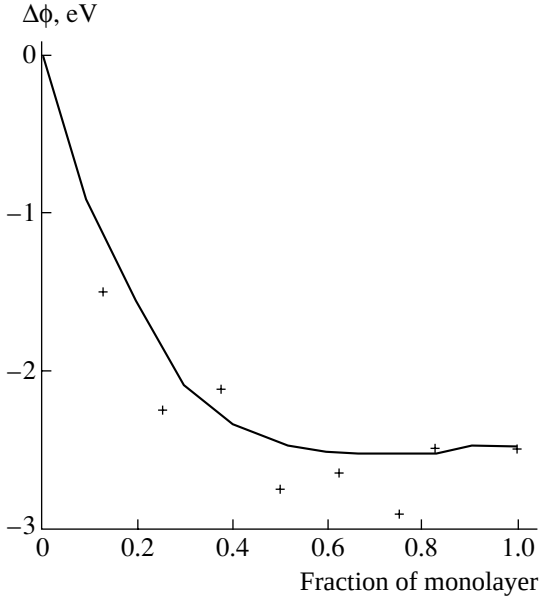

Fig. 2. Same as in Fig. 1 according to [12]. (+) Data points.

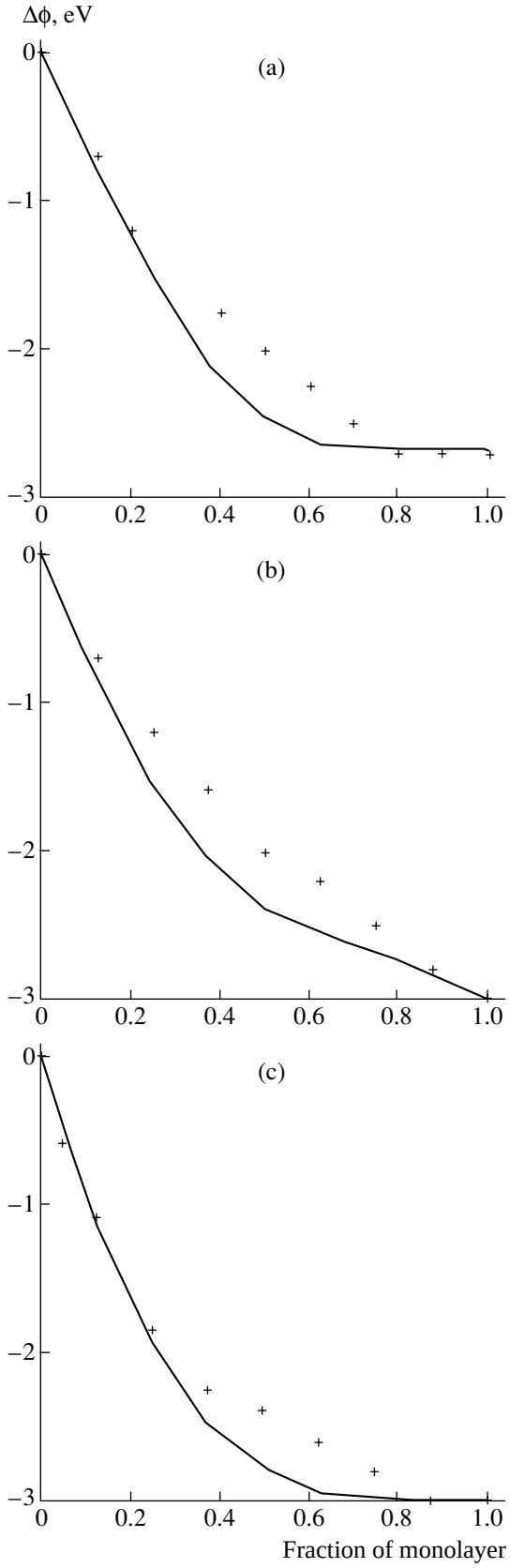

Fig. 3. Adsorption of (a) potassium, (b) rubidium, and (c) cesium on the (110) surface of gallium arsenide [14]. (+) Data points.

ity or ionization energy of the semiconductor as a reference level. However, such an approach is appropriate only for intrinsic semiconductors. For doped semiconductors, we would have to introduce the density of impurity states, as was done, e.g., in [16]. This complicates the model. In addition, nothing other than the value of $\Delta\phi$ is measured in the experiment. Therefore, we estimate the quasi-level energy by relationship (3).

The model parameters thus obtained are presented in Table 1 (row 1). Row 2 lists the values estimated from the data of [12]. The discrepancy between the experimental data in [11] and [12] probably reflects the different structures of the clean GaAs surface. The authors of [11] argue that surface symmetry is $c(8 \times 2)$, while in [12], the surface structure is identified as (4×2). Figures 1 and 2 compare the results of calculation with the experimental data from [11, 12]. In both cases, the calculation and experiment are in satisfactory agreement. However, two circumstances are noteworthy. The calculated curve *1* in Fig. 1 is monotonic, whereas the data points exhibit a weak minimum at $T = 300$ K.[1] For reasons not well understood, Fig. 2 demonstrates a great scatter of experimental data.

Consider now adsorption of potassium, rubidium, and cesium on the GaAs(110) surface, which was studied experimentally in [15]. Following [15], we take $N_{ml} = 6.4$, 5.3, and 4.8×10^{14} atoms/cm^2 for K, Rb, and Cs, respectively. The scaling procedure yields $\lambda = 1.65$, 1.77, and 2.0 Å in the same sequence. The model parameters are given in Table 2. The results of calculation are compared with the experimental data in Fig. 3. It follows that, for intermediate coverages, the experimental values of $|\Delta\phi(\Theta)|$ are noticeably lower than the calculated ones. Evidently, in this coverage range, our model somewhat overestimates the effect of depolarization in the submonolayer, although the reasons for the linear variation of $\Delta\phi(\Theta)$ are not quite clear. In general, the model results are in satisfactory agreement with the experiment, especially with regard to the simplicity of the model.

Thus, in view of [6, 7], our model adequately describes work function variations caused by alkali metal adsorption on semiconductor substrates.

REFERENCES

1. T. Bechshtedt and R. Enderlein, *Semiconductor Surfaces and Interfaces: Their Atomic and Electronic Structures* (Academic-Verlag, Berlin, 1988; Mir, Moscow, 1990).
2. W. Mönch, Rep. Prog. Phys. **53**, 221 (1990).
3. F. Bechstedt and M. Scheffler, Surf. Sci. Rep. **18**, 145 (1993).
4. T. Kato, K. Ohtomi, and M. Nakayama, Surf. Sci. **209**, 131 (1989).
5. T. U. Kampen, M. Eyckeler, and W. Mönch, Appl. Surf. Sci. **123–124**, 28 (1998).

[1] The model proposed is also capable of describing the nonmonotonic behavior of the function $\Delta\phi(\Theta)$ [6, 7].

6. S. Yu. Davydov and A. V. Pavlyk, Fiz. Tekh. Poluprovodn. (St. Petersburg) **35**, 831 (2001) [Semiconductors **35**, 796 (2001)].
7. S. Yu. Davydov and I. V. Noskov, Zh. Tekh. Fiz. **72** (11), 137 (2002) [Tech. Phys. **47**, 1481 (2002)].
8. O. M. Braun and V. K. Medvedev, Usp. Fiz. Nauk **157**, 631 (1978) [Sov. Phys. Usp. **32**, 328 (1978)].
9. J. P. Muscat and D. M. Newns, J. Phys. **7**, 2630 (1974).
10. S. Yu. Davydov, Fiz. Tverd. Tela (Leningrad) **19**, 3376 (1977) [Sov. Phys. Solid State **19**, 1971 (1977)].
11. M. Kamaratos and E. Bauer, J. Appl. Phys. **70**, 7564 (1991).
12. K. Yamada, J. Asanari, M. Naitoh, and S. Nishigaki, Surf. Sci. **402–404**, 683 (1998).
13. J. Derrien and A. D'Avitaya, Surf. Sci. **65**, 668 (1977).
14. J. E. Ortega and R. Miranda, Appl. Surf. Sci. **56–58**, 211 (1992).
15. *A Handbook of Physical Quantities*, Ed. by I. S. Grigoriev and E. Z. Meilikhov (Énergoatomizdat, Moscow, 1991; CRC, Boca Raton, 1997).
16. S. Yu. Davydov, Fiz. Tekh. Poluprovodn. (St. Petersburg) **31**, 1236 (1997) [Semiconductors **31**, 1062 (1997)].

Translated by M. Lebedev

Technical Physics, Vol. 49, No. 4, 2004, pp. 479–484. Translated from Zhurnal Tekhnicheskoĭ Fiziki, Vol. 74, No. 4, 2004, pp. 102–107.

SURFACES, ELECTRON AND ION EMISSION

Thin Carbon Films. I: Growth by Charged Particle Beams

A. P. Semyonov and I. A. Semyonova

Department of Physical Problems, Buryat Scientific Center, Siberian Division, Russian Academy of Sciences, Ulan-Ude, 670047 Buryat Republic, Russia

e-mail: semenov@pres.bsc.buryatia.ru

Received March 28, 2003; in final form, August 18, 2003

Abstract—A magnetron-discharge-based source of ions and electrons with cold hollow and uncooled rodlike cathodes that offers improved physical and technical characteristics is considered. © *2004 MAIK "Nauka/Interperiodica".*

INTRODUCTION

Development of equipment for thin-film growth by ion-beam sputtering implies the design of efficient and reliable gas-discharge ion sources, among which those based on cold-cathode discharge seem to be the most promising [1]. The basic commonly recognized advantages of using cold-cathode discharge for generating sputtering ion beams are (i) an extremely long time ($>10^3$ h) of maintaining the discharge initiated in a chemically active gas (versus <10 h for filamentary cathodes under the same conditions) and (ii) a relatively low price of an extracted ion (the applied power is less than that needed for cathode heating). Other no less important advantages of cold-cathode systems are an extremely high mechanical robustness, cost efficiency, simple design, and maintainability. Taken together, these advantages, keeping pace with the general requirements for ion sources, extend the thin-film growth potentialities.

EXPERIMENTAL

In currently used sources of electrons and ions that are based on cold-hollow-reflex cathode discharge, the energy delivered to the discharge gap evolves mainly at the electrodes and is removed by a cooling system. This energy may enhance the efficiency of such plasma emissive devices if an uncooled rodlike cathode is placed on the discharge axis. In this way, the reflex electrodes of a hollow-cathode discharge turn into the electrodes initiating a hollow-cathode magnetron (HCM) discharge [2]. Figure 1 shows schematically the electrode structure of a hollow-cathode magnetron discharge where the cathode is heated to temperatures of thermionic emission. Along with cavity cathode *3*, the system includes rodlike cathode *2* with a diameter ranging from 0.25 to 4 mm, which is placed on the cavity axis coaxially with the output aperture and is free to move in the opening of cathode *6*. During current measurements, cathode *2* is electrically insulated from hollow cathode *3*. The rod is coaxial with 12-mm-long cylindrical anode *1* 18 mm in diameter. Ring-shaped magnet *5* produces an axial magnetic induction of 0.1 T. The working gas is pumped off through the opening in reflex cathode *6*. This opening can also transmit a plasma when the discharger serves as a plasma source (to provide electrons or ions) or play the role of a nozzle ejecting atomic particles when a discharge chamber is incorporated into a source of atomic hydrogen. Direct measurement of the rod temperature was carried out by an OPPIR-017 pyrometer. A plasma-forming gas (air) flows through opening *4* at the edge of the cavity. The gas flow rate was 0.8–1.2 (mPa m^3)/s. The plasma parameters were measured by a cylindrical tungsten probe 0.05 mm in diameter, which was introduced into the opening of cathode *6*. Its working length was limited to 1 mm (the rest of the probe was covered by alundum). For high-voltage extraction of cathode-plasma particles, an accelerating electrode was placed at the axis of reflex cathode *6*. An ion source based on hollow-cathode magnetron discharge (Fig. 2) was incorporated into a VUP-5 vacuum station redesigned for thin-film

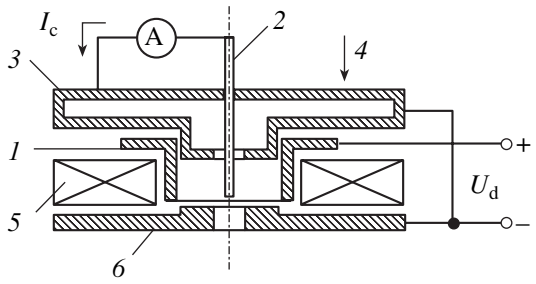

Fig. 1. Electrode configuration generating a hollow-cathode magnetron discharge: (*1*) anode, (*2*) rodlike cathode, (*3*) hollow cathode, (*4*) gas delivery, (*5*) magnet, and (*6*) emitting cathode.

Fig. 2. General view of the gas-discharge plasma source.

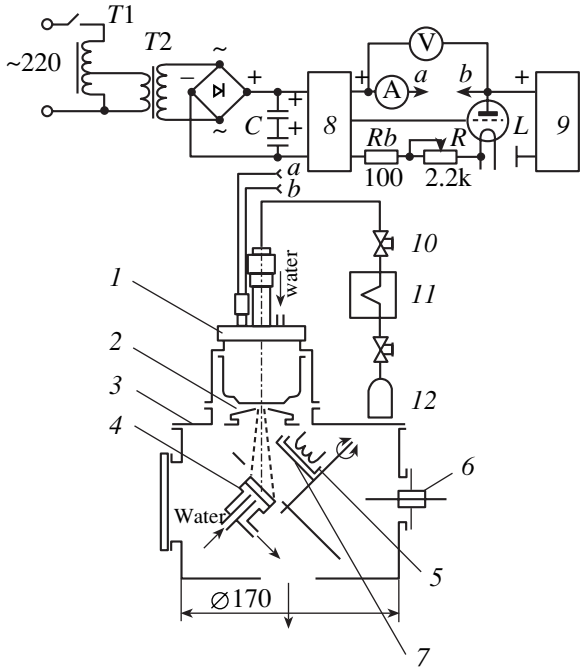

Fig. 3. Design of the ion-beam sputterer: (*1*) plasma source of charged particles, (*2*) accelerating electrode, (*3*) sputtering chamber, (*4*) target holder, (*5*) furnace, (*6*) mechanical drive, (*7*) shutter, (*8*) regulated discharge-current source, (*9*) high-voltage rectifier, (*10*) leak, (*11*) flow gauge, and (*12*) gas tank.

deposition by ion-beam sputtering (Fig. 3). In the final form, the sputterer, in essence, consists of vacuum chamber *3*, where ion source *1* is mounted. Through an aperture on the axis of accelerating cathode *2*, the ion beam arrives at the working space and strikes target *4*. The target has a diameter of 30–50 mm and is placed on a holder cooled by running water. The incident ion beam forms an angle of 45°–60° with the normal to the surface. The end face of the accelerating electrode and the surface being sputtered are spaced 40–70 mm apart. Molybdenum furnace *5* with a resistive tungsten heater is used to keep the substrate temperature within 373–1473 K. The furnace with substrates is placed near the accelerating cathode so that the growth surface of the substrate is parallel to the target being sputtered by ions. The working chamber is evacuated to a residual pressure ranging between 10^{-4} and 10^{-3} Pa. During film growth, the pressure in the working space is kept within $(2–3) \times 10^{-2}$ Pa.

RESULTS AND DISCUSSION

The characteristics of the gas-discharge source of ions and electrons that is considered in this work to a great extent depend on the HCM discharge properties. Figure 4 illustrates the behavior of the discharge under various conditions, showing the currents of the rodlike (curve *1*), hollow (curve *2*), and reflex (curve *3*) cathodes, as well as the maintaining (discharge) voltage (curve *4*), versus the discharge current when the radius of the uncooled tungsten rodlike cathode is r_c = 0.75 mm. Argon, air, hydrogen, nitrogen, and oxygen were used as a working gas with a flow rate on the order of 1.2 (mPa m^3)/s. The average pressure in the cathode cavity was ≈10 Pa. Characteristic discharge conditions may be distinguished in Fig. 4. Low discharge currents (0.02–0.05 A) initiate and maintain a low-current magnetron discharge with the ascending *I–V* characteristic. The distribution of the current among the cathodes is fairly uniform. The region of cathode potential drop in front of the cavity aperture prevents the discharge plasma from penetrating into the cathode cavity. The near-cathode ion sheath covers the cathode cavity aperture and separates the plasma from the cavity, so that the cavity has no effect on the discharge. As the discharge current grows, the inequality $l_c \le (r_a - r_c)$ (where r_a is the cavity aperture radius, r_c is the rod radius, and l_c is the characteristic length of cathode voltage drop region in front of the cavity aperture) becomes valid. As a result, the ion sheath at the cavity aperture breaks down and the cathode cavity is filled with the plasma with a potential close to the anode potential ($U_c \sim 0.8U_d$). The length l_c decreases with discharge current if $3I_d dU_d/2U_d dI_d < 1$ [3]. Note that high currents in the hollow cathode are due to the ions produced by fast secondary electrons entering the plasma from the region of cathode voltage drop.

The cathodic rod is heated to 2.3×10^3 K by the energy coming from the near-cathode discharge region.

Pyrometer indications were corrected for plasma radiation. The temperature T_c was measured after fast quenching of the discharge (see table). If the temperature is assumed to drop at a rate of ≈10^6 K/s, the temperature value measured during plasma decay (for ~10^{-5} s) is ≈10 K lower than the true value. To measure T_c accurately, a thermoelectric tungsten–rhenium calibration converter was formed on the end face of the tungsten rod by making a VR-5/20 rhenium–tungsten junction. The tungsten–rhenium junction was heated to

T_c and did not disturb the discharge structure and conditions. In this case, a considerable redistribution of the cathode currents is observed. Specifically, the hollow cathode current I_h steeply rises, the rodlike cathode current I_c slightly increases, and the reflex cathode current I_r decreases. The maintaining voltage drops stepwise from 525 to 350 V. In the interval $0.2 < I_d < 0.4$ A, the discharge behaves as a hollow-cathode glow discharge, for which the hollow cathode current substantially exceeds the rodlike and reflex cathode currents. The maintaining voltage slightly increases. At a discharge current of 0.4 A, the discharge conditions change. The temperature of the rodlike cathode grows rapidly from 2.3×10^3 to 2.5×10^3 K, and its current increases abruptly from 0.05 to 0.2 A. At the same time, the hollow cathode current decreases from 0.3 to 0.17 A, so that $I_c > I_h$. The redistribution of the cathode currents is accompanied by a sharp drop of the maintaining voltage from 360 to 210 V, since the discharge takes the low-voltage high-current form. As the discharge current grows from 0.45 to 0.6 A, the sustaining voltage lowers gradually; the rod temperature rises to 2.6×10^3 K; and the currents I_h, I_c, and I_r increase (I_c with the highest rate). The processes that take place in the plasma near the rodlike cathode (Fig. 1) define the parameters of the discharge as a whole, and the dependences observed (Fig. 4) indicate that the rodlike cathode has a decisive effect on the discharge (the transition to the conditions specified by the rod-cathode is marked by a step in the discharge voltage and cathode currents at $I_d \sim 0.4$ A). Such behavior is akin to the so-called hollow-cathode effect, which shows up at $I_d \sim 0.1$ A. The decisive effect of the rodlike cathode is observed when its current equals 0.5 of the discharge current, while the hollow and reflex cathodes account for 0.3 and 0.2 of the discharge current, respectively. The fraction of the thermionic current reaches $(0.3–0.35)I_d$. The descending current–voltage dependence of the discharge is likely due to a change in the emission mechanism of the rodlike cathode; namely, the contribution from thermal electron emission to ionization in the cathodic sheath becomes considerable. Primary electrons due to electron–ion and thermal electron emission may leave the rodlike cathode surface with appreciably different initial velocities. If one assumes that the initial velocity of thermal electrons is lower that the velocity of electrons escaping from the cathode as a result of γ processes, the magnetic field acting on thermal electrons seemingly increases and a reduction of the discharge voltage may be expected if the condition $l_c \sim R_L$ is fulfilled (where R_L is the Larmor radius of an electron), which is the case in experiment. The descending *I–V* characteristic of the discharge cuts significantly the cost of an extracted ion and, thus, raises the energy efficiency of the system.

Along with pyrometric measurements, the cathodic rod temperature and the fraction of the thermionic current in the total cathodic current were estimated by

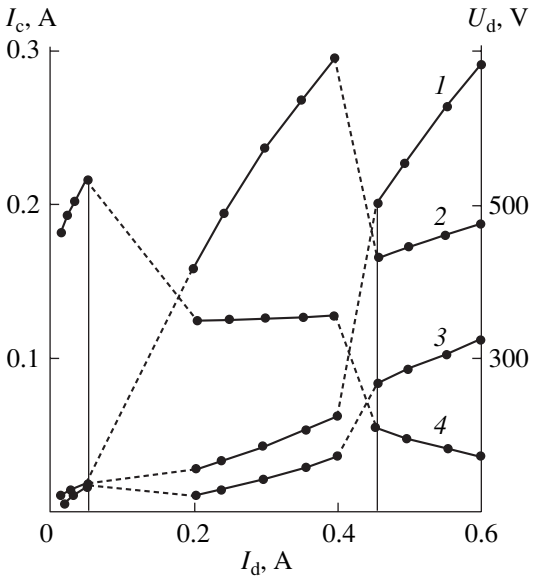

Fig. 4. (*1*) Tungsten rodlike, (*2*) hollow, and (*3*) reflex cathode currents and (*4*) maintaining voltage vs. the discharge current. $r_c = 0.75$ mm.

replacing rod *2* (Fig. 1) with two closely spaced parallel vanadium and rhenium rods insulated from each other and from hollow cathode *3*. The diameters of the rods and the spacing between their axes were 0.25 and 0.75 mm, respectively. The current of each of the cathodic rods can be calculated by the expression

$$I_c = I_i(1 + \gamma) + I_e, \quad (1)$$

where I_i is the ionic current toward the rod, I_e is the thermionic current, and γ is the electron–ion emission factor.

Under the assumption that the ionic currents toward the rods are equal to each other and the rods are cooled by the thermionic currents roughly to the same extent (hence, the difference in γ and ε, where ε is the emissivity, is small), the difference between the currents of the

Rodlike cathode temperature at different discharge currents

Discharge current, A	Rodlike cathode temperature T_c, 10^3 K
0.2	2.3
0.4	2.5
0.66	2.6
1.0	2.65
1.32	2.7
1.77	2.75

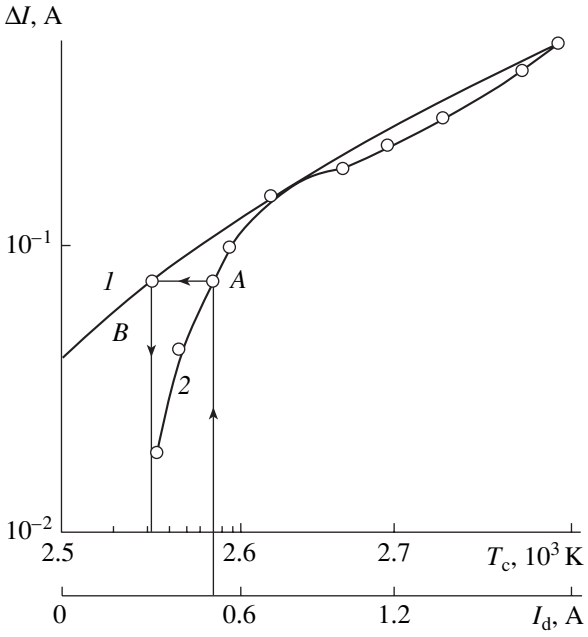

Fig. 5. Difference in the currents of the rods (*1*) as a function of temperature (calculation) and (*2*) discharge current (experiment).

rods in the discharge may be represented in the form

$$\Delta I = I_{cW} - I_{cRe} \sim (I_{eW} - I_{eRe}). \quad (2)$$

The thermionic current was calculated by the Richardson formula

$$I_e = AT_c^2 S_c \exp(-e\varphi_0/kT_c), \quad (3)$$

where T_c is the temperature of the cathodic rod, S_c is its surface area, k is the Boltzmann constant, φ_0 is the work function, and A is the emission constant.

We assumed in our calculations that $A = 7.5 \times 10^5$ A/(m^2 K^2) and $\varphi_0 = 4.54$ eV for tungsten and $A = 2.6 \times 10^6$ A/(m^2 K^2) and $\varphi_0 = 5.0$ eV for rhenium.

Comparing the calculated $\Delta I(T_c)$ and experimental $\Delta I(I_d)$ dependences (Fig. 5), where I_d is the discharge current, one can estimate the temperature of the rods at different I_d. For example, point A (Fig. 5) shows the difference ΔI in the currents of the rods measured at the discharge current 0.5 A. The temperature 2.53×10^3 K (point B in Fig. 5) corresponds to this point. As I_d changes from 0.6 to 2 A, the temperature of the cathodic rods increases from 2.6×10^3 to 2.78×10^3 K. Note that the difference in the rod currents becomes considerable (Fig. 5). However, in the experiments with two tungsten rods, the difference in their currents was within 5%. This suggests that both rods were under identical conditions and that the difference in the currents of the tungsten and rhenium rods is associated mainly with their different thermionic properties. Since heating of the cathodic rod greatly increases its thermionic current, one might expect that the power required for the discharge current to reach a desired level also depends on the thermionic properties of this rod.

Let us estimate the feasibility of the descending I–V characteristic of the discharge under the conditions of thermionic emission from the cathodic rod. We make the following assumptions: (i) the plasma potential U_0 is close to the potential U_a of the anode (the plasma potential was determined at the inflection point of the I–V curve for a single cylindrical probe), $U_0 = (0.8–0.85)U_a$; (ii) the plasma density gradient along the length of the rod is insignificant; (iii) the rod is uniformly heated along its length by ions accelerated in the cathodic sheath; and (iv) collisions in the space charge region between the plasma and the rod are absent (the working gas pressure in the discharge chamber is low, 0.9–1 Pa; such pressures correspond to the condition $\lambda_e > l_c$, where λ_e is the electron free path and l_c is the length of the cathode potential drop region; the cathode potential obeys the Child's law).

The cathodic rod current can be represented in the form

$$I_c = K_1 I_d, \quad (4)$$

where the coefficient K_1 is found from the experimental dependence $I_c(I_d)$ (Fig. 6).

The cathodic rod temperature is defined by the balance between the energy being released by ions accelerated in the cathode potential drop region and the energy radiated by the rod:

$$T_c = (K_2 I_i U_d)^{1/4}, \quad (5)$$

where I_i is the ion current toward the rod; U_d is the discharge voltage; $K_2 = (6\pi L r_c \varepsilon\sigma)^{-1}$; L and r_c are the length and radius of the cathodic rod, respectively; ε is the emissivity; and σ is the Stefan–Boltzmann constant.

The expression for thermionic current in the presence of an electric field near the rod surface can be written as

$$I_e = K_3 T_c^2 \exp(K_4 U_d^{-1/8} - K_5 T_c^{-1}), \quad (6)$$

where $K_3 = AS_c$, $S_c = 2\pi r_c L$, $K_4 = (e^{11} M_i)^{1/8} (2^{5/2}\pi^2 k^4 K_2 \varepsilon_0^3 S_c)^{-1/4}$, ε_0 is the permittivity, M_i is the ion mass, e is the elementary charge, $K_5 = e\varphi_0 k^{-1}$, and $e\varphi_0$ is the effective work function.

Substituting (4)–(6) into Eq. (1), we find the relationship between U_d and I_d in the form

$$K_1 I_d = K_6 T_c^4 U_d^{-1} + K_3 T_c^2 \exp(K_4 U_d^{-1/8} - K_5 T_c^{-1}), \quad (7)$$

where $K_6 = (1 + \gamma) K_2^{-1}$.

Figure 6 shows the calculated dependence $U_d(I_d)$ obtained by substituting tungsten rod temperatures T_c measured at different discharge currents. We suggest that the descending I–V curve of the magnetron dis-

charge with the heated cathodic rod may be associated with thermionic emission from the cathodic rod under the given experimental conditions. Note also that the higher the thermionic capacity of the cathodic rod, the lower the maintaining voltage of the discharge. Our electronic configuration of the HCM discharge with the rodlike cathode makes it possible to provide efficient emission of charged particles from the near-axial plasma of the discharge with the electron and ion currents accounting for 0.4–0.45 and 0.08–0.12 of the total discharge current, respectively. The correlation between the emissivity and the discharge-current dependence of the plasma density in the absence of an accelerating voltage is indirect evidence that the effect of emission on the discharge plasma density and the effect of the discharge current on the exposed (emitting) area of the plasma are insignificant. The densities of the thermionic and ion currents attained in the experiment (40 and 0.6–0.75 A/cm^2, respectively) are indicative of a fairly high emissivity of the HCM discharge plasma. These findings were employed in the design of the plasma source with an uncooled rod cathode (Fig. 2). Although the cathodic rod is heated in the HCM discharge plasma to temperatures of thermionic emission, it is free from the well-known drawbacks of directly heated (filamentary) cathodes. The advantages of our design appear because the cathode is heated by plasma ions accelerated by the electric field of the cathodic sheath. This circumstance makes heating circuits, which contain high-current vacuum-tight feedthroughs, unnecessary. Also, this eliminates the need for high-power supplies, which usually demand reliable insulation, since they usually are under a high potential of the ion-accelerating field. One-sided mounting of the rod by its part near the cold edge greatly simplifies the design of the electron–ion source and suppresses the effect of mechanical stresses, which usually arise in filamentary cathodes as a result of their heating, cooling, or operation in high magnetic fields. Efficient electron emission from a directly heated cathode requires that the heating current be several tens of amperes. In this case, the cathode may be locally overheated, which shortens its service life. In contrast, a rod cathode remains efficient up to its ultimate (smallest) thickness of 10^{-2} mm in the region of most intensive heating. The descending run of the *I–V* curve of the discharge and the linear growth of the cathode plasma density with increasing discharge current up to an ultimate value of ≈2 A are explained by smooth glowing-to-arc discharge transition. This remarkable feature provides high technological properties of ion–electron sources based on hollow-cathode discharge in our electrode configuration. In particular, our experimental values are as follows: the maintaining voltage varies in the range 85–180 V; the discharge current is up to 2 A; the ion beam current is 0.1–0.15 A; the cost of an extracted ion is 1–2 W/mA, which is two to five times lower than in the conventional ion sources; the electron beam density is 1 A; and the energy efficiency is 15 mA/W, which is six times higher than that of electron emitters based on hollow-cathode electric discharge. Such efficient gas-discharge sources allow for a considerable increase in output ion and electron currents as the glow discharge smoothly switches to a diffusion arc at $I_d > 2$ A.

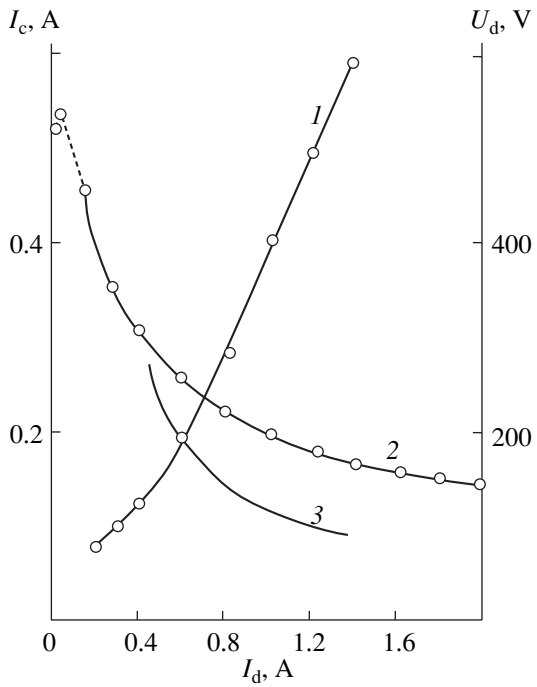

Fig. 6. (*1*) Rodlike cathode current and (*2*) experimental and (*3*) calculated maintaining voltage vs. the discharge current.

CONCLUSIONS

The electrode structure of a hollow-cathode magnetron discharge suggested in this work allows one to generate high-current ion beams at a low cost of an extracted ion and electron beams at a high energy efficiency [4, 5]. Compared with conventional sources, such a configuration offers a higher density plasma due to thermionic emission arising when the glow discharge gradually switches to a high-current vacuum arc that is free of a cathode spot. It also makes it possible to extend the application of HCM-discharge plasma source. Specifically, the new sources may be used for sharpening tungsten needles by ion sputtering and efficient generation of atomic hydrogen through the high-temperature activation of molecular hydrogen. This is of special importance in diamond-like carbon film growth and semiconductor surfaces processing.

ACKNOWLEDGMENTS

This work was supported by INTAS, project no. 2001-2399, and partially by the Lavrent'ev Competi-

tion of Young Scientists (Siberian Division, Russian Academy of Sciences), project no. 37.

REFERENCES

1. A. P. Semyonov, *Sputtering Ion Beams: Production and Application* (Izd. Buryat. Nauchn. Tsentr Sib. Otd. Ross. Akad. Nauk, Ulan-Ude, 1999) [in Russian].
2. A. P. Semyonov, USSR Inventor's Certificate No. 1375024 (1985).
3. M. A. Zav'yalov, Yu. E. Kreĭndel', A. A. Novikov, and L. P. Shanturin, *Plasma Processes in Electron Guns* (Énergoatomizdat, Moscow, 1989) [in Russian].
4. A. P. Semyonov and I. A. Semyonova, Izv. Vyssh. Uchebn. Zaved. Fiz., No. 9, 69 (2001).
5. A. P. Semyonov and I. A. Semyonova, in *Proceedings of the 5th International Conference on Vacuum Technology and Equipment, Khar'kov, 2002*, pp. 227–235.

Translated by A. Sidorova

Technical Physics, Vol. 49, No. 4, 2004, pp. 485–493. Translated from Zhurnal Tekhnicheskoĭ Fiziki, Vol. 74, No. 4, 2004, pp. 108–116.

EXPERIMENTAL INSTRUMENTS AND TECHNIQUES

Near-Field Microwave Tomography of Biological Objects

A. N. Reznik and N. V. Yurasova

Institute of Physics of Microstructures, Russian Academy of Sciences, Nizhni Novgorod, 603950 Russia

e-mail: reznik@ipm.sci-nnov.ru

Received October 20, 2003

Abstract—A method of finding the subsurface temperature distribution in biological media from near-field microwave probing data is suggested. The electrodynamic problem of probe response to a temperature profile disturbance $\Delta T(z)$ in a medium is solved. An integral equation that relates the shift of the resonant frequency of the probe to the function $\Delta T(z)$ is derived. The effective near-field probing depth is shown to depend on the probe aperture, its elevation above the surface, and the wavelength. In this method, several probes operate simultaneously, receiving signals from different depths, and the temperature profile is reconstructed by inverting the related integral equation. The components and parameters of a measuring facility that provides the temperature profile reconstruction accurate to 0.5°C to a depth of up to 5 cm are established. The procedure of near-field diagnostics is simulated in a computer experiment to check the accuracy predicted. Calculation is performed based on a model of permittivity of biological media. *© 2004 MAIK "Nauka/Interperiodica".*

INTRODUCTION

Measuring the internal temperature of biological objects is of great importance in medical applications. Inflammatory processes and tumors in the human organism are usually localized, and the temperature rises at the focus of inflammation. If a sore tissue is located sufficiently deep, temperature variations on the surface are absent or weak.

Measuring the tissue temperature under the conditions of hyperthermia is a primary problem of temperature diagnostics. This way of treating malignant tumors dates back to the 1960s, and a large body of relevant theoretical and experimental data has been collected to date (see, e.g., [1–3]). During hyperthermia, the temperature is raised to 41–42°C for a time with a special external heater. This increase in temperature is often concentrated directly on the tumor (local hyperthermia). It is necessary that the elevated temperature be kept within a very narrow interval, since overheating destroys good cells and underheating stimulates, rather than suppresses, the growth of malignant cells. Thus, temperature control during hyperthermia is currently a key medical problem, especially in view of the fact that not the temperature at a separate point must be measured but the temperature profile $T(z)$ across the depth must be constructed.

Obvious disadvantages of today's invasive (contact) methods of measuring the internal temperature are inconvenience for patients, the effect of contact sensors on temperature distributions being recorded, and the complexity of point-to-point profile construction. Among the noninvasive (noncontact) methods of thermometry currently available are IR thermal imaging [4], microwave radiometry [5], and nuclear magnetic resonance [6]. However, none of them has gained wide acceptance because of substantial inherent drawbacks. For example, thermal imaging, because of a low penetration of IR radiation (less than 1 mm), may be used only for skin investigation. Microwave radiometry, though being free of this disadvantage, is sensitive to external interference. In addition, the latter method needs compact high-efficiency antennas, which is a technical challenge. Thus, the need for new techniques of subsurface temperature measurement that are free of above disadvantages seems obvious.

In this work, we suggest a method based on near-field microwave probing. Near-field diagnostics has become common in studying the surface distribution of permittivity [7]. However, near-field probing has not yet been applied for vertical tomography, by which the permittivity, $\varepsilon(z)$, or temperature, $T(z)$, profile is reconstructed. The potentialities of a near-field detector (NFD) will be demonstrated below. Also, we will determine the NFD parameters providing a desired sensitivity and accuracy of $T(z)$ reconstruction as applied to biological objects.

The key element of an NFD is a probe with an aperture diameter D that is much smaller than the radiation wavelength λ ($D \ll \lambda$). At present, advanced near-field microwave measuring systems offer the ratio D/λ at a level of 10^{-6} [8]. The possibility of producing probes with apertures much smaller than the dimension of radiating antennas results from an extremely high sensitivity of NFDs to a permittivity variation near the probe. Since D is responsible for the spatial resolution of the device, NFDs are often called near-field microscopes. Today, the resolution of NFDs is 1 μm or higher, i.e., is comparable to the resolution of optical microscopes. However, a superhigh resolution can be achieved at a sacrifice in penetrating power. In other

1063-7842/04/4904-0485$26.00

words, a very important advantage of microwaves over IR radiation (a much higher penetration into many, including biological, media) may be lost. It is clear that the effective near-field probing depth d_{eff} is related to the probe size D, although this issue calls for special investigation, which is performed in this work. Temperature diagnostics of the human body requires that the spatial resolution be at least 1–2 cm, which provides a probing depth of at least 3–5 cm. Whether or not this requirement can be satisfied will be shown below.

A prerequisite for the application of NFDs to temperature diagnostics of biological objects is the assumption that the complex permittivity $\varepsilon = \varepsilon_1 - i\varepsilon_2$ of these objects is temperature-dependent. Unfortunately, published data on direct measurement of this dependence are lacking. Therefore, we constructed a physical model of permittivity of biological objects that supports this hypothesis and also allows us to estimate the temperature sensitivity of a near-field measuring system.

MODEL OF PERMITTIVITY OF BIOLOGICAL OBJECTS

Our model is based on the assumption that a biological medium is a two-component system consisting of a dry insulator (with permittivity ε_i) and water (ε_w). The permittivity ε_{eff} of the mixture (biological medium) is found by the formula

$$\left\langle \frac{\varepsilon - \varepsilon_{eff}}{\varepsilon + 2\varepsilon_{eff}} \right\rangle = 0, \quad (1)$$

which follows from the equation for self-consistent field [9] (in (1), averaging is over the volume). If the volume content of water is ρ, we have

$$\rho \frac{\varepsilon_w(f, T) - \varepsilon_{eff}}{\varepsilon_w(f, T) + 2\varepsilon_{eff}} + (1-\rho)\frac{\varepsilon_i - \varepsilon_{eff}}{\varepsilon_i + 2\varepsilon_{eff}} = 0. \quad (2)$$

The permittivity ε_{eff} can be determined by solving algebraic equation (2) (later on, the subscript "eff" is omitted). We assume that ε_i is constant, while ε_w is a known function of temperature and frequency: $\varepsilon_w = \varepsilon_w(f, T)$. The function $\varepsilon_w(f, T)$ can be calculated, e.g., in terms of the semiempirical theory[10]. Formulas for ε_w that are used in this theory involve the degree of mineralization of water as an independent parameter (the degree of mineralization is related to the salinity S of water and specifies its conductivity σ). Then, to calculate the function $\varepsilon = \varepsilon(f, T)$, one needs to know three free parameters: ε_i, ρ, and σ. Their values are taken such that the model gives the best fit to published data for the frequency dependence of ε (these dependences are usually given for the normal body temperature $T = 37°C$). Figure 1 shows the calculated frequency dependences of the real and imaginary parts of the permittivity for a fatty tissue together with data points from [11]. For $\varepsilon_i = 1.2$, $\rho = 0.3$, and $\sigma = 2.13$ $(\Omega\ \mathrm{m})^{-1}$, agreement between the theory and experiment is fairly good. Similar results have also been obtained for other tissues (the related values of ε_i, ρ, and σ are listed in Table 1).

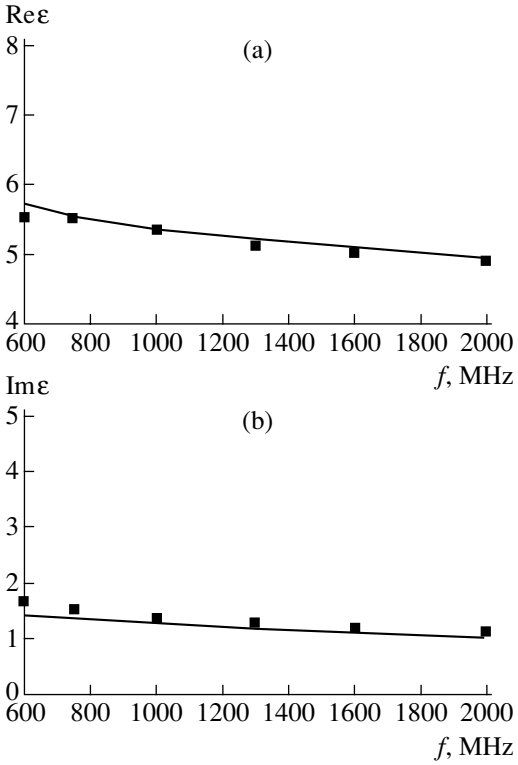

Fig. 1. (a) Real and (b) imaginary parts of the permittivity of fatty tissue vs. the frequency. Curves, calculation; symbols, data points from [11].

Thus, the model of two-component medium describes adequately the spectral dependence of ε for biological media. It may be assumed that dependences $\varepsilon(T)$ following from this model also reflect the real situation.

NEAR-FIELD DIAGNOSTICS OF VARIABLE-PERMITTIVITY MEDIA

The design of an NFD is depicted in Fig. 2. The probe is a microwave antenna with an aperture size D much smaller than the wavelength, $D \ll \lambda$. The aperture is placed in a vacuum at an elevation of $h \ll \lambda$ above the absorbing half-space surface. The permittivity of the medium varies with height:

$$\varepsilon(z) = \varepsilon_0 + \Delta\varepsilon(z), \quad (3)$$

where $\varepsilon_0 = \mathrm{const}$ is the undisturbed permittivity value and the correction $\Delta\varepsilon(z)$ is due to the temperature profile variation ($\Delta T(z)$) upon heating.

As the permittivity near the aperture of the antenna changes, so does the input impedance of the antenna $Z = R + iX$ because of a disturbance of the quasi-stationary electromagnetic field near the antenna. This, in turn, changes the coefficient Γ of reflection from the antenna

input (this coefficient is measured with a reflectometer). This change $\Delta\Gamma$ bears information on the disturbance of the permittivity, $\Delta\varepsilon$, and temperature, ΔT, in the vicinity of the probe. To improve the NFD sensitivity, the antenna is connected to the wave-guiding input of the reflectometer via a matching resonator, perfect matching being achieved at the resonant frequency f_0 ($\Gamma(f_0) = 0$). In this case, a shift in the frequency f_0 is the response to a disturbance of ε and the largest variations $\Delta\Gamma$ take place near the maximal steepness of the frequency response (i.e., when the working point is somewhat displaced relative to f_0). Since the antenna and matching resonator can be integrated on a single support, this integrated unit will be called the resonant probe.

Our further aim is to calculate a shift in the frequency f_0, which is related to the disturbance $\Delta\varepsilon(z)$. To this end, we represent the equivalent circuit of a resonant probe as a section of a twin line with a wave resistance Z_1 that is terminated by an impedance Z at one end and is open-circuited at the other end (Fig. 3). The system is excited in the plane *A*–*A* by means of a waveguide with an impedance Z_0, which simultaneously acts as a receiver of the reflected power. In this circuit, the section of the line serves as a matching resonator. The system is considered matched when the input impedance Z_{in} in the plane *A*–*A* equals the impedance Z_0. This condition is written in the form of two equations: $\mathrm{Re}Z_{in}(f_0) = Z_0$ and $\mathrm{Im}Z_{in}(f_0) = 0$. Detailed analysis of this circuit is given in [12], where matching was provided by properly selecting the resonator's arm length $l_{s,1}$.

If Z_1, $R \ll |X|$ (this conditions is met in electrically small antennas with $D \ll \lambda$), we have $l_s + l_1 \approx (\Lambda/2)(1 - Z_1/(|X|\pi))$, where $\Lambda = c/(\sqrt{\varepsilon_1} f_0)$ is the resonant wavelength, c is the speed of light in free space, and ε_1 is the effective permittivity of the line. Then, at $\Delta X/X \ll 1$, the frequency shift is given by

$$\frac{\delta f}{f_0} = \frac{Z_1}{\pi}\frac{\Delta X}{X^2}. \qquad (4)$$

Thus, a frequency response of the measuring system depends on the shift ΔX of the probe reactance, which is related to the disturbance of permittivity. Note that the distortion of the frequency response is associated not only with the shift in the resonant frequency f_0 but also with a change in the resonance curve width. It was shown [12] that the bandwidth of an electrically small antenna depends largely on losses in the matching resonator and insignificantly on losses due to radiation into the environment; therefore, the variation of the Q factor of the probe will be neglected.

The problem of calculating δf by formula (4) is reduced to finding the relationship between the disturbances of the reactance, ΔX, and permittivity profile $\Delta\varepsilon(z)$. This relationship can be found from the Poynting's theorem for harmonic fields with a frequency ω [13]:

$$X = \frac{4\omega}{|I|^2}\int_V \frac{|\mathbf{H}|^2 - \mathrm{Re}(\varepsilon)|\mathbf{E}|^2}{16\pi} dV, \qquad (5)$$

where I is the current at the input terminals of the antenna, **E** and **H** are the electric and magnetic fields in the environment, and ε is the permittivity of the environment. According to (3), $\varepsilon = \varepsilon(z)$ for $z < 0$ and $\varepsilon = 1$ for $z > 0$.

As is common for antenna problems, reactance (5) is determined by integrating the fields from sources specified on the antenna aperture over the environment. Quasi-stationary fields in such integrals obviously play a decisive role. Unfortunately, an analytical representation for the fields **E** and **H** in a half-space with an arbitrary (nonuniform) profile $\varepsilon(z)$ is absent. However, in the case considered, the problem can be considerably simplified.

We take into consideration that the change in the temperature of the medium in medical applications

Table 1. Parameters of biological tissues

	ρ	σ, $(\Omega\ \mathrm{m})^{-1}$	ε_d	α, $^\circ\mathrm{C}^{-1}$
Fat	0.3	2.13	1.2	0.016
Muscles	0.87	1.32	1.2	0.226
Skin	0.7	1.1	1.2	0.096

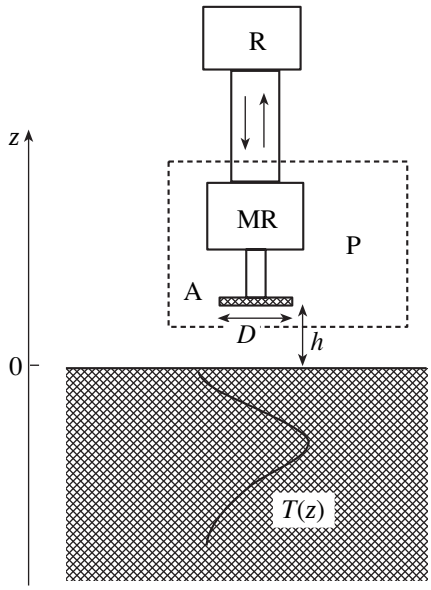

Fig. 2. Near-field measuring scheme: A, antenna; MR, matching resonator; R, reflectometer; and P, probe.

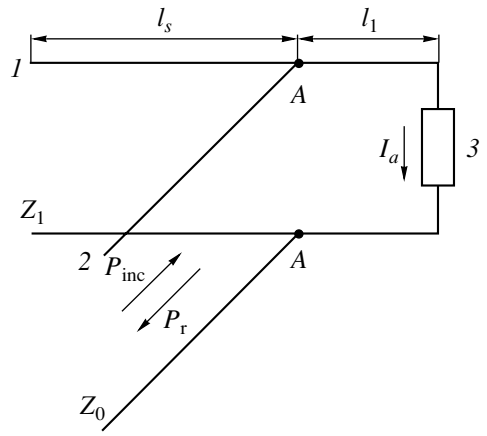

Fig. 3. Equivalent circuit of the antenna: *1*, matching line; *2*, supply line; *3*, loading resistor; P_{inc}, incident power; and P_r, reflected power.

usually does not exceed 5°C. Accordingly, the permittivity of the medium is disturbed only slightly: $|\Delta\varepsilon|/|\varepsilon_0| < 0.05$. In this case, the desired fields can be represented as a series according to the perturbation theory:

$$\mathbf{E} = \mathbf{E}^0 + \mathbf{E}^1 + \ldots, \tag{6a}$$

$$\mathbf{H} = \mathbf{H}^0 + \mathbf{H}^1 + \ldots, \tag{6b}$$

where $\mathbf{E}^0$ and $\mathbf{H}^0$ are the fields in the homogeneous upper and lower half-spaces and $\mathbf{E}^1$ and $\mathbf{H}^1 \sim \Delta\varepsilon$ are first-order perturbations due to temperature nonuniformity.

Calculating X by formula (5), we leave only first-order terms in $\Delta\varepsilon$ (see expansion (6)). In terms of the perturbation theory, the zero- and first-order fields are found by solving the Maxwell equations with given external sources in a piecewise homogeneous medium:

$$\varepsilon = \begin{cases} 1, & z \geq 0 \\ \varepsilon_0, & z < 0. \end{cases}$$

Since the Green's function for such an electrodynamic problem is well known (see, e.g., [14]), its solution is straightforward. Omitting tedious mathematics, we give the final solution as

$$\Delta X(D, h, \lambda) = \int_{-\infty}^{0} dz' \mathrm{Im}(\Delta\varepsilon(z'))K(z', D, h, \lambda). \tag{7}$$

The kernel K of this integral is given in the Appendix. We only note that formula (7) was derived under the assumption $\mathrm{Im}(\Delta\varepsilon) \gg \mathrm{Re}(\Delta\varepsilon)$. Calculations showed that $\mathrm{Re}(\Delta\varepsilon)/\mathrm{Im}(\Delta\varepsilon)$ is invariably less than 0.1 for temperature variations in biological objects.

AVERAGE DEPTH TEMPERATURE AND EFFECTIVE PROBING DEPTH

We substitute (7) into (4) and take into account that $\mathrm{Im}(\Delta\varepsilon(z)) = \alpha(\lambda)\Delta T(z)$ if the temperature varies insignificantly (the temperature gradient $\alpha(\lambda) = (\partial \mathrm{Im}\varepsilon/\partial T)_{T = T_0}$ for various types of biological tissues is given in Table 1 for $\lambda = 30$ cm and $T_0 = 37$°C). Then, we have

$$\frac{\delta f}{f_0}(D, h, \lambda) = \frac{Z_1\alpha(\lambda)}{\pi X_0^2(D, h, \lambda)} \times \int_{-\infty}^{0} dz'\Delta T(z')K(z', D, h, \lambda). \tag{8}$$

Let us define the average depth temperature ΔT_{av} as an increment of the temperature of a uniformly heated medium that provides the same frequency shift as an inhomogeneous medium with $\Delta T(z) \neq \mathrm{const}$. With such a definition, it follows from (8) that

$$\Delta T_{av}(D, h, \lambda) = \int_{-\infty}^{0} dz'\Delta T(z')\tilde{K}(D, h, \lambda), \tag{9}$$

where

$$\tilde{K} = K(z)/\int_{-\infty}^{0} dz'K(z')$$

is the normalized kernel; that is,

$$\int_{-\infty}^{0} dz\tilde{K}(z) = 1.$$

Then, for $\Delta T(z) = \Delta T = \mathrm{const}$, we find from (9) that $\Delta T_{av} = \Delta T$.

In practice, the average temperature of the medium can be measured by calibrating a near field thermometer. During calibration, the frequency shift δf_0 is measured when the medium is heated from the initial temperature T_0 to $T_0 + \Delta T_0$. The quantity $\Delta T_0/\delta f_0$ defines a scale-adjusting factor, which is subsequently employed for conversion to ΔT_{av} upon measuring δf in an inhomogeneous medium. In fact, using expression (8) at $\Delta T_0 = \mathrm{const}$, we obtain

$$\delta f_0/f_0 = Z_1\alpha(\lambda)/(\pi X_0^2(D, h, \lambda))\Delta T_0\int_{-\infty}^{0} dz'K(z');$$

hence, $\Delta T_{av} = \Delta T_0\delta f/\delta f_0$.

It is natural that for calibration one should use either a medium studied or a standard with similar dielectric properties, since the parameters α and X_0, as well as the function $K(z)$ in (8), depend on ε. The major difference between calibrated NFDs and contact thermometers is

that the former measure the temperature ΔT_{av} averaged over the vicinity of the probe (see Eq. (9)). In other words, NFDs are capable of remote temperature control. Calculation by formulas (A.1)–(A.4) demonstrates that the kernel of Eq. (9) can be approximated by the simple exponential dependence

$$\tilde{K}(z) = d_{\text{eff}}^{-1}\exp(z/d_{\text{eff}}), \quad (10)$$

which decays with increasing depth ($z < 0$). The parameter $d_{\text{eff}} = d_{\text{eff}}(D, h, \lambda)$ is the effective probing depth of an NFD, since it defines the characteristic interval of integration of the temperature over z in Eq. (9). The value of d_{eff} can be found from the relationship

$$d_{\text{eff}} = \left|\int_{-\infty}^{0} dz' z' \tilde{K}(z')\right|. \quad (11)$$

The dependence of d_{eff} on D and λ at $h = 0$ calculated by (11) is shown in Fig. 4. The kernel $K(z)$ was calculated by formulas (A.1)–(A.4), and the electric and magnetic fields at the antenna aperture were approximated by the radially symmetric Gaussian distribution

$$H_a(r) = E_a(r) = E_0\exp(-4r^2/D^2), \quad (12)$$

where the characteristic scale D is the probe aperture size. Hereafter, the medium studied is a fatty tissue at $T_0 = 37°C$. As follows from Fig. 4, with λ fixed, the probing depth varies with D within $0 \le d_{\text{eff}} < d_{\text{sk}}$, where $d_{\text{sk}}(\lambda)$ is the skin depth. As D decreases, so does d_{eff}, tending to zero. As D increases, d_{eff} also increases, approaching d_{sk}. These results support our statement that an improvement in the NFD resolution by decreasing the probe size leads to a decrease in d_{eff}. Obviously, specific limitations depend on the permittivity of the medium under study. For a fatty tissue, it is important that the probing depth may be high ($d_{\text{eff}} = 3$–5 cm) even if antennas are relatively small ($D = 1.0$–1.5 cm) (Fig. 4). Thus, NFDs are promising for medical diagnostics.

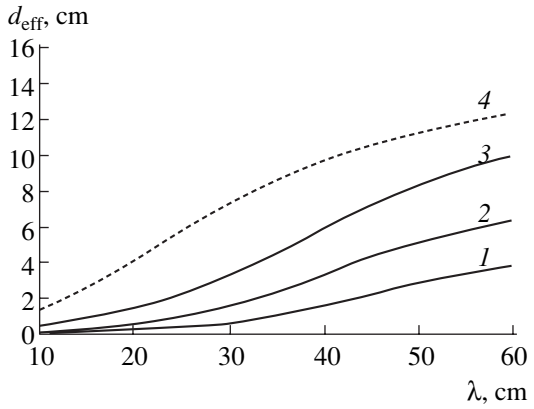

Fig. 4. Effective probing length d_{eff} vs. the wavelength for D = (*1*) 0.5, (*2*) 1, and (*3*) 3 cm; (*4*) the function $d_{\text{sk}}(\lambda)$.

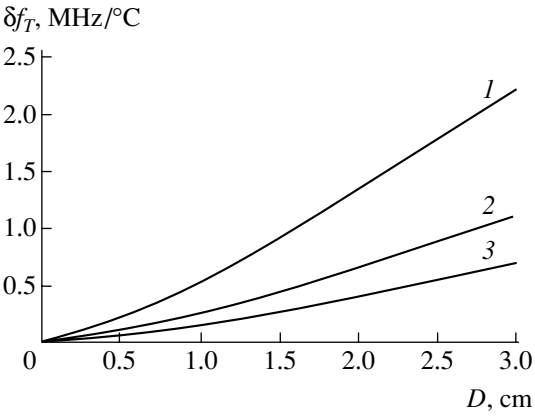

Fig. 5. Response of the resonant system to the temperature change $\Delta T = 1°C$ vs. the antenna size D. λ = (*1*) 15, (*2*) 25, and (*3*) 35 cm.

TEMPERATURE SENSITIVITY OF A NEAR-FIELD DETECTOR

According to Fig. 4, at a given D, the effective depth d_{eff} may be increased by increasing the NFD operating wavelength. However, the probing depth of the measuring system is limited by the sensitivity of the reflectometer to probe reflection coefficient variations. It is natural to expect that the probe response to a temperature change decreases with decreasing ratio D/λ. Figure 5 plots the temperature responses $\delta f_T(D)$ calculated by (8) for various λ at $\Delta T = 1°C = \text{const}$. The wave impedance of the matching resonator is $Z_1 = 50\ \Omega$, and the reactance $X_0(D, \lambda)$ was calculated from (5) for an aperture with field distribution (12) placed on the surface ($h = 0$) of a homogeneous half-space (fatty tissue). As follows from Fig. 5, the response $\delta f_T(D)$ actually drops monotonically with decreasing D/λ and allows us to estimate the temperature sensitivity of NFDs as applied to biological objects.

The change $\delta\Gamma$ in the reflection coefficient of the probe that is associated with a shift in its resonant frequency f_0 is given by

$$\delta\Gamma = \delta\Gamma_f \delta f_T \delta T, \quad (13)$$

where δT is the temperature sensitivity of the detector and $\delta\Gamma_f$ is the steepness of the resonance curve of the probe at an operating frequency f.

For the Lorentzian shape of the frequency response, the steepness is maximal if f is shifted by the line halfwidth from f_0. In this case, $\delta\Gamma_f = Q/2f$, where Q is the Q factor of the probe. For decimeter waves, the Q factor varies in the wide range $50 \lesssim Q \lesssim 5000$. The extreme values of Q are typical of probes for which matching devices are stripline and cavity resonators, respectively. Since stripline resonators are compact and, therefore, more appropriate, we will take $Q = 50$, although the

Table 2. NFD parameters

D, cm	λ, cm	d_{eff}, cm	δf_T, MHz/°C
3	35	5	0.7
2.5	32	3	0.6
2	30	2	0.5
1	30	1.5	0.5
1.5	20	1	0.6
1	15	0.5	0.5

sensitivity is lower in this case. For temperature diagnostics of biological media, it is necessary that the sensitivity of a near-field thermometer be at least $\delta T = 0.1$°C. Then, taking the probe parameters D and λ such that the temperature response is no less than $\delta f_T \approx 0.5$ MHz/°C (Fig. 5), we find that, for $f = 1$ GHz, the necessary sensitivity of the reflectometer to reflection coefficient variation is $\delta\Gamma \geq 10^{-3}$. Since such a value is practically feasible (recall that we measure relative increments $\Delta\Gamma$), the temperature sensitivity $\delta T = 0.1$°C will certainly be achieved for $\delta f_T > 0.5$ MHz/°C. In view of the calculation data for δf_T in Fig. 5, Table 2 lists the NFD parameters that extend the probing depth range $0.5 < d_{eff} < 5$ cm for a fatty tissue and at the same time provide a necessary temperature sensitivity.

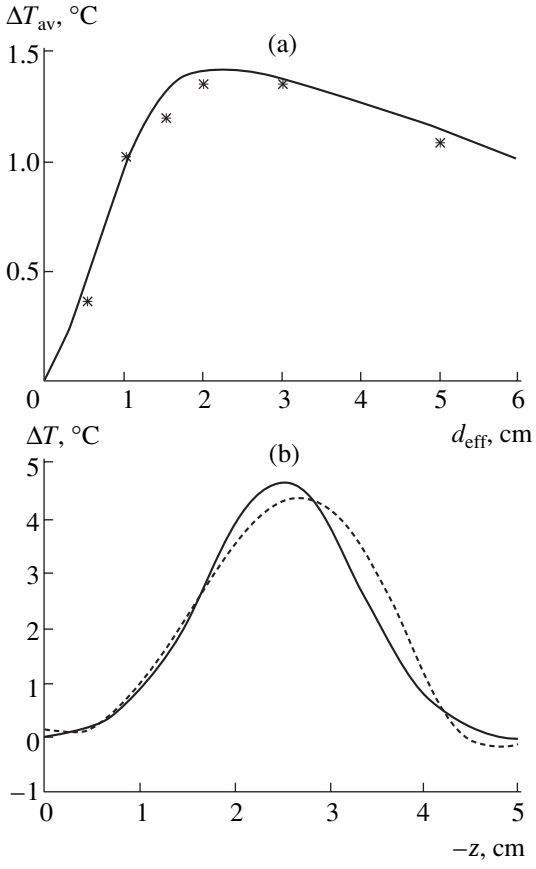

Fig. 6. (a) Dependence $\Delta T_{av}(d_{eff})$ (curves, calculation; symbols, experiment) and (b) the initial profile $\Delta T(z)$ given by (15) (continuous curve) and its reconstruction (dashed line).

TEMPERATURE PROFILE RECONSTRUCTION

As follows from the above, a typical feature of NFDs is the dependence of the probing depth on the probe parameters: $d_{eff} = d_{eff}(D, h, \lambda)$, which allows us to suggest a new way of finding the depth temperature profile $\Delta T(z)$. We have shown that near-field location data may be used to measure the weighted average temperature ΔT_{av} with a characteristic scale of averaging over the depth (d_{eff}). The simultaneous measurement of ΔT_{av} at several d_{eff} makes it possible to extract information on the temperature from different depths and reconstruct the temperature profile $\Delta T(z)$ by inverting Eq. (9).

With respect to the desired profile $\Delta T(z)$, relationship (9) is the Fredholm integral equation of the first kind, i.e., the ill-posed inverse problem [15]. To solve it numerically, one must know *a priori* information about a desired function. An effective method of inverting Eq. (9) consists in expanding the profile $\Delta T(z)$ in basis functions and seeking for expansion coefficients by measuring the left-hand side of (9) at a number of points corresponding to different scales d_{eff}. In this article, we expand the profile in a power series:

$$\Delta T(z) = T(z) - T_0 = \sum_{n=1}^{N} a_{n-1} z^{(n-1)}, \qquad (14)$$

where $T_0 = 37$°C is the undisturbed temperature, a_n are expansion coefficients to be determined, and N is the number of independent measurements differing in d_{eff}.

The results of computer simulation of the reconstruction procedure are shown in Fig. 6. The initial profile was given by

$$\Delta T(z) = 5\exp\left(-2\left(\frac{z + 2.5}{1.5}\right)^2\right) \qquad (15)$$

with a maximum at a depth $z_m = 2.5$ cm and a temperature drop $\Delta T_m = 5$°C. Such a profile seems typical under the conditions of local hyperthermia. "Experimental data" were calculated based on the requirement that N probes uniformly cover the depth range $0 \leq z \leq z_{max} \approx 5$ cm. The values of D and λ at $h = 0$ for several probes are listed in Table 2. The experimental values of ΔT_{av}^n ($n = 1, 2, \ldots, N$) were calculated by formula (9) with the profile $\Delta T(z)$ in the form of (15). The values calculated are complemented by a random "measurement error" generated by a random number generator with the

Gaussian probability density function, zero mean deviation, and given standard deviation δT. The dependence $\Delta T_{av}(d_{eff})$ calculated is shown in Fig. 6a, where experimental data simulated for NFDs with the parameters from Table 2 at $\delta T = 0.1$°C are also shown. The initial and reconstructed dependences $\Delta T(z)$ are given in Fig. 6b. For $N = 6$ and $\delta T = 0.1$°C, the profile reconstructed deviates from the initial one by no more than 0.5°C throughout the depth range. The reconstruction procedure was repeated several times with different realizations of random error. In all cases, the reconstruction error was no more than 0.5°C. Thus, the given values of the parameters N and δT, along with those of D and λ from Table 2, may be considered as requisite values for the measuring system to reconstruct the temperature profile with an accuracy of ≈0.5°C. Determination of these parameters is the primary goal of computer simulation preceding experiments. It should be noted that the above requirements for the parameter values are appropriate for our specific reconstruction technique and expansion (14). Clearly, expansion (14) uses *a priori* information on a desired profile to a minimal extent. If, for example, the function $\Delta T(z)$ is supposed to have a single maximum, we should take basis functions for expansion (14) such that they have a maximum. This will cut the number N of measurements and loosen the requirement for the measurement accuracy. The profile of $\Delta T(z)$ may be reconstructed with more sophisticated techniques, e.g., with the Tikhonov method of generalized residual [15], which proved its efficiency in inverse problems like (9) [16].

CONCLUSIONS

In this work, we show that the tomography of absorbing media may be carried out by means of near-field microwave location. The diagnostics method suggested may be applied to various media for determining physical parameters influencing their permittivity. A similar approach can obviously be devised for devices operating in the IR and optical ranges. The design and parameters of a particular device, as well as an achievable measurement accuracy, depend of the dielectric properties of the medium under study. Here, the applicability of the method to temperature diagnostics of biological objects is demonstrated. It appears that near-field tomography may be of practical value in medical applications (in particular, one can gain information on the tissue temperature during hyperthermia), since reliable noninvasive methods of subsurface temperature measurement are lacking at present. Certainly, further (first of all experimental) investigations are needed to draw final inferences about the prospects of this method.

In this work, the problem is considered in a simple physical statement where a constant-permittivity half-space with an initial depth-invariable temperature $T_0 = \text{const}$ is heated to some disturbed state with $T(z) = T_0 + \Delta T(z)$. Actually, the human body has a nonuniform temperature distribution (the skin surface temperature is lower than that of internal tissues). However, the generalization of the solution for a medium that initially is slightly nonuniform presents no problem. It will suffice to apply formula (8) not only to the disturbed but also to the initial state and take the difference between the disturbed and initial profiles. The final form of formula (9) will remain unchanged in this case, and this difference will be taken as $\Delta T(z)$. Of interest is also the generalization of this theory for a layered medium with layers greatly differing in ε (such as the human body). The solution of this problem faces purely technical difficulties, since the Green's function for such a medium is derivable. One may expect that the general form of Eq. (9) with the exponential kernel $K(z)$ will persist; however, some quantity averaged over all layers is taken to mean the characteristic spatial scale d_{eff} in this case.

One more simplification is that our method is applied to measuring relative temperatures. That is why we selected temperature control during hyperthermia among a variety of medical applications. During hyperthermia, a temperature increment relative to the initial (undisturbed) temperature is of greatest interest. Absolute temperatures are much more difficult to measure with NFDs, since the devices are extremely sensitive to permittivity variation. Even insignificant temperature-unrelated changes in the permittivity of biological tissues may cause a hard-to-control offset of the resonance frequency that exceeds the temperature variation of f_0. Minimization of these difficulties, which is a challenge, will enhance the potentialities and expand the application of the method.

ACKNOWLEDGMENTS

This work was supported by the Russian Foundation for Basic Research (project nos. 03-02-16086 and 03-02-06100).

APPENDIX

KERNEL OF INTEGRAL EQUATION (9)

$$K(z) = K_m(z) + K_v(z), \tag{A.1}$$

$$K_m(z) = \frac{1}{c\lambda(2)^9}\iint d^2\kappa \left|\frac{k_0 + \sqrt{k_0^2 - \kappa^2}}{\sqrt{k_0^2 - \kappa^2}}\right|^2$$

$$\times \operatorname{Re}\left[\frac{k_0}{\sqrt{\varepsilon_0 k_0^2 - \kappa^2}}(A_1^m + A_2^m \exp(2i\operatorname{Re}\sqrt{\varepsilon_0 k_0^2 - \kappa^2}z))\right]$$

$$\times \exp(-2\operatorname{Im}\sqrt{\varepsilon_0 k_0^2 - \kappa^2}z)\exp(2\operatorname{Im}\sqrt{k_0^2 - \kappa^2}h)|E_a(\kappa)|^2,$$

$$A_1^m = \left(\frac{iB_1}{\mathrm{Im}\sqrt{\varepsilon_0 k_0^2 - \kappa^2}} - \frac{B_2}{\mathrm{Re}\sqrt{\varepsilon_0 k_0^2 - \kappa^2}}\right)$$

$$- \mathrm{Re}(\varepsilon_0)\left(\frac{iB_3}{\mathrm{Im}\sqrt{\varepsilon_0 k_0^2 - \kappa^2}} - \frac{B_4}{\mathrm{Re}\sqrt{\varepsilon_0 k_0^2 - \kappa^2}}\right),$$

$$A_2^m = \left(\frac{B_2}{\mathrm{Re}\sqrt{\varepsilon_0 k_0^2 - \kappa^2}} - \frac{iB_5}{\mathrm{Im}\sqrt{\varepsilon_0 k_0^2 - \kappa^2}}\right)$$

$$- \mathrm{Re}(\varepsilon_0)\left(\frac{iB_4}{\mathrm{Re}\sqrt{\varepsilon_0 k_0^2 - \kappa^2}} - \frac{iB_6}{\mathrm{Im}\sqrt{\varepsilon_0 k_0^2 - \kappa^2}}\right),$$

$$B_1 = |T_E|^2 \frac{\kappa_x^2}{\kappa^2}\frac{\kappa^2 + \left|\sqrt{\varepsilon_0 k_0^2 - \kappa^2}\right|^2}{k_0^2} + |T_H|^2 \frac{\kappa_y^2}{\kappa^2},$$

$$B_2 = |T_E|^2 \frac{\kappa_x^2}{\kappa^2}\frac{\kappa^2 - \left|\sqrt{\varepsilon_0 k_0^2 - \kappa^2}\right|^2}{k_0^2} + |T_H|^2 \frac{\kappa_y^2}{\kappa^2}\frac{2\kappa^2 - \varepsilon_0 k_0^2}{\varepsilon_0 k_0^2},$$

$$B_3 = |T_E|^2 \frac{\kappa_x^2}{\kappa^2} + |T_H|^2 \frac{\kappa_y^2}{\kappa^2}\frac{\kappa^2 + \left|\sqrt{\varepsilon_0 k_0^2 - \kappa^2}\right|^2}{|\varepsilon_0 k_0|^2},$$

$$B_4 = |T_E|^2 \frac{\kappa_x^2}{\kappa^2} + |T_H|^2 \frac{\kappa_y^2}{\kappa^2}\frac{\kappa^2 - \left|\sqrt{\varepsilon_0 k_0^2 - \kappa^2}\right|^2}{|\varepsilon_0 k_0|^2}\frac{2\kappa^2 - \varepsilon_0 k_0^2}{\varepsilon_0 k_0^2},$$

$$B_5 = |T_E|^2 R_E \frac{\kappa_x^2}{\kappa^2}\frac{\kappa^2 + \left|\sqrt{\varepsilon_0 k_0^2 - \kappa^2}\right|^2}{k_0^2} + |T_H|^2 R_H \frac{\kappa_y^2}{\kappa^2}\frac{2\kappa^2 - \varepsilon_0 k_0^2}{\varepsilon_0 k_0^2},$$

$$B_6 = |T_E|^2 R_E \frac{\kappa_x^2}{\kappa^2} + |T_H|^2 R_H \frac{\kappa_y^2}{\kappa^2} \times \frac{\kappa^2 + \left|\sqrt{\varepsilon_0 k_0^2 - \kappa^2}\right|^2}{k_0^2}\frac{2\kappa^2 - \varepsilon_0 k_0^2}{\varepsilon_0 k_0^2}; \quad \text{(A.2)}$$

$$K_v(z) = \frac{1}{c\lambda(2)^9}\iint d^2\kappa \left|\frac{k_0 + \sqrt{k_0^2 - \kappa^2}}{\sqrt{k_0^2 - \kappa^2}}\right|^2$$

$$\times \mathrm{Re}\left[\frac{k_0}{\sqrt{\varepsilon_0 k_0^2 - \kappa^2}}(A_1^v + A_2^v \exp(2i\mathrm{Re}\sqrt{\varepsilon_0 k_0^2 - \kappa^2}\, z))\right]$$

$$\times \exp(-2\mathrm{Im}\sqrt{\varepsilon_0 k_0^2 - \kappa^2}\, z)\exp(2\mathrm{Im}\sqrt{k_0^2 - \kappa^2}\, h)|E_a(\kappa)|^2,$$

$$A_1^v = |T_E|^2 \frac{\kappa_x^2}{\kappa^2}\frac{k_0}{\sqrt{k_0^2 - \kappa^2}}\left[\frac{\kappa^2 - k_0^2 + \left|\sqrt{k_0^2 - \kappa^2}\right|^2}{k_0^2} R_E^* + \frac{k_0(\kappa^2 - k_0^2 + \left|\sqrt{k_0^2 - \kappa^2}\right|^2) + 2i(\kappa^2 - k_0^2)\mathrm{Im}\sqrt{k_0^2 - \kappa^2}}{k_0^2(k_0 + \sqrt{k_0^2 - \kappa^2}^*)}\right],$$

$$A_2^v = |T_H|^2 \frac{\kappa_y^2}{\kappa^2}\frac{\sqrt{\varepsilon_0 k_0^2 - \kappa^2}}{\sqrt{k_0^2 - \kappa^2}} \times \frac{2\kappa^2 - \varepsilon_0 k_0^2}{|\varepsilon_0 k_0|^2}\left[\frac{2i\mathrm{Im}\sqrt{k_0^2 - \kappa^2}}{k_0} R_H^* + \frac{k_0(\kappa^2 - k_0^2 - \left|\sqrt{k_0^2 - \kappa^2}\right|^2) + 2ik_0^2\mathrm{Im}\sqrt{k_0^2 - \kappa^2}}{k_0^2(k_0 + \sqrt{k_0^2 - \kappa^2}^*)}\right],$$

$$E_a(\kappa) = \frac{1}{(2\pi)^2}\iint d^2 r E_a(\mathbf{r})\exp(i\kappa\cdot\mathbf{r}). \quad \text{(A.3)}$$

Here, $E_a(r)$ is a given field distribution over the antenna aperture; $k_0 = 2\pi/\lambda$ is the wavenumber in free space; $\kappa^2 = \kappa_x^2 + \kappa_y^2$; and R_E, R_H, T_E, and T_H are the Fresnel reflection and transmission coefficients for a plane wave of two polarizations:

$$R_E = \frac{\sqrt{k_0^2 - \kappa^2} - \sqrt{\varepsilon_0 k_0^2 - \kappa^2}}{\sqrt{k_0^2 - \kappa^2} + \sqrt{\varepsilon_0 k_0^2 - \kappa^2}},$$

$$R_H = \frac{\varepsilon_0\sqrt{k_0^2 - \kappa^2} - \sqrt{\varepsilon_0 k_0^2 - \kappa^2}}{\varepsilon_0\sqrt{k_0^2 - \kappa^2} + \sqrt{\varepsilon_0 k_0^2 - \kappa^2}}, \quad \text{(A.4)}$$

$$T_{E,H} = R_{E,H} + 1.$$

REFERENCES

1. A. Guy, J. Lehmann, J. McDougall, *et al.*, in *Thermal Problems in Biotechnology* (American Society of Mechanical Engineers, New York, 1968), pp. 26–45.
2. D. Christensen and C. Durney, J. Microw. Power **16** (2), 89 (1981).
3. C. K. Chou, Bioelectromagnetics **13**, 581 (1992).
4. F. Gustrau and A. Bahr, IEEE Trans. Microwave Theory Tech. **50**, 2393 (2002).
5. V. S. Troitskiĭ, I. F. Belov, V. P. Gorbachev, *et al.*, Usp. Fiz. Nauk **134**, 155 (1981) [Sov. Phys. Usp. **24**, 430 (1981)].
6. W. S. Hinshaw and A. H. Lent, Proc. IEEE **71**, 338 (1983).

7. B. T. Rosner and D. W. van der Weide, Rev. Sci. Instrum. **73**, 2505 (2002).
8. I. Takeuchi, T. Wei, E. Duewer, *et al.*, Appl. Phys. Lett. **71**, 2026 (1997).
9. Yu. I. Petrov, *Physics of Small Particles* (Nauka, Moscow, 1982) [in Russian].
10. L. A. Klein and C. T. Swift, IEEE Trans. Antennas Propag. **25**, 104 (1977).
11. S. Gabriel, R. W. Lau, and C. Gabriel, Phys. Med. Biol. **41**, 2251 (1996).
12. A. Yu. Klimov, Z. F. Krasil'nik, A. N. Reznik, *et al.*, Sverkhprovodimost: Fiz., Khim., Tekh. **6**, 2150 (1993).
13. G. T. Markov and D. M. Sazonov, *Antennas* (Énergiya, Moscow, 1975).
14. E. L. Feĭnberg, *Propagation of Radio Waves along the Earth Surface* (Izd. Akad. Nauk SSSR, Moscow, 1961) [in Russian].
15. A. N. Tikhonov, A. V. Goncharskiĭ, V. V. Stepanov, and A. G. Yagola, *Regularizing Algorithms and a priori Information* (Nauka, Moscow, 1983) [in Russian].
16. K. P. Gaĭkovich, A. N. Reznik, M. I. Sumin, *et al.*, Izv. Akad. Nauk, Fiz. Atmos. Okeana **23**, 761 (1987).

Translated by V. Isaakyan

Technical Physics, Vol. 49, No. 4, 2004, pp. 494–498. Translated from Zhurnal Tekhnicheskoĭ Fiziki, Vol. 74, No. 4, 2004, pp. 117–122.

EXPERIMENTAL INSTRUMENTS AND TECHNIQUES

Self-Organization and Supramolecular Chemistry of Protein Films from the Nano- to the Macroscale

E. Rapis

Laboratory of Applied Physics, Tel-Aviv University, 64230 Ramat-Aviv, Israel

Received September 25, 2003

Abstract—Experimental data obtained with optical, polarization, scanning electron, and confocal laser microscopes reveal a previously unknown supramolecular modification of protein self-organization ("protos"). This modification arises upon condensation in the open nonequilibrium water–protein system. The process gives rise to the liquid crystal phase of nanostructured eddylike protos films epitaxially growing on the nano- and macrolevels. The model of protein spontaneous self-organization allows one to visualize and study the nonlinear dynamics of condensation and self-organization of protein films with a supramolecular configuration on the nano- and macroscale under abiotic and biotic conditions. This model may help in creating an atlas for protein identification, as well as for diagnostics of pathogenic processes in the living organism that disturb protein self-organization. © *2004 MAIK "Nauka/Interperiodica"*.

INTRODUCTION

Not much is known today about the self-organization and supramolecular chemistry of protein on the nano- and macroscale [1–6].

Structuring in protein at the molecular level is investigated mainly by X-ray diffraction, which is capable of detecting long-range order with strong covalent bonds. With X-ray diffraction analysis, protein structures at the angstrom level have been visualized [7–10]. This method also dominates in the rapidly developing field of biology called proteomics [11–15]. Proteomics deals with the functioning of protein and its configuration from the atomic to the cellular level.

It has recently been speculated that the structure of individual molecules bears little information on protein functioning compared with the structure of a large complex [7]. Protein molecular chain folding as an information carrier is confronted with noncovalent macromolecular complexes with their unique structure and biological function [7]. The impression arises that nature creates its functioning ensembles of vital importance at the nanolevel, where polymer synthesis, cellular growth, cell division, etc., take place [2].

It is known that, along with covalent bonds, supramolecular chemistry with its weak noncovalent van der Waals bonds also makes a large contribution to the structuring and functioning of biological systems, including protein, up to the macrolevel. However, investigation of self-organization in proteins at the meso- and macrolevel in terms of supramolecular chemistry is still in its infancy.

Generally accepted methods of analysis of protein topology (morphology) at the nano- and macrolevel in the course of spontaneous self-organization in view of the specific supramolecular chemistry of proteins is as yet lacking.

However, supramolecular chemistry and its related configurations have drawn the attention of researchers in the last decade [1, 2]. This direction is gradually becoming a new independent interdisciplinary science (at the interface between biology and physical chemistry), which is being effectively developed by Lehn with coworkers [1, 2, 15–18]. It studies the evolution of condensing matter from simple division to complex phenomena of self-organization.

From the available data in this field, it follows that the primary stage of aggregation is molecular "recognition," causing supramolecular catalytic reactions. Next is self-assembling, i.e., mere collection and aggregation of components. The final stage is spontaneous self-organization, where the system executes an intrinsic program of generating a self-organizing discrete supramolecular architecture, this process being algorithmically repeated from the nano- to the macrolevel. Examples are the cooperative behavior of such ensembles as molecular crystals, liquid crystals, micellas, polymers, and colloids [2, 6].

The published data suggest that a kinetically controlled nonequilibrium process arises, giving rise to ordered coherent dissipative structures with hierarchical links and nonlinear dynamics.

Self-organization produces supramolecular functioning structures, the properties of which depend on their nature, chemical constitution, and interaction between them [16]. In chemical polymers, supramolecular behavior initiates the formation of domains (Fig. 1) with supramolecular chains of monomer complexes.

Thus, there appear specific configurations of blocks (Fig. 1) and film membranes, which form networks fea-

1063-7842/04/4904-0494$26.00

turing macroscopic quasi-crystalline substructures with autocatalysis and complementarity [2]. Such domains and blocks play a major part in self-organization of matter and living cell evolution [2]. Hence, supramolecular behavior is inherent in the self-organization of organic polymers and living systems.

This has been supported by numerous investigations into the phenomenological properties and functionality of organic polymers. Most frequently, the phase state of epitaxially growing liquid-crystal films is of interest. These films produce 3D supramolecular dissipative structures with nucleation, which have a conic shape, fractal geometry, and vortices of spiral and chiral symmetry. Such a material offers semiconducting properties and optical activity, is anisotropic, and has ferromagnetic or antiferromagnetic polarization [19–25].

Thus, it becomes obvious that one cannot carefully study proteins, polymers most intensely functioning in a living organism, ignoring their supramolecular structure. This point is of key importance for a better understanding of the process of self-organization and self-assembly in protein systems at the cellular and macroscopic levels.

Our experience on visualizing the self-organization dynamics in the protein–water colloid [4, 5, 25, 26] appreciably helped us in studying the supramolecular architecture of protein in terms of noncovalent chemistry.

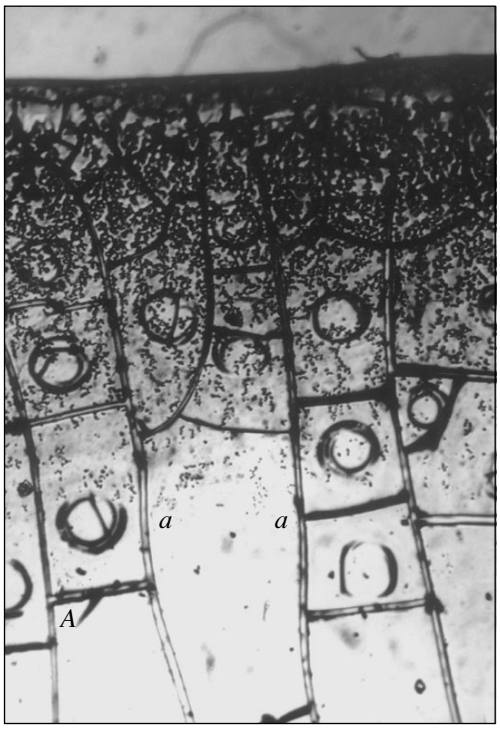

Fig. 1. Nonequilibrium form of protein (protos) under an optical microscope. Geometrically similar blocks (cells) with nuclei are seen. ×200.

EXPERIMENTAL

We performed experiments with the fast and slow evaporation of water from the water–protein colloid with the subsequent dynamic visualization of protein condensation and self-organization under equilibrium and nonequilibrium conditions *in vitro*. The colloid with different proteins (albumin, globulin, hemoglobin, lysozyme, gamma globulin, etc.) was placed on a hard wettable substrate (glass or plastic) and dried either uncovered (the open system, the first series of experiments) at room temperature and atmospheric pressure or covered by cover glass (the closed system, the second series of experiments). In this way, we varied the protein condensation kinetics. The self-organization dynamics was visualized with optical, polarization, scanning electron, and confocal laser microscopes. A total of three thousand runs were carried out. The method of investigation was detailed elsewhere [5, 26, 27].

RESULTS

When the water was rapidly evaporated from the open water–protein system *in vitro* under natural conditions (at room temperature and atmospheric pressure without any admixtures and perturbations), autowaves arose in the excited nonequilibrium system. The self-organization of the protein was observed with the formation of its nonequilibrium post-translational modification (protos), which features specific symmetries of dissipative nanostructures at the meso- and macrolevels (Figs. 1–6).

In the closed equilibrium system with the slow evaporation of the water under the same temperature and pressure, another process takes place: the crystallization of the protein into a structure with long-range order (irrespective of the film size) and another type of symmetry (for details, see [5, 26, 27]).

Thus, we studied the self-organization (self-assembling during condensation) of protein, the character and phenomenology of its structures, and their symmetry under nonequilibrium conditions *in vitro*. It was found that the process of protein self-organization is radically different from protein condensation [8–10].

The protos modification of protein *in vitro* is shown to have the same types and scales of symmetry as in protein *in vivo*. Self-organization (self-assembling) of protein occurs when the dehydration of the water–protein system is fast. In a living organism, self-organization may attend adenosine triphosphoric (ATP) acid hydrolysis in protein phosphorylation and also appear in the case of usual water evaporation from the open system *in vitro.*

DISCUSSION

Our experiments demonstrate that a supramolecular architecture with its related function arises when the

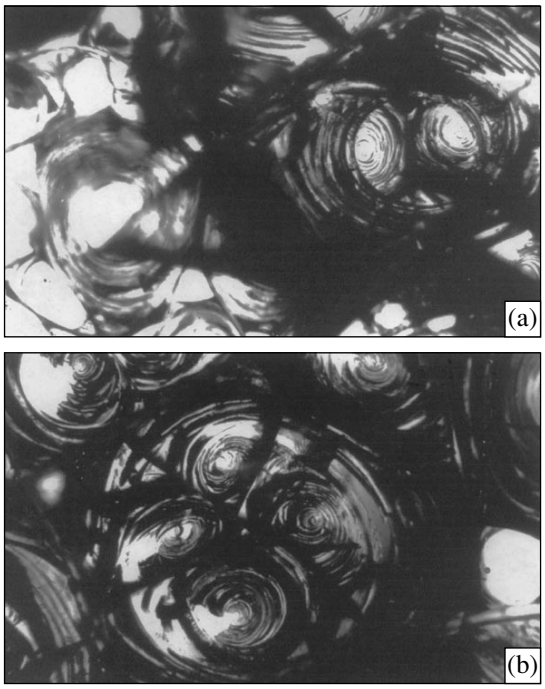

Fig. 2. (a, b) A series of large-scale (rectilinear and spiral) defects split a nonequilibrium protein film into cells with shell-like nuclei. Three-dimensional opposite vorticities, slight asymmetry, and stacked films with attraction domains are seen. The central area of the field of the primary ("mother") spiral is split into two, four, and a greater number of small ("daughter") vortices. Optical microscope, ×185.

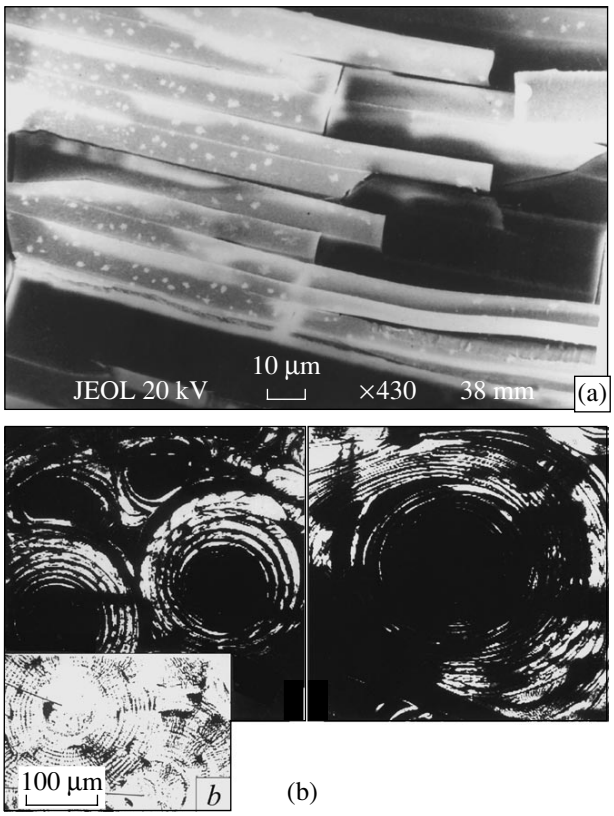

Fig. 3. (a) Electron micrograph of protein samples in the form of parallelepipeds (cleavage, side view). Stacked similar films are cut by defects to form steps with a smooth surface and aggregates inside. JEOL scanning electron microscope, ×10000. (b) Electron micrographs of protein vortex structures *in vitro* are similar to the cross-sectional view of tubular human bones (the inset below).

condensation rate in the water–protein system is relatively high (higher than in the closed system). More specifically, self-organization (self-assembling) was observed only in the open system, which is far from equilibrium. Under these conditions, the behavior (phenomenology) of protein coincides with the supramolecular properties of organic polymers [19–25]; namely, stacked epitaxially growing liquid-crystal films appear, causing the formation of 3D conic supramolecular nanostructures. Their distinctive features are opposite vorticities, nonlinear dynamics, autocatalysis and self-complementarity (Figs. 2–6), optical activity, anisotropy, etc.

Under the other experimental conditions, i.e., in the closed and, hence, more equilibrium water–protein system, the liquid-crystal phase with the coherent synchronous autocatalytic processes of self-organization of protein with supramolecular properties do not occur; instead, protein acquires a crystal structure with long-range order [5, 26, 27].

Thus, the identical chemical processes attending protein condensation (dehydration, aggregation, and polymerization) lead to radically different results under different kinetic conditions. The high initial viscosity of the water–protein colloid renders the process appreciably nonequilibrium even if the rate of evaporation of the solvent is moderate. In this case, a specific type of turbulence, elastic turbulence, arises [28].

The fact that the system is far from equilibrium makes it pass from the nonequilibrium state to equilibrium via energy dissipation, causing self-organization. Self-organization goes through conformation transitions, releasing an energy for the protein "engine." This is consistent with the notion [1, 2] that self-organization is the source of forces that favor the evolution of the biological world from inanimate matter [2].

It should be emphasized that, as follows from our experiments, protein self-organization in the open system *in vitro* proceeds without any other ingredients of a living organism, i.e., under abiotic conditions in the absence of the ATP acid hydrolysis energy, which is today viewed as a necessary source for self-organization of protein.

We also found that the energy of condensation of the nonequilibrium protein–water system *in vitro* is necessary and sufficient for the protein to self-organize and take supramolecular properties. This generates the hypothesis that the mechanism of self-organization *in vivo* is the same. As is known, ATP acid, when com-

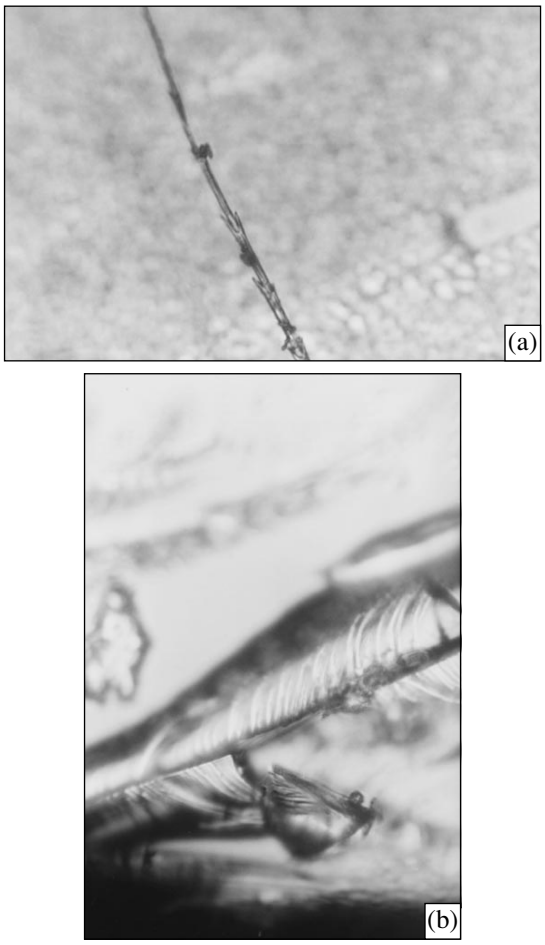

Fig. 4. Formation of small appendages (branches) on opposite sides of the mother protein film *in vitro*. The demonstration of mirror symmetry that arises during the growth of blades of grass and trees (branches, leaves). (a) Bladelike form and (b) form similar to a fish skeleton. ×200.

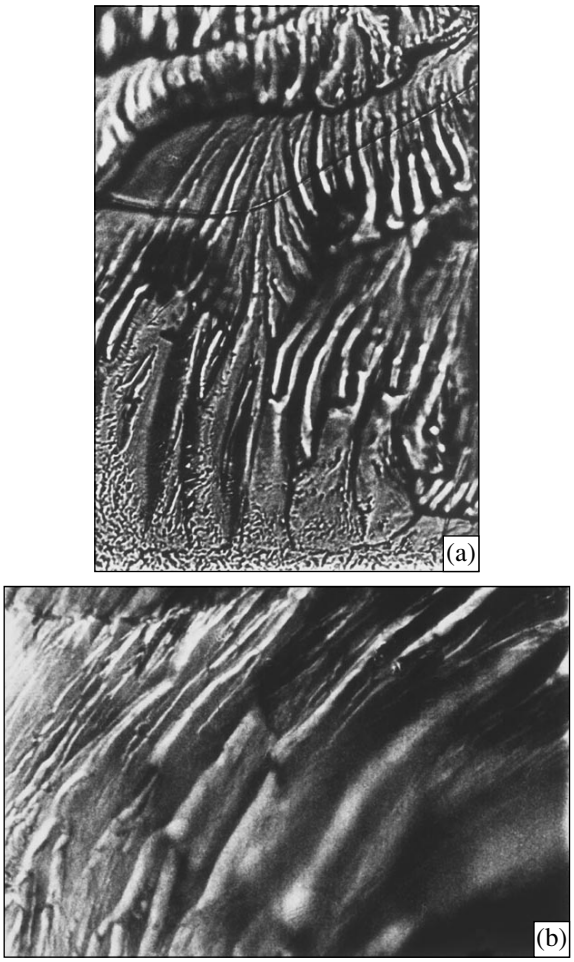

Fig. 5. (a) Demonstration of fractal properties of the structures. The volume of the features decreases with distance from the base. (b) Doubled blocks shearing one support form three-block protein structures with a conic top. Joining of the fractal elements are akin to the self-complementary ("key-in-lock") joining of biological fragments. Thickening of the joint areas, spiral twisting of the films, discreteness, and dichotomy are distinctly observed. Optical microscope, ×320.

bined with protein, rapidly hydrolyzes (absorbs water), providing conditions for the high-rate dehydration of the water–protein system, i.e., passes it into the highly nonequilibrium state. To see whether such a scenario is a possibility in a living organism (the complex nonequilibrium and nonlinear system) [29, 30], we compared the morphology of the protein nonequilibrium modification "protos" on glass (*in vitro*) and in the living (*in vivo*). In both cases, we observed spiral, mirror, chiral, radial, longitudinal, and "porcupine" symmetries, as well as fractal geometry from the nano- to the macroscale (Figs. 1–6).

The same is indicated by a variety of biological observations. For example, the activity of protein not only in a living organism but also under the abiotic conditions *in vitro* (both on glass and in a test tube) follows from many biochemical, histochemical, immunologic, and other investigations (Anfinsen's tests, antigen–antibody reactions, etc.).

Fig. 6. (*a*) Cone-shaped (fine-pointed) self-similar films of decreasing fractal dimension. Shell-like funnel-type structures *in vitro* are observed. Optical microscope with a UV filter. (*b*) Similar forms of cone-shaped fractal structures *in vivo* (in the ridge of an insect).

Moreover, biologists know the properties of protein in a living organism that are completely the same as the phenomenological properties of polymers with their supramolecular constitution. These are the presence of the liquid-crystal phase with eddylike structures and stacked films from the nano- to the macroscale, as well as with fractal geometry (Figs. 3, 6); optical activity; birefringence [5] and other catalytic and autocatalytic properties; and self-complementarity and complementarity (antigen–antibody interaction). Many tissues of the protein nature in a living organism have a similar structure (bones; hair; nerve, muscular, and connective tissues (collagenous fibers); fibrin; etc. At the same time, it is well known that a living organism is always an open dynamic far-from-equilibrium system, which is necessary for the process of self-organization with dissipative structures to occur [29–32].

Even more convincing evidence in favor of the hypothesis comes from the recent advances in studying nanostructures. According to [33], nanostructures are the focus of interest for biology, physics, and electronic engineering. Of most interest is that organic polymers (protein, DNA), on the one hand [33], are becoming a promising material for electron devices [33, 34]; on the other hand, molecules of protein, as well as its nanostructures, cells, and tissues, are now artificially grown to replace living tissues in medicine [3, 36, 37].

Thus, based on the above, we may argue that different proteins in biological systems behave according to the same program written in terms of supramolecular chemistry. Physically, this means condensation of the open nonequilibrium water–protein system, giving rise to the same configuration and function of protein during the self-organization process (both *in vitro* and *in vivo*).

ACKNOWLEDGMENTS

I thank Profs. A. Amus'i, A. Arel', E. Braudo, V. Buravtsev, A. Botin, V. Volkov, E. Gol'braĭkh, A. Zaikin, M. Klinger, L. Manevich, S. Moiseev, Yu. Neéman, and I. Prigogine for valuable comments, fruitful discussion, and encouragement.

REFERENCES

1. J. M. Lehn, *Supramolecular Chemistry* (VCH, New York, 1995), Chap. 9.
2. J. M. Lehn, Proc. Natl. Acad. Sci. USA **99**, 4763 (2002).
3. S. I. Stupp, V. Le Bonheur, K. Walker, *et al.*, Science **276**, 384 (1997).
4. M. Pralle, C. Whitaker, P. Braun, and S. Stupp, Macromolecules **33**, 3550 (2000).
5. E. Rapis, *Protein and Life (Self-Assembling and Symmetry of Protein Nanostructures)* (MiltaPKPTIT, Moscow, 2002).
6. M. Suarez, J. M. Lehn, and S. C. Zimmerman, J. Am. Chem. Soc. **120**, 9526 (1998).
7. A. Sali, R. Glaeser, T. Earnest, and W. Baumeister, Nature **422**, 216 (2003).
8. J. Knowles, Science **299**, 2002 (2003).
9. H. Zhang, Z. Yang, Y. Shen, and L. Tong, Science **299**, 2064 (2003).
10. S. D. Lahiri, G. Zhang, D. Dunaway-Mariano, and K. N. Allen, Science **299**, 2067 (2003).
11. S. Hanash, Nature **422**, 226 (2003).
12. B. Marte, Nature **422**, 191 (2003).
13. E. Phizicky, P. I. H. Bastiaens, H. Zhu, *et al.*, Nature **422**, 208 (2003).
14. M. Tyers and M. Mann, Nature **422**, 193 (2003).
15. J. M. Lehn, Chem.-Eur. J. **6**, 2097 (2000).
16. J. M. Lehn, *Supramolecular Science: Where It Is and Where It Is Going*, Ed. by R. Ungaro and E. Dalcanale (Kluwer, Dordrecht, 1999), pp. 287–304.
17. J. M. Lehn, Chem.-Eur. J. **6**, 2097 (2000).
18. J. M. Lehn, *Supramolecular Polymers*, Ed. by A. Ciferri (Dekker, New York, 2000), pp. 615–641.
19. V. Berl, M. J. Krische, I. Hue, *et al.*, Chem.-Eur. J. **6**, 1938 (2000).
20. *Supramolecular Polymers*, Ed. by A. Cifferri (Dekker, New York, 2000).
21. C. Tschierske, Nature **413**, 682 (2002).
22. M. Sawamura, K. Kawai, Y. Matsuo, *et al.*, Nature **419**, 702 (2002).
23. V. Perele, *et al.*, Nature **417**, 384 (2002).
24. S. Hudson, H. T. Jung, V. Percec, *et al.*, Science **278**, 449 (1997).
25. F. Meyer, Z. U. Heringdorf, M. C. Reuter, and R. M. Tromp, Nature **412**, 517 (2001).
26. E. Rapis and G. Gasanowa, Zh. Tekh. Fiz. **61** (4), 62 (1991) [Sov. Phys. Tech. Phys. **36**, 406 (1991)].
27. E. Rapis, Zh. Tekh. Fiz. **70** (1), 122 (2000) [Tech. Phys. **45**, 121 (2000)].
28. A. Groisman and V. Steinberg, Nature **409**, 53 (2000).
29. M. Eigen, Naturwissenschaften **58**, 465 (1971).
30. *Self-Organizing Systems*, Ed. by F. E. Yates (Plenum Press, New York, 1987).
31. S. Brackmann, Biophys. Chem. **66**, 133 (1997).
32. I. Prigogine and I. Stengers, *Order from Chaos* (Progress, Moscow, 1986).
33. J. Rundqvist, *Investigations of Directed Protein Immobilization to Nano-Patterns Manufactured with E-beam Lithography*, Licenciate Thesis, Nanostructure Physics, KTH, 2003.
34. A. Bard, *Integrated Chemical Systems: A Chemical Approach to Nanotechnology* (Wiley, New York, 1994).
35. E. Chandross and R. D. Miller, Chem. Rev. **99**, 1641 (1999).
36. F. Menger and K. D. Gabrielson, Angew. Chem. Int. Ed. Engl. **34**, 2091 (1995).
37. C. Paleos, Z. Sideratou, and D. Tsiourvas, ChemBioChem **2**, 305 (2001).

Translated by V. Isaakyan

Technical Physics, Vol. 49, No. 4, 2004, pp. 499–501. Translated from Zhurnal Tekhnicheskoĭ Fiziki, Vol. 74, No. 4, 2004, pp. 123–125.

SHORT COMMUNICATIONS

Crystalline Microundulator

N. A. Korkhmazyan, N. N. Korkhmazyan, and N. E. Babadganyan

Abovyan State Pedagogical University, Yerevan, Armenia

Received May 20, 2003

Abstract—A theory of radiation in a crystalline microundulator is developed. It is shown that crystalline microundulators may be used as effective alternative radiation sources in the wavelength range λ = 0.1–1.0 Å.

Crystalline undulators have been the subject of intensive research in recent years [1–5]. It is known [6–8] that, when a single crystal of $Si_{1-x}Ge_x$ solid solution grows under a constant concentration gradient along the $[1\bar{1}1]$ direction, the related atomic planes diverge in a fanwise manner and (111) atomic planes normal to them bend to form a channel with a certain radius of curvature. In [5], a similar set of plane-parallel equispaced plates with a periodically varying direction of curvature was viewed as a microundulator (Fig. 1). For a number of technical reasons, a crystalline microundulator may be the device of choice, e.g., in the X-ray range λ = 0.1–1.0, which is usually used in X-ray diffraction studies.

As follows from Fig. 1, a relativistic particle falling into the channel moves along a piecewise circular periodic trajectory with an oscillation frequency of $\Omega = 2\pi\beta c/L$, where $L = 2(a + b)$ is the period of the undulator, a is the thickness of the plates, and b is the plate spacing. In addition, inside the plate, the particle executes oscillations with a frequency much higher than Ω: $\Omega_{ch} \gg \Omega$. The efficiency of such undulators can be estimated from the angular–frequency radiation distribution given by [9]

$$\frac{dW}{d\omega dO} = \frac{e^2\omega^2}{4\pi^2c^3}|\mathbf{I}|^2,\ \mathbf{I} = \int_{-\infty}^{+\infty}[\mathbf{n}\times\mathbf{v}]\exp i[\omega t - \mathbf{k}\cdot\mathbf{r}(t)]dt. \quad (1)$$

Here, $\mathbf{r}(t) = [x(t), 0, z = \beta ct]$ is the radius vector of the particle, $\mathbf{n} = (\sin\theta\cos\varphi, \sin\theta\cos\varphi, \cos\theta)$ is the unit vector in the direction of the photon emitted, and βc is the longitudinal velocity of the particle.

For a smoothly joined trajectory of the particle, we have (up to smalls on the order of $a^2/16R \ll 1$)

$$x = \begin{cases} az/2R, & 0 \le z \le b/2 \\ x_0 - (z(a+b)/2)^2/2R + a_{ch}\sin\dfrac{\Omega_{ch}}{\beta c}(z - b/2) \\ b/2 \le z \le (2a+b)/2 \\ a(a+b-z)/2R, & (2a+b)/2 \le z \le a+b, \end{cases} \quad (2)$$

where a_{ch} is the oscillation amplitude in the channel (the amplitude is of atomic size) and R is the radius of curvature of the channel. Introducing the new variable

$$z = \varphi(a+b)/\pi, \quad (3)$$

we arrive at

$$x = \begin{cases} a(a+b)\varphi/2\pi R, & 0 \le \varphi \le \pi b/2(a+b) \equiv \varphi_1; \\ x_0 - (a+b)^2(\varphi - \pi/2)^2/2\pi^2R + a_{ch}\sin\dfrac{\Omega_{ch}}{\Omega}(\varphi - \pi b/L), \\ \varphi_1 \le \pi b/2(a+b) \le \varphi \le \pi(2a+b)/2(a+b) \equiv \varphi_2; \\ a(a+b)(\pi - \varphi)/2\pi R, & \varphi_2 \le \varphi \le \pi \end{cases} \quad (4)$$

instead of (2).

It is known [10] that odd periodic functions may be expanded only in a sine Fourier series:

$$x(\varphi) = \sum_{m=1}^{\infty} a_m \sin m\varphi, \quad a_m = \frac{1}{\pi}\int_0^{2\pi} x\sin m\varphi d\varphi. \quad (5)$$

Since $x(\varphi + \pi) = -x(\varphi)$, only the Fourier coefficients with odd numbers are other than zero. Therefore, (5) may be replaced by

$$x = \sum_{n=1}^{\infty} a_{2n-1}\sin(2n-1)\varphi, \quad (6)$$

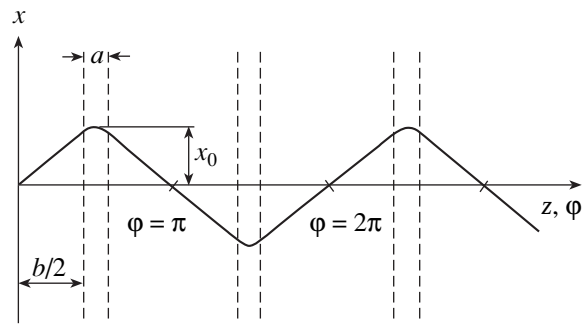

Fig. 1. Trajectory of a particle in a crystalline undulator.

1063-7842/04/4904-0499$26.00 © 2004 MAIK "Nauka/Interperiodica"

where

$$a_{2n-1} = \frac{2}{\pi}\int_0^\pi x\sin(2n-1)\varphi d\varphi.$$

The contribution from channel oscillations to the coefficient a_{2n-1} has the form

$$\frac{2}{n}a_{ch}\int_0^\pi \sin\frac{\Omega_{ch}}{\Omega}(\varphi-\pi b/L)\sin(2n-1)\varphi d\varphi. \quad (7)$$

In practice, the amplitude a_{ch} is usually more than two orders of magnitude smaller than x_0 and $\Omega_{ch} \gg \Omega$. Therefore, this contribution may be neglected if n is small, since $(2n-1) \ll \Omega_{ch}/\Omega$ and the first sine in (7) is a rapidly oscillating function in this case. In other words, oscillations inside the crystal may be ignored for lower harmonics of the undulator.

Substituting $z = \beta ct$ into (3), we find that $\varphi = \Omega t$ and substitute this expression into the first formula of (6). The vector integrand in (1) is represented in the form

$$[\mathbf{n}\times\mathbf{v}] = \mathbf{A} + \sum_{n=1}^{\infty}\mathbf{B}_{2n-1}\cos(2n-1)\Omega t, \quad (8)$$

where

$$\mathbf{A} = \beta c\sin\theta(\mathbf{i}\sin\varphi - \mathbf{j}\cos\varphi),$$
$$\mathbf{B}_{2n-1} = U_{2n-1}(\mathbf{j}\cos\theta - \mathbf{k}\sin\theta\sin\varphi),$$
$$U_{2n-1} = (2n-1)\Omega a_{2n-1},$$

and (**i**, **j**, **k**) are the unit vectors in the x, y, and z directions.

Relativistic particles emit hard radiation at angles $\theta \approx \sqrt{1-\beta^2} = 1/\gamma$ to the velocity. The angle of inclination of rectilinear parts of the trajectories is $a/2R$. Therefore, radiations from various parts of the trajectory interfere if the condition

$$a/2R \le 1/\gamma \quad (9)$$

is met.

Substituting (4) into (6) yields

$$a_{2n-1} = -\frac{(-1)^n}{2n-1}\frac{1}{2\pi R}\left[a^2 + \frac{8}{\pi^2}\frac{(a+b)^2}{(2n-1)^2}\right] \times \sin\frac{\pi}{2}\frac{(2n-1)a}{a+b}. \quad (10)$$

From (10), it follows that a_{2n-1} decreases with increasing harmonic number. On the other hand, it is known from the theory of undulator radiation that the radiation intensity is proportional to a_{2n-1}^2. Therefore, we will study only the first two harmonics. Then, in view of (6) and (8), we have

$$[\mathbf{n}\times\mathbf{v}] = \mathbf{A} + \mathbf{B}_1\cos\Omega t + \mathbf{B}_3\cos 3\Omega t;$$
$$x = a_1\sin\Omega t + a_3\sin 3\Omega t. \quad (11)$$

With an accuracy of several percent, the exponential in (1) can be represented in the form

$$\exp i(\omega t - \mathbf{k}\cdot\mathbf{r}) = \left[1 - ik_x a_1\sin\Omega t + \frac{1}{2}(-ik_x a_1\sin\Omega t)^2 - ik_x a_3\sin 3\Omega t\right]\exp i\omega(1-\beta\cos\theta)t \quad (12)$$

if the limitation

$$|ik_x x| \le \frac{\omega}{c}x_0\sin\theta\cos\varphi \le \frac{\omega}{c}\frac{x_0}{\gamma} \le 0.7 \quad (13)$$

is imposed on the frequency.

The value of x_0 can be found from Fig. 1:

$$x_n = \frac{a(a+2b)}{8R}; \quad (14)$$

therefore, instead of (13), we have

$$\omega \le \frac{5.6cR}{a(a+2b)}\gamma. \quad (15)$$

Substituting (11) and (12) into (1) and taking into account that all δ functions with nonzero arguments are zero, we arrive at

$$\mathbf{I} = \frac{1}{2}\sum_{n=1}^{2}(k_x a_{2n-1}\mathbf{A} + \mathbf{B}_{2n-1})\int_{-\infty}^{\infty}\exp i[\omega(1-\beta\cos\theta) - (2n-1)\Omega]t dt + \frac{1}{4}\left(\frac{1}{2}(k_x a_1)^2\mathbf{A} + k_x a_1\mathbf{B}_1\right) \times \int_{-\infty}^{\infty}\exp i[\omega(1-\beta\cos\theta) - 2\Omega]t dt. \quad (16)$$

Here, the first two terms stand for the first two harmonics; the third term is a correction to the first harmonic. Squaring this expression and replacing one integral by the $2\pi\delta$ function and the other by the time of radiation $T \longrightarrow \infty$, we find

$$\mathbf{I} = \frac{\pi T}{2\beta\omega}\sum_{n=1}^{2}(k_x a_{2n-1}\mathbf{A} + \mathbf{B}_{2n-1})^2 \times \delta\left[\cos\theta - \left(\frac{1}{\beta} - \frac{(2n-1)\Omega}{\beta\omega}\right)\right] \times \frac{\pi T}{8\beta\omega}\left[\frac{1}{2}(k_x a_1)^2\mathbf{A} + k_x a_1\mathbf{B}_1\right]^2\delta\left[\cos\theta - \left(\frac{1}{\beta} - \frac{2\Omega}{\beta\omega}\right)\right]. \quad (17)$$

Substituting (17) into (1) and integrating over the angular range, we arrive at an expression for the spec-

tral density per unit transit length of the particle that is well known from the theory of undulator radiation [11]:

$$I_1 = \frac{dW_1}{d\omega dz} = \gamma^2 \frac{e^2 a_1^2 \Omega^3}{4c^4} \xi [1 + (1 - 2\xi)^2],$$
$$\xi = \omega/2\Omega\gamma^2, \quad 0 \le \xi \le 1;$$
$$I_2 = \frac{dW_2}{d\omega dz} = \gamma^2 \frac{e^2 a_1^2 \Omega^3}{4c^4} 9\left(\frac{a_3}{a_1}\right)^2 \xi \left[1 + \left(1 - \frac{2}{3}\xi\right)^2\right], \quad (18)$$
$$0 \le \xi \le 3.$$

In a similar way, we find for the correction

$$\Delta I_1 = \gamma^4 \frac{e^2 a_1^2 \Omega^3}{4c^4} \xi (2 - \xi)[1 + 3(1 - \xi)^2], \quad 0 \le \xi \le 2, \quad (19)$$

where $\xi = \omega/2\Omega\gamma^2$ is the dimensionless frequency. To illustrate the results obtained, consider a ten-period crystalline undulator with $a = 0.01$ cm, $b = 0.7$ cm, $R = 200$ cm, $\gamma = 10^4$ ($E = 5$ GeV), and the dechanneling length $L_d = 0.2$ cm. For these parameters, formula (10) gives for the Fourier coefficients of the first two harmonics

$$a_1 = 7.1 \times 10^{-6} \text{ cm}, \quad a_3 = 0.79 \times 10^{-6} \text{ cm},$$
$$(a_3/a_1)^2 = 0.012. \quad (20)$$

For frequencies ξ lying in the range 0.9–1.0, the radiation wavelength is roughly equal to 0.7 Å. The number of photons with this wavelength that are emitted from the unit path length give 0.5×10^{-4} kV/cm. For comparison, a magnetic undulator with $L = 10$ cm (spacing), $H = 500$ Oe, and $E \approx 13$ GeV generates 0.36×10^{-4} kV/cm in the same frequency range. It should be noted that the number of photons emitted cannot be increased by enhancing the magnetic field, since the bipolarity condition is violated and the spectrum diffuses in this case.

From formulas (18), it follows that the radiation at the second harmonic is negligible, $I_2/I_1 \approx 0.06$, near the peak frequency of the first harmonic ($\xi = 1$). The frequency dependences of the intensities of both harmonics are shown in Fig. 2. Correction (19) is indistinguishable in Fig. 2, since $\Delta I_1/I_1 = 0.013$. For the case considered, conditions (9) and (15) are readily fulfilled. Formulas (18) are also valid for the specific case $b = 0$. From (10), it is seen that the undulator does not emit in the limit $R \longrightarrow \infty$. In this case, the trajectory is given by $x_{ch} = a_{ch} \sin \Omega_{ch} t$, according to (4); i.e., the trajectory is the same as upon channeling. Therefore, we ignored an insignificant shift of x_0 and the initial phase $\Omega_{ch} b/2\beta c$.

Thus, as follows from the theory developed in this work, crystalline microundulators seem to be more promising radiation sources in the wavelength range $\lambda \le 0.1$ Å.

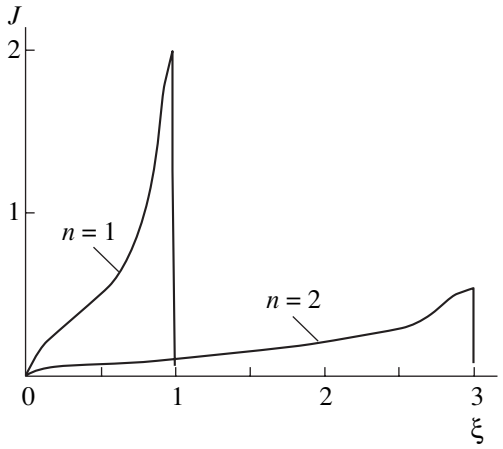

Fig. 2. Spectral distribution of the first two harmonics in a crystalline undulator. The intensity is given in units of $\Omega^3(\gamma e a_1/2c^2)^2$; the frequency, in units of $2\Omega\gamma^2$. Here, a_1 is the first harmonic amplitude and Ω is the oscillation frequency of the particle.

REFERENCES

1. A. V. Corol, A. V. Solov'yov, and W. Greiner, Int. J. Mod. Phys. E **8**, 49 (1999).
2. U. Mikkelsen and E. Uggerhoj, Nucl. Instrum. Methods Phys. Res. B **160**, 435 (2000).
3. R. O. Avakian, K. T. Avetyan, K. A. Ispirian, and E. A. Melikyan, in *NATO Advanced Research Workshop on Electron–Proton Interaction in Dense Media, Nor-Amberd, 2001*, NATO Science Series, Vol. 49, p. 277.
4. R. O. Avakian, L. A. Gevorgian, K. A. Ispirian, and R. K. Ispirian, Nucl. Instrum. Methods Phys. Res. B **173**, 112 (2001).
5. R. O. Avakian, K. E. Avetyan, K. A. Ispirian, and É. G. Melikyan, Izv. Nats. Akad. Nauk Arm., Ser. Fiz. (in press).
6. A. Erko, F. Schäfers, W. Gudat, *et al.*, Nucl. Instrum. Methods **374**, 408 (1996).
7. M. Veldkamp, A. Erko, *et al.*, Mater. Sci. Forum **308**, 597 (1999).
8. M. Veldkamp, A. Erko, W. Gudat, *et al.*, Jpn. J. Appl. Phys., Suppl. 1 **38**, 612 (1999).
9. J. D. Jackson, *Classical Electrodynamics*, 2nd ed. (Wiley, New York, 1975; Mir, Moscow, 1965).
10. A. Angot, *Complements de Mathematiques a l'Usage des Ingenieurs de l'Electrotechnique et des Telecommunications*, 2nd ed. (Editions de la Revue d'Optique, Paris, 1962; Nauka, Moscow, 1964).
11. N. A. Korkhmazyan, Izv. Akad. Nauk Arm. SSR, Fiz., No. 8, 405 (1973); Radiat. Eff. **56**, 33 (1981).

Translated by V. Isaakyan

Technical Physics, Vol. 49, No. 4, 2004, pp. 502–504. Translated from Zhurnal Tekhnicheskoĭ Fiziki, Vol. 74, No. 4, 2004, pp. 126–128.

SHORT COMMUNICATIONS

Kinetics of an RF Low-Pressure Discharge with a Condensed Phase

V. I. Strunin, A. A. Lyakhov, G. Zh. Khudaĭbergenov, and V. V. Shkurkin

Omsk State University, pr. Mira 55, Omsk, 644077 Russia

e-mail: strunin@omsu.omskreg.ru

Received July 7, 2003

Abstract—The electron energy distribution function in an RF low-pressure plasma is found in the presence of dust particles. The effect of microscopic objects on the electroneutrality of the plasma and the electron energy distribution is estimated. © *2004 MAIK "Nauka/Interperiodica".*

INTRODUCTION

Charged dust particles are often present in plasma-chemical reactors [1, 2], arising as a result of polymerization, interaction between the products of plasma-chemical reactions and the reactor walls, and cathode sputtering. The presence of a condensed phase in etchers and plasma-chemical reactors degrades the surface quality of wafers etched and films grown [3]. The particle size may vary between 0.01 and 100 μm. Dust particles present in a plasma have a negative charge Q_d because of the higher mobility of electrons compared to that of ions. This charge may be significant and (when the concentration of microparticles is high) influence considerably the plasma parameters; in particular, it may affect the electron energy distribution [4–6]. The charge Q_d and its related floating potential at the surface ϕ_s are found from the equality condition (in the absence of emission) for electron and positive-ion currents on each dust particle. The corresponding absorption cross sections can be estimated in the approximation of limited orbital motion by using the well-known formulas of the probe theory [7].

CALCULATION

In this study, we consider the effect of dust particles that are charged in an argon-discharge plasma (via the processes mentioned above) on the electron energy distribution function (EEDF). Suppose that all the particles are spherical and identical in size. Then, the Debye potential, which screens the region around a particle, is expressed as follows:

$$\phi(r) = \phi_s \frac{a}{r} \exp[-(r-a)/\lambda_L]. \quad (1)$$

The Debye screening length is given by

$$\frac{1}{\lambda_L} = \sqrt{\frac{e^2 n}{\varepsilon_0}\left(\frac{1}{kT_e} + \frac{1}{2E_0}\right)},$$

where ϕ_s is the floating potential on the particle surface, a is the radius of the particle, n is the plasma volume concentration, and E_0 is the average energy of the ions.

The charge Q_d of a dust particle is related to the ion, I_i, and electron, I_e, currents through particle–particle collisions:

$$\frac{dQ_d}{dt} = I_e + I_i. \quad (2)$$

The electron current toward a dust particle can be expressed as

$$I_e = -\pi a^2 e n_e \int_{-e\phi_s}^{\infty} \left(1 + \frac{e\phi_s}{u}\right)\sqrt{\frac{2u}{m_e}} f \sqrt{u}\, du, \quad (3)$$

where n_e is the electron concentration, u is the kinetic energy of the electrons, and f is the EEDF.

The expression for the ion component is simpler and better understood, since the ion distribution function is known and, as a rule, is Maxwellian. The ion current toward a dust particle has the form

$$I_i = \pi a^2 e n_i \sqrt{\frac{2E_0}{m_i}}\left(1 - \frac{e\phi_s}{E_0}\right), \quad (4)$$

where n_i is the ion concentration.

The floating potential ϕ_s of a particle is related to the particle charge by the expression

$$\phi_s = \frac{Q_d}{4\pi\varepsilon_0 a}.$$

Taking into account that $n_e + n_d Q_d/e = n_i$, one may express the ratio n_e/n_i as

$$\frac{n_e}{n_i} = 1 + \frac{n_d}{n_i}\frac{Q_d}{e}, \quad (5)$$

where n_d is the dust particle concentration.

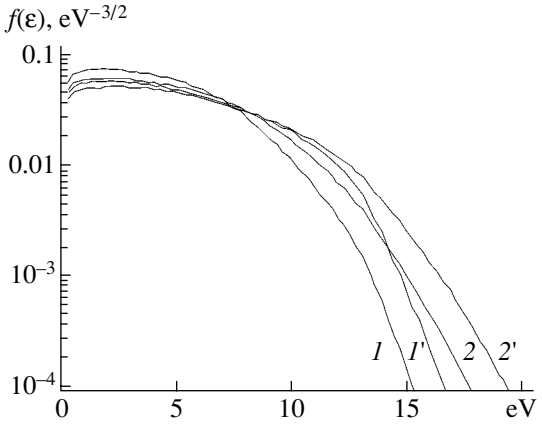

Fig. 1. EEDF in the RF argon-discharge plasma (*1*') with and (*2*') without the condensed phase at E/N = (*1*) 50 and (*2*) 100 Td. $n_d = 3 \times 10^7$ cm^{-3}.

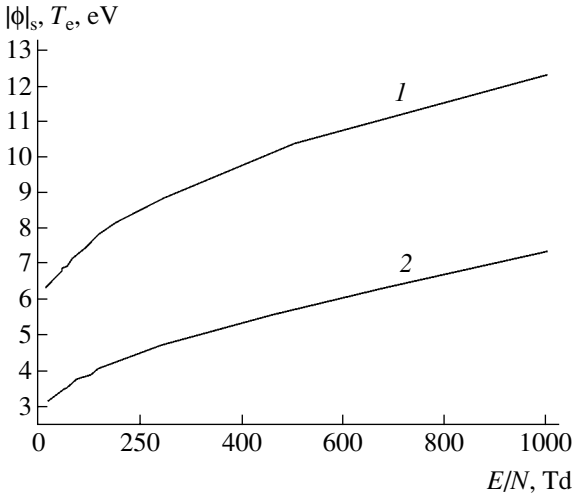

Fig. 2. (*1*) Floating potential φ_s of a dust particle and (*2*) the electron temperature T_e in the RF argon-discharge plasma.

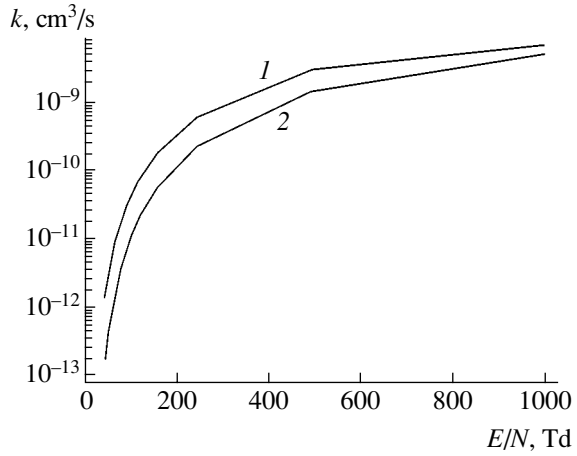

Fig. 3. Ionization rate constant of an argon atom in the RF plasma (*1*) without and (*2*) with the condensed phase.

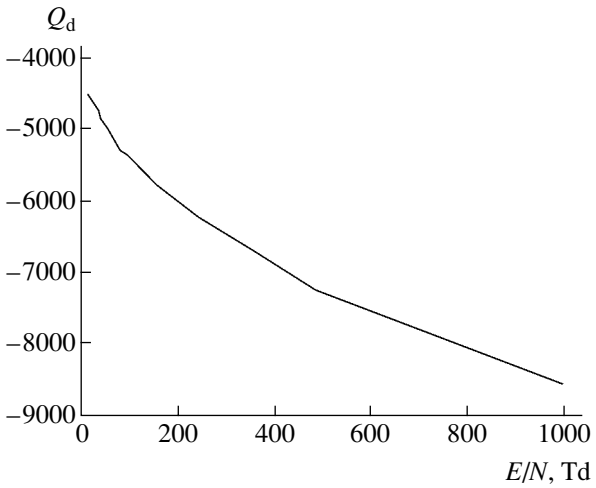

Fig. 4. Charge Q_d of a dust particle vs. applied field E/N.

In view of expression (1) for the electron–particle interaction potential, the cross section of elastic electron–particle scattering can be written as follows [8]:

$$\sigma_{ed}^{e}(u) = \pi a^2 \left(\frac{-e\phi_s}{u}\right)^2 \exp(2a/\lambda_L)\ln\Lambda,$$
$$\ln\Lambda \approx \left(\frac{\lambda_L T_e}{a(-e\phi_s)}\right), \quad (6)$$

where T_e is the electron energy in eV.

According to [5], the cross section of electron attachment to a dust particle is given by

$$\sigma_{ed}^{c} = \begin{cases} 0, & u < -e\phi_s \\ \pi a^2(1 + e\phi_s/u), & u \geq -e\phi_s. \end{cases} \quad (7)$$

In explicit form, this expression demonstrates that only fast electrons may be absorbed by dust particles.

RESULTS AND DISCUSSION

We simulated the EEDF in an RF argon-discharge plasma in the presence of dust particles, as well as charging of a dust particle according to expression (2). Figure 1 shows the EEDFs in the RF plasma for several dust particle concentrations. The distributions were calculated for dust particles of radius $r_d = 10^{-4}$ cm and concentration $n_d = 3 \times 10^7$ cm^{-3}. The values of E/N (the Townsend coefficient) varied in the range 25–1000 Td. The ion concentration was given parametrically and equaled $n_i = 3 \times 10^{11}$ cm^{-3}. The electron concentration in the plasma was calculated by formula (5).

At the initial stage of calculation, the charge of the particles was taken to be –1. Then, the EEDF was calculated by formulas (3) and (4), the ion and electron currents toward a dust particle were found, and the charge was calculated from relationship (2). The fulfillment of the equality $I_e = I_i$ indicated that the calculation

cycle was over. The time step was $\tau = 10^{-12}$ s. As is seen from Fig. 1, the presence of dust particles in the plasma leads to the depletion of the high-energy part of the distribution function.

Figure 2 plots the floating potential of a dust particle and the electron temperature in the RF plasma versus E/N. The particle potential is independent of the particle size and is governed by only the surface adsorption of electrons and ions. It depends on the electrophysical and thermophysical parameters of the plasma and the particle material (n_e, n_i, T_e, and T_i). The increase in the floating potential with increasing electric field intensity is caused by a rise in the electron temperature T_e and an increase in the fraction of high-energy electrons in the EEDF. The floating potential of the particles exceeds T_e approximately by 50% for the same values of E/N, which is in agreement with estimates made in [8]. Dust modifies the EEDF, causing the other discharge characteristics to change. For example, a decrease in the electron concentration in the high-energy part of the EEDF because of the attachment of fast electrons to dust particles lowers the ionization rate constant of argon (Fig. 3). The charge of a particle may be as high as 10^3 electron charges in this case (Fig. 4). In this situation, the discharge self-maintenance condition may be violated. To maintain the discharge, the ionization rate (and, hence, the electric field intensity) must be raised. This, in turn, necessitates an increase in the power delivered to the discharge.

Thus, we studied the effect of dust particles on the EEDF and, accordingly, on the kinetic coefficients of processes occurring with the participation of electrons and ions and on the gas discharge maintenance conditions. It is shown that one should consider this effect when simulating plasma-chemical reactions.

REFERENCES

1. V. N. Tsytovich, Usp. Fiz. Nauk **167**, 57 (1997) [Phys. Usp. **40**, 53 (1997)].
2. A. Piel and A. Melzer, Plasma Phys. Controlled Fusion **44**, 1 (2002).
3. W. Siefert, Thin Solid Films **120**, 267 (1984).
4. M. McCaughey and M. Kushner, J. Appl. Phys. **69**, 6952 (1991).
5. S. Choi and M. Kushner, IEEE Trans. Plasma Sci. **22**, 138 (1994).
6. J. Boeuf, Phys. Rev. A **46**, 7910 (1992).
7. V. I. Demidov, N. B. Kolokolov, and A. A. Kudryavtsev, *Probing of Low-Temperature Plasma* (Énergoatomizdat, Moscow, 1996) [in Russian].
8. D. Wang and J. Dong, J. Appl. Phys. **81**, 38 (1997).

Translated by Yu. Vishnyakov

Technical Physics, Vol. 49, No. 4, 2004, pp. 505–508. Translated from Zhurnal Tekhnicheskoĭ Fiziki, Vol. 74, No. 4, 2004, pp. 129–132.

SHORT COMMUNICATIONS

Fractal Dimension of the Surface upon Martensitic Transformation in Titanium Nickelide

S. N. Kulkov and Yu. P. Mironov

Institute of Strength Physics and Materials Science, Siberian Division, Russian Academy of Sciences, Akademicheskiĭ pr. 2/1, Tomsk, 634055 Russia

e-mail: kulkov@ms.tsc.ru

Received July 10, 2003

Abstract—The fractal dimension of the residual deformation relief on the surface of titanium nickelide is shown to be sensitive to the deformation mechanism. It decreases under phase-transformation-induced inelasticity and increases under plasticity. At the time the basic deformation mechanism changes, fluctuations are maximal. The experimental dependence of the microstrain on the fractal dimension for the initial austenitic phase is not a single-valued function: it consists of two groups of data points that correspond to different deformation mechanisms. © *2004 MAIK "Nauka/Interperiodica".*

INTRODUCTION

Deformation relief forming on a solid surface is related to deformation mechanisms that occur at several scale levels. It was shown [1–3] that the relief can be analyzed in terms of fractal geometry, which allowed one to track its evolution under mechanical and other actions [4, 5]. However, physical quantities and deformation mechanisms that are related to the fractal characteristics of a surface have not been systematically studied. Therefore, it would be of interest to study the fractal characteristics of deformation relief in materials where deformation mechanisms at various stages of deformation are known to be distinctly different. One such material is an alloy that undergoes strain-inducing martensitic transformation. During loading of the alloy, the stage of elastic deformation is followed by that of phase-transformation-induced (phase) inelasticity, and then the material plastically deforms. In the load–strain diagram, stages where one or another deformation mechanism dominates are clearly seen. The phase and structural state of the material at each of the stages can be determined by X-ray diffraction analysis.

The purpose of this work is to find the relation of a macrostrain and lattice parameters of the microstructure with the fractal characteristics of the surface upon strain-inducing martensitic transformation in TiNi.

EXPERIMENTAL

Dumbbell-shaped specimens with a 22-mm-long and 5-mm-wide portion to be deformed were cut out from a 1-mm-thick sheet of Ti–$Ni_{50.7}$ intermetallic, mechanically polished with diamond pastes (down to ASM 1/0 superfine diamond paste), vacuum annealed at 110°C for 1 h, and furnace cooled. The specimens were subjected to stepwise extension on an INSTRON-1185 testing machine at room temperature to record load–extension diagrams. After each step (i.e., after relieving), three preselected characteristic surface areas were imaged by means of an RÉM-200 scanning electron microscope at ten magnifications. The minimal and maximal scan areas measured 10×10 and 750×750 μm.

To obtain the fractal characteristics, we applied the technique [6] based on the Mandelbrot vertical section method [7] to the SEM images. In computer scanning, the images were represented as a dot pattern of 512×512 dots and the ratio L/L_0 (where L is the apparent length of the scan line over the scan surface and L_0 is the projection of this line onto the plane) was determined from their brightness (the secondary electron current). The value of $\ln(L/L_0)$ was taken to be the measure of the surface roughness. Then, we plotted L/L_0 against the magnification in the log–log coordinates (so-called fractal plots). These plots had a shape close to an inverse sigmoid. The fractal dimension D_f was calculated through the absolute value of the slope B of the middle segment of the linearly approximated fractal plot, $D_r = 1 + |B|$, and, therefore, served as an integral characteristic of the surface [7].

The phase state and microstructure modifications after each loading and relieving were examined using a DRON-UM1 X-ray diffractometer (CuK_α radiation).

RESULTS AND DISCUSSION

For residual strains within 2%, inelasticity in the specimen is induced by the $B2 \longrightarrow B19'$ martensite transformation. The inelasticity consists of the reversible (superelastic) and irreversible, or memorizable (at a given temperature), components. At this stage, deformation is due only to martensitic transformation and

1063-7842/04/4904-0505$26.00 © 2004 MAIK "Nauka/Interperiodica"

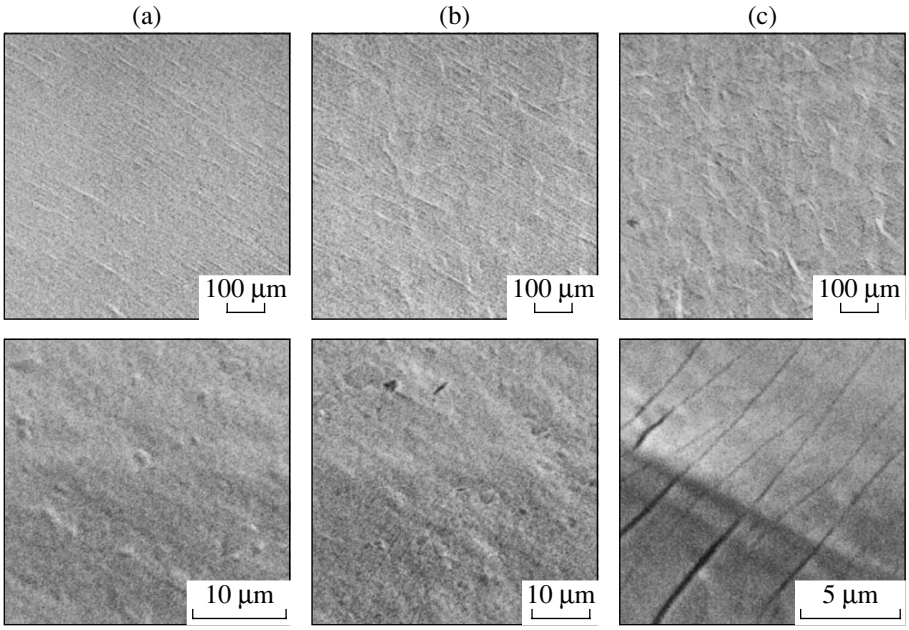

Fig. 1. SEM images of the titanium nickelide surface at a residual strain of (a) 1, (b) 2.8, and (c) 5%.

this mechanism causes a relief in the form of martensite lamellas. This relief appears during loading and almost completely disappears upon relieving: the traces of the lamellas have a weak contrast against the background of the initial relief (Fig. 1a).

The residual strain may rise to 3% at the same temperature only when the plastic component arises, which turns the superelastic component into the memorizable one. Strain hardening and the broadening of X-ray diffraction lines indicate that the amount of structure defects increases. The surface relief in the form of parallel lines of localized strain that run normally to the loading direction is clearly visible at high magnifications (Fig. 1b). On the contrary, the relief appearing as areas of weak surface extrusion is distinctly observed at low magnifications (Fig. 1b). The characteristic size of the extrusion areas is 30–100 μm, which is slightly larger than the grain mean size (about 20 μm).

When the residual strain exceeds 4%, the number of localized strain lines increases substantially and they occupy extended regions of the material via the formation of new lines, which run approximately parallel to the already existing ones (Fig. 1c). At low magnifications, the surface appears as consisting of individual grains because of their nonuniform extrusion (Fig. 1c). At this stage, the material hardens and the macrostress reaches the yield point, which is more than twice as high as the stress of $B2 \longrightarrow B19'$ phase transformation. According to X-ray diffraction data, microstrains also grow significantly, and the austenite–martensite transformation ceases. The set of the above findings indicate that martensite-induced inelasticity make a minor contribution to the macrostrain, whereas plasticity, on the contrary, becomes the basic mechanism of deformation.

For a given dot pattern, the surface roughness $\ln(L/L_0)$ increases with the residual macrodeformation only slightly. However, we failed to find the detailed form of this dependence. It seems likely that the technique applied to determine the roughness from SEM images gives overestimated values, since the roughness thus determined not only depends on the surface profile but is also affected by the contrast from inclusions, voids, etc.

A typical dependence of the surface roughness on the magnification is given in Fig. 2. In most cases, this quantity behaves as a fractal one: it drops with increasing magnification and is nearly constant at the lowest and highest magnifications. Figure 2 also demonstrates the interpolating straight line whose slope specifies the fractal dimension D_f. The dependence of the dimension D_f on the residual strain in the specimen is given in Fig. 3. When using different-degree polynomials to approximate this dependence, we found that the change of a linear function to a parabola improves the correlation coefficient most significantly: with a further rise in the degree of polynomial, this coefficient increases only slightly. We therefore assumed that the parabolic function (Fig. 3) is the best approximation. It has a minimum at a residual macrostrain of about 2% and then sharply grows, far exceeding the initial decline. The approximating parabolas $D_f(\varepsilon_{\sigma=0})$ constructed for several surface areas of the deformed specimen were found to virtually coincide with each other; that is, the strain range where D_f decreases terminates at a residual strain of about 2% and is associated solely with the martensi-

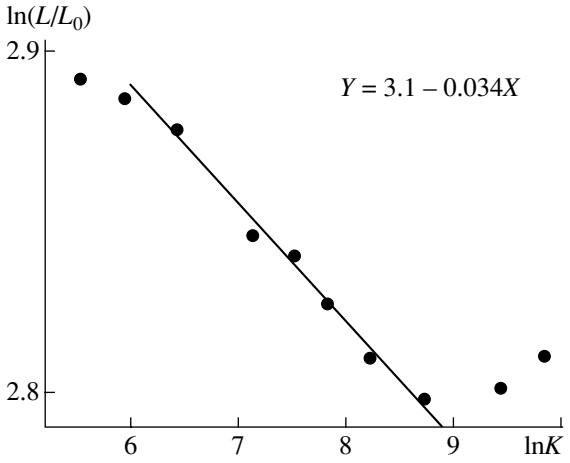

Fig. 2. Typical fractal plot (the residual strain is 3.4%).

tic mechanism of deformation. The initial point of increase in $D_f(\varepsilon_{\sigma=0})$ coincides with the onset of localized plastic deformation, and the development of the deformation relief leads to a substantial increase in D_f.

The decrease in D_f at small strains may be assigned to the specific feature of the residual martensite-related relief. If the characteristic size of the relief is small, the surface roughness at high magnifications may appear to be higher than at low magnifications. Because of this, the right-hand side of the fractal curve in Fig. 2 ascends, which, in turn, may decrease its slope and, hence, the value of D_f. Thus, two basic deformation mechanisms, forming reliefs of different types, make contributions of opposite sign to the variation of $D_f(\varepsilon_{\sigma=0})$.

The measurement errors given in the plots are obtained by statistically processing the data with allowance for errors of individual measurements [6, 7]. As is seen from Fig. 3, the fluctuations of D_f are maximal (exceed the errors) at low strains and near the minimum. Note that, in this range, elastic deformation changes to phase inelasticity and then to plastic deformation.

Figure 4a shows the full width at half maximum (FWHM) of X-ray diffraction lines (with greatly differing interplanar spacings d_{hkl} in the $B2$ lattice) versus the fractal dimension D_f. The arrows indicate the direction of growth of the residual strain. The FWHM data points for the (321) line are seen to split into two groups, which are interpolated by different dependences: the lower branch, by a near-parabola curve; the upper one, by a straight line. For the (110) line, the FWHM curve at high D_f can also be subdivided into two branches; however, in this case, the half-width is small compared with that for the (321) line. Assuming that a major contribution to the FWHM comes from lattice microstrains, we plotted the microstrains against the fractal dimension in Fig. 4b. For both reflections mentioned above, the microstrain curves run in a similar way and

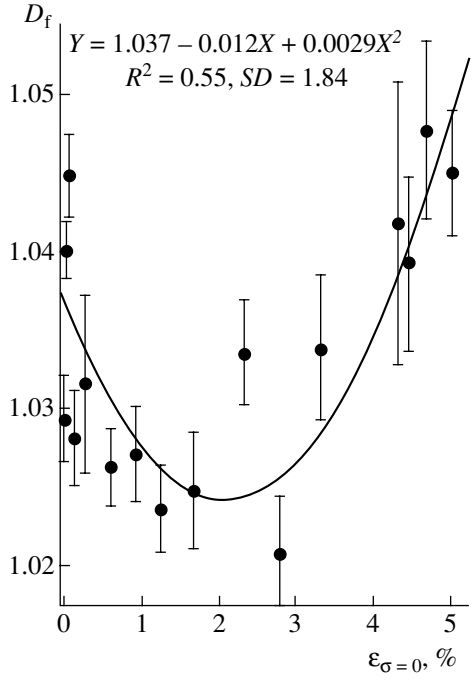

Fig. 3. Dependence of the fractal dimension D_f on the residual strain.

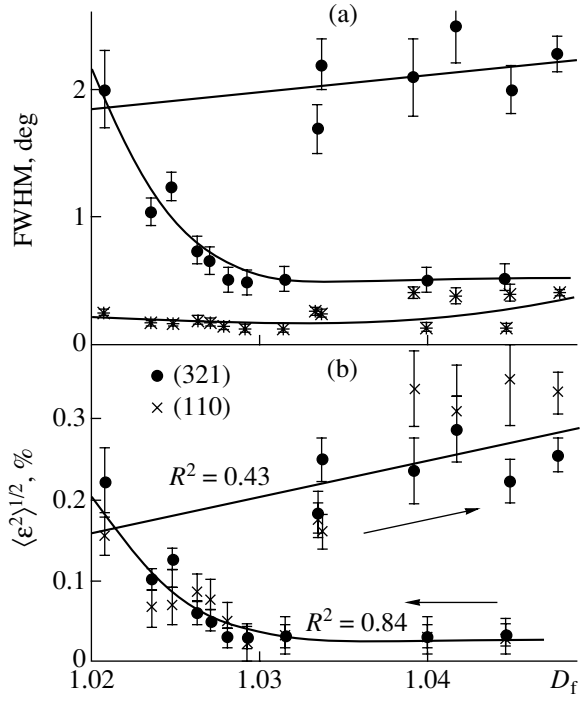

Fig. 4. (a) FWHM of X-ray diffraction lines and (b) microstrains in different atomic planes of the $B2$ lattice vs. the fractal dimension D_f of the titanium nickelide surface during tension. (×) (110) reflection and (●) (321) reflection.

almost coincide quantitatively. Two branches can be distinguished in the plot: linearly increasing and decreasing with increasing D_f. The data points corresponding to the onset of deformation are at the lower right corner of the plot. The lower branch as a whole corresponds to the martensitic mechanism of deformation, where the FWHM grows first slowly and then rapidly. The upper (linear) branch corresponds to intense surface patterning during plastic deformation. In other words, the smooth and long-term transition from phase inelasticity to plasticity is clearly outlined via the presence of small-D_f range in this plot.

CONCLUSIONS

Thus, when titanium nickelide deforms via phase inelasticity alone, the fractal dimension D_f decreases and visually detectable traces of the residual deformation relief in SEM images are absent. As the material begins hardening and plastic microstrains appear, two types of deformation relief are observed first locally and then throughout the specimen and the fractal dimension D_f increases.

Fluctuations of the fractal dimension D_f, which attend the growth of the residual strain, are maximum in the range of change of the basic deformation mechanism.

The dependence of the $B2$ lattice microstrain on the fractal dimension D_f is not a single-valued function; it is divided into two groups of data points according to different mechanisms of titanium nickelide deformation.

REFERENCES

1. V. S. Ivanova, *Synergetics: Strength and Fracture of Metallic Materials* (Nauka, Moscow, 1992) [in Russian].
2. A. I. Olemskoĭ and A. Ya. Flat, Usp. Fiz. Nauk **163** (12), 1 (1993) [Phys. Usp. **36**, 1087 (1993)].
3. V. S. Ivanova, A. S. Balankin, I. Zh. Bunin, and A. A. Oksagoev, *Synergetics and Fractals in Materials Science* (Nauka, Moscow, 1994) [in Russian].
4. V. E. Panin, P. V. Kuznetsov, E. E. Deryugin, *et al.*, Fiz. Met. Metalloved. **84**, 118 (1997).
5. P. V. Kuznetsov, V. E. Panin, and J. Schreiber, Theor. Appl. Fract. Mech. **35**, 171 (2001).
6. Z. H. Huang, J. F. Tian, and Z. G. Wang, Mater. Sci. Eng. A **118**, 19 (1989).
7. B. B. Mandelbrot, *The Fractal Geometry Nature* (Freeman, New York, 1983).

Translated by K. Shakhlevich

Technical Physics, Vol. 49, No. 4, 2004, pp. 509–511. Translated from Zhurnal Tekhnicheskoĭ Fiziki, Vol. 74, No. 4, 2004, pp. 133–134.

SHORT COMMUNICATIONS

Kinetic Theory of Rarefied Plasma: The Effective Action Method

I. N. Kosarev

Russian Federal Nuclear Center, Institute of Experimental Physics, Sarov, Nizhni Novgorod Oblast, 607190 Russia
e-mail: kosarev@vniief.ru

Received July 17, 2003

Abstract—A kinetic theory of rarefied plasma that is based on the construction of propagators for distribution functions is developed. The feature of this theory, which is physically equivalent to the standard kinetic theory, is that propagators being constructed for distribution functions are themselves dependent on these distribution functions. © *2004 MAIK "Nauka/Interperiodica".*

The standard kinetic theory for rarefied plasma, where $nr_D^3 \gg 1$ (n is the particle concentration, r_D is the Debye radius of the plasma), is based on a set of integro-differential equations. These are the Boltzmann kinetic equations with collision integral (for particles of each sort) and the Maxwell equations. In the latter, the charge density and current density are expressed through one-particle distribution functions, which, in turn, are determined from the kinetic equations (see, e.g., [1]). In this work, the author suggests a kinetic theory of rarefied plasma (a physical equivalent to the standard kinetic theory) that is based on the construction of propagators for distribution functions, these propagators being dependent on these functions. With such an approach, the study of plasma kinetics is reduced to solving a set of integro-differential equations, so that the problem may be simplified.

Consider a volume V that contains N_a particles of sort a and N_b particles of sort b. In the case of a classical plasma, it suffices to take into account only the contribution of the classical trajectory in the path integral [2], which specifies the propagator of a particle. The classical propagator for the density matrix $\rho(\mathbf{r}, \mathbf{r}', t)$ has the form

$$K_a^M(2,1) = \mu\exp\{(i/\hbar)(S_0(\mathbf{r}_2, t_2; \mathbf{r}_1, t_1) - S_a(\mathbf{r}_2', t_2; \mathbf{r}_1', t_1)\},$$
$$\mu = \left(\frac{m_a}{2\pi\hbar(t_2 - t_1)}\right)^3, \quad (1)$$

where

$$S_a(\mathbf{r}_2, t_2; \mathbf{r}_1, t_1) = \int_{t_1}^{t_2} dt\left\{\frac{m_a\mathbf{v}_a^2(t)}{2} - \sum_{i=2}^{N_a} U_{aa}(\mathbf{R}_i(t) - \mathbf{r}_a(t))\right\} - \int_{t_1}^{t_2} dt\left\{\sum_{j=1}^{N_b} U_{ab}(\mathbf{R}_j(t) - \mathbf{r}_a(t)) - \mathbf{F}_a(t)\mathbf{r}_a(t)\right\} \quad (2)$$

is the classical action of a particle with mass m_a, $\mathbf{v}_a(t)$ and $\mathbf{r}_a(t)$ are the velocity and radius vector of the particle, U_{aa} and U_{ab} are the potential energies of particle–particle interaction, $\mathbf{R}_i$ is the radius vector of a scatterer, and $\mathbf{F}_a$ is the external force acting on the particle. In a rarefied plasma, the characteristic correlation (interaction) time is much shorter than the characteristic relaxation time [1]. Therefore, one may assume that scatterers in (1) and (2) describe piecewise rectilinear trajectories and pass rectilinear segments for a time that is smaller than the relaxation time but longer than the correlation time. In this case, ensemble averaging of propagator (1) is carried out with a multiparticle distribution function where only pair correlations are taken into account (polarization approximation [1]). Such averaging results in an effective-action propagator. In the limit $N \longrightarrow \infty$ and $V \longrightarrow \infty$, the averaged propagator has the form

$$\frac{1}{\mu}K_a(2,1) = \exp\left\{\frac{i}{\hbar}\int_{t_1}^{t_2} dt\left(\frac{m_a\mathbf{v}_a^2(t)}{2} - \frac{m_a\mathbf{v}_a'^2(t)}{2}\right) + n_a V_{aa}^{st} + n_b V_{ba}^{st}\right\}\exp\left\{\frac{i}{\hbar}\int_{t_1}^{t_2} dt(\mathbf{F}_a(t)\cdot\mathbf{r}_a(t) - \mathbf{F}_a(t)\cdot\mathbf{r}_a'(t))\right\}$$
$$+ \sum_{ij = aa, ba, bb}\frac{n_i n_j}{2}\int d\mathbf{R}_1 d\mathbf{R}_2 d\mathbf{p}_1 d\mathbf{p}_2 g_{ij}(\mathbf{R}_1, \mathbf{p}_1, \mathbf{R}_2, \mathbf{p}_2, t_1)$$
$$\times\exp\left\{\frac{i}{\hbar}\int_{t_1}^{t_2} dt\sum_{k=1,2}(-U_{ij}(\mathbf{R}_k - \mathbf{v}_k(t_2 - t) - \mathbf{r}_{a,ij}(t))\right\} \quad (3)$$

1063-7842/04/4904-0509$26.00 © 2004 MAIK "Nauka/Interperiodica"

$$\times \exp\left\{\frac{i}{\hbar}\int_{t_1}^{t_2} dt \sum_{k=1,2} (U_{ij}(\mathbf{R}_k - \mathbf{v}_k(t_2 - t) - \mathbf{r}'_{a,ij}(t)))\right\}$$

$$\times \exp\left\{\frac{i}{\hbar}\int_{t_1}^{t_2} dt\left(\frac{m_a \mathbf{v}^2_{a,ij}(t)}{2} - \frac{m_a \mathbf{v}^2_{a,ij}(t)}{2}\right) + n_a V^{st}_{aa} + n_b V^{st}_{ba}\right\}$$

$$\times \exp\left\{\frac{i}{\hbar}\int_{t_1}^{t_2} dt(\mathbf{F}_a(t)\cdot \mathbf{r}_{a,ij}(t) - \mathbf{F}_a(t)\cdot \mathbf{r}'_{a,ij}(t))\right\}.$$

Here, $g_{ba}(\mathbf{R}_1, \mathbf{p}_1, \mathbf{R}_2, \mathbf{p}_2, t)$ is the pair correlation function, which is expressed through the single-particle distribution functions $f_{a,b}(\mathbf{r}, \mathbf{p}, t)$ (p is the particle momentum) [1],

$$V^{\mathrm{col}}_{ba} = \int d\mathbf{p} d\mathbf{R} f_h(\mathbf{R}, \mathbf{p}, t_1)$$

$$\times \exp\left\{-\frac{i}{\hbar}\int_{t_1}^{t_2} dt(U_{ba}(\mathbf{R} - \mathbf{v}(t_2 - t) - \mathbf{r}_a(t)) \right. \qquad (4)$$

$$\left. - U_{ba}(\mathbf{R} - \mathbf{v}(t_2 - t) - \mathbf{r}'_a(t)))\right\} - 1,$$

and V^{col}_{ba} is the collision volume (the linear Stark effect in the line broadening theory [3]).

In the case of Coulomb interaction, the Weisskopf radius is on the order of the minimal impact parameter $r_{\min}$ in the Landau collision integral [4]. The averaged effect of the scatterer fields on the particle trajectory in (3) can be taken into consideration in terms of the perturbation theory where $r_{\min}/r_D$ and $nr^3_{\min}$ are small parameters (r_D is the Debye radius, which defines the characteristic correlation length of plasma particles).

The first term in (3) describes the evolution of the distribution function in the self-consistent field approximation, and the term with the collision integral in the exponent defines the deceleration (acceleration) of a plasma particle due to the self-consistent field. The other terms describe the effect of the collision integral on the plasma kinetics.

If an external force is so high that $Fr_{\min} \geq U(r_{\min})$, the effect of such a force on the correlation function should be regarded [1].

In the case of a relativistic plasma, one should substitute the relativistic expression for the kinetic energy of a particle into (3) and take into consideration both the scalar and the vector potentials of scatterers [5]. The correlation functions of the particles should also be relativistic [1].

For a quantum plasma, when calculating the path integral, which defines the propagator, one must consider the contributions of all trajectories rather than of the classical trajectory alone. Statistical averaging is carried out over the density matrix. In the polarization approximation, the quantum correlation function is expressed through one-particle density matrices in the Wigner representation ([1, part 3 and references therein]). The averaged propagator is given by

$$K_a(2,1) = \int D[\mathbf{r}_a(t)] \int D[\mathbf{r}'_a(t)]$$

$$\times \exp\left\{\frac{i}{\hbar}\int_{t_1}^{t_2} dt\left(\frac{m_a \mathbf{v}^2_a(t)}{2} - \frac{m_a \mathbf{v}'^2_a(t)}{2}\right)\right\}$$

$$\times \exp\left\{\frac{i}{\hbar}\int_{t_1}^{t_2} dt(\mathbf{F}_a(t)\cdot \mathbf{r}_a(t) - \mathbf{F}_a(t)\cdot \mathbf{r}'_a(t)) \right.$$

$$\left. + n_a V^{\mathrm{col}}_{aa} + n_b V^{\mathrm{col}}_{ba}\right\}$$

$$+ \sum_{i,j = aa, ba, bb} \frac{n_i n_j}{2} \int d\mathbf{R}_1 d\mathbf{R}_2 d\mathbf{R}'_1 d\mathbf{R}'_2$$

$$\times (g_{ij}(\mathbf{R}_1, \mathbf{R}_1, \mathbf{R}_2, \mathbf{R}_2, t_1)\rho_i(\mathbf{R}'_1, \mathbf{R}'_1, t_1)\rho_j(\mathbf{R}'_2, \mathbf{R}'_2, t_1)$$

$$+ g_{ij}(\mathbf{R}'_1, \mathbf{R}'_1, \mathbf{R}'_2, \mathbf{R}'_2, t_1)\rho_i(\mathbf{R}_1, \mathbf{R}_1, t_1)\rho_j(\mathbf{R}_2, \mathbf{R}_2, t_1)) \qquad (5)$$

$$\times \int D[\mathbf{r}_a(t)] \int D[\mathbf{r}'_a(t)] \int_{\mathbf{R}_1(t_1) = \mathbf{R}'_1}^{\mathbf{R}_1(t_2) = \mathbf{R}_1} D[\mathbf{R}_1(t)] \int_{\mathbf{R}_2(t_1) = \mathbf{R}'_2}^{\mathbf{R}_2(t_2) = \mathbf{R}_2} D[\mathbf{R}_2(t)]$$

$$\times \exp\left\{\frac{i}{\hbar}\int_{t_1}^{t_2} dt \sum_{k=1,2}\left(\frac{m_k \dot{R}_k(t)}{2} - U_{ij}(\mathbf{R}_k(t) - \mathbf{r}_a(t))\right)\right\}$$

$$\times \exp\left\{\frac{i}{\hbar}\int_{t_1}^{t_2} dt \sum_{k=1,2} (U_{ij}(\mathbf{R}_k(t) - \mathbf{r}'_a(t)))\right\}$$

$$\times \exp\left\{\frac{i}{\hbar}\int_{t_1}^{t_2} dt\left(\frac{m_a \mathbf{v}^2_a(t)}{2} - \frac{m_a \mathbf{v}'^2_a(t)}{2}\right) + n_a V^{\mathrm{col}}_{aa} + n_b V^{\mathrm{col}}_{ba}\right\}$$

$$\times \exp\left\{\frac{i}{\hbar}\int_{t_1}^{t_2} dt(\mathbf{F}_a(t)\cdot \mathbf{r}_a(t) - \mathbf{F}_a(t)\cdot \mathbf{r}'_a(t))\right\},$$

where

$$V_{ba}^{\mathrm{col}} = \int d\mathbf{R}'\, d\mathbf{R}\, \rho_b(\mathbf{R}, \mathbf{R}, t_1)\rho_a(\mathbf{R}', \mathbf{R}', t_1) \int_{\mathbf{R}(t_1)=\mathbf{R}'}^{\mathbf{R}(t_2)=\mathbf{R}} D[\mathbf{R}(t)]$$

$$\times \left[\exp\left\{ -\frac{i}{\hbar} \int_{t_1}^{t_2} dt \left(\frac{m_b \dot{R}(t)}{2} + U_{ba}(\mathbf{R}(t) - \mathbf{r}_a(t)) \right.\right.\right.$$

$$\left.\left.\left. - U_{ba}(\mathbf{R}(t) - \mathbf{r}_a'(t)) \right) \right\} - 1 \right]$$

is the collision volume.

For a rarefied plasma, the path integrals for scattering particles in (4) and (5) can be calculated in terms of the perturbation theory [2]. The averaged effect of scatterers on a probe particle is also found from the perturbation theory. Exchange interaction is included in the quantum correlation function.

To conclude, expressions (3) and (5) can be considered as a solution to the kinetic problems for short times, i.e., when the distribution function varies insignificantly.

REFERENCES

1. Yu. L. Klimontovich, *Kinetic Theory of Nonideal Gases and Nonideal Plasmas* (Nauka, Moscow, 1975; Pergamon, Oxford, 1982).
2. R. P. Feynman and A. R. Hibbs, *Quantum Mechanics and Path Integrals* (McGraw-Hill, New York, 1965; Mir, Moscow, 1968).
3. H. Griem, *Plasma Spectroscopy* (McGraw-Hill, New York, 1964; Atomizdat, Moscow, 1969); I. I. Sobel'man, *Introduction to the Theory of Atomic Spectra* (Fizmatgiz, Moscow, 1963) [in Russian].
4. E. M. Lifshitz and L. P. Pitaevskii, *Physical Kinetics* (Nauka, Moscow, 1979; Pergamon, Oxford, 1981).
5. L. D. Landau and E. M. Lifshitz, *The Classical Theory of Fields* (Nauka, Moscow, 1973; Pergamon, Oxford, 1975).

Translated by V. Isaakyan

Technical Physics, Vol. 49, No. 4, 2004, pp. 512–515. Translated from Zhurnal Tekhnicheskoĭ Fiziki, Vol. 74, No. 4, 2004, pp. 135–138.

SHORT COMMUNICATIONS

Effect of Mechanical Deformation on the Critical Current in $YBa_2Cu_3O_{7-b}$ Superconducting Films

E. M. Ibragimova*, M. U. Kalanov*, M. A. Kirk, and S. R. Foltyn*****

** Institute of Nuclear Physics, Academy of Sciences of Uzbekistan, Tashkent, 702132 Uzbekistan*

e-mail: ibragimova@inp.uz

*** Argonne National Laboratory, Argonne, Illinois, USA*

**** Los Alamos National Laboratory, New Mexico, USA*

Received September 25, 2003

Abstract—It is shown that local mechanical bending of $YBa_2Cu_3O_{7-b}$ Ag-coated superconducting films deposited on flexible metal substrates in the temperature interval 77–300 K may increase the critical density J_c of the transport current to values as high as 10^6 A/cm^2 or even higher at 77 K. Also, bending decreases the voltage criterion. This means a rise in the intergranular conductivity and, accordingly, a reduction of Joule losses.

In accordance with requirements of high-current electronics, superconducting motors, transformers, and transmission lines must withstand current densities of $J_c > 10^6$ A/cm^2 at 77 K in magnetic fields up to 2 T. To provide a high efficiency and low losses, the insulating layer must be thin and robust. In the Russian project of superconducting transformer, insulation as thin as 10^{-6} m is expected to raise the interturn breakdown voltage to 300 V [1]. Japanese companies are projecting the production of 100- to 1000-m-long and 100-μm-thick tapes coated by an YBaCuO layer that is capable of withstanding $J_c > 10^4$–10^5 A/cm^2 at 77 K [2]. The current status of high-current superconducting technology demonstrates that Bi-based HTSC tapes withstand current densities of 0.14×10^6 A/cm^2 in magnetic fields of 1–8 T only at 4.2 K (although they have $T_c > 77$ K [1]), while YBaCuO tapes may pass currents of density higher than 10^6 A/cm^2 at 77 K [2–4]. To this end, it is necessary to provide good (tough) intergranular contacts (with a small, <7°, misorientation between grains) to provide a high critical transport current, $I_c \sim 100$ A [5]. This is possible when both the metal substrate surface and the $ZrO_2CeO_2 : Y_2O_3$ dielectric buffer layer coated by a superconducting film are biaxially textured [3, 4]. Candidate materials for a buffer spacer between a YBaCuO layer and a substrate (such as MgO, $BaZrO_2$, and $ZrO_2 : Y_2O_3$ [2–4]; α-Al_2O_3: CeO_2 [6]; and $LaAlO_3$ [7]) must not only provide as close lattice matching with superconductors as possible but also have a very high permittivity (≈1000), especially at near-T_c temperatures [8]. However, provision of uniform texture throughout a flexible HTSC tape is still a challenge. Even for a 1-m-long tape, local values of J_c differ by ≈50% [3] and may differ by a factor of 3 [2].

Today, various ways of texturing to increase J_c passing through low-angle grain boundaries in long superconductors are under development. One of them is periodic compacting. In the case of Bi(2223)/Ag tapes, this method makes it possible to raise J_c by 30–40% at 77 K [9].

In this study, we apply local mechanical bending (above and below the elastic limit) in the temperature range 77–300 K to $YBa_2Cu_3O_{7-b}$ superconducting films deposited on flexible metal substrates for greater critical transport current density J_c at 77 K.

Thick (~10^{-6} m) Ag-coated $YBa_2Cu_3O_{7-b}$ films deposited on a 5-mm-wide and 0.3-mm-thick steel tape used as a substrate were prepared at the Los Alamos National Laboratory (USA). The best of them have $J_c > 10^6$ A/cm^{-2} at 75 K in the absence of magnetic field [4]. Specimens studied were 1-cm-long tape fragments (marked a–f) in each of which a superconducting bridge 5- to 6-mm-long and 250- to 300-μm-wide was formed. The cross-sectional area of the bridge varied in the range $(2–3) \times 10^{-6}$ cm^{-2} (see table).

The *I–V* characteristics of the specimens were taken at the Argonne National Laboratory at 77 K by the standard four-point probe method. The specimen was placed in a cooled cell and pressed against strip gold contacts. The spacings between the current and voltage contact pads were 6 and 2 mm, respectively. For this geometry, the range 5×10^{-7}–10^{-6} V may be considered a voltage criterion for a kink (kink voltage range) in the *I–V* curve constructed in the log–log coordinates. To avoid Joule heating by a current of up to 10 A passing through the bridge with the cross-sectional area mentioned above, we used a pulsed current generator (pulse

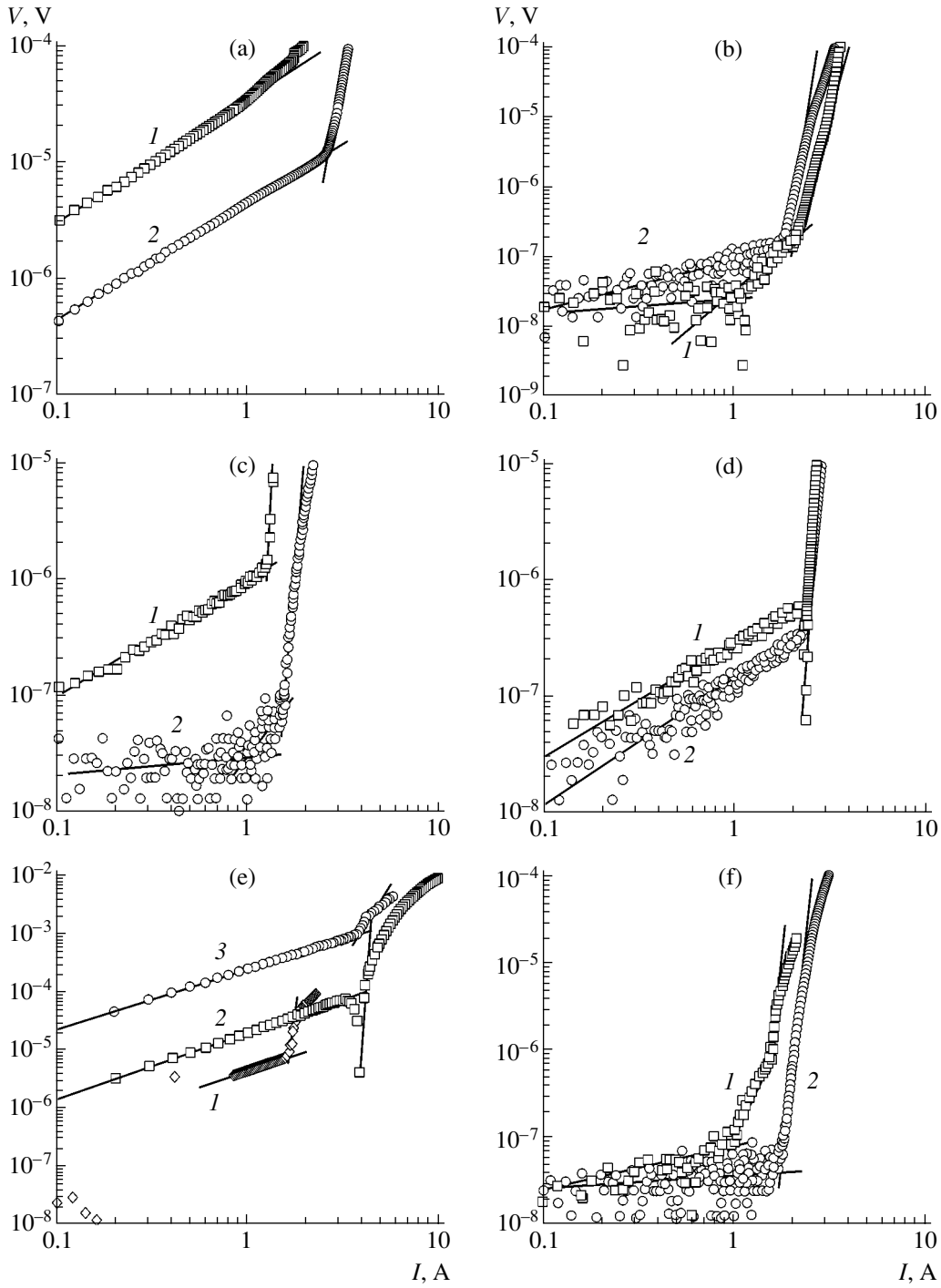

Fig. 1. Effect of bending on the *I–V* characteristics of Ag-coated YBaCuO films at 77 K in the self-field. (a), (e), and (f), are strongly (plastically) deformed specimens; (b), (c), and (d) are weakly (elastically) deformed specimens. Specimen (e) was subjected to post-deformation annealing in oxygen at 500°C. The lines are the quadratic means of data points (symbols). (*1*) As-prepared specimens, (*2*) deformed specimens, and (*3*) annealed specimen.

duration 10^{-6} s). The initial values of T_c measured by both inductive and resistive methods were about 90 K (the lowest value was 88 K). In the absence of an external magnetic field, the values of J_c for as-prepared specimens (a)–(f) at 77 K varied in the range (0.40–0.93) × 10^6 A/cm^2 (see table). This more than twofold difference in J_c, which was observed in 2-m-long conductors in local measurements, is a serious obstacle to the application of these superconductors in power industry [2].

The effect of deformation on the critical current density in Ag-coated YBaCuO films deposited on a flexible substrate at 77 K (in the self-field)

Specimen	Cross-sectional area, 10^{-6} cm^2	As-prepared specimens			Deformed specimens			Relative change J_c, %
		I_c, A	J_c, MA/cm^2	V_c, 10^{-6}V	I_c, A	J_c, MA/cm^2	V_c, 10^{-6}V	
*A**	2.07	1.2	0.58	40.0	2.7	1.3	13.0	+124
B	2.64	2.0	0.76	0.17	1.8	0.68	0.12	–11
C	3.11	1.26	0.4	1.3	1.56	0.5	0.07	+25
D	2.46	2.3	0.93	0.6	2.3	0.93	0.4	0
*E**	3.0	1.7	0.57	8.0	3.9	1.3	50.0	+128
*F**	2.24	1.0	0.45	0.1	1.8	0.8	0.05	+78

Note: I_c, the critical current flowing through the specimen; J_c, the critical current density; V_c, the voltage criterion (voltage at which J_c is reached). *A**, *E**, and *F** stand for strongly (plastically) deformed specimens; *B*, *C*, and *D* are weakly (elastically) deformed specimens.

Bending was carried out in a cryogenic cell in such a way as to simulate possible operating conditions for preparing solenoids. At 300 K, the center of the specimen was pressed by controllably turning a screw. Next, the cell with the specimen was cooled to 77 K and slowly heated as liquid nitrogen was evaporated. Specimens (a), (e), and (f) with initially low values of J_c were strongly deformed (above the elastic limit), whereas specimens (b), (c), and (d) were deformed weakly (below this limit). We could compare the effect of high (plastic) and weak (elastic) deformation on specimens (c) and (f), in which the critical current densities J_c were equally low. For comparison, one of the strongly deformed specimens (e) was annealed in oxygen at 500°C for 1 h and then slowly cooled in order for mechanical stresses to relax. The *I–V* characteristics (in the log–log coordinates) of all the specimens (a)–(f) before and after deformation, along with the *I–V* curve for specimen (e) annealed in oxygen, are depicted in Fig. 1. The figure shows the quadratic means of data points (squares correspond to the as-prepared specimens; circles, to the deformed ones). It is seen that the *I–V* characteristics for the as-prepared specimens ((b), (e), and (f)) have two kinks, i.e., two values of J_c corresponding to different superconducting clusters. This indicates that the film is textured nonuniformly.

The values of the critical current I_c found experimentally, the critical (kink) voltage V_c, the calculated cross-sectional areas of the superconducting bridges, and the critical current densities J_c, with their variation due to deformation, are listed in the table.

In weakly deformed specimens (b) and (c), J_c changed insignificantly, while in specimen (d), the initially high value of J_c remained the same. However, for specimen (c) with the initially low value of J_c, the voltage V_c decreased almost 20-fold, although J_c increased only by 25%. It follows that the intergranular conductivity is enhanced and, accordingly, the Joule losses decrease.

Specimens (a) and (e), which were subjected to strong plastic deformation, showed a more than twofold increase in the critical current. In specimen (f) from the same series of the specimens, the critical current J_c increased only by 78%. It appears that specimens (a) and (f) were deformed under optimal conditions, as a result of which the severalfold rise in J_c was accompanied by the severalfold reduction of the kink voltage. In specimen (e), where J_c grew to the maximal extent, the kink voltage, on the contrary, decreased by a factor of 5. Comparing the effect of plastic and elastic deformation on specimens (c) and (f) with the equally low values of J_c, one can see how loose intergranular contacts become tough with the corresponding decrease in the voltage V_c.

For example, testing (with a 1-cm step) tape sections with initially low values of J_c, $(0.4–0.5) \times 10^6$ A/cm^2, and controllably bending these sections, one can enhance the related values of J_c up to $\geq 10^6$ A/cm^2, improve the longitudinal homogeneity of the tapes, and thus improve considerably the transport characteristics of long superconducting tapes. As was mentioned above, periodic compacting of Bi(2223)/Ag tapes makes it possible to raise J_c by 30–40% [9].

Thus, we experimentally showed that local bending (at 77 K) may change the *I–V* characteristics of Ag-coated $YBa_2Cu_3O_{7-b}$ superconducting films deposited on flexible steel substrates. Namely, the critical current density increases considerably (by a factor of 2), while the voltage criterion (kink voltage) decreases. This indicates that the intergranular conductivity rises and Joule losses drop.

REFERENCES

1. N. A. Chernoplekov, Usp. Fiz. Nauk **172**, 716 (2002).
2. Y. Shiohara and T. Izumi, Mater. Res. Soc. Symp. Proc. **659**, II.1.1 (2001).
3. S. R. Foltyn, P. N. Arendt, P. C. Dowden, *et al.*, IEEE Trans. Appl. Supercond. **9**, 1519 (1999).
4. Q. X. Jia, S. R. Foltyn, P. N. Arendt, and J. F. Smith, Appl. Phys. Lett. **80**, 1601 (2002).
5. M. Watahiki, W. J. Jang, N. Sakai, and M. Murakami, Physica C **296**, 43 (1998).
6. E. K. Hollmann, D. A. Plotkin, S. V. Razumov, and A. V. Tumarin, Zh. Tekh. Fiz. **69** (9), 132 (1999) [Tech. Phys. **44**, 1119 (1999)].
7. O. I. Lebedev, J.-F. Hamet, G. Van Tendeloo, *et al.*, J. Appl. Phys. **90**, 5261 (2001).
8. P. Lunkenheimer, V. Bobnar, A. V. Pronin, *et al.*, Phys. Rev. B **66**, 052105 (2002).
9. F. Marti, Y. B. Huang, G. Witz, *et al.*, IEEE Trans. Appl. Supercond. **9**, 2521 (1999).

Translated by Yu. Vishnyakov

Technical Physics, Vol. 49, No. 4, 2004, pp. 516–519. Translated from Zhurnal Tekhnicheskoĭ Fiziki, Vol. 74, No. 4, 2004, pp. 139–142.

SHORT COMMUNICATIONS

Modification of the Copper Slab Surface Submicrorelief by Applying High-Density Electric Current

I. P. Shcherbakov, D. V. Churaev, and V. N. Svetlov

Ioffe Physicotechnical Institute, Russian Academy of Sciences, Politekhnicheskaya ul. 26, St. Petersburg, 194021 Russia

e-mail: sherbakov.mhd@mail.ioffe.ru

Received September 30, 2003

Abstract—The modification of the copper slab surface submicrorelief by applying a current pulse of density higher than J_{thr}. The passage of a high-density current is shown to change the pattern of the copper slab polished surface, resulting in the formation of regular periodic structures. These structures are produced when moving dislocations emerge on the specimen surface. © *2004 MAIK "Nauka/Interperiodica".*

INTRODUCTION

Metals usually take a desired shape when subjected to plastic deformation. However, plastic deformation is sometimes impossible, so that special methods are invoked. One of them that has already gained much recognition is the application of high-density (up to 100 kA/cm^2) current pulses to a metallic material. When passing through metallic conductors, electric current causes many secondary effects, such as Joule heating, generation of electromagnetic fields, scattering of conduction electrons by phonons and lattice defects, etc. Obviously, if such a high current density were applied for a long time, the metal would evaporate almost instantaneously because of Joule heat evolution. To avoid this, very short (≈100 μs) low-frequency (≈1 Hz) current pulses are applied. Such a method of processing was called electroplastic deformation [1, 2]. In spite of wide use of this method, its underlying mechanism still remains unclear.

The drift motion of conduction electrons in a metal under the action of an electric field causes electric current. In a perfect crystal, this motion does not experience dissipation (resistance). In an imperfect crystal, conduction electrons interact with defects like dislocations, thermal motion of atoms, etc. In this case, dislocations are under the action of the electronic drag force F_N, which is proportional to the drift velocity V of electrons [3]:

$$F_N = B_N V, \quad V = -j/(en), \tag{1}$$

where j is the electric current density, e is the elementary charge, n is the concentration of conduction electrons, and B_N is the coefficient of dislocation–electron drag.

Thus, the action of force (1) is equivalent to the application of a mechanical stress to the specimen:

$$S_N = F_N/b,$$

where b is the Burgers vector.

It was shown [4–6] that the application of a mechanical stress to noble metals (Cu, Ag, and Au) generates submicrodefects on the surface in the form of a prism with a vertex angle of ≈70°. It is known [7] that Cu, Ag, and Au have the fcc lattice where the angle between the (111) and $(11\bar{1})$ easy slip planes roughly equals ≈70.5°. It is therefore natural to suppose that these defects arise when moving dislocations cross the surface of the metal [5, 6].

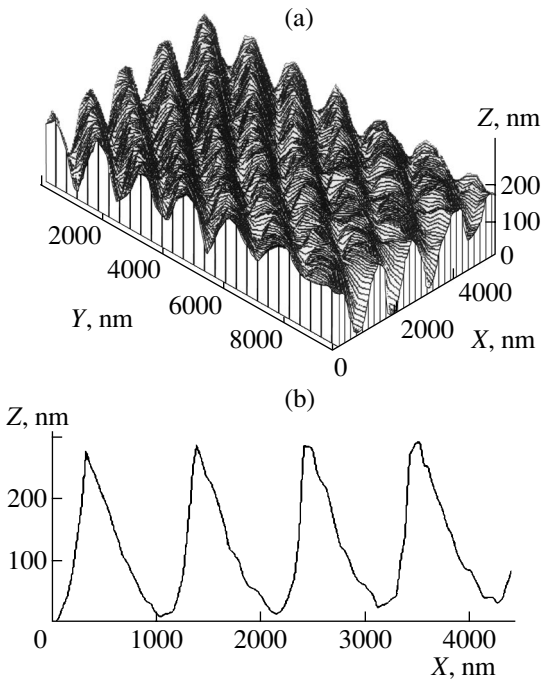

Fig. 1. Topogram taken from the GaAs diffraction grating (height $h \approx 0.25$ μm, spacing $L \approx 1$ μm) covered by a gold layer.

1063-7842/04/4904-0516$26.00 © 2004 MAIK "Nauka/Interperiodica"

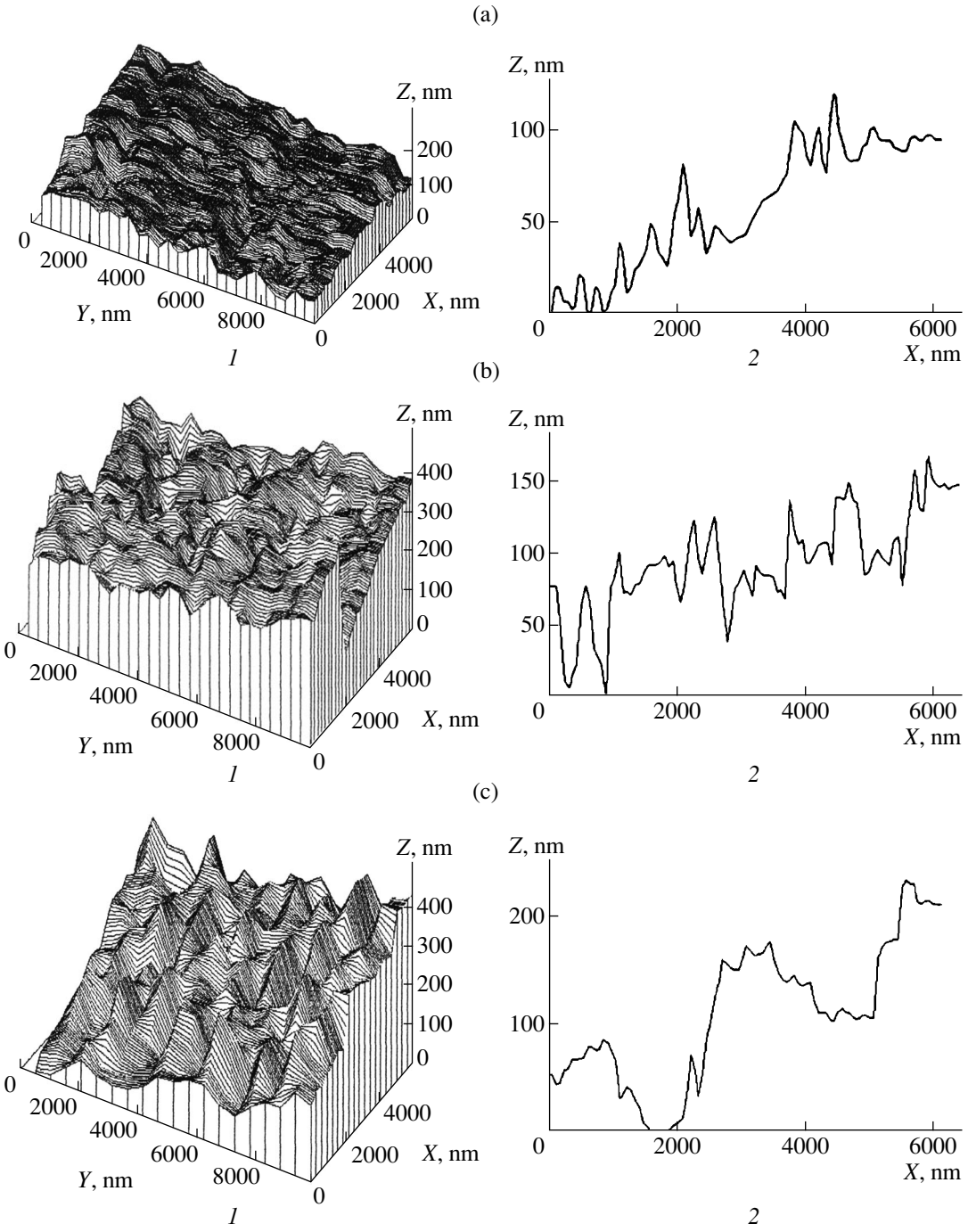

Fig. 2. Fragments of 3D topograms taken from the copper specimen (a) after polishing, (b) after polishing and application of the current with density $J = 200$ kA/cm^2, and (c) after polishing and application of the current with $J = 700$ kA/cm^2.

One may assume that an electric field acting on metallic conductors will also modify their surface. This work is aimed at checking this assumption.

EXPERIMENTAL

We studied the profiles of 99.96% pure 30-μm-thick copper platelets measuring 3.3×1.6 cm. The surface pattern was examined with an RTP-1 scanning tunnel profilometer (designed by the Research Institute of Physics at St. Petersburg State University and manufactured by the Éra production cooperative).

The resolution, operating stability, and calibration of the instrument were checked with a GaAs diffraction grating (the height and spacing are, respectively, $h = 0.25$ μm and $L = 1$ μm) covered by a gold layer.

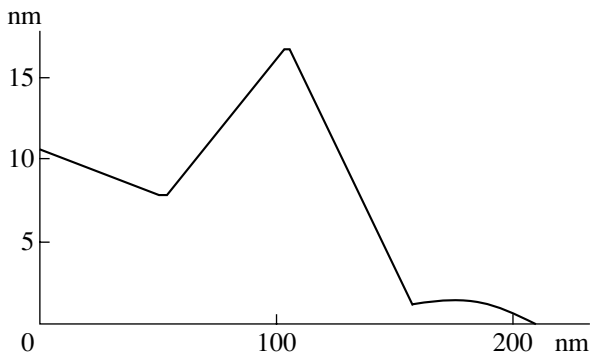

Fig. 3. Shape of one of the defects formed.

Figure 1a shows the 3D image of the diffraction grating, where the height and spacing of the grating are distinctly seen. From the section *XZ* of the image (Fig. 1b), the height and spacing are estimated as $h \approx 250$ nm and $L \approx 1000$ nm. This is in agreement with the actual grating parameters and means that the tunnel microscope operates properly. To be sure that the operating conditions of the instrument are chosen in a proper way and it reliably displays the actual surface of the specimen, we took the topogram of the grating before and after imaging the surface. Measuring tips were made of a tungsten wire by electrochemical etching. The shape of the tips was estimated by comparing with the finest defects in the topograms. In the profilometer, the tip can travel no more than 1 μm normally to the surface. Surface microirregularities higher than 1 μm were removed by polishing with diamond pastes. Then, the specimens were rinsed in acetone and alcohol. A current was applied to the copper specimen by means of a capacitor bank (capacitance 400 μF, voltage up to 5 kV), which was discharged when the voltage reached the desired value.

The parameters of the discharge were recorded with a Rogowski loop (discharge current *I*) and ohmic voltage divider (discharge voltage *U*), which was connected to an ADC. The data were stored on a computer. The current and voltage waveforms were obtained by using a special program devised for processing oscillograms.

RESULTS OF MEASUREMENTS

Figure 2 demonstrates fragments of the 3D topograms taken from the surface of the copper specimen (a) before and (b, c) after applying 300-μs-long current pulses of various density that exceeds the threshold value $J_{thr} = 50$ kA/cm^2. At lower densities, no changes in the submicrorelief were observed. It is seen that the passage of the current modifies the surface microrelief of the specimens: the surface relief of the specimens that were only polished (Fig. 2a *1*) differs from the relief of those polished and subjected to the pulses (Figs. 2b *1*, 2c *1*). Figure 2a *2* shows the surface profile of the polished copper specimen in the section *XZ*. Surface irregularities are seen to vary in height (depth) from 15 to 30 nm, and their transverse dimensions vary from 50 to 200 nm. The linear density of defects is near 2.5×10^{-3} nm^{-1}.

The passage of the current changes significantly not only the surface relief (Fig. 2b *1*) but also the size and density of defects. At $J = 200$ kA/cm^2, initially fine defects merge together. The height (depth) of coarser defects increases to 30–100 nm; their transverse dimensions, to 1000–2000 nm. The density of defects decreases to $\approx 10^{-3}$ nm^{-1} (Fig. 2b *2*).

At $J = 700$ kA/cm^2, the surface exhibits regular periodic structures (Fig. 2c *1*). The height (depth) and the transverse dimensions of these structures increase still further: to 100–200 and to 1800–2500 nm, respectively. At the same time, the density of defects decreases to $\approx 0.5 \times 10^{-3}$ nm^{-1} (Fig. 2c *2*). On all the topograms, the basic features forming the relief are irregularities almost equal in shape and size that, when superposed, produce the profiles observed on the sections of the surfaces. The enlarged view of one such defect is shown in Fig. 3. The height (depth) of these imperfections vary from 15 to 30 nm; their transverse size, from 50 to 200 nm. In the volume, they appear as prisms three faces of which are nearly perpendicular to the specimen surface and the fourth one makes an angle of ≈30° with the surface. The prism angle is ≈70° (Fig. 3). The orientation of the defect walls in Figs. 2b and 2c suggests that these defects arise when dislocations emerge on the surface under the action of stresses (as in the case described in [4, 5]). The defects present on the polished surface not processed by the current are also associated with the emergence of dislocations on the surface. During mechanical polishing, dislocations are known to reach the surface, moving along easy slip planes, and create a specific surface pattern shown in Fig. 2a [7].

CONCLUSIONS

It is shown that, passing through copper specimens, a current of higher-than-threshold density changes the submicrorelief of the surface: new defects originate and old polishing-related ones rearrange into regular clusters the size of which depend on the current density.

The shape and orientation of nanodefects on the surface confirm the supposition that they arise when movable dislocations emerge on the specimen surface.

Our investigation supports the assumption that the dislocation mechanism is behind pattern modification on metal surfaces subjected to electric current pulses. This offers the possibility of controlling this modification and thereby creating a desired microrelief.

REFERENCES

1. V. I. Spitsyn and O. A. Troitskiĭ, *Electroplastic Deformation of Metals* (Nauka, Moscow, 1985) [in Russian].
2. V. E. Gromov, L. B. Zuev, E. V. Kozlov, and V. Ya. Tsellermaĭer, *Electrically Stimulated Ductility of Metals and Alloys* (Nedra, Moscow, 1996) [in Russian].
3. M. I. Kaganov, V. Ya. Kravchenko, and V. D. Natsik, Usp. Fiz. Nauk **11**, 655 (1993).
4. V. I. Vettegren', V. L. Gilyarov, S. N. Rakhimov, and V. N. Svetlov, Fiz. Tverd. Tela (St. Petersburg) **40**, 668 (1998) [Phys. Solid State **40**, 614 (1998)].
5. V. I. Vettegren', S. N. Rakhimov, and V. N. Svetlov, Fiz. Tverd. Tela (St. Petersburg) **40**, 2180 (1998) [Phys. Solid State **40**, 1977 (1998)].
6. K. B. Abramova, V. I. Vettegren', I. P. Shcherbakov, *et al.*, Zh. Tekh. Fiz. **69** (12), 102 (1999) [Tech. Phys. **44**, 1491 (1999)]; B. R. Chandra, M. S. Ryan, R. Seema, *et al.*, Cryst. Res. Technol. **31**, 495 (1996).
7. I. I. Novikov, *Defects of the Crystal Structure of Metals* (Metallurgiya, Moscow, 1983) [in Russian].

Translated by V. Isaakyan